Solid-state reaction of a Ni(Co) thin film with InGaAs : microstructural analyses

Seifeddine Zhiou

To cite this version:

Seifeddine Zhiou. Solid-state reaction of a Ni(Co) thin film with InGaAs : microstructural analyses. Mechanics of materials [physics.class-ph]. Université Grenoble Alpes, 2016. English. NNT : 2016GREAY067 . tel-01592201

HAL Id: tel-01592201
https://theses.hal.science/tel-01592201v1

Submitted on 22 Sep 2017

Communauté
UNIVERSITÉ Grenoble Alpes

THÈSE

Pour obtenir le grade de

DOCTEUR DE LA COMMUNAUTÉ UNIVERSITÉ GRENOBLE ALPES

Spécialité : **Physique des matériaux**

Arrêté ministériel : 25 mai 2016

Présentée par

Seifeddine ZHIOU

Thèse dirigée par **Patrice GERGAUD**

préparée au sein du **Laboratoire d'Electronique et de Technologie de l'Information (CEA, LETI)**
dans **l'École Doctorale de Physique de Grenoble**

Réaction à l'état solide d'un film mince de Ni(Co) avec InGaAs: analyses microstructurales

Thèse soutenue publiquement le **17 novembre 2016** devant le jury composé de :

M. Roland MADAR
Directeur de Recherches émérite, LMGP, Président de jury
M. Khalid HOUMMADA
MCF., Aix-Marseille Univ.-IM2NP, Rapporteur
M. Christian LAVOIE
Professeur, Ecole Polytechnique de Montréal/IBM, Rapporteur
M. Christophe DETAVERNIER
Professeur, Université de Gand, Examinateur
M. Joris PROOST
Professeur, Université Catholique du Louvain, Examinateur
M. Patrice GERGAUD
Ingénieur de recherche, CEA-LETI, Membre
M. Hubert RENEVIER
Professeur, Grenoble INP – LMGP, Examinateur
M. Philippe RODRIGUEZ
Ingénieur de recherche, CEA-LETI, Membre
M. Fabrice NEMOUCHI
Ingénieur de recherche, CEA-LETI, Invité

À la mémoire de Abderraouf Zhiou…

À Naama, Dhouha et Nour…

“Je ne me persuade pas aisément qu’Epicure, Platon et Pythagore nous aient donné pour argent comptant leurs Atomes, leurs Idées et leurs Nombres. Ils étaient trop sages pour établir leurs articles de foi de choses si incertaines et si débattables.”

—Michel de Montaigne, *Les Essais – Livre II*

Remerciements

Ainsi je me trouve en train d'écrire les mots qui préfacent ce manuscrit mais qui, paradoxalement, sont les derniers à être écrits. Cette thèse, fruit d'un travail sur trois années, a été rendue possible grâce à la présence de plusieurs personnes.

Je remercie chaleureusement Roland Madar, Christian Lavoie, Khalid Hoummada, Christophe Detavernier, Hubert Renevier et Joris Proost pour avoir accepté de juger et critiquer mon travail ainsi que pour leur intérêt manifeste à cette thèse et leur volonté d'échanger sur le sujet.

Je remercie Patrice Gergaud pour avoir dirigé ce travail de thèse et lui exprime ma gratitude pour les enseignements qu'il m'a transmis. Merci Patrice pour tes conseils, ta disponibilité, ta patience et ton écoute. J'avais la chance de t'avoir comme directeur de thèse, je suis honoré d'avoir été formé à la recherche à tes côtés, je te suis reconnaissant pour m'avoir donné les moyens de réussir et je souhaite autant pour tout étudiant qui se lance dans une thèse de doctorat.

Cette thèse a été aussi co-encadrée par la « team contact » du Leti. Je ne remercierais jamais assez mes encadrants Fabrice Nemouchi et Philippe Rodriguez pour leur aide, leur disponibilité et leurs conseils. Votre suivi, votre soutien et votre présence au quotidien ont été indispensables à la réussite de ce projet de thèse. J'ai beaucoup appris à vos côtés, et entre thermodynamique, réactions aux interfaces, propriétés des contacts, etc. j'ai aussi appris qu'il ne fallait jamais mettre de petits pots de crème dans sa poche arrière, surtout en transports en communs franciscain ! Merci pour tout !

Je tiens à remercier mes deux collègues successifs de bureau. Merci à David Laloum pour les conversations, ô combien riches, constructives et pas du tout futiles, que nous avons pu avoir au bureau, dehors, ou à table. Sinon une dernière fois David, non la X1 c'est bien meilleur que la PS4 et le sera encore plus en fin d'année. Bon courage pour la nouvelle voie que tu t'es choisie et plein de bonheur pour toi, pour Audrey et pour le petit Simon. Merci également à Guillaume Freychet camarde de bureau au P355 cette fois-ci, dont la motivation est presque contagieuse et dont l'énergie n'est dépassée que par son imagination lorsqu'il s'agit de lancer des blagues. Que la force soit avec vous !

Je tiens à remercier Jean-Claude Royer et Nicolas Lhermet, nos chefs de service successifs, pour m'avoir accueilli au sein du Service de Caractérisation des Matériaux et Composants au Leti. Merci également à François Bertin, animateur scientifique, pour son intérêt porté à ce sujet de thèse.

Merci à la « team RX » que je côtoyais quotidiennement, Nicolas Vaxelaire, Fréderic Fillot, Pierre Bleuet et Caroline Curfs et merci aussi aux deux assistantes, Sophie Riondet du côté Leti et Sylvaine Cetra du côté LTM grâce auxquelles les tâches administratives ont été rendues bien plus faciles.

J'adresse également mes remerciements aux personnes avec qui j'ai collaboré de près ou de loin, la team ESRF-D2AM : Tra Nguyen, Nathalie Boudet, Nils Blanc, Stéphan Arnaud et Jayanth Channagiri mais aussi Elodie Ghegin, Emilie Bourjot, Zineb Saghi, Laetitia Rapenne, Sylvie Favier, Coralie Sésé et Stéphane Coindeau.

L'excellente ambiance de travail a été primordiale durant ces années pour la réussite de cette thèse. Ainsi, les amis, que ce soit à H1, plus rarement à H3, en soirée, ou simplement en pause-café vous avez rendu le quotidien moins monotone et le travail bien plus intéressant. Merci aux anciens thésards, aux plus jeunes d'entre nous, aux stagiaires et aux post-docs. Sylvain Pouch, Alexandre Lissowski, Tanguy Terlier, Wael Hourani, Charlotte Zborowski (un des rare soutiens pour aller à H3 le midi), Gael Goret (dont l'aide était indispensable et fort utile pour Python), Billal Allouch, Tony Printemps, Céline Hadji, Djawahar Ferrah, Viktoria Gorbenko (merci encore une fois pour le travail de relecture sur la thèse !), Paul Risterucci, Thibaut Bénéfice, Luis Perini, Munique Kazar, Vincent Guigoz, Rafael Kluender, Dario Sanchez (qui a enrichi notre vocabulaire en portugais-brésilien, je suis passé de 0 à 4 mots appris en 3 années), Arnaud Bordes, Eric Langer (vive der König, vive die Pommes !), Pablo Fernandez, Michelle Alvares, Mathieu Frégnaux, Youcef Kerdja, Armande Capitaine, Jorge Morales, Maiglid Moreno, Cécile Cadoux, Anass Benayad, Brice Eychenne, Kim Hokwon, Axel Pic. Je souhaite bon courage à tous les stagiaires (padawan, comme diraient certains) et thésards qui continuent le travail et une bonne continuation aux autres.

Enfin, une pensée particulière à ma famille qui a été toujours là quand il le fallait, merci du fond du cœur à Naama, Nour et Dhouha.

Contents

Abstract

Cette thèse porte sur l'analyse microstructurale d'intermétalliques formés par réaction à l'état solide entre une couche mince de métal Ni(Co) et un substrat d'InGaAs et s'inscrit dans le cadre du développement de reprises de contact pour les dispositifs MOSFET sub-10 nm ou les applications photoniques. Ce travail comporte une partie relative au développement d'une méthodologie de diffraction des rayons x adaptée à ces composés très texturés et deux parties distinctes où nous décrivons et discutons les résultats expérimentaux. L'étude microstructurale (phase, texture...) des intermétalliques obtenus par réaction à l'état solide est rendue complexe par la formation transitoire de phases métastables, non stœchiométriques parfois, contraintes mécaniquement, et présentant en général des orientations cristallines (texture cristallographique) très marquées. Du fait de cette complexité microstructurale, ces intermétalliques n'ont souvent pas été caractérisés de façon complète et peu de connaissances se trouvent sur leur structure et leur formation. Aussi, et pour caractériser de façon complète et sans omettre des phases ou des orientations dans le système Ni-In-Ga-As, nous avons contribué au développement d'une méthode de mesure globale et rapide par diffraction des rayons X permettant de reconstruire une cartographie large 3D de l'espace réciproque. Les données recueillies par cette méthode sont reconstruites afin d'extraire soit des diagrammes de diffraction dits « détexturés », soit des figures de pôle...permettant une analyse semi quantitative de la microstructure des échantillons.

Dans la première partie des résultats expérimentaux, nous nous intéressons à la caractérisation des intermétalliques formés à partir d'empilements Ni/InGaAs/InP recuits ex-situ à différentes températures. Nous décrivons la formation des intermétalliques, leurs textures, et leurs paramètres structuraux. Nous relevons certains aspects de la microstructure qui évoluent en fonction de la température de recuit comme l'anisotropie de texture, la stœchiométrie des intermétalliques et le domaine d'existence thermique et nous proposons des hypothèses qui peuvent expliquer l'évolution de ces phénomènes. Cette première étude faite sur des substrats InP a été confrontée aux résultats obtenus pour des intermétalliques similaires réalisés sur substrats InGaAs/GaAs/Si. En effet, les substrats Si sont les substrats industriellement ciblés pour la réalisation de composés logiques à canal III-V à grande échelle (sur des plaquettes de 300mm de diamètre). Ensuite, nous avons comparé la métallisation de la couche d'InGaAs dans le cas de Ni pur avec la métallisation d'InGaAs lorsqu'un élément d'alliage (Co) est ajouté à la couche de Ni. Ainsi, l'analyse microstructurale révèle des différences notamment sur

les textures qui ont été interprétées sur la base de considérations thermodynamiques, mais aussi structurales comme l'alignement des deux couches entre elles, liées à des aspects plus cinétiques.

Dans la deuxième partie de ce travail, nous présentons les résultats des analyses in situ effectuées par cartographies de l'espace réciproque en 3D au synchrotron ESRF à Grenoble. Il s'agit de suivre en temps réel par diffraction des rayons X, les réactions à l'état solide des échantillons du type Ni (7 nm et 20 nm)/InGaAs/InP et $Ni_{0.9}Co_{0.1}$ (20 nm)/InGaAs/InP lors de recuits par rampes... Ensuite, nous avons effectué des recuits isothermes sur les échantillons de type Ni (20 nm)/InGaAs/InP. Ces différentes mesures, couplées avec des hypothèses sur la croissance nous ont permis d'extraire les paramètres cinétiques relatifs à la formation de la première phase d'intermétallique. Les textures observées et leur évolution lors des recuits thermiques in situ sont différents des recuits ex situ. Ceci peut notamment être expliqué par un mode de recuit différent dans le cas in situ où la cinétique du système est plus lente, favorisant ainsi des structures et textures qui pourraient êtreplus stables.

This thesis focuses on the microstructural analysis of intermetallics formed by solid-state reaction between a thin layer of Ni (Co) metal and an InGaAs substrate and was carried out in the framework of contact development for sub-10 nm MOSFET but have also photonic applications. This work includes a part related to the development of an X-ray diffraction methodology adapted to highly textured compounds and two distinct parts in which we describe and discuss the experimental results.

The microstructural study (phase, texture ...) of intermetallics obtained by solid-state reaction is complicated due to the formation of transient metastable, often non-stoichiometric and mechanically stressed phases. These phases have generally very marked crystalline orientations (crystallographic texture). Because of this microstructural complexity, these intermetallic have often been not fully characterized and there is little knowledge about their structure and formation. Moreover, and to fully characterize the Ni-In-Ga-As system without omitting phases or textures, we have contributed to the development of a comprehensive method of rapid measurement by X-ray diffraction to reconstruct large 3D maps of the reciprocal space. The collected data through this method are reconstructed to extract either diffraction diagrams called "detextured" diagrams or pole figures ... which allows a semi-quantitative analysis of the intermetallic microstructure. In the first part of the experimental results, we focus on the characterization of intermetallic formed through Ni / InGaAs / InP stacks and annealed ex situ at different temperatures. We describe the formation of the intermetallics, textures, and structural parameters. We note some aspects which vary depending on the annealing temperature such as the texture anisotropy, the stoichiometry of intermetallic and range of thermal existence and propose hypotheses that can explain the evolution of these phenomena. The studies on InP substrates were compared to results obtained for similar intermetallic made on GaAs / Si substrates. Indeed, the Si substrates are targeted for industrials to achieve logic compounds III-V channel large-scale (on 300 mm wafers). Then, we compared the metallization of the InGaAs layer in the case of pure Ni metallization with the results when an alloying element (cobalt) was added to the Ni layer. The microstructural analysis revealed several differences especially texture differences. These differences were interpreted on the basis of thermodynamic considerations, but also on the basis of structural alignment of the two layers together which are also linked to more kinetic aspects.

In the second part of this work, we present the analysis results of studies performed by in situ 3D Reciprocal Space Mapping on the ESRF synchrotron in Grenoble. We followed the formation and stability of the intermetallics by real-time X-ray diffraction measurements, for different kind of samples: Ni (7 nm and 20 nm) / InGaAs / InP and $Ni_{0.9}Co_{0.1}$ (20 nm) / InGaAs / InP, using ramp annealing... Then, we performed isothermal annealings for Ni(20 nm) / InGaAs / InP samples. These measurements, coupled with assumptions on the intermetallic growth, allowed us to extract the kinetic parameters for the formation of the first phase of the intermetallic. The observed textures and their evolution during in situ thermal annealings are different than ex situ annealing. This can be explained by a different mode of annealing in the case of in situ where the kinetics of the system is slower, thus favoring the most stable structures and textures.

Introduction générale

En réduisant la taille des dispositifs électroniques à base de Si à des dimensions nanométriques, les transistors MOSFET (Metal Oxide Semiconductor Field Effect Transistor) atteignent leurs limites fondamentales. En effet, bien que les limites relatives aux procédés de fabrication aient été largement surpassées (notamment en ce qui concerne la résolution d'impression de photolithographie qui a été amplement améliorée), les limites physiques relatives au Si et le comportement des porteurs de charge à des épaisseurs extrêmes sont difficilement surmontables. Une deuxième problématique liée aux dispositifs à base de silicium est la problématique de dissipation de puissance à l'état statique de transistor (la puissance statique servant à maintenir les états logiques à leur valeur entre une permutation de signal). En effet, la dissipation est reliée aux courants de fuites dans le dispositif, ces courants étant inévitables. Cette problématique est d'autant plus importante lorsque les transistors sont de taille nanométrique et leur densité d'intégration extrêmement élevée ce qui provoque des problèmes de surchauffe. Ainsi, il s'avère que les prochains nœuds technologiques des transistor CMOS soient compliqués à concevoir du fait des propriétés intrinsèque du Si. Cependant, deux solutions majeures s'offrent pour pallier à ces problématiques. La première solution consisterait à revoir l'architecture des transistors planaires « classiques » et à imaginer de nouvelles architectures, moins couteuses en termes d'énergie de fonctionnement et qui permettent de mieux contrôler les courants de fuite. Cette solution est plus ou moins aboutie et se manifeste dans les transistors à canal enfouit FD-SOI (Fully Depleted Silicon On Insulator), des transistors dits « tri-gate » où le contrôle de courant dans la grille (et donc du champ électrostatique agissant sur les porteurs de charge dans le canal) se fait non pas par une seule direction, mais par trois directions à la fois. Une deuxième solution aussi intéressante que radicale est le changement de matériau de canal en remplaçant le silicium par un matériau qui offre une mobilité de porteurs de charge plus importante. En effet, si la mobilité de porteurs de charges est plus importante, il serait possible de fournir moins d'énergie pour le fonctionnement du transistor et continuer à obtenir des performances acceptables pour le nœud technologique visé. A cet effet, les composés III-V, et notamment les composés $\text{In}_x\text{Ga}_{1-x}\text{As}$ constituent des candidats idéaux pour remplacer le silicium. En effet, ces composés présentent une mobilité de porteurs de charge par rapport au silicium (à titre d'exemple, la mobilité des porteurs de charge de l'$\text{In}_{0.53}\text{Ga}_{0.47}\text{As}$ est environ 10 fois supérieure à celle du Si).

Les possibilités de fabrication de composants microélectroniques à base de matériaux III-V ont commencé à être explorées pendant les années 60. Cependant, la piste des matériaux III-V a été délaissée à cause des oxydes à l'interface trop compliqués à graver. Toujours est-il, des études récentes ont réussi à démontrer la capacité à surmonter cette problématique et la faisabilité des transistors MOSFET à base d'InGaAs à échelle nanométrique. Ces études encourageantes ont aussi démontré en pratique que les performances des transistors MOS à canal III-V sont meilleures que les performances des transistors à canal Si à échelle réduite. Cependant, de nombreuses difficultés restent à surmonter et de nombreuses étapes de fabrication du transistor restent à étudier pour pouvoir aboutir à un procédé industriellement viable.

Parmi ces problématiques se trouvent les problématiques de la grille, du nettoyage de la couche de canal ainsi que la problématique de la reprise de contact à la source et au drain. L'une des problématiques majeures est l'injection de courant dans le canal aux niveaux des sources et drains. La réalisation de contact métal/Semiconducteur de faible résistivité et compatible avec les procédés industriels en vigueur est une problématique de premier plan. Cette dernière problématique constitue le sujet d'étude de cette thèse. Ainsi nous allons nous intéresser dans cette thèse à l'étude de la formation et la stabilité d'intermétalliques formés par réactions à l'état solide entre un métal ultrafin et une couche d'InGaAs

Ainsi, dans le **premier chapitre** nous allons tout d'abord décrire des généralités sur les réactions à l'état solide dans le cas des couches minces ainsi que la formation et la cinétique de formation de phases. Ensuite, nous allons étayer les différents éléments de bibliographie sur GaAs et sur InGaAs. Ces éléments constituent une base de compréhension indispensable pour ce travail, mais montrent aussi les questions soulevées par les travaux sur les composés Ni-GaAs et le débat qui s'en est suivi, notamment en ce qui concerne la séquence de phase et la définition des intermétalliques formés.

Dans le **deuxième chapitre** nous allons décrire le dispositif expérimental qui a été mis en place pour pouvoir étudier les intermétalliques formés par réactions à l'état solide entre un métal (typiquement le Ni). En effet, cette thèse se déroule dans un contexte de développement d'une technique de caractérisation de diffraction de rayons X qui permet de scanner rapidement et de manière quasi-complète l'espace réciproque. En réalité, il est difficile de caractériser ce type d'intermétallique, dont il existe peu de littérature dessus, par des moyens de diffraction de rayons x classiques. Les couches minces formées sont souvent texturés et une caractérisation par DRX symétriques ne peut être suffisante pour les définir. Ainsi, nous décrivons dans ce chapitre les éléments nécessaires pour comprendre la technique de caractérisation développée : les cartographies de l'espace réciproque en 3D.

Dans le **troisième chapitre**, nous nous intéressons à l'étude ex situ des intermétalliques formés sur pleine plaque par réactions à l'état solide entre une couche ultra-mince sur de Ni et une couche d'InGaAs sur un substrat d'InP. Nous décrivons dans ce chapitre l'évolution des textures, des paramètres structuraux, de la composition, de la séquence de phase, de la résistivité et de la qualité interfaciale des films d'intermétalliques formés en fonction de la température de recuit. Nous nous intéressons par la suite à l'effet du substrat sur la formation de l'intermétallique en étudiant cette fois-ci des empilements Ni/InGaAs/GaAs/Si[1]. Enfin, nous nous intéressons aux effets d'ajout d'autres éléments sur la couche de Ni pur en l'alliant avec du Co. En effet, réaliser des alliages peut changer considérablement certains paramètres de l'intermétallique comme la stabilité thermique ou la température de formation.

Dans le **quatrième et dernier chapitre**, nous décrivons les résultats des études in situ des intermétalliques. Ces études ont été réalisés au synchrotron ESRF à Grenoble et ont permis de décrire avec plus de détails la formation et l'évolution de l'intermétallique en fonction de la température de recuit. Ces études ont aussi permis de mettre en évidence l'effet de l'alliage ainsi que celui de l'épaisseur sur la formation de l'intermétallique. Finalement, nous décrivons les paramètres cinétiques qui ont été calculés à partir des mesures d'isothermes de températures sur des échantillons Ni/InGaAs/InP.

---

[1] En effet, le substrat visé est le Si. Si notre étude porte majoritairement sur des empilements de type Ni/InGaAs/InP, c'est parce que ce type d'empilement offre la meilleure qualité cristalline pour la couche d'InGaAs et constitue ainsi des conditions idéales de croissance d'intermétallique.

Introduction

Motivations and challenges of nowadays Si-based devices

Si-based microelectronics is reaching fundamental limits when it comes to scaling new devices. While process-related limits were stretched to extraordinary horizons (photolithography resolution is barely a problem for CMOS fabrication), the limits are deeply related with the physical properties of Si and the behavior of charge carriers in extremely thin films. While we will not address solution related to Si-components or Si-based materials in this work, we think it is important to enumerate some relevant challenges that justifies Si replacement. Indeed, understanding these limits help us define the motivations to replace silicon with III-V materials.

Short-Channel effects

The reduction of the gate length to ultimate scales causes the emergence of parasitic electrostatic effects called short-channel effects. These effects disturb the control of the conductivity between the drain and the source by the applied potential V_{GS} between the gate and the source [1]. In fact, when transistors are downscaled, the source and drain are brought closer. This is problematic because one also brings closer the drain-substrate and source-substrate depletion regions (see Figure 1). Normally, these depletion regions are an obstacle for current towards the substrate. The major charge carrier in the source and drain regions will encounter a potential barrier that prevents them from diffusing into the bulk (and eventually the same thing for the major charge carriers in the bulk towards the source and drain). When V_{DS} increases (the potential between the source and the drain), the drain-substrate depletion region widen and can, in case of low l_G (gate length), join the source-substrate depletion region: this is called the punch-through phenomena (see Figure 1). The potential barrier at the source-substrate frontier shrinks and the major charge carriers from the source can diffuse under these conditions into the substrate and then drift into the drain-substrate depletion zone. Thus, a leakage current passing through the substrate between the source and the drain is established. In this case, the diffusion current is no longer controlled by the gate.

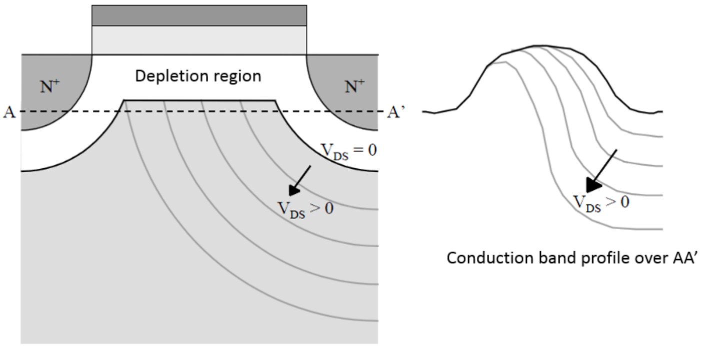

Figure 1 – Illustration of the punch-though phenomena in the case of a blocked NMOS.

Gate Insulator Thickness

Silicon dioxide has remained for several decades the preferred gate insulator for Si-based MOSFETs. SiO_2 was downscaled to fit recent technological nodes from 300 nm for 10 μm to 1.2 nm for 65 nm technological nodes. This thickness reduction of the oxide is important in order to have a larger C_{ox} (Oxide capacitance) and thus having a larger I_{on} (ON current) which in its turn helps to maximize the circuit speed. However, beyond 1.5 nm, tunneling leakage occurs. Indeed, at 1.2 nm, SiO_2 leaks 10^3 A/cm^2. Therefore, if an IC chip contains 1 mm^2 of 1.2 nm SiO_2 thin film, the oxide leakage alone would reach 10 A. This current leakage is sufficient to drain a cell phone battery in few minutes.

Introduction of III-V compounds in logical devices

Substrate problematics

One of the major problematics preventing the use of InGaAs alloys is the possibility of making good quality epitaxial layers of III-V materials on a substrate that respects some criteria. The corresponding criteria are robustness of the substrate, economically viable and of course the possibility to grow good quality InGaAs on top of it. InP might seem to be good a candidate as a substrate, especially because its lattice parameter matches the one of $In_{0.53}Ga_{0.47}$ and thus allows high quality epitaxy of III-V materials on it. Alas, InP is highly expensive, it is fragile and is not available in 300 mm wafers. Moreover, InP substrates would be incompatible with most Si tools used nowadays in the semi-conductor industry because it would require special holders to fit in 300 mm-tools. One solution is to figure out the technology to obtain good epitaxial InGaAs layers on Si substrates. The pre-deposition of buffer layers before the III-V material is a way to minimize the defects in the active III-V area and help absorb the crystallographic dislocations. Since InGaAs is polar on some of its planes and direction (because it yields a non-centrosymmetric zinc-blende structure), special care to the homogeneity of the III-V bulk. Recent extremely encouraging results showed the possibility of the control of the occurrence of anti-phase domains in GaAs deposited on Si using low miscut substrates [2].

Scaling issues

The continuous down-scaling of transistors is driven, not only by the gate shrinkage, but also by three essential characteristics. First of all, dimension reduction which allows higher integration density. Then, the switching energy and the switching speed. Dimension and switching energy continued to decrease while integration density and switching speed has continued to increase. With decreasing dimensions, dynamic and static power dissipation increase. Here, we refer to the power dissipation associated with the switching of logic states as dynamic power. While the static power refers to the power spent to maintain logical states at their value between state switching. Static power dissipation is related to current leakage within the device and cannot be avoided. With the increase of integration density, power dissipation has become a major problem of CMOS-based electronic devices and the MOSFET scaling has entered the “power-constrained scaling” era. Indeed, it requires robust packaging and cooling in order to enhance the device performance at lower scales. One way to solve this problem is to reduce the switching energy, thus the operating voltage, between two states. Ultimately, reducing the operating voltage will impact the switching speed of the CMOS.

In order to solve this dilemma, the introduction of a new channel material can be considered [3, 4]. Indeed, III-V materials and especially InGaAs and GaAs materials present remarkable mobility of charge carriers compared to silicon. For example, the mobility of charge carriers in $In_{0.53}Ga_{0.47}As$ compounds is 10 times higher than in Si (see Figure 2). In this case, a reduction of the operating voltage will much less impact the switching speed, and the integration density can follow its original trend in time.

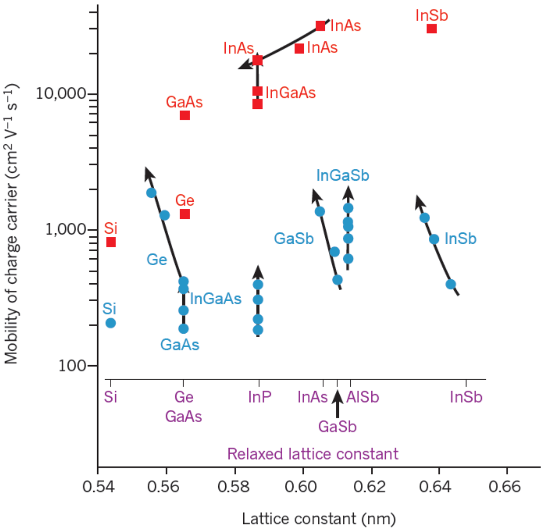

Figure 2 – Electron and hole mobility of group III–V compound semiconductors. The highest room-temperature mobility of electrons (red) and holes (blue) in inversion layers and quantum wells is shown as a function of the actual semiconductor lattice parameter [5].

The possibility of using III-V compounds in ultimate scaled devices was recently reviewed [5]. J. Del Alamo reports the most recent attempts to realize a III-V functional MOSFET device. The best device performance was obtained on InGaAs burried-channel structures equipped with an InP barrier layer using Atomic Layer Deposited (ALD) TiSiO as the dielectric [6]. This 75 nm device displays outstanding performances in regard to the current drive and subthreshold characteristics, even in comparison with state-of-the-art silicon MOSFETs. Moreover, Del Alamo lists the general problematics that should be solved in order to make reliable III-V MOSFETs. Some of these problematics will be discussed in the following sections.

The electrical performance and possible issues of III-V MOSFET compounds can be tackled through the acquired knowledge on III-V HEMT (High-Electron-Mobility-Transistors) devices [7]. In fact, III-V HEMT devices are widely spread, and the industry is quite mature when it comes to III-V integrated circuits. This spread is largely due to mobile devices and their highly demanding data treatment requirements. InGaAs and InAs HEMTs present injection velocity (v_{inj}) of 4.1 $cm.s^{-1}$ at an operating voltage of 0.5 V which is approximately 2 times higher than v_{inj} of strained Si at an operating voltage of 1 V [8].

Nevertheless, the comparison of III-V HEMT devices and possible III-V logic devices remain limited as HEMT devices tolerate high gate leakage and are mainly bulk-based devices whereas III-V logic devices are targeted to be thin film-based devices. Moreover there are several critical issues that a possible switch from Si to III-V device will trigger. As it is the case for Si-based MOSFETs, gate insulator thickness and short-channel effects are very serious challenges for III-V materials. However, literature has reported encouraging results on practical III-V FET transistors. Indeed, III-V quantum-well FETs have higher intrinsic speed, i.e., lower gate delay CV/I, and lower energy delay product than Si MOSFETs at a given transistor gate length L_G [9].

Gate Stack

Gate stack is crucial in the MOSFET design and consists of a metallic gate, a dielectric layer to prevent current leakage and the semiconductor itself. Historically, the choice of silicon as a channel material was much a result of the excellent qualities of its native oxide. Indeed, SiO_2 has remained for several decades an excellent choice as a gate dielectric: easy to control and to form. Alas, no equivalent gate oxide exists for III-V materials. In fact, III-V oxides result in a pinning of the Fermi level [10]. Fermi level pinning remains a nemesis for electrical engineers and results ultimately in the inability to modulate the electrostatic field inside the semiconductor. This phenomenon induces reverse band bending and thus initiate the production of electrical fields that deflect charge carriers from the channel into the interface states where they are annihilated. Thus, it is impossible to directly use III-V native oxides for MOSFET elaboration. GaAs remain the most mature III-V material used to elaborate MOSFETs and proposed solutions included the in situ deposition of oxides such as Ga_2O_3 [11, 12], which proved to be efficient to enhance device performances. Atomic Layer Deposition (ALD) of Al_2O_3 allowed obtaining of good quality ex situ deposited gate dielectric. The ALD was efficient even with the presence of native III-V oxides on top of GaAs surface as a “clean-up” effect takes place during the deposition and the oxide is eliminated [13, 14]. Such results permitted the realization of sustainable InGaAs MOSFETs [15]. Interface states are inevitable in such deposition conditions. Nevertheless, several interface engineering solutions were proposed. These solutions are maily inspired by the progress made on silicon MOSFETs and consist of the deposition of interfacial layers, post-deposition treatment and pre-cleaning. The interface quality can also be engineered through substrate orientation. Indeed, better interface quality and device performances were obtained using (1 1 1) GaAs oriented substrate rather than (1 0 0) oriented substrate [16].

It was also demonstrated that Indium addition into GaAs improves drastically the MOSFET performance and that the best results are obtained for InAs MOSFETs [17]. Gate stack scaling must also take into consideration channel mobility. Indeed, dielectric/semiconductor interface can present roughness and interface state eventually induce Coulomb scattering that degrades charge carrier mobility inside the channel. A buried-channel can help solving this problem by interposing a wide-band semiconductor channel between the channel and the oxide [18]. This solution has yet to be experimented on very short devices.

There is a lot of different ways to exploit in order to engineer proper gate stacks for III-V MOSFETs. GaAs-based devices are the most mature MOSFETs, and taking benefit from the science on these devices, along with the mature experience on III-V HEMTs and actual silicon technologies, it is not foolish to imagine boosting the research towards elaborating industrially-scaled, reliable and reproducible gates for very short channel devices.

Yet other critical issues remain to be solved and understood. In the next paragraph we will introduce the contact issue for III-V logical devices. First of all we will review contact elaboration for III-V HEMTs. Then we will enumerate the metallization of GaAs bulks. Finally, we will present the very recent results on InGaAs metallization.

Contact issues

One of the challenges for very short silicon MOSFETs is to minimize parasitic capacitance from one part of the transistor structure to another. This challenge remains the same if InGaAs MOSFETs are to be developed. InGaAs HEMTs have a source resistance of 150-200 Ω/µm [5], yet extremely short-scaled devices require a source resistance below 50 Ω/µm [5]. While HEMTs are large devices, scaling down the device dimension does not help getting a lower resistance as simulations on such devices demonstrate [19]. A self-aligned silicide-like process is likely the most promising solution in order to reach source resistance as low as 50 Ω/µm. Indeed there are two major ways to form ohmic contacts. One can consider unreacted contacts and the heat-treated contacts. Unreacted contacts are directly deposited on the substrate and must not be exposed to overheat or else the deposited contact layers would intermix or be dissolved into the substrate. Heat-treated contacts on the other hand are obtained by depositing a metallic layer on the substrate, and then making this layer react with the bulk by giving it enough thermal budget. A solid-state reaction occurs and new phases are formed including intermetallic phases. These intermetallic phases can indeed form a suitable ohmic contact for the MOSFET.

We will be interested in the formation of intermetallics by solid-state reaction between metals and III-V compounds. This kind of reaction has been reported in literature especially for GaAs and AlAs [20–24]. There was a dense work to characterize GaAs intermetallics since the mid-1980. Pd, Co, Pt and especially Ni are widely scoped as metal candidates [25]. Aside from electrical performances, there was also a great need to understand the so-formed material from a phase/phase sequence/texture/thermodynamics point of view. The understanding of the material is of great importance to correctly scale process steps. Indeed, when it comes to thin films, there is an utmost need to control the phase formation and interface uniformity of the intermetallic. The so-formed phase upon solid-state phase reaction must be in thermodynamic equilibrium with the substrate so that the contact stays stable, uniform and reproducible. In the following section we will be interested in the material characterization of Ni-GaAs intermetallics which has been widely explored. These early results on GaAs are important and constitute crucial information at the beginning of this work. Indeed, Indium is completely miscible in the InGaAs zinc-blende structure and Ni-InGaAs intermetallics can be regarded, to a certain extent, as a ternary system.

Conclusion

Silicon has reached its limits as a channel material and one solution, among others, is to replace it with a material that allows reaching higher mobility of charge carriers in the channel. Changing the channel material issues new challenges however. Among these challenges is the formation of contact materials for III-V MOSFET devices. From a process point view, one would like to make a silicide-like process and to make contacts following a solid-state reaction between the metal and the III-V material. The so-formed intermetallic can be optimized in order to present better uniformity, resistivity or interface. The target channel substrate is ideally the $In_{0.53}Ga_{0.47}As$ substrates. This stoichiometry choice is not arbitrary since it is exactly at $In_{0.53}Ga_{0.47}As$ that the $In_xGa_{1-x}As$ lattice parameter perfectly matches the lattice parameter of InP and thus can be easily studied on InP substrates. Therefore a great deal of the hereby work is done on InP substrates with the latter proportion of In and Ga. However, on the long term, Si substrates must be targeted, and issues related to such substrates, such as III-V bulk defects and antiphase domains must be addressed. The present work does clearly not claim to present a process related such as integration studies or electrical performance studies. Rather, we focused on studying the material itself in order to give key parameters to process people in order to properly form the contacts on future CMOS or power devices. Therefore, we will describe in this manuscript the solid-state reaction between Ni and InGaAs compounds. This reaction was barely studied and attempts to characterize the materials will be enumerated in **Chapter 2** along with the already acquired science on similar reaction on GaAs layers. In **Chapter 2** we will also see a brief history of silicides because the outcomes of research on silicides are fundamental to explain, understand and characterize intermetallics formed on InGaAs. In **Chapter 3** we will describe the experimental procedure that was developed to characterize such materials and explain the need to explore such materials through methods like 3D-Reciprocal Space Mapping. **Chapter 4** will deal with the phase formation and texture of the Ni-InGaAs intermetallic along with a discussion on the orientation of the intermetallic and influence of substrate on these orientations. The phase transition will be discussed in the light of the knowledge acquired on reaction of Ni with GaAs. Finally **Chapter 5** will present the in-situ measurements results for the intermetallic and the kinetic parameters associated with the formation of Ni-InGaAs.

Résumé du chapitre 1

La réaction à l'état solide entre un métal et un substrat d'InGaAs a été peu étudiée. En effet, il y eu un regain d'intérêt pour les MOSFETs III-V, et typiquement, les MOSFETs à substrat InGaAs depuis les années 2010. Nous nous intéressons à une étape importante de la fabrication de ces composants électroniques logiques : la métallisation de la couche de semi-conducteur pour former des contacts à caractère ohmique à la source et au drain. Historiquement, la réalisation de cette étape sur Si se fait par réaction à l'état solide entre un métal (ou un composé métallique) et la couche de silicium pour réaliser des intermétalliques. La méthode la plus courante pour aboutir à des intermétalliques est le procédé SALICIDE (self-aligned silicide[2]). Ce procédé permet d'obtenir des intermétalliques sans recourir à des étapes supplémentaires de photolithographie. De nombreux métaux, ou composés de métaux ont été utilisés pour réaliser des intermétalliques sur Si. Parmi les intermétalliques les plus étudiés et les plus utilisés par l'industrie de la microélectronique nous retrouvons le $CoSi_2$, le $TiSi_2$, et le NiSi. A chaque nœud technologique, les conditions de dépôt et de recuit de l'intermétallique doivent être réétudiées afin de se conformer aux performances attendues du dispositif électronique en terme d'épaisseur, de régularité d'interface et de résistivité. En atteignant des épaisseurs limites de la taille grille (et donc fatalement d'épaisseur limite de l'intermétallique formant la reprise de contact), des limitations physiques se mettent à se manifester. Ainsi au-delà de 200 um, le $TiSi_2$ présente une résistivité trop élevée liée à un changement de phase. Le $CoSi_2$ présente, quant à lui, des interfaces non uniformes une fois l'épaisseur du métal déposé atteint une épaisseur limite.

Dans ce chapitre, nous nous intéressons tout d'abord à la description de la réaction à l'état solide entre un couple d'éléments. On énumère les régimes de croissance qui peuvent être linéaire, parabolique ou encore dans la plupart des cas, des régimes linéaire-paraboliques. Ces différents régimes peuvent être formalisés en fonction du taux de réaction, de l'énergie d'activation ainsi que le taux de réaction maximal. Dans le cas d'un régime linéaire, l'épaisseur de la phase formée est très faible et ne limite pas la réaction. Dans ce cas, la croissance est limitée par la réaction à l'interface. Dans le cas d'un régime parabolique, l'épaisseur de la phase formée entre le couple est importante. Ainsi la croissance n'est plus limitée par la réaction à l'interface mais par la diffusion à l'intérieur de la phase formée. Ce chapitre est aussi l'occasion d'énoncer aussi les notions qui permettent de comprendre l'alignement de

---

[2] Siliciure auto-aligné.

couches minces. Ainsi, les couches minces peuvent être épitaxiées, avoir une texture de fibre, ne pas avoir de texture, mais aussi et plus récemment il a été démontré que des couches minces peuvent avoir des textures axiotaxiales. La réaction à l'état solide entre Ni et une couche de GaAs a été largement étudiée depuis les années 80 et jusqu'aux années 90. Plusieurs études se sont intéressées à l'établissement de diagramme de phase ternaire Ni-Ga-As. Les résultats de ces études présentent plusieurs différences notamment en ce qui concerne la définition des phases et des domaines d'homogénéités des phases d'intermétalliques formés. En effet, le travail de Guérin et Guivarc'h sur des poudres d'intermétallique Ni-GaAs démontre l'existence de 5 phases d'intermétalliques toutes hexagonales et appartenant au groupe d'espace $P6_3/mmc$. Ces phases se distinguent par des domaines d'homogénéité assez larges et ont des stichométries allant de Ni_3GaAs jusqu'à NiAs. En plus, un ordre/désordre s'établit lorsque ces phases sont formées en fonction de la nature de la phase. Ces intermétalliques peuvent aussi être caractérisés par le rapport axial c/a et sont toutes métastable à l'exception de NiAs et de son extension en solution solide. Le travail de Zheng, publié simultanément aux travaux de Guérin et Guivarc'h, définit les phases d'intermétallique autrement. En effet, Zheng considère qu'une seule phase ternaire existe (la phase Ni_3GaAs) et considère que les autres phases avec des stœchiométrie entre Ni_3GaAs et NiAs ne sont que des phases binaires avec des solubilités ternaires plus ou moins importantes. Zheng n'exclut pas aussi que certaines phases, à priori hexagonale, soient en fait des phases monocliniques déformées vu la grande ressemblance de symétrie entre les deux groupes d'espace considérés. Finalement, les travaux d'Ingerly et al. en 1996 sur le système Ni-Ga-As débouchent sur un nouveau diagramme de phase et démontrent que toutes les phases formées sont des phases binaires avec des extensions ternaires très larges. Quel que soit l'étude sur Ni-GaAs, il en ressort que toutes les phases formées dans ce système sont métastables à l'exception de la phase NiAs. Ces différentes études réalisées sur des poudres montrent aussi la difficulté de caractériser les intermétalliques formés sur III-V.

D'autres équipes se sont intéressées plutôt à la formation de l'intermétallique en couche minces en faisant réagir une couche de Ni avec un substrat InGaAs. Ces études démontrent que le premier intermétallique se forme généralement à basse température (entre 200 °C et 250 °C) et que ce premier intermétallique formé est généralement celui qui est riche en Ni (Ni_3GaAs). Les intermétalliques formés sont fortement texturées (i. e. présentent une orientation préférée) et présnetent l'orientation suivante : $(0001)_{Ni_2GaAs}||(111)_{GaAs}$; $[1\bar{2}10]_{Ni_2GaAs}||[\bar{1}10]_{GaAs}$ La séquence de phase est différente selon les auteurs et cette différence s'explique surtout par des conditions de dépôt/recuits différentes. La tendance générale est que, au fur et à mesure que la température de recuit augmente, le ratio axial c/a de l'intermétallique hexagonal augmente et l'intermétallique passe d'une structure hexagonale riche en Ni à basse température à une structure hexagonale NiAs, moins riche en Ni, à haute température. La plupart des auteurs rapportent aussi la formation de composés binaires cubiques NiGa à la fin de la réaction. Quant aux travaux sur la réaction à l'état solide entre un film mince et un substrat d'InGaAs, elles restent assez limitées. Les études sur ce sujet portent sur la formation d'intermétallique à basse température (entre 200 et 350 °C). Tout comme le

Ni-GaAs, les études sur Ni-InGaAs démontrent la formation d'un intermétallique hexagonal fortement texturé. L'intermétallique possède un caractère ohmique et une orientation différente de celle qui a été rapporté pour Ni-GaAs. Ces études restent incomplètes de par au moins deux aspects : la caractérisation de l'intermétallique s'est faite la plupart du temps en analysant une partie limitée de l'espace réciproque. En effet, et de par l'aspect texturé des films formés, il est tout à fait possible d'omettre certaines phases ou orientations si une analyse complète de l'espace réciproque par diffraction des rayons X n'est pas effectué. Ceci a été longtemps le cas pour certaines phases de siliciures comme la phase θ, longtemps considérée comme ayant une symétrie orthorhombique alors qu'elle possède une symétrie hexagonale ou encore les germaniures comme la phase γ dont la symétrie hexagonale a été récemment démontrée. Le deuxième aspect manquant à ces études est l'aspect relatif à la formation et stabilité des intermétalliques. En effet, la plage de recuit rapportée par la littérature est limitée. Ainsi, une séquence de phase et un modèle d'évolution de stœchiométrie et/ou de phase n'a pas pu être rapporté. En plus, aucune étude in situ n'a été faite pour extraire les paramètres cinétiques relatifs à la formation de ces intermétalliques.

Finalement, il y a une nécessité d'une part de faire une étude qui se base sur une analyse complète de l'espace réciproque par une méthode rapide et appropriée. D'autre part, il est nécessaire d'effectuer une étude exhaustive ex situ et in situ pour mieux comprendre les mécanismes régissants la formation et la stabilité de ces intermétalliques.

1 State-of-the-art and issues

In this first chapter, we will first define the solid-state reaction (SSR) between materials and the diffusion treatments that are involved during an SSR in the case of thin films. We will then be interested in a particular step in the elaboration which is the intermetallic formation on top of the source and drain of MOSFETs. Hence, we will describe the SSR between metals in the case of a Si-MOSFET and Si along with the SALICIDE process. Previous studies of Si-based intermetallics are valuable, not only because it gives insights on the solid-state reaction between metals and semiconductors for thin films, but also because important outcomes concerning the materials or the characterization methodologies were described or developed thanks to research on silicides. In the third part of this chapter, we will enumerate the previous studies of the SSR between metals and III-V materials. Especially Ni/GaAs and more recently Ni/InGaAs.

1.1 Solid-state reactions in the case of thin films

One can describe the evolution of the kinetics of a heterogeneous reaction in terms of two processes: separate nucleation and growth of the transformed regions. The nucleation process is classically explained by random fluctuation in a metastable assembly [26]. The earliest works on nucleation were conducted on the simplest case of a pure vapor condensed to form a liquid. A simple example of nucleation is the creation of water vapor from boiling water. The formation of the gaseous phase happens at temperature T above a critical temperature T_c. Below T_c, the free energy of the liquid water is lower than the free energy of the vapor and above T_c the free energy of the liquid water is higher than the one of vapor. At $T = T_c$ no phase transformation can occur as both free energies of vapor and liquid water are equal ($\Delta G_p = 0$). If $\Delta G_p \neq 0$, then the most stable phase will nucleate. As the formation of a nucleus implies the necessary creation of a new interface between the nucleus and the original system, the gain in volume free energy is counterbalanced by an increase in surface energy. As a result, the nucleation process is controlled by the competition between both contributions. The theory of nucleation from these earliest works was expanded to solid-state reactions.

Indeed, a similar situation is encountered when two bulk elements A and B are put into contact. Above a certain temperature T$_c$, a solid-state reaction occurs and germ-nuclei are formed. After the formation of a germ-nuclei, the phase grows laterally along the surface until a uniform layer is formed. Then the phase grows normally to surface. Instead of the initial A/B system with one interface, the system presents now two interfaces A/AB and AB/B and two phases A, B and AB [27]. In our case, the growth of the phase is controlled by the diffusion of either metal atoms or In, Ga and As atoms through the so-formed phase, then, controlled by the chemical reaction between reactants at the interface leading to the formation of the new phase.

1.1.1 Diffusion mechanisms

The diffusion of atoms is the phenomenon of matter transportation under the effect of a gradient of chemical potential that is often considered equivalent to a gradient of concentration. In fact, the motion to another site is possible only when the neighbor site is vacant: it is the vacancy diffusion. If the atom is sufficiently small, then a diffusion through interstitial sites can be considered: it is the interstitial diffusion (see Figure 1.1).

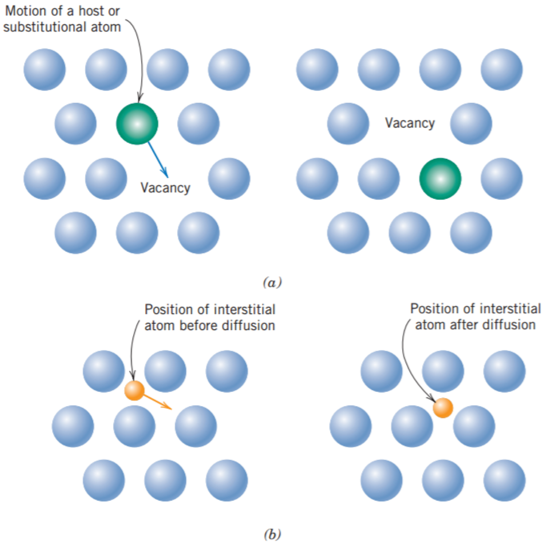

Figure 1.1 – Schematic representations of (a) vacancy diffusion and (b) interstitial diffusion (adapted from [28]).

To jump from a site to another one, an atom must cross an energy barrier ΔG_p which corresponds to the free enthalpy or Gibbs energy and which is defined by:

$$\Delta G_p = \Delta H - T\Delta S \tag{1.1}$$

$$\Delta H = \Delta H_f + \Delta H_m \tag{1.2}$$

ΔH is the enthalpy change of reaction and is the result of the addition of the standard enthalpy of formation ΔH_f and ΔH_m, the enthalpy of migration of either atoms or vacancies. T and ΔS are respectively the temperature and the entropy.

The probability P of crossing the energy barrier is thermally dependent and is written:

$$P \approx exp(-\frac{\Delta G_p}{kT}) \tag{1.3}$$

In the case of polycrystalline samples, the diffusion can be either a volumetric diffusion across the crystal, an inter-granular diffusion or a diffusion along the dislocation (which is also called pipe diffusion). The diffusion of atoms is generally faster along dislocations and grain boundaries than along the volume of the crystal.

1.1.2 Atom flux

When two bulks of species A and species B are put into contact, and in the presence of a gradient of concentration C, the atom flux J can be expressed using the Fick's law:

$$J = -D \times \frac{\partial C}{\partial L} \tag{1.4}$$

D is the coefficient of diffusion and follows an Arrhenius equation.

The migration of atoms of one species can be expressed through the gradient of chemical potential μ_i, where i designates the species A or B:

$$J_i = -X_i \times N \times \frac{D_i}{kT} \times \frac{\mathrm{d}\mu_i}{\mathrm{d}L} \tag{1.5}$$

Where J_i is the flux of atoms i through the formed phase, X_i the atomic fraction of species i in the phase, N the total number of atoms per unit of volume in the phase, k the Boltzmann constant and T the temperature.

1.1.3 Phase formation

Phase formation in thin films couples is regarded as sequential in opposition of simultaneous phase formation in bulk couples. Silicide studies have shown that often only one or two silicide phases are formed when a reaction occurs between the thin film couple [29–31]. Several treatments and approaches can be used to describe the phase formation.

1.1.4 Linear-Parabolic treatment

The linear Parabolic treatment was first used to describe the formation of silicon dioxide. Several authors including d'Heurle, Gas and Philibert [32, 33] have described the phase formation of thin films using this treatment.

1.1.4.1 Formation of one phase between materials A and B

If a compound AB grows between two pure elements A and B by the diffusion of A atoms (see Figure 1.2), one obtains the following equation:

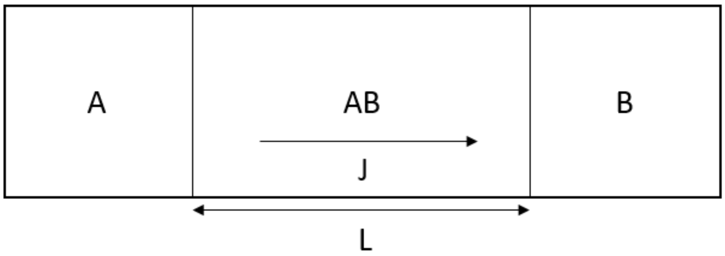

Figure 1.2 – Schematic presentation of the AB phase growth between the pure elements A and B by the diffusion of A atoms.

$$J_A = C_A \times M_A \times \frac{\mathrm{d}\mu_A}{\mathrm{d}L} \tag{1.6}$$

Where the mobility is $M_A = \frac{D_A}{kT}$, J_A is the diffusion flux of element A, C_A is the concentration of element A, μ_A is the chemical potential of species A, L is the position or length of the AB compound, D_A diffusion coefficient of the element A.

If one assumes that the intrinsic diffusion coefficient D_A is not a function of the concentration, we obtain:

$$J_A = C_A \times \frac{D_A}{kT} \times \frac{\Delta g_A}{L} \tag{1.7}$$

Where $\frac{\Delta g_A}{L}$ is the Gibbs energy per A atom of the reaction A + B= AB. To be more specific, it is the required energy to move one mole of A atoms from the A/AB interface across the AB layer to the AB/B interface. In other words, it is the driving force for diffusion $\Delta\mu_A$.

Since we have:

$$\frac{\mathrm{d}L}{\mathrm{d}t} = J_A \times v_A \tag{1.8}$$

Where v_A is the molar volume of species A.

and:

$$C_A = \frac{1}{v_A} \tag{1.9}$$

then:

$$\frac{\mathrm{d}L}{\mathrm{d}t} = D_A \times \frac{\Delta g_A}{kT} \times \frac{1}{L} \tag{1.10}$$

If we integrate the Equation 1.10, we obtain the parabolic growth law:

$$L^2 = K_d t \tag{1.11}$$

Where K_d is the parabolic rate constant.

However, if we consider Equation 1.11 at very small layer thickness, then $L \approx 0$ and $\frac{\mathrm{d}L}{\mathrm{d}t} \approx \infty$. Therefore, d'Heurle et al. [31–33] introduced the concept of linear-parabolic kinetics. The starting point is Equation 1.10. If we introduce a "kinetic parameter" to take into account reactions at the interfaces, then:

$$\frac{\mathrm{d}L}{\mathrm{d}t} = D_A \times \frac{\Delta g_A}{kT} \times \frac{1}{L + K''} \tag{1.12}$$

As the thickness of the layer approaches zero $L \to 0$ then Equation 1.12 is rewritten:

$$\frac{\mathrm{d}L}{\mathrm{d}t} \approx D_A \times \frac{\Delta g_A}{kT} \times \frac{1}{K''} \tag{1.13}$$

and if one integrate this equation, we obtain:

$$L^2 + K'L = K(t + t_0) \tag{1.14}$$

Where $K' = K''$

Indeed, when the layer thickness increases and the reaction time becomes longer, then we retrieve the "normal" parabolic growth equation

$$L^2 \rightarrow \infty \Rightarrow L^2 \approx Kt \tag{1.15}$$

1.1.5 Linear treatment

At the beginning of the reaction, the AB compound film thickness is small, and element A and B are always available through the two interfaces. Therefore, the limiting factor of the AB compound film formation is the reaction at the interfaces and the thickness can be written as the following:

$$L = K_r t \tag{1.16}$$

Where K_r (cm.s^{-1}) is a constant characteristic of the interfacial reactions. This constant is thermally activated and depends on temperature following the Arrhenius law expressed at equation 1.17:

$$K_r = K_{r0} exp(\frac{E_a}{kT}) \tag{1.17}$$

Where E$_a$ is the energy of activation and K$_{r0}$ is a pre-exponential factor.

However, if the reaction goes further, the thickness of the AB compound film will increase and the path used by A and B elements to reach each interface will increase. Thus, the reaction at the interface will become less and less important.

1.1.6 Parabolic treatment

At sufficient AB layer thickness, we can consider that the growth of the AB compound is no longer controlled by the interface reactivity but rather by the number of atoms (or flux) reaching the interface. The thickness is then written as the following:

$$L^2 = K_d t \tag{1.18}$$

Where K_d is also a thermally activated constant and is expressed in cm.s^{-2}.

1.1.7 Simultaneous and sequential growth

The sequential formation of phases is widely reported [32, 34, 35]. In the case of thin films, phase growth is usually sequential rather than simultaneous. The sequential growth can be explained by a competition between reaction kinetics at the interface and diffusion of metal in the growing phases. When two phases grow simultaneously, the variation of their thickness depends on the flux inside each phase. This couple of flux J_1 and J_2 is used to explain the sequential growth of phases. Hereby, we will present the equations that describe simultaneous growth, then, we will present those that describe sequential growth.

1.1.7.1 Simultaneous growth

Several phases appear at the same time in the case of simultaneous growth. Figure 1.3 presents a scheme of the simultaneous growth of two phase A_2B and AB by solid state reaction between a metal A and a semi-conductor B. In this example, we consider that diffusing species is the metal (so that J_A»J_B). The reactions occur at the two interfaces A_2B/AB and AB/B.

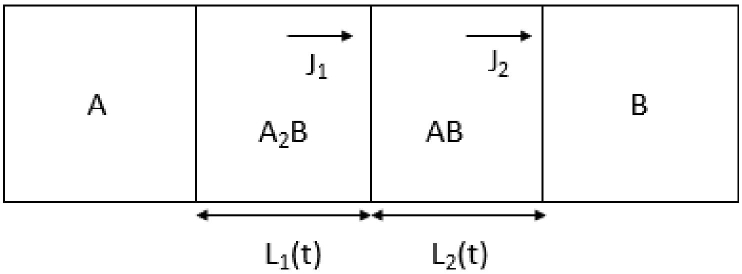

Figure 1.3 – Schematic presentation of the simultaneous growth of two phases.

The flux J_1 represents the flux of A atoms in phase A_2B and J_1 represents the flux of atoms in AB. The growth of each phase does not depend only on the characteristics of the phase (reaction kinetics, diffusion coefficient), but also on characteristics of all the phases present in the diffusion couple A/B. The growth of the phase A_2B occurs at the interface A_2B/AB and follows the following reaction:

$$A + AB \rightarrow A_2B \tag{1.19}$$

The growth of phase AB occurs at the interface A_2B/AB and also AB/B. At the first interface, the reaction frees one atom from A_2B in the following way:

$$A_2B \rightarrow A + AB \tag{1.20}$$

This atom diffuses through the phase AB to react with the semi-conductor at the second interface AB/B:

$$A + B \rightarrow AB \tag{1.21}$$

Hence, the reaction of formation and consumption happen simultaneously at different interfaces. The thickness variations L_1 and L_2 of phases A_2B and AB are related to the diffusion flux J_1 and J_2 of the metal A in phases A_2B and AB respectively by the following relationships:

$$\frac{\mathrm{d}L_1}{\mathrm{d}t} = J_1 - J_2 \tag{1.22}$$

$$\frac{\mathrm{d}L_2}{\mathrm{d}t} = 2J_2 - J_1 \tag{1.23}$$

This equation system shows that there is a coupling between the growth rate of different phases.

1.1.7.2 Sequential growth

The growth rate of a phase does not only depend on its intrinsic growth parameters but also depends on all the parameters of all forming phases. If one suppose that every phase present a linear-parabolic growth, one can suppose that the flux of atoms through the phase 1 (J_1) is limited by the process of diffusion whereas the flux through phase 2 (J_2) is controlled by the reaction rate :

$$J_1 = \frac{K_d}{L_1} \text{ and } J_2 = K_r \tag{1.24}$$

Thus

$$\frac{\mathrm{d}L_1}{\mathrm{d}t} = \frac{K_d}{L_1} - K_r \text{ and } \frac{\mathrm{d}L_2}{\mathrm{d}t} = 2K_r - \frac{K_d}{L_1} \tag{1.25}$$

In this case, phase 2 begins to grow when the first phase reaches a critical thickness in the following manner [35]:

$$\frac{\mathrm{d}L_2}{\mathrm{d}t} > 0 \text{ and } L_1 > \frac{K_d}{2K_r} \tag{1.26}$$

For thin films, the critical thickness, that can be considered as controlled by the reaction rate of phase 2 and by the diffusion coefficient of the metal in phase 1, is often of the same order than the thickness of the metallic film. The metallic film is completely consumed before the appearance of new phases, which induces a sequential formation of phases.

1.2 Silicide contacts

On top of the active zones of a MOSFET, there exists a “contact” zone made of an intermetallic that allows to make a physical and electrical link between the contact in the circuit and the active doped zones of the MOSFET. On silicon, these intermetallic contacts are called silicides. Silicides must meet some essential qualities in order to be integrated into circuits. The most important ones are the thermal stability and contact resistance of the silicide. Thus, it is important to understand the formation of the intermetallic in order to control its stability.

Silicides are usually formed using a SALICIDE (Self-Aligned Silicide) process. This process consists of depositing a metal on top of the active regions and the gate, and making this metal react by bringing a thermal budget. The process is done simultaneously on these regions and an intermetallic is formed through solid-state reaction without need for further photolithography steps. Obviously, excess metal that did not react is removed using selective chemical etching. A SALICIDE process is illustrated in Figure 1.4.

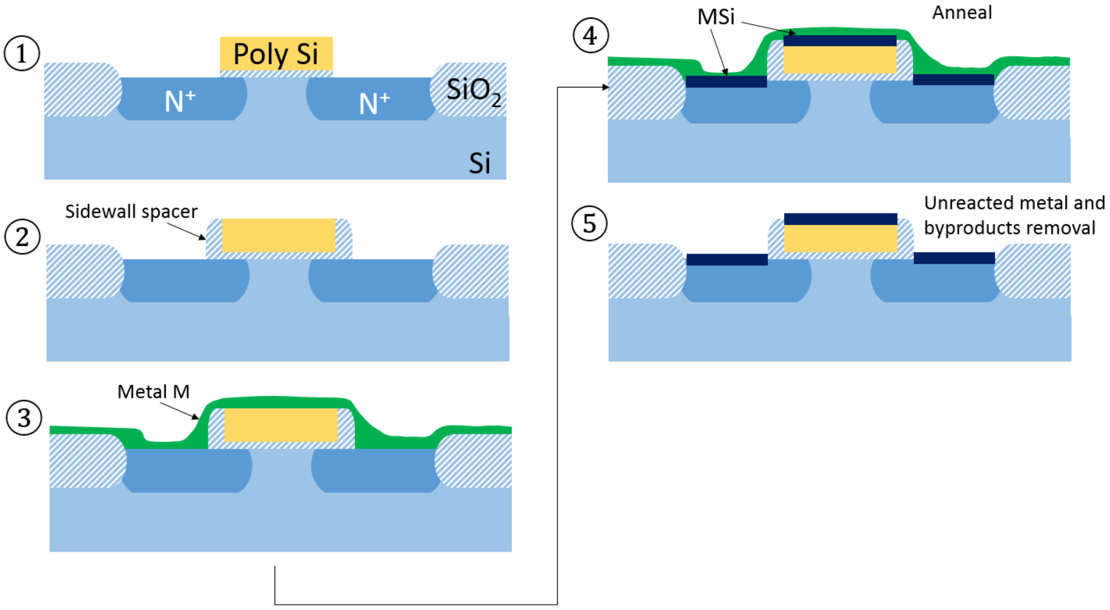

Figure 1.4 – Salicide process steps and formation of the intermetallics on Source/Drain (S/D) regions and on the gate of the MOSFET.

Since their introduction in the 1970’s [36–38] in the CMOS fabrication process, silicides have constituted materials of choice when it comes to producing contacts for Si-CMOS devices. Indeed they generally present a low electrical resistivity, have good passivation properties and can be thermodynamically stable. The qualities of a good silicide can be enumerated as the following:

- Thin film silicides according to the corresponding technological node;
- Low resistivity (14 $\mu\Omega$ for the 14 nm technological node);
- Low silicon consumption to prevent breaking through the junction or, in the case of Silicon on Insulator MOSFETs, breaking near the burried oxide layer;
- Thermal stability to avoid degradation at high annealing temperatures;
- Low thermal budget of formation to avoid degradation of already deposited layers of the device;
- Suitable growth constraints and thus suitable coefficient of thermal expansion;
- Good quality of the interfacial layer, so that no agglomeration of the silicide occurs (which causes resistivity degradation).

Literature on silicides is abundant and different materials were explored such as NiSi, PtSi, $TiSi_2$, $MoSi_2$, $CoSi_2$... The microelectronic industry has used several types of silicides according to the technological nodes and the evolution of needs in order to respect the criteria for having a good silicide contact. $TiSi_2$ has represented the main stream silicide contact up to the 0.2 μm technological node. However, beyond a certain width of lines, a limitation of the titanium salicide emerged. Indeed low resistance $TiSi_2$ is formed through a phase transformation from C49 (60-90 $\mu\Omega$/cm) to C54 (14-18 $\mu\Omega$/cm). Unfortunately, this transformation becomes extremely difficult for thin films, and hence, the so-formed Ti silicides are no longer suitable [39].

Then, cobalt silicide constituted a popular replacement for Ti silicides. Indeed, $CoSi_2$ needs a lower thermal budget to be formed and up to a certain gate dimension, it does not suffer a degradation of resistivity at narrow lines. However, as the transistor gate length reaches the 50 nm, Co silicide suffers from a rise of resistivity and its Si consumption ratio becomes very important. Thus, nickel silicides were proposed [40]. Nickel silicides present very interesting features and meet most of the qualities required from a good silicide contact. NiSi has a lower density in Si compared to $CoSi_2$ and thus, Si consumption is limited during the solid-state reaction. During the reaction, Ni is the diffusing species, and thus Si mobility is limited and bridging becomes less likely to happen. On top of that, NiSi has a much smoother interface than $CoSi_2$ which leads to lower resistivity, but also the possibility to get safely closer near the buried oxide for SOI transistors. Finally, these silicides are fit for both Si and SiGe (low resistivity when reacted with both substrates) and thus can be used in a co-integration scheme of transistors.

The phase diagram of the Ni-Si system is rather complex and presents multiple stable phases at temperatures lower than 800 °C. Most of these phases are Ni-rich phases ($Ni_{31}Si_{12}$, Ni_3Si,

Ni_2Si, Ni_3Si_2 and θ-Ni_2Si). Space groups and lattice parameters of these phases are reported in Table 1.1.

Table 1.1 – Summary of the main silicide phases [41]

Silicide phase	Symmetry	Space group	Lattice parameters a (Å)	 b (Å)	 c (Å)
Ni_3Si	Cubic	Pm3m	3.50	3.50	3.50
Ni_2Si	Orthorombic	Pbnm	7.07	5.01	3.73
θ-Ni_2Si	Hexagonal	$P6_3mmc$	3.80	3.80	4.90
$Ni_{31}Si_{12}$	Hexagonal	P321	6.67	6.67	12.29
NiSi	Orthorombic	Pnma	5.18	3.34	5.62
$NiSi_2$	Cubic	Fm-3m	5.41	5.41	5.41

The phase sequence of the Ni-Si system for thin films has been widely reported in the literature [42–49]. The phase sequence is subject to more or less important changes according to the type of the substrate, film thickness, dopant... The sequential formation of nickel-silicide begins with the formation of Ni-rich phases at lower temperatures [50], then NiSi and $NiSi_2$ are respectively formed afterwards at higher annealing temperatures. Ni was found to be the diffusing species [51, 52] and the formation of Ni_2Si and NiSi was demonstrated to be a diffusion-controlled formation, while the $NiSi_2$ is controlled by germination [51]. Yet, the phase identification has remained debated for several years. Indeed, early studies of Ni on Si reaction wrongly identified an intermediate phase as orthorhombic Ni_3Si_2 [53], while a complete texture study over large parts of the reciprocal space undertook by S. Gaudet et al. [54] showed that this phase is rather an hexagonal one (θ-Ni_2Si).

1.3 Crystallographic elements

The following paragraphs are fundamental to understand the different works that were carried on the GaAs metallization. We will enumerate certain crystallographic considerations that were used to explain the observations on the solid-state reaction between Ni and GaAs.

1.3.1 Texture and orientations of thin film

Polycrystalline thin films are formed of a large number of crystallites. The orientation of these crystallites is not necessarily isotropic but most of the times the crystallites present a preferred disposal, within a certain range, along a crystallographic direction, called preferential orientation. This preferential orientation is often defined according to the sample reference and is identified in comparison to a crystallographic plane ($h\,k\,l$) and a crystallographic direction [1 1 1] of the sample reference. This anisotropy in the crystallite orientation is called texture. Contrary to powder samples, in which the crystallites are randomly oriented, the diffraction pattern of textured materials characterized by symmetric θ-2θ (Bragg-Brentano geometry[1]) X-Ray diffraction will always present missing planes. The diffracting planes using symmetric θ-2θ on textured materials will however yield an enhancement of their intensity because nearly all crystallites are oriented in the same way. The nature of the anisotropy of crystallite orientation and the distribution of grain orientation has a great influence on material properties, especially in microelectronics since crystallographic plane density is not the same according to the different $(h\,k\,l)$ planes. For example in microelectronics, it is preferable to have $(0\,0\,1)$ oriented Si wafer because mobility of charge carriers along the [100] axis is better than along other axis. Moreover, preferable orientation control is important in order to enhance the morphology of thin films. Texture can be evidenced using X-Ray diffraction either simply by performing θ-2θ scans, or by performing pole figure (to probe larger parts of the reciprocal space), by Electron Backscatter Diffraction (EBSD) or by Transmission Electron Microscopy (TEM). Figure 1.5a shows a sketch of the case where there is no preferable orientation of the film (random orientation). Usually, we identify 3 types of different textures:

- Fiber texture: there exists an axis of infinite cyclic symmetry (cylindrical symmetry) in either sample coordinates or in crystal coordinates. In other words, fiber-textured films always present the same parallel surface to substrate (with its axis normal to the surface), but with no preferable crystallographic direction of the film according to a crystallographic direction of substrate (see Figure 1.5b).

- Epitaxial texture: if the unit cell of the film material is sufficiently close to the unit cell of the substrate, then two crystal structures often align (see Figure 1.5c).

- Axiotaxial texture: an axiotaxy can be understood as an off-normal fiber texture. Planes of both film and substrate, with similar interplanar distances, are aligned with the presence of an off-normal axis of cyclic symmetry [54, 58] (see Figure 1.5d).

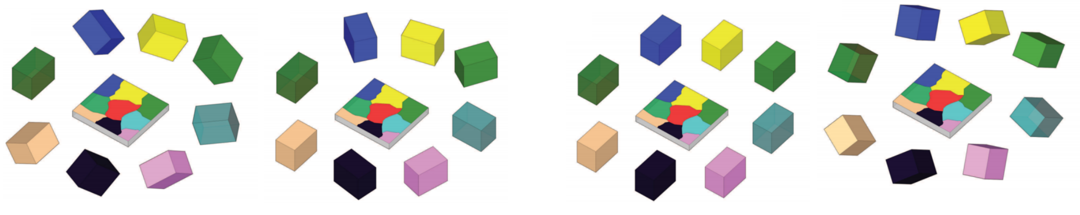

(a) (b) (c) (d)

Figure 1.5 – Distribution of the crystallographic orientations: (a) random texture, (b) fiber texture, (c) epitaxial texture, (d) axiotaxial texture (adapted from [59]).

---

[1] It is called the Bragg-Brentano geometry because of the involvement of the Braggs (W.H. and W.L. Bragg) in the development of reflection geometry for diffractometers [55], while Brentano proposed the para-focusing principle [56, 57].

Axiotaxy is a periodic 1D alignment along one direction corresponding to the alignment of planes of the substrate and planes of the film. Indeed, two family of crystallographic planes having different interplanar distances can be aligned if the two planes are tilted the one against the others in order to reduce the mismatch in terms of projected d-spacing (Figure 1.6a). However, this works only for a flat interface. Since thin films formed by solid-state reaction present usually roughness at their interface, it is expected that lattice mismatch varies all along the grain interface if the film and substrate planes present different d-spacing. The alignment of planes with different d-spacing is no longer possible and only planes with similar d-spacing can be aligned through plane tilting (Figure 1.6b).

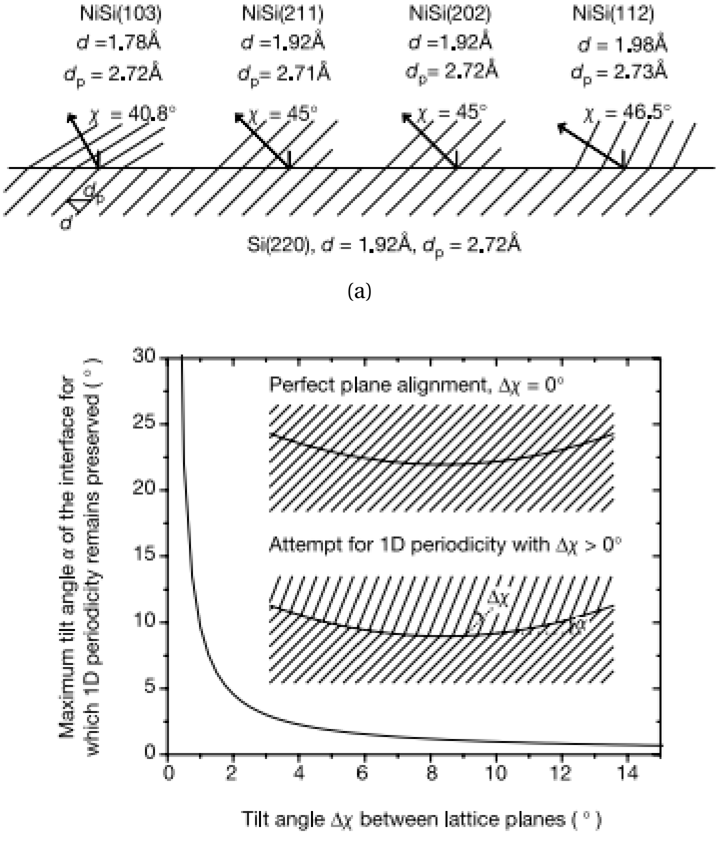

(a)

(b)

Figure 1.6 – (a) Possibility of achieving a 1D periodic interface through a tilting by Δ_χ of lattice planes to compensate the lattice mismatch in d-spacing. Thus, the mismatch is reduced in projected d-spacing Δd_p, (b) The graph shows the maximum angle α through which the interface can curve while maintaining good 1D periodicity (defined as mismatch $\Delta d_p < 0.5\%$ as function of the tilt angle Δ_χ. The lower the allowed value of α, the more stable the 1D periodic nature of the interface in respect to interfacial curvature. [58].

Grains with axiotaxial alignment present a low interfacial energy and consequently present a higher probability of forming. Thus, agglomeration is also favored for axiotaxial grains since the interfacial curvature does not induce higher interfacial energy in the direction of plane alignment.

Axiotaxy is manifested in pole figures as fiber-like texture that is centered around an off-normal axis in place of a normal axis.

1.3.2 The NiAs structure type

NiAs-type structures are hexagonal crystallographic structures that yield a great variety of structural, electrical and magnetic properties thanks to the incomplete *d* shells of the component transition metal atoms [60]. Such structure contains transition metal atoms in combination with metalloid/post-transition metal atoms. The transition metal atoms are located on the octahedral holes in the close-packed hexagonal array of metalloid/post-transition metal atoms. The metalloid/post-transition metal atoms are surrounded by six transition metal atoms in the form of trigonal prism(see Figure 1.7). Close-packing is achieved when the axial ratio $c/a = \sqrt{8/3} = 1.633$. Another packing is the pseudo-cubic packing which is achieved when $c/a = \sqrt{3/2} = 1.225$, in which the hexagonal structure can be interpreted using symmetrical elements of an equivalent cubic zinc-blende structure. NiAs structures can take up transition metal atoms partially or fully in the trigonal bi-pyramidal holes where it can reach the T_2X composition (the structure is then called filled-up and is referred to as the Ni_2In type) but can also omit one or two transition metals on the transition-metal-subcell to reach either the TX composition or the TX_2 composition. The filling or omitting of these sites can be done either randomly or by the occurrence of an ordering giving rise to superlattices based on the NiAs structure [61].

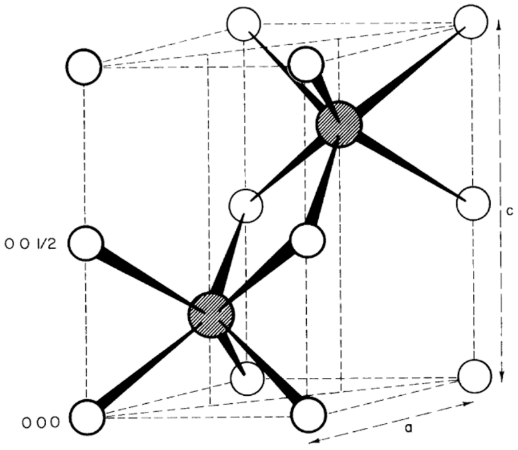

Figure 1.7 – The hexagonal NiAs, $B8_1$ structure. Non-filled circles represent metallic atoms and hatched circles represent the metalloid/post-transition metal atoms [60].

This structure was used to describe many intermetallics formed by reaction of metals with III-V materials and will be used to describe results later on.

1.3.3 Superstructures

Crystalline structures can exhibit a compositional ordering of elements inside the primary lattice giving birth to additional structure superimposed to the initial one and yielding a longer periodicity. Compositional order occurs generally when there is a difference in atomic size or charge. Hence, in disordered alloys [2] of composition AB, any given atom site will be occupied indifferently by either atom A or atom B, but on ordering, atom A and atom B segregate more or less. The segregation to a particular atom site induces little or no deformation of the lattice. In disordered crystals, cryptographically equivalent planes are statistically identical whereas on ordered states, there can exist an alternation of A-rich planes and B-rich planes. On one hand, the ordering lowers the symmetry of the superlattice and, therefore the superstructure exhibits fewer systematic absences resulting in more diffraction peaks. On the other hand, superimposed structures result in additional diffraction spots hardly detected by X-Ray diffraction, if not at all. Synchrotron radiation is of great interest when studying superstructures because of its coherent extremely intense incident beam. Figure 1.8 depicts an example of powder diffraction pattern from Cu_3Au superstructure.

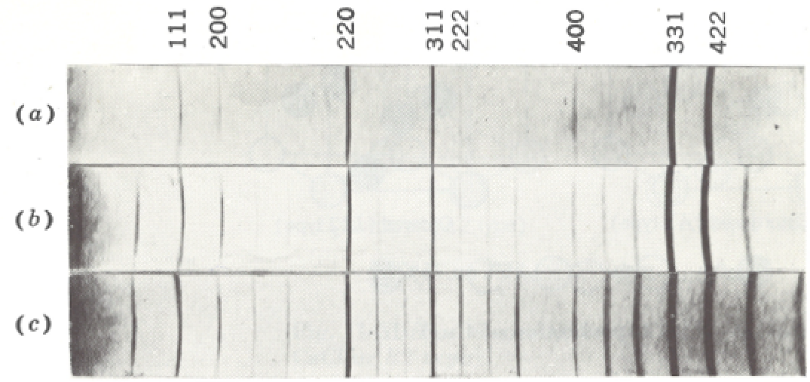

Figure 1.8 – Powder diffraction patterns of the superlattice Cu_3Au (a) Disordered, (b) partially ordered, (c) highly ordered, (From [62]).

1.4 Solid-State reaction between Ni and GaAs

The reaction between Ni and GaAs has been widely explored. First attempts to characterize the resulting material were performed on thin films and dates back to the 1980's [24, 63, 64] and eventually culminated in the establishment of different phase diagrams for the ternary (Ni, Ga, As) systems [23, 65, 66]. Multiple data and different experimental approaches gave birth to different interpretations especially when it comes to stoichiometry and phase stability. We will try to enumerate these different results and make a critical review. The different ternary phases that were reported in literature are summarized in Table 1.2 according to the phase

---

[2] We will refer by ordered/disordered alloys, the alloys presenting superstructures or not. This is not to be confused with crystalline/amorphous states of matter.

diagram established by Guérin [23].

1.4.1 Ni-GaAs formation on thin films

Early studies on the phase formation when Ni and GaAs are put in contact were carried out on thin films. This was amply justified by the aim of such studies to understand the formation of contacts for GaAs MOSFETS. Ogawa was among the first to be interested in studying the phase formation of thin film[3] Ni-GaAs intermetallics [63]. Ogawa demonstrated that a solid-state reaction occurs when a 110 nm of Ni is brought onto contact with a GaAs substrate and is annealed under a hydrogen atmosphere for a temperature ranging from 150 °C to 500 °C. The so-formed intermetallic was characterized to exhibit an hexagonal structure of B8 type yielding a superstructure or not depending on the annealing temperature. RHEED (Reflection high-energy electron diffraction) measurements show that the intermetallic conserves a Ni_2GaAs chemical composition. This intermetallic forms after a 200 °C annealing for 5 min and encounters a complete degradation into NiAs and β-NiGa at 500 °C. It is demonstrated that only polycrystalline Ni_2GaAs is formed at 200 °C. Both polycrystalline and single crystal co-exist after a 300 °C annealing. At 400 °C, ordered (i.e. presenting a superstructure) Ni_2GaAs is formed.

1.4.2 Structure of Ni-GaAs intermetallics

Sands and Keramidas carried out experiments on similar samples [24]. Samples were prepared by depositing 44 nm thick Ni layer on pre-cleaned GaAs by electron gun evaporation. Transmission Electron Microscopy (TEM) and Energy Dispersive X-Ray Spectroscopy (EDS) has revealed some discrepancies compared to the previous work. In fact a different stoichiometry was measured. The nominal composition found by EDS is Ni_3GaAs for similar annealing temperature to Ogawa (200 °C and 315 °C). This result was further confirmed by measuring the unit cell volume which should have contained 3 Ni atoms. The intermetallic film thickness was measured to be 88 nm making the thickness increase by a factor of 2. The proposed crystallographic structure is the same and is based on the “half-filled” form of the B8 hexagonal structure. Two Ni atoms occupy the (0,0,0) and (0,0,1/2) positions and also one position between the (1/3,2/3,3/4) and (2/3,1/3,2/4) positions. Ga and As occupy the (1/3,2/3,1/4) and (2/3,1/3,1/4) positions. The measured intermetallic exhibits again superstructures at 315 °C. Sands et al. support that such ordering is due to Ni vacancies and that the probable lattice parameters of the superlattice are $2a_0 \times c$ and $3a_0 \times c$. As the B8 structure can hypothetically accommodate from 2 to 4 Ni atoms, the homogeneity range is supposed to be quite broad. NiGa and NiAs are formed at high temperature (400 °C). As a consequence, Ni_3GaAs is not a stable phase in the presence of excess GaAs. Indeed, the formation of binary phases from Ni_3GaAs involves further consumption of GaAs.

---

[3] While thin films refer to a layer of material whose thickness vary from few angstroms to few micrometers, the thickness range appreciation may change according to the field of research. Accordingly, nowadays electronic engineers tend to refer to thin films as sub-10 nm thick films.

	Phase D	Phase B	Phase A	Phase C	Phase E	NiAs
From the Ni-Ga-As Phase diagram in [23]	from 1.26	1.31	1.32	1.26	1.27	1.39
	to 1.31	1.32	1.35	1.27		
Ogawa [63]						
300 °C - 20 min	1.292					
300 °C - 5h						
Finstad [68]						
350 °C - 20 min			1.344			
Lahav [64]						
300 °C - 4 h			1.316			
Sands [24, 69]						
220 °C - 10 min	1.285					
315 °C - 10 min		1.305				
410 °C - 10 min			1.322			
480 °C - 10 min					1.371	
Guivarc'h [67]						
200 °C - 1 h	1.306					
250 °C - 1 h			1.310 & 1.318		1.374	
350 °C - 1 h					1.370	
400 °C - short				1.274	1.369	
400 °C - 1 h				1.276		1.383
450 °C - 1 h				1.274		1.387
600 °C - 1 h				1.271		1.39
Chen [70]						
300 °C - 1 h		1.31				

Table 1.2 – Summary of Ni-GaAs phases in thin films as depicted by literature from the Ni-Ga-As phase diagram established by Guérin and Guivarc'h [23, 67]. The hexagonal phases are defined by their axial ratio c/a

1.4.3 Texture of Ni-GaAs intermetallics

Several authors have investigated the texture of Ni-GaAs intermetallics by means of symmetric X-Ray diffraction and TEM analysis on both (1 0 0) and (1 1 1) orientated GaAs substrates. In the case of (1 0 0), one crystallographic orientation was common for the works of Ogawa, Guivarc'h and Lahav [63, 64, 67], which is the following orientation:

$(0\,0\,0\,1)_{\mathrm{Ni_2GaAs}} || (1\,1\,1)_{\mathrm{GaAs}}$; $[1\,\bar{2}\,1\,0]_{\mathrm{Ni_2GaAs}} || [\bar{1}\,1\,0]_{\mathrm{GaAs}}$

While Sands [24] found the following orientation:

$(0\,1\,\bar{1}\,2)_{\mathrm{Ni}_x\mathrm{GaAs}} || (0\,\bar{1}\,1)_{\mathrm{GaAs}}$; $[2\,\bar{1}\,\bar{1}\,0]_{\mathrm{Ni}_x\mathrm{GaAs}} || [0\,0\,1]_{\mathrm{GaAs}}$

These two orientations are nominally the same (with slight variation of the $(0\,1\,\bar{1}\,2)$ plane with respect to the $(0\,\bar{1}\,1)$ plane of GaAs). Nevertheless, Sands et al. [24] discussed also the intermetallic orientation and noted a slight deviation by 2° of the c axis of the hexagonal structure from the [1 1 1] direction of the semiconductor. Lahav et al. [64] observed on the other side a deviation of the $(1\,0\,\bar{1}\,1)$ planes of the intermetallic from the sample surface. The deviation of the $(1\,0\,\bar{1}\,1)$ plane from the surface is explained using symmetrical considerations. In fact, the intermetallic can be described (at least at early stages of formation) using a pseudo-cubic hexagonal structure. When c/a is close to 1.225, the hexagonal structure has a symmetry close to four-fold in the $(1\,0\,\bar{1}\,1)$ and these planes are parallel to the (1 0 0) plane of the parent zinc-blende structure. If the c/a axial ratio deviates from the ideal pseudo-cubic value, then a rotation of these planes occurs. Lahav believes that the angular mismatch between the intermetallic and the substrate is a more meaningful criteria for epitaxial quality (i.e. misfit calculation) than the lattice parameters of both structures.

In any case, the intermetallic grows with its c axis parallel to the (1 1 1) of the GaAs.

1.4.4 Phase sequence and stability of the intermetallics on thin films

In this section we will confront three different results that emerged from three different teams in their attempt to establish a ternary phase diagram for the Ni-Ga-As system. A series of 5 papers and correspondences between authors illustrates the difficulties of result interpretations due to the crystallographic nature of the studied intermetallic but also because of the different experimental approaches in either characterizing the intermetallics or in elaborating the samples.

Ogawa [63] observed no particular phase sequence . However, he suggested rather a broad range of homogeneity of the $\mathrm{Ni_2GaAs}$ phase although he observed superstructure formation. At 500 °C, $\mathrm{Ni_2GaAs}$ has decomposed into NiAs and β-NiGa. Sands et al. [24] did not observe any particular phase sequence neither but stated that $\mathrm{Ni_3GaAs}$ is probably a metastable phase[4].

---

[4] A metastable state is an equilibrium state where the phase is kinetically stable but thermodynamically unstable. The transformation to a stable state is slow, or even sometimes infinitely slow. One can understand metastability

Table 1.3 – Phase sequence of Ni-GaAs intermetallics on thin films as reported by literature

	GaAs	200-400 °C	400 -580 °C	600 °C
Ogawa [63]	(111)	Ni_2GaAs	NiAs + NiGa	
Lahav [64]	(100) (111)	Ni_2GaAs	NiAs + $Ni_{2-x}GaAs_{1-x}$ Ni_2GaAs	NiAs + NiGa
Sands [24]	(100)	Ni_xGaAs	$Ni_3Ga_{2-y}As_y$ + $Ni_2Ga_xAs_{2-x}$	NiAs + NiGa
Yu [71]	(100)	Ni_3GaAs	$Ni_{2.4}GaAs$	NiAs + NiGa
Guérin [67]	(100) (111)	phase D then phase A + phase C phase D then phase E + phase C	NiAs + phase C NiAs + phase C	NiAs + NiGa + ϵ phase C

The results found by the other authors is summarized in Table 1.3. The final decomposition of the intermetallic results often in the formation of two binary compounds (NiAs and NiGa) at higher annealing temperatures (600 °C). The discrepancies between the different results might be explained by different sample preparation conditions. Moreover, all authors stipulate that ternary phases that are formed during the annealings are metastable and yield a broad homogeneity range. Furthermore, a characterization problematic makes accurate calculations of lattice parameters rather tricky in these thin films. The exclusive use of symmetrical X-Ray diffraction measurements provides poor data to make such calculations. For example some authors needed to grow the intermetallic on two different substrate orientations in order to access to different crystallographic planes parallel to the sample surface by X-Ray diffraction and thus calculate the lattice parameter using only two interplanar distances coming from two different samples.

The establishment of a phase diagram was a subject of interest for several research teams. Indeed, a consequent research was done to establish a phase diagram [23, 65, 66] for the Ni-Ga-As system. As for thin films, the results were quite different according to authors as we will show in the next sections.

1.4.4.1 Ni-Ga-As phase diagram as established by Guérin and Guivarc'h *1989*

The work carried out by Guérin and Guivarc'h [23] has resulted in the elaboration of a phase diagram (see Figure 1.9). Indeed, Guérin et al. have identified in total 5 hexagonal intermetallics that can be differentiated either by their *c/a* parameter or by ordered/disordered state and present a rather broad range of homogeneity.

Sample preparation was performed as the following: the proper amounts of the Ni, Ga and As elements were weighed in the required amounts for each sample. Each sample was placed in

---

by considering the potential energy of the physical-chemical system. A metastable phase would be characterized by a state corresponding to a local energy minimum. To achieve a stable state, the system potential energy must correspond to the global energy minimum.

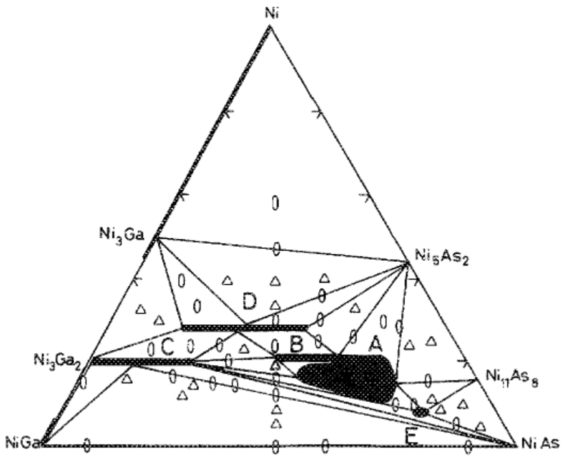

Figure 1.9 – Emphasized Ni-Ga-As diagram between the Ni_3Ga-Ni_5As_2 and NiGa-NiAs tie lines. The isothermal section of the solidus portion of the bulk Ni-Ga-As ternary diagram have features that are valid from 298 K up to the first eutectic point (T > 1073 K) [23].

a silica tube and brought to vacuum. The samples were annealed first at 700 °C for 2 days in order to prevent a possible reaction between the silica and the powders. Then the samples were cooled to room temperature. Pellets were formed from the obtained powders and were then re-annealed to homogenize the samples for 3 days at 1000 °C. A first cooling was applied to the samples down to 800 °C at a slow rate (5-10 °C/h). Some samples were then cooled down to room temperature either slowly for some samples or quenched into cold water directly from 800 °C for the other samples. It is important to note that Guérin and Guivarc'h stated that no structural modification occurs according to the two different cooling methods. Moreover, they used slow cooling in order to obtain single crystals. In total, they formed 40 different samples and the reaction products were then analyzed using a symmetrical diffractometer(ground samples into a fine powder) and using the Weisenberg, Laüe and Buerger methods (on single crystals).

X-Ray diffraction helped established a phase diagram for the Ni-Ga-As system and the identification of 5 different phases with broad domain of homogeneity. They are listed above in Tables 1.4, 1.5, 1.6, 1.7 and 1.8.

All the phases on the Ni-Ga-As isothermal section of the ternary phase diagram derive structurally from the NiAs lattice. These phases have rather broad homogeneity ranges and their compositions varies between the two tie lines in Figure 1.9 (NiGa-NiAs and Ni_3Ga-Ni_5As_2). Phase B, C and E present an ordering that can be attributed to different hypotheses. These assumption are coherent with the description of the NiAs-type lattice by Kjekshus and Pearson [60] and can be summarized as the following:

- An ordering of the Ni atoms inside the metallic subcell in the B8 system.

Table 1.4 – Crystallographic data for phase A (a,c)

at. % composition	$Ni_{59}Ga_{18}As_{23}$	$Ni_{58}Ga_{16}As_{26}$	$Ni_{56}Ga_{11}As_{33}$	$Ni_{60}Ga_{10}As_{30}$
Formula	$Ni_{2.9}Ga_{0.9}As_{1.1}$	$Ni_{2.75}Ga_{0.75}As_{1.25}$	$Ni_{2.5}Ga_{0.5}As_{1.5}$	$Ni_3Ga_{0.5}As_{1.5}$
a (Å)	3.821 ± 1	3.796 ± 3	3.719 ± 2	3.826 ± 2
c (Å)	5.037 ± 2	5.041 ± 4	5.033 ± 2	5.109 ± 2
V ($nm^3 \times 10^3$)	63.69	62.90	60.30	64.76
c/a	1.318	1.327	1.353	1.335

Table 1.5 – Crystallographic data for phase B ($a\sqrt{3}$,3c)

at. % composition	$Ni_{60}Ga_{20}As_{20}$	$Ni_{60}Ga_{15}As_{25}$
Formula	Ni_3GaAs	$Ni_3Ga_{0.75}As_{1.25}$
a (Å)	3.863 ± 2	3.840 ± 2
c (Å)	5.061 ± 3	5.073 ± 3
V ($nm^3 \times 10^3$)	65.37	64.78
c/a	1.310	1.321

Table 1.6 – Crystallographic data for phase C (2a,4c)

at. % composition	$Ni_{60}Ga_{38}As_2$	$Ni_{60}Ga_{35}As_5$	$Ni_{60}Ga_{30}As_{10}$
Formula	$Ni_3Ga_{1.9}As_{0.1}$	$Ni_3Ga_{1.75}As_{0.25}$	$Ni_3Ga_{1.5}As_{0.5}$
a (Å)	3.956 ± 4	3.949 ± 5	3.940 ± 4
c (Å)	4.982 ± 8	5.006 ± 8	5.004 ± 9
V ($nm^3 \times 10^3$)	67.50	67.60	67.30
c/a	1.259	1.267	1.270

Table 1.7 – Crystallographic data for phase D(a,c)

at. % composition	$Ni_{64}Ga_{29}As_7$	$Ni_{64}Ga_{18}As_{18}$	$Ni_{64}Ga_{15}As_{21}$
Formula	$Ni_{3.55}Ga_{1.6}As_{0.4}$	$Ni_{3.55}GaAs$	$Ni_{3.55}Ga_{0.83}As_{1.16}$
a (Å)	3.997 ± 1	3.941 ± 2	3.896 ± 2
c (Å)	5.034 ± 1	5.060 ± 2	5.103 ± 3
V ($nm^3 \times 10^3$)	69.65	68.06	67.08
c/a	1.259	1.284	1.310

Table 1.8 – Crystallographic data for phase E (3*a*,2*c*)

at. % composition	$Ni_{54}Ga_8As_{38}$	$Ni_{50}As_{50}$
Formula	$Ni_{1.16}Ga_{0.16}As_{0.83}$	NiAs
a (Å)	3.675 ± 8	3.618 ± 2
c (Å)	5.040 ± 6	5.034 ± 2
V ($nm^3 \times 10^3$)	58.95	57.06
c/a	1.371	1.391

- An ordering of the Ga and As atoms.
- An ordering of vacancies that can happen on the (*2a*) sites of Ni, on the Ni sites in the metallic sub-cell or on the Ga and As sites on the (*2c*) sites.

The other two phases, A and D are fully disordered and the corresponding powder diffraction diagram shows no extra-reflections corresponding to superstructures. Only binary phases are in thermodynamic equilibrium with GaAs: NiGa, Ni_2Ga_3 and NiAs (and eventually their extensions). All ternary phases are not stable when Ni reacts with GaAs because of the lack of any tie line between Ni and GaAs. The average composition of the formed phases when Ni and GaAs are put into contact will therefore remain on the vertical line connecting Ni and GaAs and the reaction would continue until the so-formed phases are sufficiently rich in Ga or As and form stable binaries.

It is clear from the phase diagram that the first intermetallic to form is of a Ni_3GaAs chemical composition. The only stable phase to form in the phase diagram is NiAs and its solid solution. This result confirms former results on metallization on thin films (discussed earlier in this chapter) where most of the identified Ni_xGaAs phases were metastable phases. But unlike former results by Sands et al., Guérin and Guivarc'h observed 2 phases with superlattice being formed.

1.4.4.2 Ni-Ga-As phase diagram as established by Zheng et al. *1989*

Simultaneously with the publishing of the Guérin and Guivarc'h work, another team published results on the phase equilibria of Ga-Ni-As at 600 °C [65]. The experimental procedure included the preparation of powders with the required amounts of Ni, Ga and As for each sample. The annealing procedure included a primary annealing at 600 °C for 10 days then a secondary annealing at 600 °C for 30 days after pulverization. The samples were then quenched in ice-water. Lattice parameters and crystalline structure were analyzed through X-Ray diffraction and composition analysis was carried out using a scanning electron microscope.

Surprisingly, instead of 5 ternary phases, Zheng et al. interpreted only one ternary phase (Ni_3GaAs) and identified the others as binary phases with extensive ternary solubilities. The observed phases are identified as γ'-$Ni_{13}Ga_9$, γ-Ni_3Ga_2 and the ternary phase T-Ni_3GaAs. The authors identified the γ' as a monoclinic phase possessing a very complex structure due to superlattice occurrence but were not able to index all peaks from the diffraction pattern. Yet the structure of this γ' remain ambiguous as researchers have indexed also its peaks in the B8 structure using superlattice considerations. In [65], the authors also noticed the fact that the T phase and the γ phase have very similar lattice parameters and the same crystalline structure (B8) and thus they do not exclude that Ni_3GaAs can be considered as a ternary extension of the binary phase γ-Ni_3Ga_2 within a considerable range of composition.

1.4.4.3 Ni-Ga-As phase diagram as established by Ingerly et al. *1996*

In 1995, a team from the University of Wisconsin-Madison made a new attempt in order to establish the phase diagram of the Ni-Ga-As system [66]. The procedure to establish the isothermal phase equilibria diagram is the same as the one carried out by Zheng: powder mixtures of GaAs and Ga, As and Ni elemental powders were prepared. The powder mixtures were uniaxially pressed into pellets using a pressure of 30,000 psi. These pellets were then sealed in quartz ampoules and brought to vacuum. A first annealing at 600 °C for 10 days was performed, then the pellets were pulverized and pressed and released from the ampoules. A second annealing at 600 °C followed for 30 days. The samples were then quenched in ice water.

Ingerly et al. analyzed the different samples using an X-Ray diffractometer and electron microprobe using wavelength-dispersive spectroscopy of X-Ray to characterize the different samples. Contrary to former studies, this study showed that at 600 °C there is a formation of at most one hexagonal ternary intermetallic. The remaining phases were either binary NiAs or NiAs-based solid solutions.

On the contrary to Guérin et al. and Zheng et al. results, the study from 1995 shows that the T phase (Ni_3GaAs) is formally a ternary extension of the NiAs solid solution at 600 °C. They also state that four of the five ternary phase fields identified by Guérin and Guivarc'h are comprised in the NiAs solid solution field. Moreover, they stress the point risen early by Zheng et al. that the C phase is most likely a ternary extension of the γ-$Ni_{13}Ga_9$ phase rather than a stand-alone ternary phase as they could not satisfactorily index all peaks coming from the diffraction pattern of the corresponding sample.

1.4.4.4 Discussion

Later on, the discussion between Guérin et al. and Ingerly [72, 73] revealed substantial different approaches in the comprehension and identification of the so-formed phases on the Ni, Ga and As phase diagrams. Indeed, Ingerly et al. stated that the C phase can not be clearly identified as a ternary phase and that it could be a ternary extension of the γ-$Ni_{13}Ga_9$ phase due to the non significant amount of As in the atomic composition of C phase found by

Guérin et al. While Guérin and Guivarc'h insisted on the importance of the superstructure identification as a mean to clearly separate the different phases. Moreover Ingerly et al. in their reply to the comments of Guérin and Guivarc'h to their proposed phase diagram remarked that the samples prepared by the Guérin team were homogenized at 1000 °C and slowly cooled to 800 °C. The samples then were either quenched or slowly cooled to room temperature before performing X-Ray diffraction measurement making it difficult to consider the room temperature analyzed samples representative of the annealed samples. Guérin et al. have considered that the phase diagram does not change between the temperatures of 25 and 800 °C. The lack of further chemical characterization was also pointed out while Ingerly et al. did electron probe microanalyses.

Moreover, Ingerly et al. demonstrated that a sample with a nominal composition of Ni_3GaAs have its crystalline structure change depending on the cooling rate claiming that the quenched sample shows a single phase while the slowly cooled sample exhibits additional peaks consistent with the presence of superstructure.

Hence, hexagonal superlattices are not thermodynamically stable at 600 °C (temperature at which the authors performed 30 days long annealings and then quenched the samples in ice water) and could possibly be formed during the slow cooling of the samples.

In conclusion, these papers, while contradictory in several points, show the extreme versatility of the studied phases. This versatility is further emphasized by the fact that the B8 structure easily handles superlattices. This shows also that not only the conditions of preparation of the samples is of great importance (i.e. annealing temperature, type of annealing, etc..), but also the cooling rate of the samples helps the persistence of metastable phases formed at the annealing temperature or the creation of further metastable phases (or the occurrence of an ordering) depending on the cooling conditions.

1.5 Reaction between Ni films and InGaAs layer

While there is abundant literature attesting of the performance of Ni-based contacts on InGaAs for CMOS applications [74–77], there has been few material studies since the introduction of InGaAs alloys (starting from 2010) on the reaction between Ni and InGaAs. We will enlist the different results and observations relatively to the so-formed Ni-InGaAs intermetallic.

1.5.1 Formation of Ni-InGaAs

In a similar fashion to the formation of silicides, several authors found a unique hexagonal structure with the composition $Ni_2In_{0.5}Ga_{0.5}As$ [78, 79] for similar annealing conditions (see Table 1.9).

Shekhter et al. [79] observed a unique orientation after an annealing of 250 °C using pole figure analysis (see Figure 1.11):

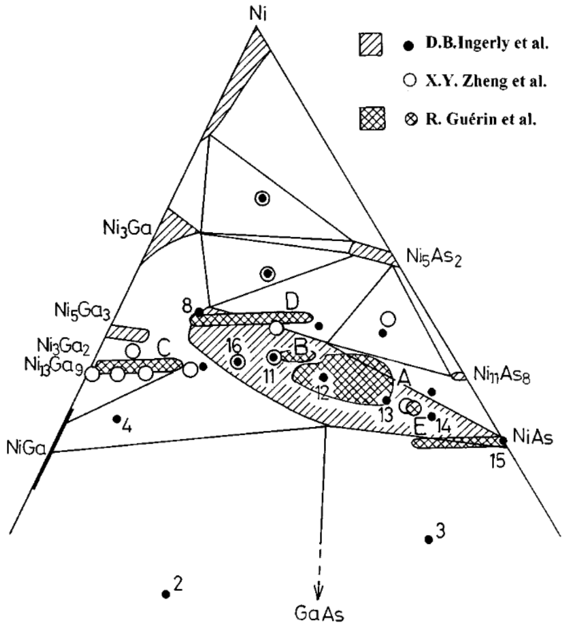

Figure 1.10 – Isothermal section of the Ni–Ga–As ternary phase diagram proposed by Ingerly et al. [66]. Extended solid solutions are represented by streaked lines while numbers correspond to the atomic composition of the samples (black circles) which have been the subject of comments in the text. Atomic composition of the samples of Zheng et al [65] (open circles) and of the ternary phases A, B, C, D and E (double streaked) given by Guérin et al. [23] are also presented, for comparison.

$(1\,0\,\bar{1}\,0)_{\text{Ni-InGaAs}} || (0\,0\,1)_{\text{InGaAs}}$; $[0\,0\,0\,1]_{\text{Ni InGaAs}} || [0\,1\,\bar{1}]_{\text{InGaAs}}$

The pole figure analysis showed also that there is a missing azimuthal variant that should appear along the [1 1 0] axis of the semiconductor. This missing orientation was stressed out by the authors and was attributed to a possible vicinal surface at the substrate that favored the growth along one axis and not the other one (although the two axes are of same crystallographic family, hence they should be thermodynamically equivalent in case of growth of an intermetallic along this direction).

Ivana et al. [78] found similar orientation but noted that at 300 °C, there was an appearance of (1 0 1) peak at the surface of the sample. This is in coherence with the result of the metallization of GaAs by Ni. Nevertheless, a diffraction peak indexed by these authors as a $(2\,0\,\bar{2}\,1)$ plane is likely wrongly indexed as this plane can not be parallel to the surface when $(1\,0\,\bar{1}\,1)||(0\,0\,1)_{\text{InGaAs}}$ and is rather likely to correspond to the $(2\,0\,\bar{2}\,2)$ plane.

Chen et al. [80] have studied reacted Ni with InGaAs in patterned structures according to the Fin orientation as well as the Fin width. It was demonstrated through HRTEM that the so-formed intermetallic yields two different orientations according to the position of the intermetallic (also called nickelide) in the Fin: one orientation where the $Ni_2In_{0.5}Ga_{0.5}As$ [0 0 0 1] direction is parallel to the substrate surface and another one where the $Ni_2In_{0.5}Ga_{0.5}As$

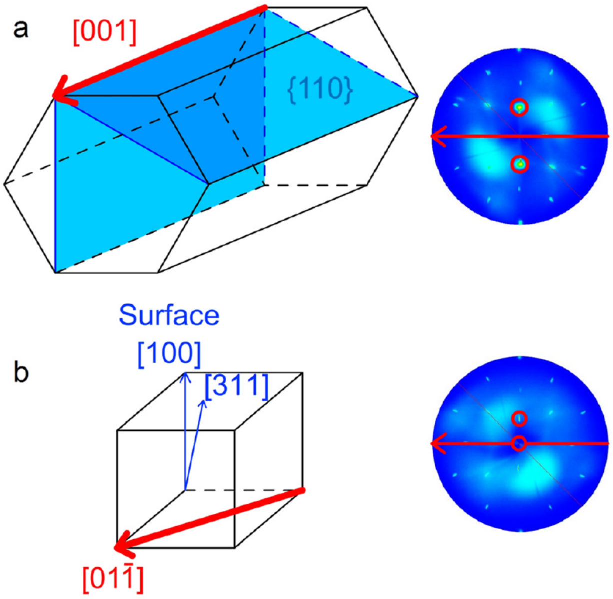

Figure 1.11 – Orientation of the hexagonal intermetallic as observed by Shekhter et al. [79]. (a) The hexagonal structure of Ni-InGaAs and the $(11\bar{2}0)$ NiInGaAs pole figure with two of the $\{110\}$ plane family (red circles) with their $[001]$ zone axis (red arrow). (b)The cubic structure of InGaAs and the $(11\bar{2}0)$ bare InGaAs pole figure with the $[311]$ vector, one of the $\langle 311\rangle$ vector groups (top red circle) and the surface normal $[100]$ (bottom red circle) with their zone axis $[01\bar{1}]$ one of the $\langle 110\rangle$ vector groups. As seen in the pole figures, the $[001]$and $[01\bar{1}]$ are parallel.

$[0001]$ direction is parallel to the $In_{0.53}Ga_{0.47}As$ $[111]$ direction (see Figure 1.12). The authors explain that the crystal rotation of the intermetallic occurs at almost 200 nm near the intermetallic/InGaAs interface and undergoes a gradual change with defective crystallites. This peculiar rotation is further emphasized by the $[0001]$ growth direction and the $(10\bar{1}1)$ facet formation which leads the nickelide segment to undergo a postgrowth crystal rotation.

The ratio for volume expansion $\frac{V_{Ni_2In_{0.5}Ga_{0.5}As}}{V_{In_{0.53}Ga_{0.47}As}}$ from $In_{0.53}Ga_{0.47}As$ to $Ni_2In_{0.5}Ga_{0.5}As$ was calculated to 1.342, while Ivana et al. found a ratio for the volume expansion of 1.7. Nickel was also found to be the diffusing element in InGaAs, as it is the case in GaAs substrates [64]. In the case of Fin channels, Ni tends to have a surface diffusion dominant process through InGaAs during the formation. In the case of larger Fin width, the diffusion is rather a volume diffusion. The nickelide formation led also to both in-plane and out-of-plane compressive strains on the Fin channels that opened up the InGaAs energy band-gap.

1.5.2 Structure of the Ni-InGaAs intermetallic

Since the reaction is pretty much similar to the Ni-GaAs one, most of the authors speculated that the structure of the Ni-InGaAs intermetallic is of the NiAs type. This is coherent with

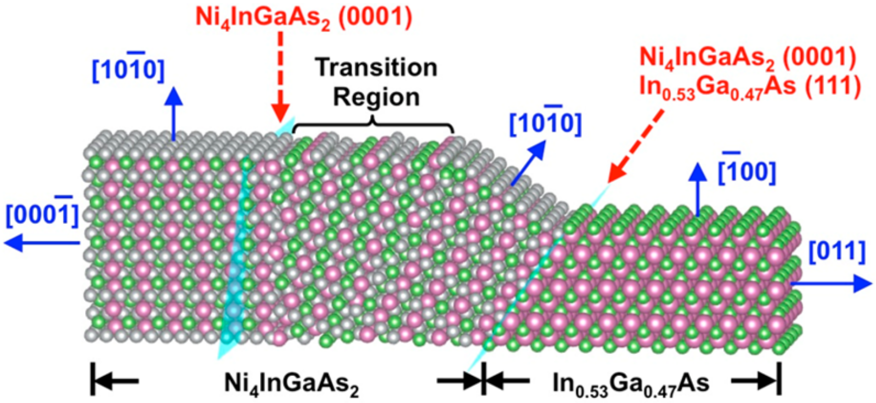

Figure 1.12 – Orientation of the hexagonal intermetallic as observed by Chen et al. [80] in an InGaAs Fin.

Table 1.9 – Lattice parameters and orientations of the Ni-InGaAs intermetallics in literature

$Ni_2In_{0.5}Ga_{0.5}As$	*a* (Å)	*c* (Å)	orientation
Ivana et al. [78]	3.96	5.16	Ni-InGaAs $[\bar{1}\bar{1}0]$ $\parallel$InGaAs [001] ; Ni-InGaAs[110]$\parallel$InGaAs [110]
Shekther et al. [79] *(refined from the given 2θ positions)*	3.89	5.09	Ni-InGaAs $(10\bar{1}0)$ $\parallel$InGaAs (001) ; Ni-InGaAs [0001] $\parallel$InGaAs $[01\bar{1}]$
Chen et al. [80]	3.93	5.10	Ni-InGaAs [0001] $\parallel$InGaAs [111] ; Ni-InGaAs [0001] $\parallel$InGaAs [001]

the large miscibility of In in the zinc-blende GaAs lattice. Indeed, the hexagonal phase was found to have a B8 structure. This structure can host in the metallic sub-cell, 2 more atoms of Ni. A completely filled NiAs structure correponding to a stoichiometry of $Ni_4In_{0.5}Ga_{0.5}As$ is presented in Figure 1.13

1.5.3 Phase sequence of the Ni-InGaAs

Though no clear phase sequence was identified when Ni is put in contact with InGaAs ($Ni_2In_{0.5}Ga_{0.5}As$ was found to be the unique phase to form either at 250 °C [79], or at temperatures between 250 and 300 °C. [80]), Ivana et al. [78] reported an appearance of new diffracting planes by XRD. Indeed, at 350 °C, the authors observe extra diffraction peaks that were associated with diffraction peaks coming form $Ni_{11}As_8$ or NiIn (see Figure 1.14).

In the end, it is clear that literature on Ni-InGaAs is scarce and incomplete in comparison of the knowledge on silicides or even on Ni-GaAs intermetallics. Moreover, characterization techniques used to identify the Ni-InGaAs intermetallics remain limited. In fact, authors did either symmetric X-Ray diffraction, STEM measurements or precise pole figures on predefined planes. These methods are not sufficient to completely decide on the so-formed phases (either structurally, or in terms of the number of formed phase) because in either cases, the reciprocal space is not completely probed. Another point that remain ambiguous is the stoichiometry of such phases. SIMS (Secondary ion mass spectrometry) and EDS measurements do not give a

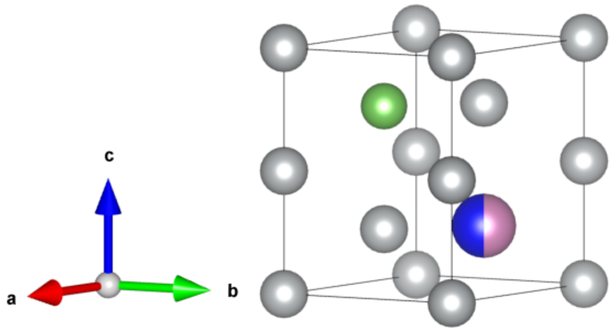

Figure 1.13 – Representation of a B8 Ni-InGaAs intermetallic with a stoichiometry of $Ni_4In_{0.5}Ga_{0.5}As$. Grey atoms correspond to Ni atoms, green atom correspond to As, blue atom correspond to In and pink atom correspond to Ga. In this example, the B8 structure is fully filled and there are 2 atoms on the metallic sub-cell.

precise chemistry of phases. Besides, the versatile nature of the B8 structure makes it difficult for only one phase with a precise stoichiometry to form. All of these points lead us to discuss in the next chapter a more global method to analyze the Ni-InGaAs intermetallics.

1.6 Conclusion

We have seen in this chapter that the study of phase formation and stability of Ni-GaAs intermetallics was widely reported in the literature. Due to different sample preparation process, some discrepancies have risen when it comes to define the stoichiometry and phase sequence of the ternary intermetallics. The work on phase diagram establishing has also given rise to a scientific debate on the accuracy of proposed phase diagrams. All of these elements makes it more challenging to study the phase of formation between Ni and InGaAs substrates. We have also seen that the silicide formation studies are also of an extreme aid when it comes to study intermetallics formations. Indeed, many theoretical basis of metallurgy were either confirmed or developed when studying silicide contacts. Moreover, extremely important characterization methods were also developed thanks to research on silicide. Indeed, the 3D Reciprocal Space Mapping (3D-RSM) as developed by Gaudet et al. [81] was crucial to correctly determine the phases during the phase sequence of silicide formation. Moreover, in the case of the metallization of GaAs thin films, most measurements were done using two different substrates in order to extract the lattice parameters of the intermetallic using symmetrical XRD. Therefore, we believe that the most correct way to analyze the formation of Ni-InGaAs intermetallics is to proceed to a complete scanning of the reciprocal space so that no phase is missing, and so that the characterization of the different phases is as accurate as possible. Therefore, the next chapter in this manuscript will deal with the different characterization methods and especially the development of 3D-RSM on both synchrotron beam-lines and on lab tools.

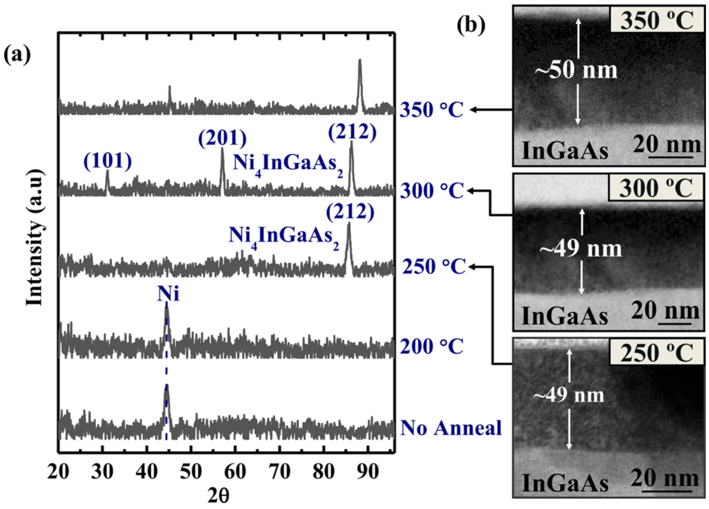

Figure 1.14 – (a) XRD general area detector diffraction system(GADDS) integrated diffraction intensity as a function of 2θ. (b) TEM images showing the thickness of 250, 300, and 350 °C formed films [78].

Résumé du chapitre 2

Nous avons vu dans le premier chapitre que la littérature rapporte des intermétalliques formés qui sont fortement texturés. La caractérisation des intermétalliques s'est basée la plupart du temps sur la diffraction symétriques des rayons X sur des couches minces. Cependant, une telle caractérisation ne donne accès qu'à une partie infime de l'espace réciproque et parait non suffisante lorsqu'il s'agit de caractériser de nouvelles phases dont aucune fiche-référence n'existe. Ainsi, et pour être sûr de ne pas omettre des phases ou des orientations et afin de mieux cerner la nature des intermétalliques, nous avons choisi de développer une méthode de mesure sur synchrotron et en laboratoire qui permet de mesurer rapidement l'espace réciproque en sa quasi-totalité. Cette méthode est la cartographie de l'espace réciproque en 3D par diffraction des rayons X et a été utilisée pour la première fois pour caractériser des siliciures en 2007. La diffraction des rayons X est particulièrement bien adaptée à l'étude des textures, structures et changement de phase de ces composés. Cependant, comme il a été montré par S. Gaudet et al et E. Bourjot et al., pour comprendre la complexité des mécanismes de formation de ces intermétalliques il est nécessaire de disposer d'une connaissance détaillée de l'espace réciproque du matériau. En collaboration avec la ligne CRG-BM02 de l'ESRF, nous avons mis en place une procédure d'acquisition et de traitement des données expérimentales permettant de disposer de cartographies en 3D de l'espace réciproque et de les analyser en temps réel. Pour optimiser le temps et la résolution d'acquisition, un détecteur 2D (XPAd 3) présentant une large ouverture angulaire a été utilisé. Un traitement informatique spécifique permet d'analyser les données acquises de plusieurs manières. Ainsi, des figures de pôle complètes peuvent être reconstruite pour analyser les textures des composés mesurés. Des intégrations complètes ou partielles sur les angles 2θ, χ ou ϕ, permettent d'obtenir un diagramme de diffraction « dé-texturé », à partir duquel l'identification des phases est possible avec un minimum d'ambiguïté. Ainsi, l'analyse combinée des figures de pôle, donnant accès à la symétrie de l'intermétallique ainsi qu'à sa texture, et l'analyse des diagrammes détexturés permettent de caractériser l'intermétallique durant sa formation et d'en apprécier la stabilité. Nous décrivons de plus dans ce chapitre la méthodologie d'acquisition en in situ effectuée sur la ligne BM02 à l'ESRF. Le dispositif expérimental y est expliqué ainsi que les différentes étapes de correction des images de diffraction.

2 Experimental Methods and Instrumentation

In this chapter we will introduce the experimental methods and acquisition strategies that were set up in order to characterize the intermetallics. As we deal with crystalline compounds, the basic physical phenomena that will be exploited is x-ray diffraction. The technique of the same name is a reference technique when it comes to studying thin film crystalline materials.

2.1 X-ray diffraction

When matter is irradiated with a beam of x-ray photons[1], it emits an x-ray beam with a wavelength equal or very close to that of the incident beam. This phenomena is known as elastic scattering. The scattered energy is by nature very weak. But in the case of a coherent reflection and when the scattering centers have non-random relative distances, the scattered waves interfere and produce diffracted waves with a much more important intensity. The analysis of the spatial distribution of diffracted intensity allows the characterization of the studied material structure.

2.1.1 Physics of the x-ray diffraction

x-ray diffraction can be observed because the scale of the x-ray electromagnetic wavelength is comparable to the one of inter-atomic distances in crystals and molecules. When the surface of a material is exposed to electromagnetic radiation in the x-ray wavelength range, the x-rays interfere with matter and three different types of interactions can be described[82–84]:

- Inelastic interaction (Compton scattering): Inelastic interaction take place with one or many free electrons of the atom. The incident X photon[2] loses a small part of its energy and the energy–momentum conservation law stipulates that its energy will take two

---

[1] The range of x-ray wavelength is placed between the ultraviolet region and the region of γ-rays emitted by radioactive substances. The interval of wavelengths of particular usefulness in crystallography ranges between 0.4 and 2.5 Å.

[2] Photons that have a wavelength in the range of x-ray wavelengths.

forms: a kinetic energy communicated to the electron (resulting in an electron recoil) and scattered x-ray having a lower energy and thus a higher wavelength. The wavelength of the scattered photon depends on the observation direction. Hence, the scattering is incoherent and no interference can take place. The Compton scattering contributes to undesirable background to the diffraction intensity.

- Photoelectric effect: The X photons can interact with electrons bound within atoms. Bonded electrons absorb the energy from the electromagnetic radiation and are excited to a higher energy level. If the electrons acquires more energy than the work function of the material, it is ejected.

- Elastic interaction (Thomson scattering): Elastic interaction takes place with free electrons of the atom, and does not modify the internal structure of the atom, and thus its internal energy. The electromagnetic wavelength scattered by the electrons is the same as the incident one. The scattering is then known as coherent scattering. In the case of ordered spatial distribution of atoms, coherent scattering can produce constructive interference known as diffraction.

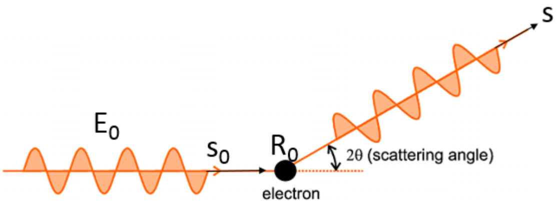

Figure 2.1 – Elastic scattering of x-rays by a single electron.

Elastic interaction is illustrated in 2.1 for a single free electron having a charge e, mass m and at position R_0. The incident beam is represented by a planar wave $E_0 \exp(-i s_0 R_0)$, where E_0 is the electrical field vector and $\boldsymbol{s_0}$ the wave vector. E_0 can be considered as independent from time and can be decomposed into two independent vectors $E_{0\pi}$ and $E_{0\sigma}$. The direction of incident and scattered radiations is given by the directions of $\boldsymbol{s_0}$ and $\boldsymbol{s}$ and the plane containing these two vectors is known as the scattering plane. For elastic scattering process one have:

$$|s_0| = |s| = \frac{2\pi}{\lambda} \tag{2.1}$$

The angle between $\boldsymbol{s}$ and $\boldsymbol{s_0}$ is the scattering angle and is usually denoted as 2θ in x-ray diffraction. Thus 2θ can be defined as in Equation 2.2:

$$2\theta = \frac{\langle \boldsymbol{s}, s_0 \rangle}{s s_0} \tag{2.2}$$

The difference between $\boldsymbol{s}$ and $\boldsymbol{s_0}$ is called the scattering vector and is denoted $\boldsymbol{Q}$:

$$\boldsymbol{Q} = \boldsymbol{s} - \boldsymbol{s_0} \tag{2.3}$$

The scattering vector has the dimensionality of an inverse length, while its direction points along the bisection of incoming and scattered beam. One can demonstrate through geometrical considerations that $|\boldsymbol{Q}| = 4\pi \sin\theta/\lambda$. Hence $|\boldsymbol{Q}|$ depends on both the geometry of the scattering process through the θ angle and also the wavelength of the incident x-ray beam.

2.1.2 Interference of scattered waves

We will now be interested in what is the core of the diffraction: the interference of scattered waves that results in the diffraction patterns in the case of multiple atoms. First we will consider the interference of scattered waves in the case of single atomic electron, then the scattering by atomic electrons and finally the coherent scattering by crystals, also known as diffraction.

To understand this process, we consider two scattering centers at O and O′ in Figure 2.2. If these two points are excited by a plane wave, they emit secondary waves which will mutually interfere.

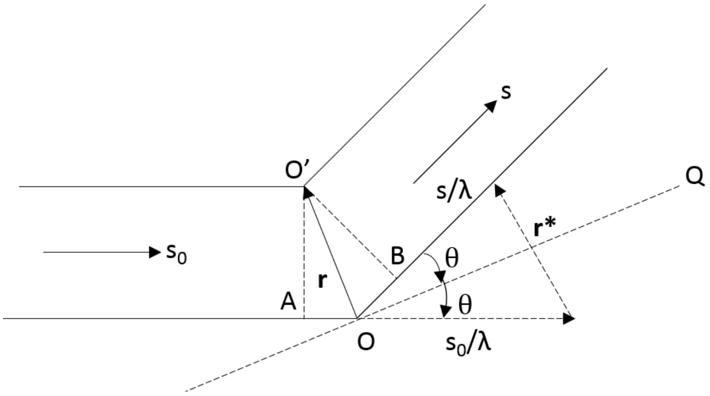

Figure 2.2 – O and O′ are the point scatterers. $\boldsymbol{s}$ and $\boldsymbol{s_0}$ are unit vectors. Therefore AO = $-\boldsymbol{r}\cdot\boldsymbol{s_0}$, BO = $\boldsymbol{r}\cdot\boldsymbol{s}$

$\boldsymbol{s}$ is the unit vector associated with the direction of the scattered wave and $\boldsymbol{s_0}$ is the unit vector associated with the incident one. In this configuration[3], we can define the phase difference between the wave scattered by O and the wave scattered in the same direction O′ as:

$$\delta = \frac{2\pi}{\lambda}(\boldsymbol{s} - \boldsymbol{s_0})\cdot\boldsymbol{r} = 2\pi\boldsymbol{r}^*\cdot\boldsymbol{r} \tag{2.4}$$

---

[3] Since the diffraction centers are "stationary" atoms, the diffraction pattern can be considered as constant in time. In this case, we can omit the time terms in the wave equation.

with

$$\boldsymbol{r}^* = \lambda^{-1}(\boldsymbol{s} - \boldsymbol{s_0}) \tag{2.5}$$

where λ is the wavelength of the incident wave.[4]

The modulus of $\boldsymbol{r}^*$ can be derived from Figure 2.2 as $\boldsymbol{r}^* = 2\sin\theta/\lambda$, where 2θ is the angle between the direction of incident x-rays and the direction of the observation.

Considering that A_O is the amplitude of the wave scattered by the scattering center O (assuming that its phase is equal to zero), the wave scattered by O′ is described by $A_{O'}\exp(2\pi i\boldsymbol{r}^* \cdot \boldsymbol{r})$. If there are N point scatterers along the path of the incident plane then:

$$F(\boldsymbol{r}^*) = \sum_{j=1}^{N} A_j \exp(2\pi i\boldsymbol{r}^* \cdot \boldsymbol{r}_j) \tag{2.6}$$

where A_j is the amplitude of the wave scattered by the j^{th} point.

If there is a certain number of electrons concentrated in O′ which undergo a Thomson scattering, we can define the scattering factor f, for which $f_{O'}$ expresses the number of electrons. Accordingly, eqn 2.6 becomes

$$F(\boldsymbol{r}^*) = \sum_{j=1}^{N} f_j \exp(2\pi i\boldsymbol{r}^* \cdot \boldsymbol{r}_j) \tag{2.7}$$

In the case of continuum of scattering centers, and considering that $\rho(\boldsymbol{r})$ is the density of electrons in an element of volume d$\boldsymbol{r}$, this volume would contain $\rho(\boldsymbol{r})\mathrm{d}\boldsymbol{r}$ electrons. The total amplitude of scattered wave is

$$F(\boldsymbol{r}^*) = \int_V \rho(\boldsymbol{r}) \exp(2\pi i\boldsymbol{r}^* \cdot \boldsymbol{r})\mathrm{d}\boldsymbol{r} = T[\rho(\boldsymbol{r})] \tag{2.8}$$

where T represents the Fourier transform operator. In crystallography the space of $\boldsymbol{r}^*$ is called the reciprocal space. According to eqn 2.8, the electron density $\rho(\boldsymbol{r})$ can be obtained by applying the Fourier inversion theorem. Indeed, the knowledge of the amplitude of the

---

[4] Note that if λ is much greater than $\boldsymbol{r}$, then the phase difference will be extremely small and negligible. Consequently, no appreciable interference phenomena will take place... Because the interatomic bound distances are between 1 and 4Å, the x-ray wavelength range is suitable to have noticeable phase difference while visible light gives no rise to interference effect.

scattered waves defines $\rho(\boldsymbol{r})$.

In the next paragraphs, we will present the scattering of X photons by atomic electrons, by atoms and finally what would of a practical use in this thesis, the scattering by crystals.

2.1.2.1 Scattering by atomic electrons

While completely incompatible, the Thomson and Compton scattering take place simultaneously. In fact, the intensity I_{eTh} of scattered radiation is the sum of coherent and incoherent scattering: $I_{coe} + I_{incoe} = I_{eTh}$. The coherent intensity I_{coe} can be calculated using these observations: atomic electrons can be represented by their distribution function $\rho_e(\boldsymbol{r}) = |\psi(\boldsymbol{r})|^2$, where $\psi(\boldsymbol{r})$ is the wave function solution of the Schrödinger equation. A volume $\mathrm{d}v$ contains $\rho_e \mathrm{d}v$ electrons and scatters elementary waves that will interfere with other scattered waves from the other elements in that volume. Thus, the electron scattering in a region of space S in which the probability of finding an electron is different from 0 will be:

$$f_e(\boldsymbol{r}^*) = \int_S \rho_e(\boldsymbol{r}) \exp(2\pi i \boldsymbol{r}^* - \boldsymbol{r}) \mathrm{d}\boldsymbol{r} \tag{2.9}$$

Hence, considering for example a spherical distribution of the electrons[5], then eqn 2.9 can be approximated to a more convenient form

$$f_e(\boldsymbol{r}^*) = \int_0^\infty U_e(\boldsymbol{r}) \frac{\sin 2\pi \boldsymbol{r}\boldsymbol{r}^*}{2\pi \boldsymbol{r}\boldsymbol{r}^*} \tag{2.10}$$

where $U_e(\boldsymbol{r}) = 4\pi r^2 \rho_e(\boldsymbol{r})$ is the radial distribution of the electron.

2.1.2.2 Scattering by atoms

To express the scattering by atoms containing Z atomic electrons, we can consider the atomic scattering factor f_a obtained by inversing the Fourier transform of the density of electrons in a volume $\mathrm{d}v$ of $\rho_a(\boldsymbol{r})$. In a first approximation, we can consider that $\rho_a(\boldsymbol{r})$ has a spherical symmetry, and in the same way as for atomic electrons scattering, we obtain

$$f_a(\boldsymbol{r}^*) = \int_0^\infty U_a(\boldsymbol{r}) \frac{\sin 2\pi \boldsymbol{r}\boldsymbol{r}^*}{2\pi \boldsymbol{r}\boldsymbol{r}^*} = \sum_{j=1}^{Z} f_{e_j} \tag{2.11}$$

---

[5] Correct for s electrons. Less correct for p, d, etc…

where $U_a(\boldsymbol{r}) = 4\pi r^2 \rho_a(\boldsymbol{r})$ is the radial distribution function for the atom.

2.1.2.3 Scattering by a crystal

In the case of a three-dimensional infinite crystal, one can start from a discrete approximation of the crystals in order to define its properties. Atoms can be described as centers of scattering characterized by their individual atomic scattering factor. An ideal crystal is constructed by the infinite repetition of identical structural units in space according to three vectors ($\boldsymbol{a}$, $\boldsymbol{b}$, $\boldsymbol{c}$). A position r represents the position of the elementary lattice of the n atom:

$$Crystal_{\infty} = Pattern \otimes Lattice \tag{2.12}$$

in other terms, the electron density function for the whole crystal is the convolution of the lattice function $L(\boldsymbol{r})$ with the electron density in the unit cell $\rho_M(\boldsymbol{r})$:

$$\rho_{\infty}(\boldsymbol{r}) = \rho_M(\boldsymbol{r}) \otimes L(\boldsymbol{r}) \tag{2.13}$$

with

$$L(\boldsymbol{r}) = \sum_{u,v,w=-\infty}^{+\infty} \delta(\boldsymbol{r} - \boldsymbol{r}_{u,v,w}) \tag{2.14}$$

where δ is the Dirac delta function, $\boldsymbol{r}_{u,v,w} = u\boldsymbol{a} + v\boldsymbol{b} + w\boldsymbol{c}$ and u, v and w are integers.

One can demonstrate that the amplitude of the wave scattered by the whole crystal is

$$F_{\infty}(\boldsymbol{r}^*) = T[\rho_M(\boldsymbol{r})] \cdot T[L(\boldsymbol{r})] = \frac{1}{V} F_M(\boldsymbol{H}) \sum_{u,v,w=-\infty}^{+\infty} \delta(\boldsymbol{r}^* - \boldsymbol{r}^*_{\boldsymbol{H}}) \tag{2.15}$$

Where V is the volume of the unit cell and $\boldsymbol{r}^*_{\boldsymbol{H}} = h\boldsymbol{a}^* + k\boldsymbol{b}^* + l\boldsymbol{c}^*$ is the generic lattice vector of the reciprocal lattice. If the scatterer object is non-periodic, the amplitude of the scattered wave $F_M(\boldsymbol{r}^*)$ can take non-zero values for any value of $\boldsymbol{r}^*$. If the scatterer centers are periodic, than an non-zero amplitude is given only when $\boldsymbol{r}^*$ coincides with a reciprocal space point:

$$\boldsymbol{r}^* = \boldsymbol{r}^*_{\boldsymbol{H}} \tag{2.16}$$

If we introduce the definition of $\boldsymbol{r}^*$ in 2.5 and multiply eqn 2.16 by $\boldsymbol{a}$, $\boldsymbol{b}$ and $\boldsymbol{c}$ the we obtain

$$\boldsymbol{a} \cdot (\boldsymbol{s} - \boldsymbol{s_0}) = h\lambda \qquad \boldsymbol{b} \cdot (\boldsymbol{s} - \boldsymbol{s_0}) = k\lambda \qquad \boldsymbol{c} \cdot (\boldsymbol{s} - \boldsymbol{s_0}) = l\lambda \tag{2.17}$$

The directions ***s*** which satisfy the equations in 2.17 are called diffraction directions and the relations in 2.17 are the Laue conditions. When we consider the diffraction by a crystal, the function $F_M(\boldsymbol{H})$ is called the structure factor of vectorial index $\boldsymbol{H}$ (or indexes h,k, l if we make reference to the components ofr_H^*) and is indicated as:

$$F_{\boldsymbol{H}} = \sum_{j=1}^{N} f_j \exp(2\pi i \boldsymbol{r}_{\boldsymbol{H}}^* \cdot \boldsymbol{r}_j) \tag{2.18}$$

where N is the number of atoms in the unit cell.

One can also write in a more explicit form:

$$F_{hkl} = \sum_{j=1}^{N} f_j \exp 2\pi i (hx_j + ky_j + lz_j) \tag{2.19}$$

2.1.2.4 Bragg's law

A qualitatively simple method for obtaining the conditions for diffraction was described in 1912 by W. L. Bragg who considered the diffraction as the consequence of the reflections of the x-ray beam by various lattice planes belonging to the same family (physically, from the atoms lying on these planes) [85].

Besides deriving it from the Laue condition (Eqn. 2.17), the Bragg equation may be obtained geometrically. In Figure 2.3, a set of crystallographic lattice planes with distances d$_{hkl}$ is irradiated by plane wave x-rays impinging on the lattice planes at an angle θ. The relative phase shift of the wave depends on the configuration of atoms as is shown for the two darker atoms in the top plane and one plane beneath. The phase shift comprises of two shares, Δ_1 and Δ_2, the sum of which equals $2d\sin\theta$ for any arbitrary angle θ. Constructive interference for the reflected wave, however, can only be achieved when the phase shift $2d\sin\theta$ is a multiple of the wavelength. Therefore, Bragg's equation is often written in the more popular form $2d\sin\theta = n\lambda$, where the integer n has the meaning of a reflection order.

2.1.3 The x-ray diffraction techniques

2.1.3.1 θ-2θ measurement

Figure 2.4a depicts the basic geometry of an x-ray powder diffractometer[6]. The angle of both the incoming and the exiting beam is θ with respect to the specimen surface. This instrument

---

[6] Also called two-circle geometry as seen Chapter 1, Bragg-Brentano geometry.

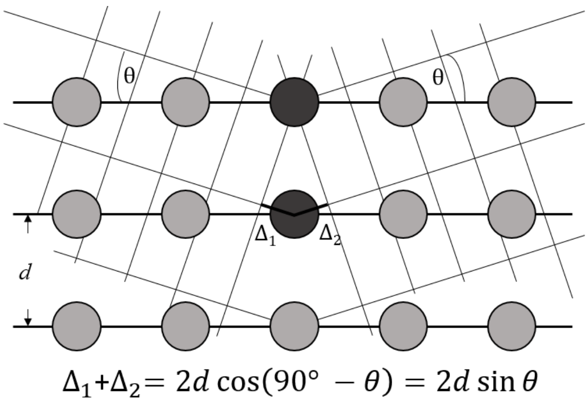

Figure 2.3 – Visualization of the Bragg equation. Maximum scattered intensity is only observed when the phase shifts add to a multiple of the incident wavelength λ.

is mainly dedicated to studying both organic and inorganic powders, hence the name powder diffractometer. This geometry can also be used to study thin films, but often requires previous knowledge of at least some characteristics of studied material (orientation, exact compound, etc.).

The diffraction pattern is collected by varying the incidence angle of the incoming x-ray beam by θ and the scattering angle by 2θ while measuring the scattered intensity $I(2\theta)$ as a function of the latter. Two angles have thus to be varied during a θ-2θ scan and various types of powder diffractometers are in use. For one set of instruments the x-ray source remains fixed while the sample is rotated around θ and the detector moves by 2θ. For other systems the sample is fixed while both the x-ray source and the detector rotate by θ simultaneously, but clockwise and anticlockwise. The rotations are performed by a so-called goniometer, which is the central part of a diffractometer. A goniometer of a powder diffractometer comprises at least two circles or two axes of rotation. Typically the sample is mounted on a rotational axis, while the detector and/or x-ray source move along the periphery, but both axes of rotation coincide.The range of sample-to-detector distance, also denoted by goniometer radius, is typically between 150–450 mm. Highly precise goniometers with 0.001° precision on both the θ and the 2θ circles are commercially available. The collected diffraction pattern I(2θ) consists of two sets of data: a vector of $2\theta_i$ positions and a second vector with the appropriate intensities I_i. The step size $\Delta 2\theta_i$ between two adjacent $2\theta_i$ should be chosen in accordance with the intended purpose of the data. The appropriate value of $\Delta 2\theta_i$ will also depend on the slit configuration of the diffractometer. The preset integration time of the detector per step in $2\theta_i$ should allow the integral intensity of the smallest peak of interest to exceed the noise fluctuations $\sigma(I)$ by a factor of 3 or 5, etc., according to the required level of statistical significance.

In a θ-2θ scan the scattering vector Q is always parallel to the substrate normal. However, due to incident beam divergence, this property is strictly respected only for the central beam, and deviation from the normal to the surface occurs for divergent beam. The two-circle goniometer used in this work is a commercial PANalytical - Empyrean diffractometer with a

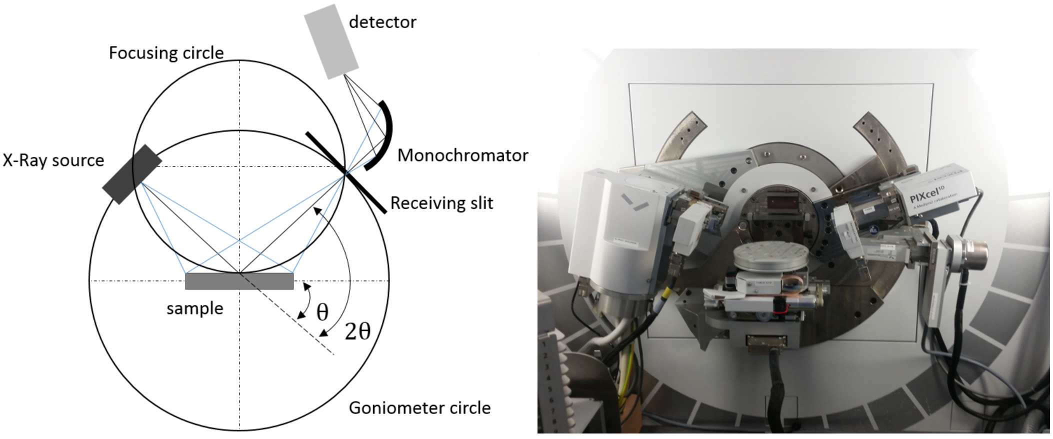

(a) (b)

Figure 2.4 – Two-circle powder diffractometer: (a) Schematics of two-circle diffractometer, (b) picture of the PANalytical Empyrean goniometer.

copper target (Figure 2.4b). An example of a θ-2θ measurement on reacted Ni/InGaAs sample is given in Figure 2.5.

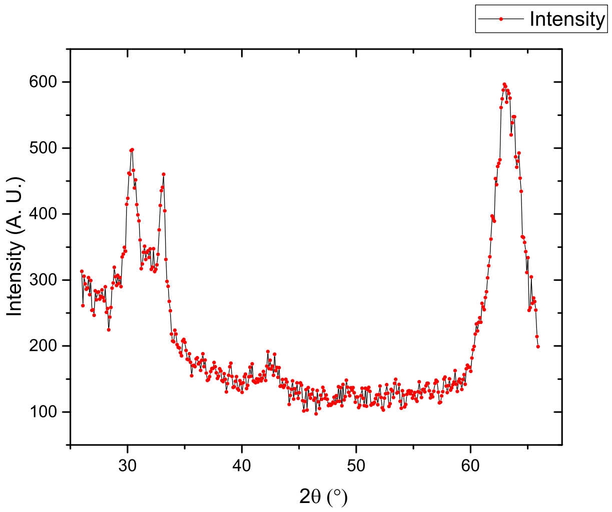

Figure 2.5 – Example of a θ-2θ measurement on reacted Ni/InGaAs sample.

2.1.3.2 Synchrotron radiation

Charged particles such as electrons radiate electromagnetic radiation transverse to their direction of acceleration. In the case of relativistic particles accelerated transverse to their direction of motion, this radiation is called synchrotron radiation and is highly collimated in the direction of motion with polarization primarily in the plane of motion. Synchrotron radiation is emitted tangent to the local radius. Since the first realization of a functioning synchrotron in 1947, synchrotron x-ray brilliance (photons/s/mm^2/mrad^2/eV), which is the figure of merit for most x-ray experiments, has tremendously increased to reach more than 11-14 orders of magnitude greater than the most powerful laboratory sources[86]. This evolution has allowed new diffraction experiments over the time and helped to stimulate a revolution in x-ray optics for both synchrotron diffraction and laboratory equipments. In the case of silicides, numerous crucial process-related or material-related information was obtained through synchrotron radiation [58, 87, 88]. The main attributes of a synchrotron source is its extreme brilliance, its highly collimated beam which make experiments much more versatile and the fact that synchrotron sources are tunable (possibility of making anomalous diffraction, adaptation to the material, etc.). Moreover, synchrotrons have small source size and a long beam-line length, which allows high-resolution imaging of structured materials [89, 90].

2.1.3.3 Description of the D2AM beam-line

All along this PhD, three synchrotron campaigns were carried out at D2AM-BM02[7], the French CRG beam-line at the European Synchrotron Radiation Facility (ESRF) at Grenoble.

As of the time of conducting these experiments, the energy of the synchrotron beam on D2AM ranges from 5 to 25 keV and can be controlled using a Si-(1 1 1)-two crystal monochromator with sagittal focusing which is located between two cylindrically bent mirrors in a compact arrangement. The beam size is 300×150 μm and the typical divergence is $3.10^{-4}\times3.10^{-3}$rd^2 (vertical×horizontal). Two area detectors were used according to their availability on the beam-line with similar structure: a Si-modules-based imXPAD detector and a CdTe-module-based imXPAD detector with a counting rate of 7×10^5 photon/sec/pixel. Pixel size on the detectors is 130×130 μm^2 and image size is 560×960 pixels. More information about the beam-line can be found at the D AM website[8].

2.1.3.4 Description of the Kappa goniometer

D2AM is equipped with a 6-circles Kappa goniometer that allows both in-plane and out-of-plane acquisition. The sample can be rotated around four axes. Because the Kappa goniometer is different from a classical Eulerian goniometer, some axes are defined with an “equivalent”, or “virtual” axis. For example, the equivalent of the motion of ω axis on a Eulerian cradle is materialized by the motion of the sample around a horizontal axis perpendicular to the incident beam. This axis is called η. A sketch of the Kappa goniometer is given at Figure 2.6.

---

[7] D2AM stands for the French “Diffraction et Diffusion Anomale Multilongueurs d’onde” or “Multi-wavelength anomalous diffraction and diffusion” and is part of the French Collaborating Research Group (CRG) at the ESRF. BM02 is the ESRF name for the beam-line.

[8] http://www.esrf.eu/UsersAndScience/Experiments/CRG/BM02

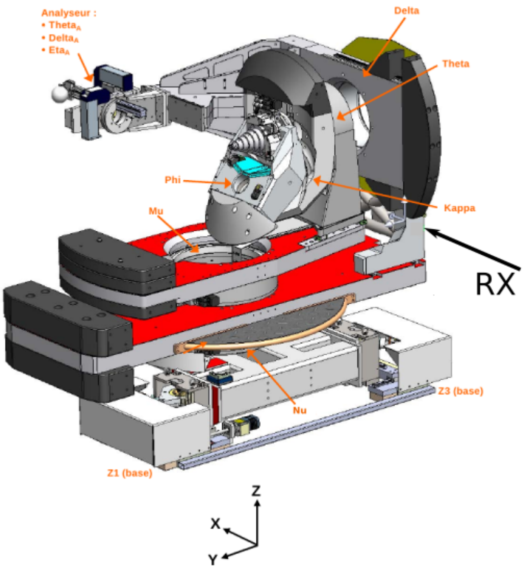

Figure 2.6 – Sketch of the Kappa goniometer installed at the D2AM beam-line at the ESRF.

2.1.3.5 Pole figures

As seen in the first chapter, polycrystalline films can, and most of the time, do present preferential orientations called texture. One way to identify texture is to use EBSD measurement in order to have a statistical measurement of the distribution of the different crystalline planes all over the surface. Using x-ray diffraction, there are multiple ways to appreciate the orientation of polycrystalline films.

The simple symmetric measurement should give hints about the orientation of a known polycrystalline film. When measuring through a θ-2θ scan, only the planes that have their diffraction vector normal to the surface are scanned. Thus one can identify the planes that are parallel to the sample surface. Moreover, by doing a scan over the ϕ[9] axis, one can also define the direction in which the crystallites are oriented. These techniques are rapid and accurate at the condition of knowing exactly what kind of material you are measuring, and having planes measurable out of the plane. Nevertheless, in the case of unknown or more complex compounds, symmetric measurements can be insufficient. First of all, the measured compound can present planes normal to the surface that are hardly detected by x-ray diffraction. Second, the identification of lattice planes of an unknown textured material uniquely through symmetric measurements is at best insufficient. Finally, numerous information is missed when doing exclusive symmetrical x-ray diffraction concerning the lattice mis-orientation, the presence of azimuthal variants and/or twins, the distribution of the crystalline orientations, etc.

---

[9] The ϕ angle measures the azimuth of the sample in the surface plane.

2.1.3.6 Eulerian cradle and description of the used 4-circles diffractometer

To get all of this information, there is a need to use a four-circle diffractometer that is called also Eulerian cradle (see Figure 2.7), and knowing exactly the nature of the material and its orientation, one must perform multiple ω scans or ϕ scans over multiple χ angles[10] and perform several θ-2θ scans. In other words, the different crystallographic planes of one family of planes must be brought to diffraction conditions by moving the sample using the crystallographic goniometer and then analyzing the different resulting diffractograms. This way of analyzing the samples can be time-consuming and is not obvious to interpret. There is however a more convenient way to represent the distribution of crystallite orientations in a sample: the pole figure measurement and representation.

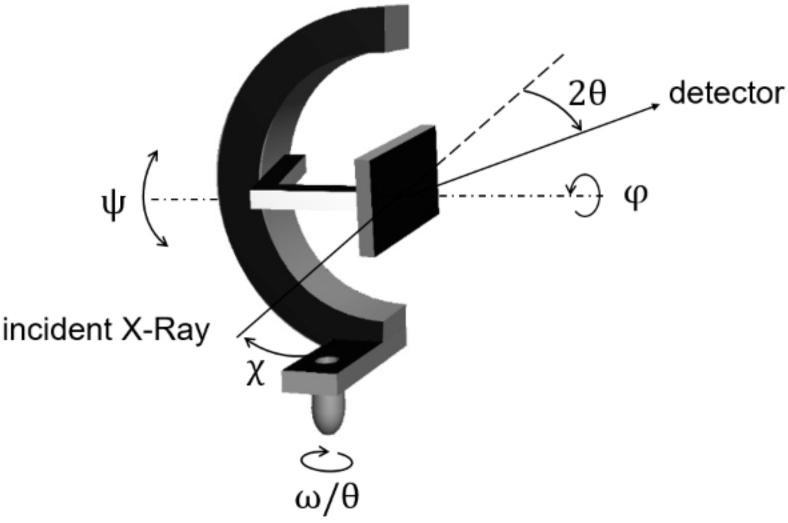

Figure 2.7 – Representation of a variant of an Eulerian cradle.

2.1.3.7 Pole figure measurement

Pole figures are basically a representation of the diffracted intensity of a sample as a function of the angles ϕ and χ at a given 2θ position of the detector (or interplanar distance) $I_{2\theta}(\phi, \chi)$

In practice, pole figures can be obtained on a Euler cradle by performing different goniometer rotations at a fixed ω and θ angles that corresponds to an interplanar distance of a given plane of the measured material. The sample is then rotated along the χ axis of the goniometer and at each measurement step on this axis, a ϕ scan is performed. A representation of the experiment is given in Figure 2.8.

Once the intensities $I_{2\theta}(\phi, \chi)$ are measured over the ϕ and χ angles, it is more convenient to project these intensities onto a two-dimensional form that is easy to solve. Stereographic

---

[10] The tilt angle χ quantifies the amount of tilting of the sample normal with respect to the scattering vector. χ angle is often referred to as Ψ. The difference between χ and Ψ is the zero reference and are both related by $\chi = 90$ř $- \Psi$.

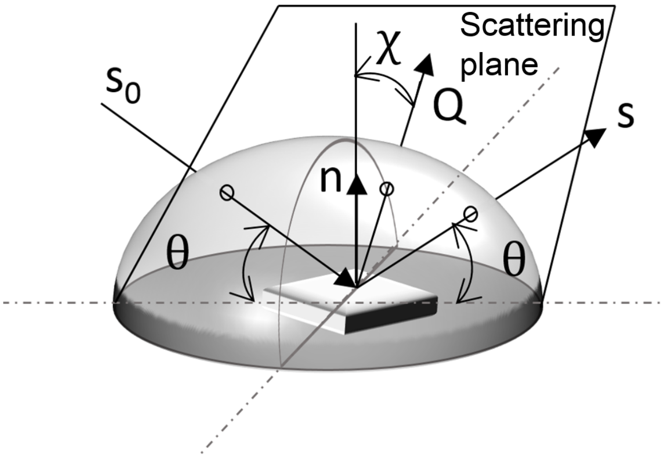

Figure 2.8 – χ tilt defined in the sample referential. In practice, the scattering vector $\boldsymbol{Q}$ is brought to diffraction conditions by rotating the sample by a χ angle.

projections of diffracting intensities projecting the intensities on the unit sphere from the north pole onto the equatorial plane. The equatorial is usually the plane of the substrate which is parallel to the surface (usually (1 0 0) or (1 1 1) planes). Consider a sphere with center O, south pole S and a point P on its surface (see Figure 2.9). The line SP intersects the equatorial plane at p. Hence, any direction OP can be represented by a corresponding stereographic projection point p on the equatorial plane.

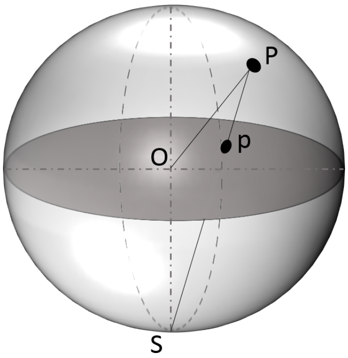

Figure 2.9 – Construction of a stereographic projection.

An example of a stereographic projection of a cubic lattice is given at Figure 2.10. If the intensity $I_{2\theta}(\phi, \chi)$ is plotted according to a stereographic projection, then the resulting stereogram is called pole figure.

In the presence of a polycrystalline or monocrystalline sample, the procedure mentioned above can be repeated for every crystallographic plane of interest. However, in order to scan continuously a large part of the reciprocal space, the procedure described above must be repeated for a large number of θ steps. The resulting pole figures can be analyzed either individually or integrated partially or totally. A number of pole figure intensities corrections

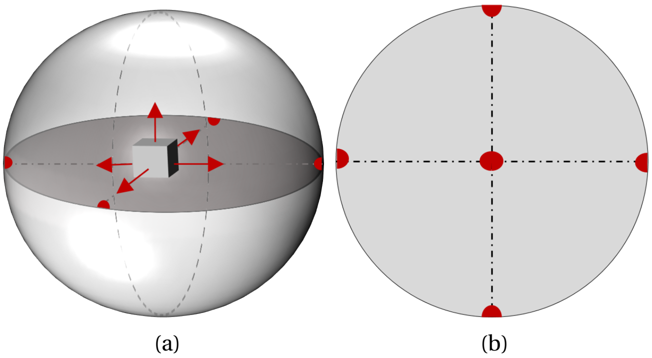
(a) (b)

Figure 2.10 – Example of a stereographic projection of a cubic lattice with its {1 0 0} planes parallel to the surface:(a) Construction of the stereographic projection, (b) stereographic projection of the {1 0 0} planes.

can be applied depending on the nature of the detector (1D detector or 2D detector) and the sample (absorption effect) [91].

2.1.3.8 Stereographic projections simulation

Stereographic projection simulation is done through Carine Crystallography 3.1[92]. This softwares requires entering a crystallographic structure with its space group and lattice parameters. Once the crystallographic lattice is created, an optional step is to define the atom position in the lattice, which can be useful in case of a powder diffraction pattern simulation. The user defines then a projection plane or a projection direction. Usually the projection plane is the (1 0 0) plane. The stereographic projection can then be obtained according to the orientation of the lattice in regard of the projection plane. A real-time simultaneous lattice motion/stereographic projection is available and can be used to adjust the stereographic projection to the experimental pole figure. An example of a stereographic simulation of the {1 1 0} planes of a cubic lattice and the corresponding pole figure is given in Figure2.11. The software gives the possibility to superpose multiple stereographic projections, which allows for example the simulation of both substrate and intermetallic compound. Some crystallographic structures can yield azimuthal variants (i. e. hexagonal structures on some planes), the simulation of these variants can be done through the superposition of rotated stereographic projections on Carine.

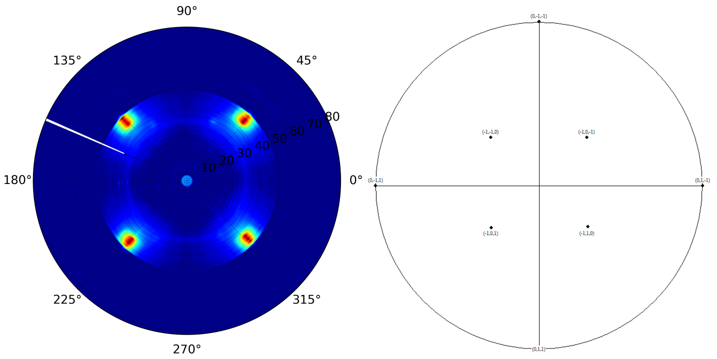

(a)

(b)

Figure 2.11 – (a) Pole Figure of {1 1 0} planes of a cubic lattice and (b) corresponding stereographic simulation on Carine Crystallography.

2.1.3.9 The Smartlab description (4-circles mode)

The main diffractometer used during this thesis is a commercial Rigaku Smartlab. The Smartlab have a 9 kW rotating anode Cu source that allows fast data collection. A parabolic multilayer x-ray mirror is permanently mounted and does not need any alignment when exchanging optical modules to go from parallel configuration to focusing one. This diffractometer allows rather rapid switching from a parallel beam to focusing optical configuration without having to do that manually by manipulating the x-ray source. This is possible thanks to a Cross Beam Optical (CBO) module. Focusing optical configuration is of a great interest in pole figure measurements. Indeed, broadening of the beam footprint on the sample surface occurs with the tilting of the sample and this defocusing increases with increasing χ. If measurements have to be performed that make use of χ tilts, the x-ray spot on the film surface has to be minimized to avoid a too strong defocusing. Hence, on laboratory diffractometer the x-ray tube has to be adjusted, in a way or the other, to the point focus configuration.

Two detectors can be used in order to perform measurements either for pole figures or for other types of measurement: a 0D scintillation counter(SC) detector that comes with a set of optics and 2D PILATUS 100K/R detector. The SC is used because of its good sensitivity, low noise level and easy handling, etc. SC detector can measure the count-rate from 0.1 to several 100,000 counts/second after counting-loss correction. Diffracted signals from a sample are collected by a circular area of a diameter around 2.5 cm. There is however no positional sensitivity for this 0D detector, thus the signals collected are all integrated into one signal. To achieve a desirable angular resolution in 2θ, suitable optics should be mounted in front of the detector. Figure 2.12 represents the Smartlab in its 4-circles geometry and corresponding optics.

The area detector is a PILATUS 100K/R, a high speed and quick read-time, single photon counting 2D detector which has got a high dynamic range and high sensitivity. In comparison

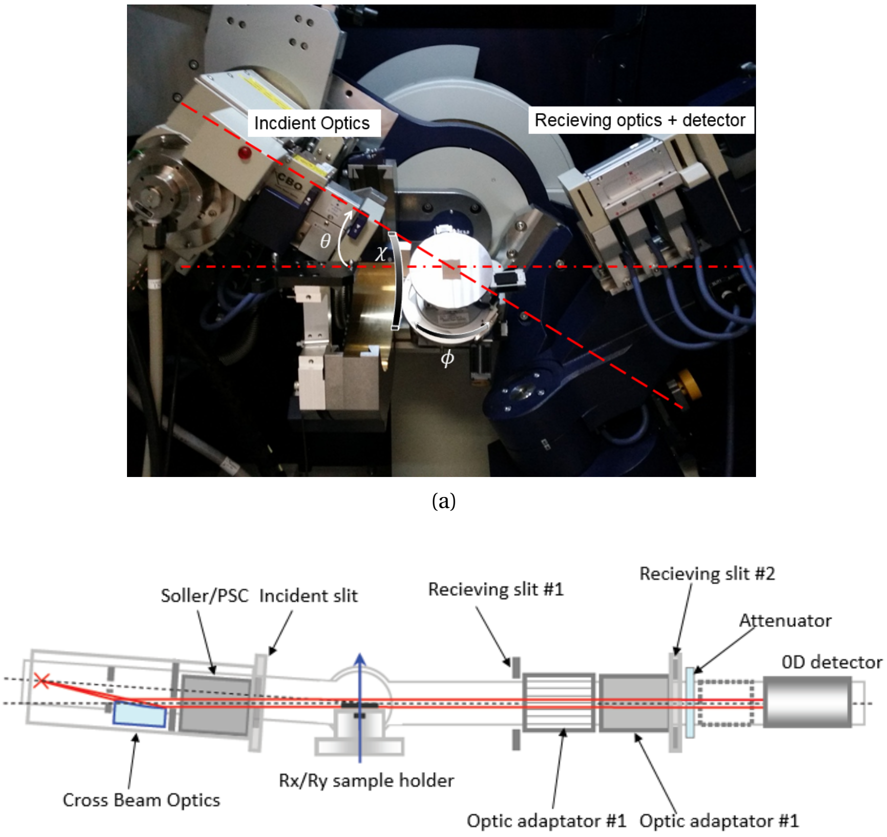

(a)

(b)

Figure 2.12 – 4-circles configuration of the smartlab: (a) Picture of the Smartlab 4-circles configuration, (b) Schematics of the Smartlab optics.

to a 2D gaseous detector, this solid-state semiconductor detector can be used in a "Time Delay Integration" (TDI) mode measurement in the same manner as a 1D detector (i.e., it will integrate the scattering vector of different directions in the course of a $2\theta/\omega$ scan).

The sample and optics alignments on the Smartlab is done automatically through a series of pre-programmed steps and iterations according to the specification of each type of measurement. An interesting feature of this diffractometer is the existence of a fifth rotational axis in addition to the Eulerian ones ω, 2θ, χ and ϕ. This fifth axis is denoted $2\theta_{\chi/\phi}$ and is a horizontal axis parallel to the θ/θ diffraction plane that allows doing in-plane measurements with a grazing incident x-ray. Figure 2.13b depicts an in-plane configuration on the Smartlab where the detector and receiving optics are moving along the in-plane $2\theta_{\chi/\phi}$ axis. A more detailed paragraph on the technique is given later on in this chapter.

2.1.4 In-plane XRD measurements

Most studied thin films are deposited on a thick substrate constituted of one layer of a material or more. The diffraction intensities from the thin films, especially if they have very small width, can be extremely weak and masked by the diffraction signal from the substrate. One solution to override this intensity problem is to use in-plane XRD techniques with a grazing incident x-ray beam in order to minimize the substrate signature and maximize the thin film intensities. Moreover, in-plane diffraction gives access to planes that are otherwise inaccessible with Bragg-Brentano geometries, or very difficult to measure in four-circles geometry due to defocusing effect at high χ angles.

The main characteristics of in-plane XRD measurements are:

- A diffraction from lattice planes that are normal to the surface of a sample can be observed;
- Diffraction from extremely thin films can be observed;
- Background intensities and diffraction from the substrate are minimized as the grazing x-ray incident beam does not penetrate over a large depth into the sample;
- There is a possibility to perform depth-profile analysis by varying the grazing incidence angle, and thus the penetration depth in the sample.

In fact, in out-of-plane geometries, the scattering vector is normal to the thin film surface while in in-plane geometries the scattering vector is parallel to the thin film surface (see Figure 2.13a). Thus, in-plane XRD measures the planes normal to the surface of a thin film. Below a certain value of an incidence angle, called the critical angle ω_c, the incident x-ray can be totally reflected because the refractive index of a material is smaller than unity. Above ω_c, x-rays can penetrate into the sample and thus gives rise to diffraction. The critical angle ω_c is a function of the wavelength of incident x-ray and the density of the studied material. If the incidence angle is close to the critical angle, then a part of incident x-ray is reflected on the sample surface and the other part penetrates into the sample. The x-ray beam that propagates in the sample in a nearly parallel direction because of the small incidence angle and can come out of the sample by diffraction from the crystallographic planes that lie normally to the sample surface or slightly tilted from the sample surface. The penetration depth t of the x-ray beam can be estimated as the following:

$$t = \frac{4.61}{2\mu} \sin\omega \tag{2.20}$$

Where ω is the incident angle of x-rays and μ is the linear absorption constant of x-rays

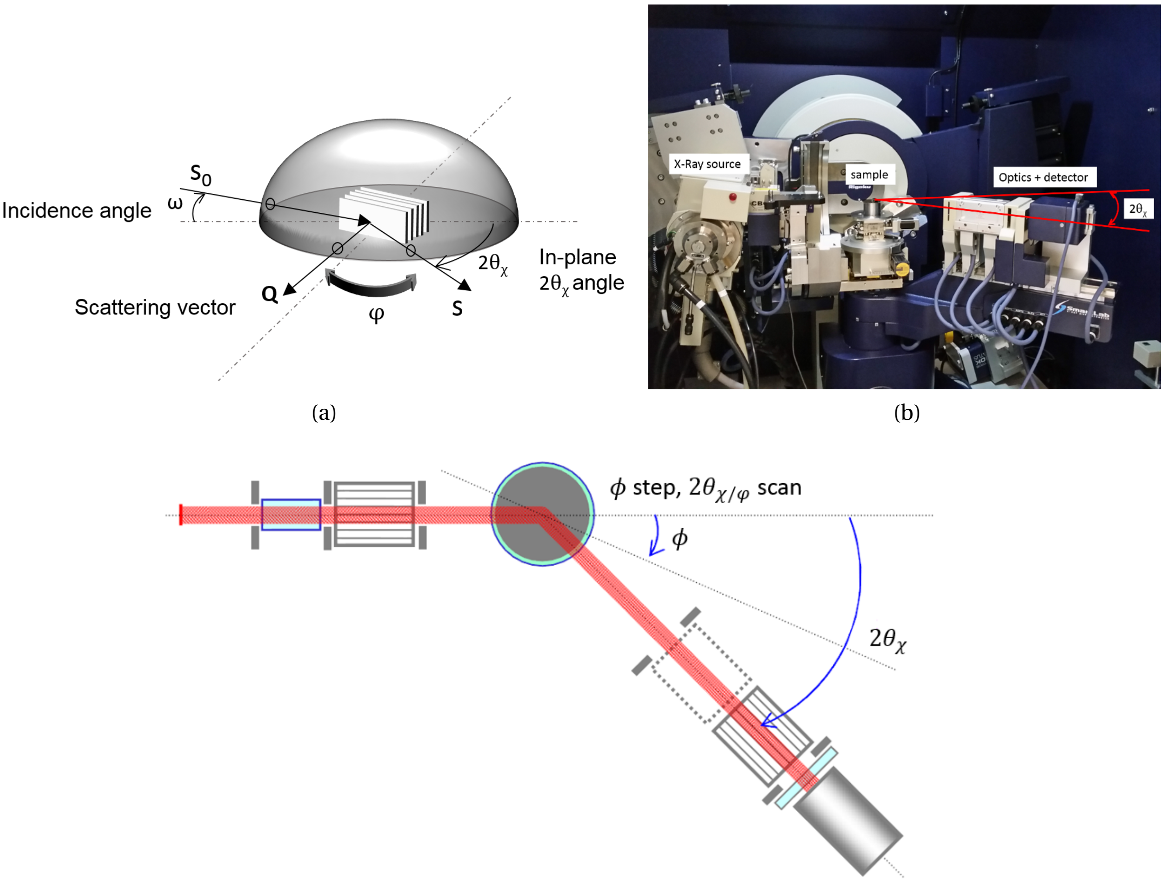

(a)

(b)

(c)

Figure 2.13 – In-plane configuration: (a) Geometry of in-plane x-ray Diffraction, (b) Picture of the in-plane geometry on a Smartlab and (c) Top view scheme of the in plane measurement.

However, if the incident angle ω is close to the critical angle ω_c, then the contribution of reflection and refraction must be taken into consideration and Eqn 2.20 is no longer valid. The penetration depth can be estimated as:

$$t = \frac{1}{\sqrt{2} \cdot \frac{2\pi}{\lambda} \cdot [\sqrt{(\omega_c^2 - \omega^2)^2 + 4\beta^2} + \omega_c^2 - \omega^2]^{\frac{1}{2}}} \qquad ; \qquad \beta = \frac{\lambda}{4\pi}\mu \tag{2.21}$$

Where λ is the wavelength of x-rays and ω_c is the critical angle for total reflection. Hence, depth-related characterization can be achieved using in-plane XRD by varying the incident angle ω.

In-plane diffraction requires the use of in-plane parallel slit collimator to control the horizontal divergence of the incident x-ray beam (typically from 0.1 to 1°). A resolution going from 0.1 to

1° on the receiving optics can be achieved with an in-plane parallel slit analyzer. Moreover, in-plane diffraction is very sensitive to the angle of the incident x-ray beam and as a consequence, the angle of incident beam must be kept constant during all the measurement. This implies that the sample surface normal must be precisely aligned with the axis of ϕ rotation of the sample stage. This precise alignment can be achieved on the Rigaku Smartlab by using the two orthogonal tilt-adjustment axes Rx and Ry on one of the available sample stages in an automatic manner.

2.1.4.1 In-plane Reciprocal Space Map

In a similar way to an $I(2\theta,\phi)$ cartography in an out-of-plane configuration, in-plane Reciprocal Space Map (in-plane RSM) can be achieved by doing multiple in-plane $I(2\theta_\chi)$ measurements for a "virtually" fixed ϕ position each. In fact, because the incident angle axis is fixed, the in-plane equivalent of the classical out-of-plane angle θ must be controlled by rotating the sample around its normal on the ϕ axis. This rotation is accompanied by a rotation of the $2\theta_\chi$ axis in order to vary $|\boldsymbol{Q}|$ and thus measure different inter-planar distances at one "virtually" fixed ϕ position. To change the ϕ position, an initial offset is applied to ϕ at the beginning of the measurement and is kept as long as the $I(2\theta_\chi)$ measurement is going on. In other words, the scattering vector $\boldsymbol{Q}$ direction can be modified by the individual motion of the ϕ axis and its module $|\boldsymbol{Q}|$ is controlled through the mutual motion of the ϕ and $2\theta_\chi$ axes. The corresponding ϕ and 2θ values are then calculated by the measurement software provided by Rigaku. An example of an in-plane RSM is given at Figure 2.14 with different coordinates and view types. The calculation corresponding ϕ and $2\theta_\chi$ angles will not be a subject of interest in this thesis as it is being automatically treated by the manufacturer's software.

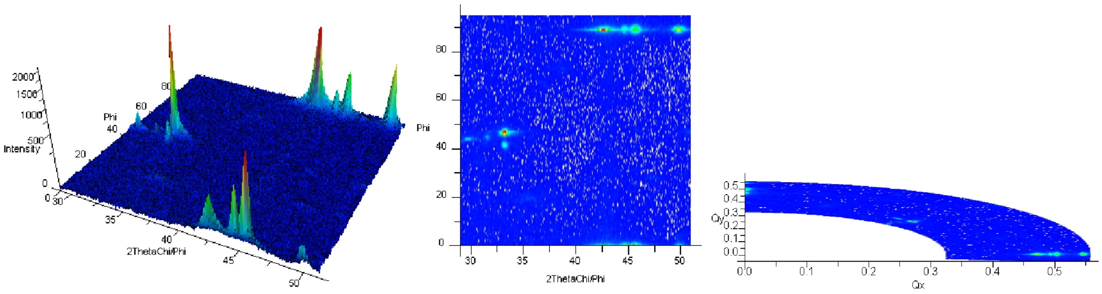

(a) (b) (c)

Figure 2.14 – Example of an in plane RSM measurement: (a) Topographical view, (b) flat view and (c) reciprocal space coordinates view.

2.1.4.2 In-plane Pole Figures

Acquisition of in-plane pole figures is done thanks to the motion of both the $2\theta_\chi$, ϕ and 2θ axes. The ω axis is fixed around the critical angle ω_c and χ is fixed to 0 all along the measurement.

Thus when performing in-plane pole figures, the sample does not have to be tilted. The control of χ-like angle is done through a combination of motion of 2θ and $2\theta_\chi$ axes. This method allows the acquisition of a whole pole figure from 0° to 90° because the goniometer can detect diffraction from lattice planes perpendicular to the sample surface in the in-plane configuration. Figure 2.15 depicts an example of in plane pole figure measurement.

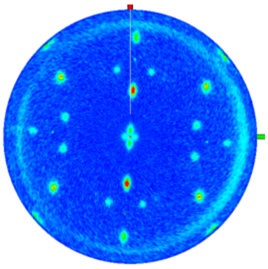

Figure 2.15 – Example of an in plane pole figure measured over a range of 90° over the χ axis.

2.1.5 3D-Reciprocal space mapping

In x-ray Diffraction, it might not be necessary to scan a large part of the reciprocal space of a well known thin film compound in order to make conclusions about its characteristics. Indeed, knowing the precise phase sequence, phase diagram, structure and using ICDD PDF files[11], one can perform limited XRD measurements (measuring only in θ-2θ mode for example) and yet make valid conclusions about the studied material. However, when dealing with poorly-documented materials, scanning only out-of-plane reflections is not sufficient to make valid conclusions. By doing so, one can miss the measurement of diffraction signals from formed phases, can access to a limited number of reflections that are not sufficient to calculate accurate lattice constants or state on the symmetry of the crystallographic lattice. Texture analysis can also be tricky if a large part of the reciprocal space is not measured. Several examples of characterized thin films by XRD were revealed to be wrongly identified because the measured diffraction was not over a large part of the reciprocal space [54, 93].

2.1.5.1 Principle

Reciprocal space maps (RSM) are usually measured by XRD to characterize these features in nanostructures or thin films. So far, 3D RSM are measured locally around one specific Bragg reflection. Although this technique is well suited for quantitative analysis of a known phase, one can easily overlook the presence of other phases. Taking advantage of synchrotron light sources and 2D detectors, larger volume of the reciprocal space can be explored by means of a series of pole figures in a reasonable time.

---

[11] ICDD stands for International Centre for Diffraction Data and maintains a database of powder diffraction patterns: the Powder Diffraction File (PDF). Until 1978, ICDD was called Joint Committee on Powder Diffraction Standards (JCPDS).

There exist many methods to access 3D reciprocal space around a specific Bragg reflection using 2D detector so far. A diffraction pattern collected by a 2D detector represents a slice in the three-dimensional reciprocal space. A local 3D RSM can be recorded by subsequent rocking curves taken at different incident angles. A 3D RSM can also be measured by tuning the x-ray energy using a synchrotron light source in order to access to a certain thickness in the reciprocal space. A third method that was used in this thesis, consists of recording a complete 3D RSM by measuring nearly full pole figures in a large range of Bragg angles. Indeed, a pole figure can be considered as the surface of a hemisphere of radius Q in the reciprocal space and the poles are the intersection of reciprocal lattice points with this hemisphere. A full 3D RSM can therefore be reconstructed by combining a great number of pole figures at different vectors Q within a given range of Q (and thus 2θ).

2.1.5.2 Ex-situ measurements methodology

Ex-situ measurements were performed on slowly quenched materials to room temperature after a Rapid Thermal Annealing (RTA). These samples were the first ones to undergo measurements in preparation of further in-situ analyses. The experiments were carried out at the D2AM beam-line. Samples were mounted on a sample stage by a set of four to six samples and were fixed by applying a slight layer of correction fluid underneath. The potential misalignment induced by this fixing material is eventually corrected later by successively aligning the sample on two opposed azimuthal positions. Synchrotron beam was monochromatic and set to an energy of 9 keV and the area detector was set to a distance of 20 cm from the samples.

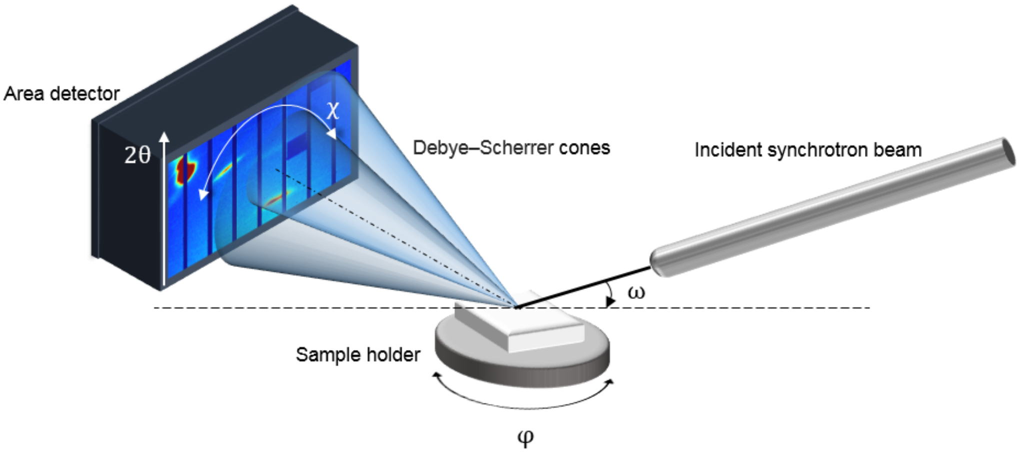

Figure 2.16 – Schematics of an are detector x-ray diffraction experiment on synchrotron. The area detectors has 2 degrees of liberty (lateral movement and a goniometer « 2θ » movement). The sample can rotate along ϕ, χ and ω.

Each sample on the sample stage was aligned separately. A CCD alignment camera with cursors indicating the position and radius of the incident beam was used to check that beam spot is always on the sample during the azimuthal rotations so that no spilling on nearby samples occur.

There was also a step of LaB_6 powder calibration measurement. The powder measurement is done for each χ, 2θ and v^{12} angular position. The already-known shape of diffraction figure of the LaB_6 powder helps correcting the detector distortions for the sample measurement. This step is done with the help of pyFAI, a ESRF software dedicated to area detectors.

Data is then acquired in a manner to cover a large part of the reciprocal space for a 2θ ranging from 20 to 45° (see Figure 2.16). Thus, the acquisition was done according to the following conditions/steps:

- Two 2θ positions, 25° and 35°;
- For each 2θ position, 2 χ position were put in place. The total χ range covered during a measurement depends on the position on the detector (i.e. different χ ranges according to the 2θ position on the detector), but globally, the range goes from 0 to 70°;
- Each measurement was repeated ay two v position of the detector. The v axis corresponds to a lateral movement of the detector. This step is important to correct the gaps in the images as the XPAD detector presents several modules that are physically separated;
- Azimuthal measurements on the ϕ axis were carried out with a step of 5° on a total range of nearly 360°.

All of the steps mentioned above help to scan a nearly complete pole figures over a range of 2θ going from 20 to 45° and thus, the set of images obtained by the measurement constitutes a Full 3D RSM. Data treatment was performed an in-house software DEVA [94] and a representation of the non projected set of pole figure is given at Figure 2.17

A summary of the measurement steps is given in the diagram in Figure 2.18:

Data reduction after the measurements was automatically performed through two main methods:

- Data integration of the images over χ and ϕ. This integration produces a classical diffraction diagram and can be understood in this manner: $I(2\theta) = \sum_{\chi}\sum_{\phi}(images)$ (see Figure 2.19). The integration can also be local and be done on some diffraction spots of interest. Local integration can be useful especially when the diffraction signal is weak and can be lost once a complete integration is done.
- Pole figure reconstruction through azimuthal integration for a certain resolution of 2θ (in this case every 0.25°). This automatic reconstruction for each experiment results in a

---

[12] v is the lateral translation of the detector.

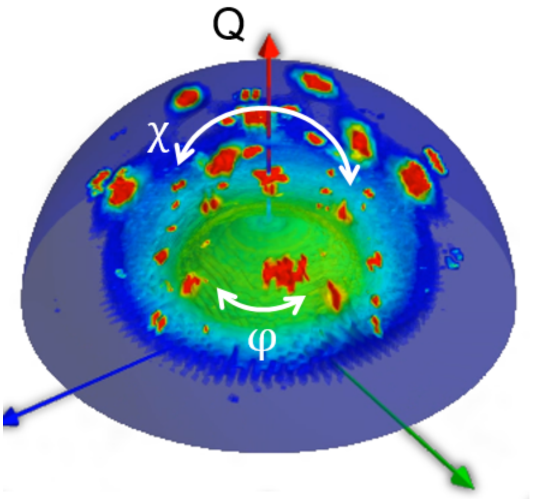

Figure 2.17 – A representation of the Full 3D Reciprocal Space Map. This representation consists of a series of non-projected pole figures on successive hemispheres. The radius of these hemispheres is Q and represents the 2θ position.

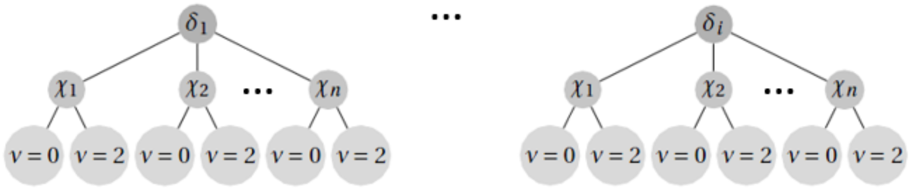

Figure 2.18 – Diagram of the measurement strategy including several δ positions of the detector, several χ positions of the sample and two lateral translations ν of the detector.

series of pole figures that can be analyzed through simulations. A stack of diffraction images with $(2\theta, \chi)$ coordinates and stacked in the ϕ direction is given in Figure 2.20. The simulation of stereographic projections were done through a commercial software: Carine Crystallography.

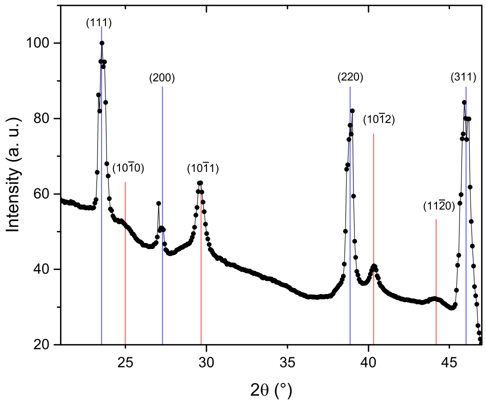

Figure 2.19 – Example of integration over χ and ϕ of synchrotron data.

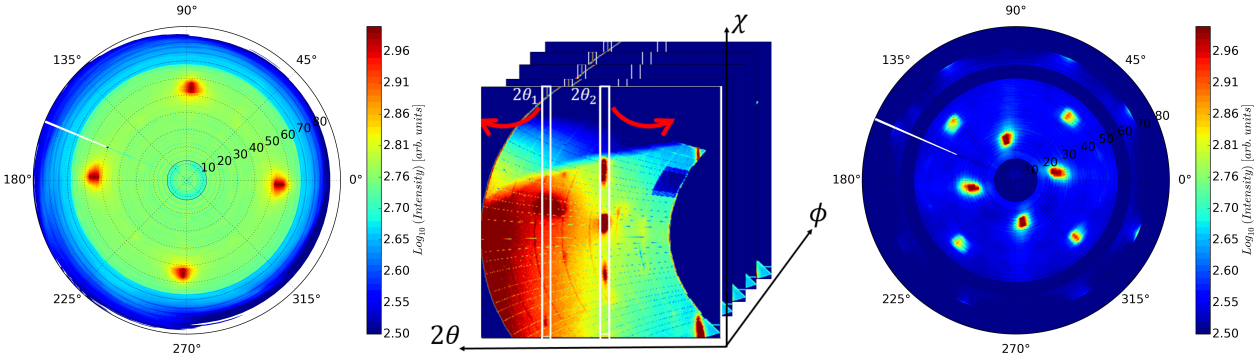

(a) (b) (c)

Figure 2.20 – Stitching process in the χ direction (a) Pole figure at the $2\theta_1$ position (b) Schematic example of a stack of diffraction images with two integration domains centered at $2\theta_1$ and $2\theta_2$ (c) Pole figure at the $2\theta_2$ position.

2.1.5.3 In-situ measurements methodology

The experiments were carried at the BM02/D2AM beam line equipped with a 6-circles goniometer (Kappa geometry) and a 2D pixel detector (XPAD[13]). The energy was set to 10 keV which is relevant in order to prevent Ga and As fluorescence. A furnace compatible with the goniometer, an Anton Paar DHS 1100, was set up in front of the x-ray beam in order to perform the annealings. To prevent atmosphere contamination during the annealing, samples were covered with a thermostable dome made of Polyether ether ketone (PEEK) or a graphite dome.

The annealings were done under constant highly pure N_2 flow. Before each measurement, the

---

[13] XPAD is a commercial hybrid pixel area detectors manufactured by imXPAD. Two different detectors were used in in-situ experiments according to their availability on the beam-line, a Si-chip detector and a CdTe detector.

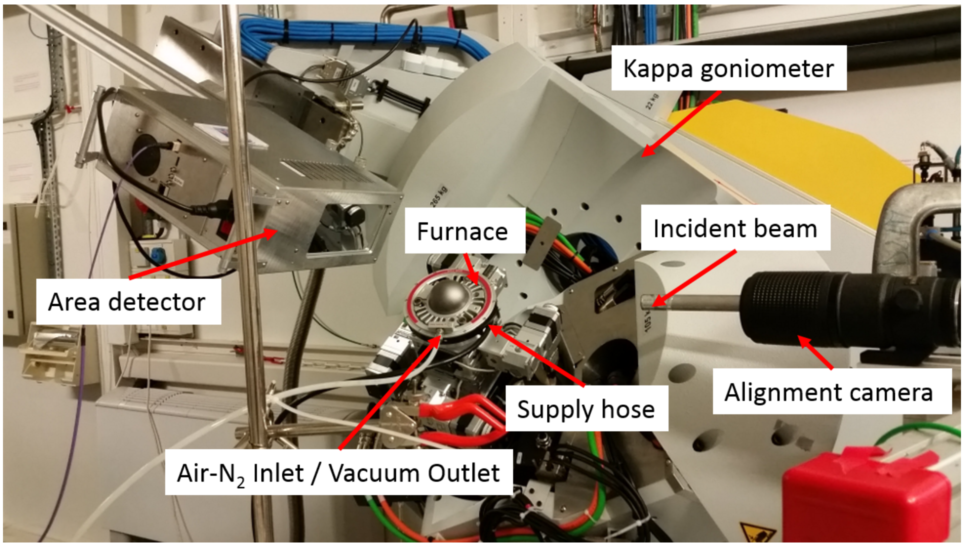

Figure 2.21 – Picture of the in-situ experiment on the D2AM beam-line. The sample is covered by a graphite dome.

sample environment under the protective dome has undergone several cycles of pumping to primary vacuum followed by N_2 injection to evacuate residual air in it. The detector was fixed at 25° and at 20 cm from the samples (which corresponds to roughly 20° of aperture range). Finally, χ angle of 50° was set, which gives a maximum range going from 0° to 70° depending on the 2θ position. Temperature was monitored throughout the main software controlling the goniometer. Measurement were done for several ϕ angle positions on 360° with a step of 5° each in order to cover a large part of the reciprocal space and reconstruct full pole figures over 360°. As the 2D camera has some dead rows and columns, we did each acquisition at ν=0° and 2° (in-plane rotation of the detector). In order to calibrate the setup, a LaB_6 powder was measured as well. A picture of the experiment is at Figure 2.21.

2.1.6 Correction of the diffraction images

2.1.6.1 Correction of the dome diffraction pattern

Since we have used a PEEK dome, which is nearly transparent to x-ray diffraction but has also a diffraction signature that corresponds to a diffraction from powder sample, diffraction peaks from the dome were also detected. One method of correcting the intensities that arise from the dome on the diffraction images, is to measure only the diffraction from the dome using a glass sample[14]. Several measurements of the diffraction from the dome was carried out at different azimuthal positions of the glass sample. The resulting images were integrated and averaged into one image. The corresponding integrated and averaged image was then defined as a reference and was subtracted from the diffraction images of the sample. Nevertheless,

---

[14] Amorphous glass, thus no, or little diffraction is expected.

since the glass sample yields a diffraction signature that corresponds to a nearly continuous background noise with a largely broadened peaks corresponding to silicon diffracting planes, the subtraction leads to a non-uniform subtraction on the diffraction images from the Ni/InGaAs/Si samples. This apparently non-uniform subtraction is not a problem for data interpretation. Indeed, qualitative data treatment, phase domain of existence, and lattice parameter calculations does not require special care for intensity. As for quantitative analysis, integration on individual poles of the intermetallic that do not come across the diffraction signature of glass was made. This way, we make sure that what we use as intensity corresponds only to the intermetallic.

2.1.6.2 Correction of the dark signal

Dark signal defines the background signal on the detector. It is the signal that the detector will carry while it is not exposed to diffracting x-ray. This signal can be quantified by the number of the so-called hot pixels. Hot pixels can be defined through numerous criteria[95]: dark signal higher than ten times the average background increase rate, or dark signal higher than 0.1 % of the maximum encoding range at the nominal exposure time or any other equivalent definition. Dark signal increases with the exposure time, thus, the measurement of this signal must be carried out at the same time exposure for the sample measurement. Correcting the diffraction images of the sample consists of a subtraction between these images the sample and the dark image.

2.1.6.3 Pixel to angular coordinates transformation

2D area detectors collects diffraction signal in the form of intersections with the Debye-Scherrer cones. Nevertheless, one wants to analyze the diffracting images as intensities as function of the apertures of the cones (2θ) angle, averaged intensity along each ring (in the same way as classical reading of powder diffraction data $I = f(2\theta)$). To do so, a pixel to angular coordinates transformation is required.

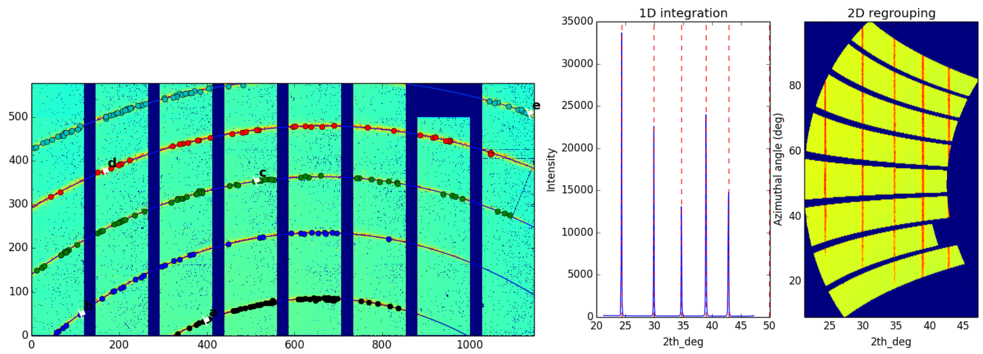

(a) (b)

Figure 2.22 – (a) Powder diffraction image in pixel coordinates before calibration by PyFAI (b) Powder diffraction image and 1D integration after pixel to angular coordinates transformation.

The method of transformation from Cartesian to polar space where the radial dimensions can expressed in distances (radius), momentum transfer (q) or scattering angle (2θ) was done through the software PyFAI. This software is a load of tools written in Python programming language and developed by J. Kieffer at ESRF to realize azimuthal integration through calibrant measurement. The method of transformation is well described[96–98] and will not be described in details in this manuscript. Separate transformation parameters must be calculated at each different geometry affecting the position of the detector in the experiment (for example, lateral displacement of the detector v). The reference sample used was LaB_6 and calibration was done on several Debye-Scherrer rings of this powder (see the example in Figure 2.22). The resulting Cartesian-to-polar transformation is a file that contains a description the geometry of the experiment that can be directly injected in DEVA to correct the images.

2.1.6.4 Module gaps correction

Two types of detectors were used during the different synchrotron campaigns on D2AM beamline, one having Si modules and the other having a CdTe modules. Si modules consist in 7 XPAD3 chips of 80×120 pixels each and CdTe modules use 2 XPAD3 chips. These modules are physically separated because they can not be perfectly arranged in a continuous manner. This results in a diffraction that contains 7 gap bands with a width of 10 pixels all along the image (see Figure 2.23).

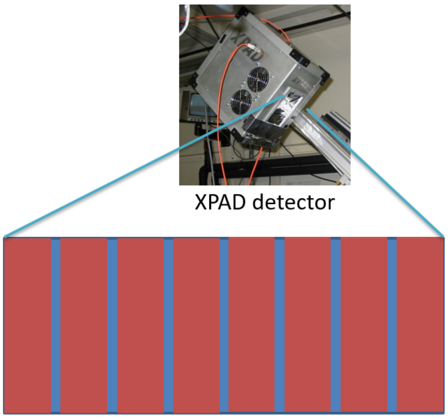

Figure 2.23 – Xpad detector and corresponding scheme of the modules arrangement in the detector.

These gaps might contain diffraction information, and since we work with highly oriented samples, it is important to acquire the missing information and correct the gaps. The missing diffraction information can be acquired by redoing the same exact measurement but with a slight lateral displacement of the detector. The displacement must be at a value that ensures that the 10 pixel gap band is measured. Thus two images measured at the same geometrical conditions, excepts a slight lateral displacement of the detectors by $2\nu°$ are acquired. The next step is to combine data from the two images in order to have a fully complete image. A superposition of the two images is done after data griding and the intensities of pixels are averaged outside the gaps to ensure homogeneous intensities all over the image. Two images measured at two different ν positions are presented at Figure 2.24, the overlap of the gaps allows to produce a fully complete image.

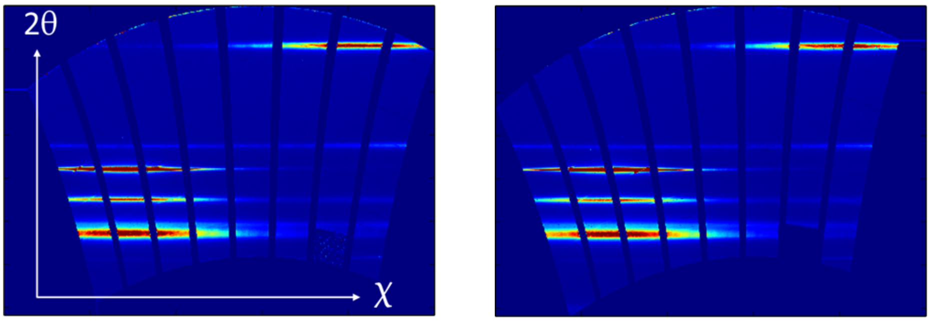

(a) (b)

Figure 2.24 – Two diffraction images at the same ϕ δ and χ position at: (a) $\nu = 0°$ and (b) $\nu = 2°$.

2.1.7 Stitching and intensity correction

Data that are measured for different detector positions (corresponding to 2θ position) and sample position (corresponding to χ position) must be “stitched" in order to have a complete integrated diffraction pattern. Intensities are averaged at the stitching junctions to ensure that overlapping does not induce intensity inhomogeneity (see Figure 2.25). Stitching the data of one experiment is done after transforming the images into a more convenient hierarchal way of representing the data. Indeed, after correcting all images, the data are transformed into a 3D matrix form through data conversion into a HDF5 file[99]. This step allows a semi-quantitative analysis on the diffraction data.

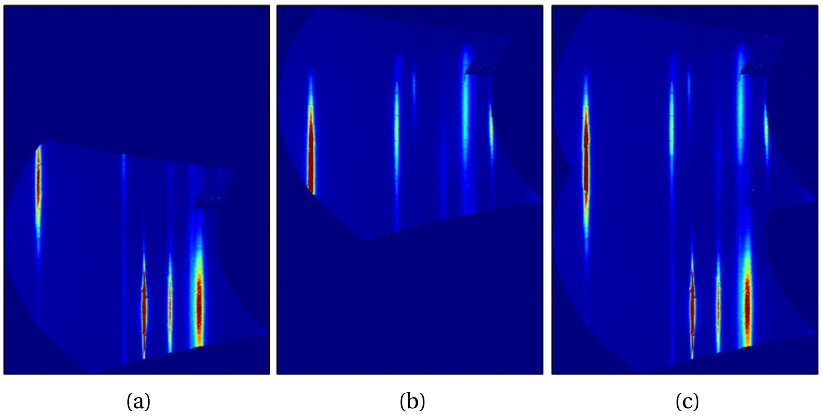

(a) (b) (c)

Figure 2.25 – Stitching process in the χ direction (a) χ_1 position and (b) χ_2 position and (c) resulting image of the two χ_1 and χ_2 image stitching.

2.2 STEM-EDS

In order to examine stoichiometry and interface between the intermetallic and InGaAs layer, STEM-EDS (Scanning Transmission Electron Microscopy-Energy Dispersive Spectroscopy) were carried out on different samples. The principle of this technique is based on the emission of characteristic x-rays from the specimen produced by an incoming energetic electron beam. These characteristic x-rays contain information about the chemical elements present in the material. It is estimated by measuring the area under the peak of the characteristic x-ray of a desired chemical element to the total area under X-spectrum. The EDS experiments were carried out on Transmission Electron Microscope TEM JEOL 2100F. Sample preparation consisted of preparing a substrate/film/glue/film/substrate “sandwich” and polishing was performed by a tripod bevel to 10 microns and followed by Ar ion milling until perforation of the interface.

Nevertheless, this technique remain semi-quantitative due to the weak resolution of analysis compared to other techniques (Atom Probe Tomography for example) and numerous peak overlaps are possible which implies to be cautious when analyzing the spectra

2.3 Conclusion

While we encountered the first motivation of the present work in Chapter one (i.e. the need to study new materials for SALICIDE-like contacts formed by solid-state reaction between a thin Ni film and InGaAs layer). This second chapter has introduced the second motivation of this work. Indeed, there is a need for a global characterization method resulting from the textured aspect of the samples. Full 3D-Reciprocal Space Mapping by means of pole figure measurement provides a solution to the texture problematic and allows a fast and sufficiently complete characterization of the reciprocal space. The method as developed on synchrotron and lab-tools allows different data reduction methods which are useful to extract different types of information. The method can be applied either on ex-situ annealed samples or to study the formation of the intermetallics in-situ. In the following two chapters, we will mainly discuss the results from this x-ray diffraction technique along with electrical results and STEM-EDS results.

Résumé du chapitre 3

Ce chapitre résume les résultats ex situ sur la formation de l'intermétallique, sa composition microstructurale et l'évolution de l'ensemble de ses caractéristiques structuraux en fonction de la température de recuit. Comme mentionné précédemment, les échantillons analysés sont des échantillons en pleine plaque et nous nous sommes surtout focalisé sur les échantillons sur substrat InP. En effet, ces échantillons offrent des conditions de croissance cristalline idéales pour l'intermétallique. Nous avons aussi comparé ces résultats sur substrat InP avec les résultats sur substrat Si, un substrat visé par l'industrie de la microélectronique pour réaliser les contacts sur III-V. Enfin, nous avons étudié l'effet de l'ajout d'éléments d'alliage à la couche de métal pur déposé.

L'analyse des figures de pôles, et l'affinement des diagrammes détexturés montrent l'existence d'une phase hexagonale d'intermétallique qui se forme dès 250 °C. Cette phase hexagonale est fortement texturée tout comme le rapporte la littérature sur GaAs. Nous avons décrit deux orientations différentes de l'intermétallique hexagonal formé :

- une première orientation où les plans $(1\,0\,\bar{1}\,0)$ de la phase hexagonale sont couchés et sont parallèles à la surface du substrat avec l'axe c parallèle à la direction $[1\,1\,0]$: c'est le groupe A,
- une deuxième orientation où l'intermétallique fait sa croissance avec son axe c parallèle à l'axe $[1\,1\,1]$ du semi-conducteur : c'est le groupe B.

Les deux orientations des deux groupes s'expliquent par des considérations axiotaxiales, i. e. une famille de plans de la maille hexagonale s'aligne avec une famille de plan du semi-conducteur du fait que leur distances interréticulaires sont proches. Nous démontrons que dans la configuration du groupe B, les plans $(1\,0\,\bar{1}\,1)$ sont quasiment parallèles aux plans $(0\,0\,1)$ du semi-conducteur au début de la réaction. En effet, à basse température l'intermétallique formé de type B8 est pseudocubique ayant des paramètres de maille qui se rapportent à la structure zinc-blende du semi-conducteur (avec un rapport axial c/a caractéristique). A plus haute température de recuit, ses paramètres des maille (et ainsi le rapport axial c/a) s'éloignent d'une valeur c/a caractéristique du la structure hexagonale pseudo-cubique. Nous démontrons que les plans $(1\,0\,\bar{1}\,1)$ forment ainsi un angle α avec les plans $(0\,0\,1)$ du semi-conducteur et nous donnons sa valeur en fonction du rapport axial c/a. Nous démontrons avec des considérations structurales basées sur l'évolution des paramètres de maille et du volume, que l'intermétallique passe d'une stœchiométrie $Ni_3In_{0.53}Ga_{0.47}As$ à une stœchiométrie $Ni_2In_{0.53}Ga_{0.47}As$ puis finalement NiAs.

Nous mettons aussi en évidence une anisotropie de texture concernant les orientations du groupe B. La littérature rapporte la possibilité que des marches atomiques à la surface de l'échantillon, appelées miscut soient responsables de cette anisotropie selon l'axe $[1\,1\,0]$. Cependant, nous démontrons que l'orientation des intermétalliques manquants ne peut pas être nécessairement liée à la direction du miscut. Nous démontrons par contre que des parois d'antiphase peuvent être responsables de cette asymétrie des axes $\langle 1\,1\,0 \rangle$ à la surface du semi-conducteurs. Des mesures en EDS/STEM démontrent que l'intermétallique se dégrade à haute température où il y a un rejet des atomes Ga et de l'In de l'intérieur la maille hexagonale de l'intermétallique et la formation de NiAs.

Finalement, nous étudions l'influence des alliages d'intermétallique sur la formation et la stabilité des contacts. En effet, ajouter du Co au Ni pur résulte en une texture différente de l'intermétallique. Dans ce cas, seules les orientations du groupe B sont formées. Nous démontrons que cette orientation, favorable par rapport au groupe B, est le résultat d'un meilleur alignement axiotaxial dans le cas des intermétalliques de groupe B et est induite par le changement des paramètres de maille de l'intermétallique par l'ajout d'un élément allié Co.

3 Formation and stability of Ni-InGaAs

3.1 Introduction

We have seen in Chapter 1 that literature on solid-state reaction between Ni and InGaAs is very limited and that there is a need to further investigate these materials using a fast global method to scan a large part of the reciprocal space. We've also seen in Chapter 2 the different steps and experimental setup on synchrotron and on lab diffractometer in order to measure a Full 3D-Reciprocal Space Map. In this chapter, we will present results of the ex situ[1] study of the solid-state reaction between **Ni and InGaAs epitaxially grown on InP** in an extended and comprehensive way. We will focus on phase formation and on the exhibited texture of these Ni-InGaAs intermetallic layers and discuss the phase formation sequence, stoichiometry and texture using axiotaxy considerations. The choice of InP substrate gives us a reference system with the best crystalline quality that can be achieved for an $In_{0.53}Ga_{0.47}As$ layer. Moreover, depositing rather thick layers of 20 nm of pure Ni relatively simplifies (the reacting system still contains four elements) the studies of the intermetallic since it is easier to obtain better quality diffraction data from thicker films.

However, for comparison reasons, we will also examine the influence of the substrate on the formation of Ni-InGaAs intermetallics where Ni/InGaAs/GaAs/Si samples were used. Finally we will investigate the effect of adding an alloying element to Ni on the formation of the intermetallic by adding Co to the 20 nm layer of Ni and compare them to the intermetallics formed in case of pure Ni. Adding an alloying element to the pure Ni layer may help stabilize the intermetallic and produce a better interfacial layer with the substrate. The samples used in this final part are $Ni_{0.9}Co_{0.1}$/InGaAs/InP.

---

[1] Ex situ studies refer to studies that are carried out after the phase formation and cooling to room temperature. Indeed, the annealing step and x-ray diffraction measurement step were done on two different setups. In the same way, in situ studies refer to studies where the annealing and the measurement steps are done simultaneously using a particular setup. Thus, in situ measurement offers to follow on real time the different steps of the formation of a new phase.

3.2 Experimental elements

3.2.1 Sample preparation

In this study, 200 nm thick $In_{0.53}Ga_{0.47}As$ layers were epitaxially grown by Metalorganic Chemical Vapour Deposition (MOCVD) on 100 mm, (1 0 0) oriented InP wafers. Since we will not change the composition of our III-V material, we will refer indifferently to this III-V compound by InGaAs or $In_{0.53}Ga_{0.47}As$ in this paper. Afterwards, a 20 nm layer of Ni was deposited on the $In_{0.53}Ga_{0.47}As$ by means of Radio Frequency Physical Vapor Deposition (RF-PVD). The metallic layer is capped with a TiN thin film to prevent atmosphere contamination. Before the Ni / TiN metal deposition, argon direct plasma in situ pretreatments to remove native oxides were carried out using RF1 power of 130 W and RF2 power of 310 W. Ar plasma is more efficient than remote plasmas for the removal of InGaAs native oxides but results in an In/Ga-terminated surface for InGaAs [100]. The in situ etching process was calibrated on thermal silicon oxide to obtain process time versus silicon oxide equivalent thickness of 2.5 nm. In situ pretreatment and metal deposition were carried out in a 300 mm Applied Materials Endura platform usually dedicated to silicide cleaning process. Full description of the samples is given in Figure 3.1. The samples were annealed at different temperatures during 60 s and under N_2 flow using Rapid Thermal Annealing (250 °C, 300 °C, 350 °C, 450 °C and 550 °C). The different process steps are summarized in Figure 3.2.

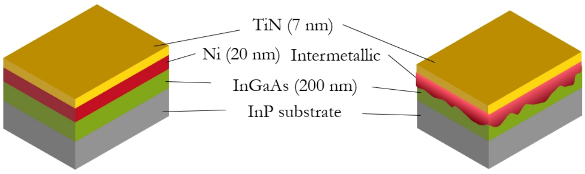

Figure 3.1 – Scheme of the stacks in the sample as-deposited (left) and after solid-state reaction (right) for a TiN/Ni/InGaAs/InP sample.

While two types of substrates were used, we focused mostly on InP substrates since this substrate is particularly suitable for epitaxial deposition of $In_{0.53}Ga_{0.47}As$ as these two compounds have exactly the same lattice parameter. However, if ever III-V CMOS are to be manufactured, they should be based on Si substrates. To this mean, we have carried also experiments on the formation of Ni on InGaAs on Si substrates (see Figure 3.3). The epitaxy of InGaAs cannot be done directly on Si because of the large mismatch between the two lattices (nearly 8 %), which causes important lattice dislocations on the InGaAs. Thus, a GaAs buffer layer is deposited before the III-V compound deposition. This buffer helps also absorbing the dislocations and reducing the lattice mismatch between InGaAs and the underneath layer (reducing it to nearly 3.8%). It is though important to stress out the fact that the Si-based samples with InGaAs layers were among the first produced in the lab and that these samples present various defects such as antiphase domains, stack defaults and higher roughness. Thus, results from these samples will not constitute a core interest in this manuscript, and main results are explored through Ni/InGaAs/InP samples.

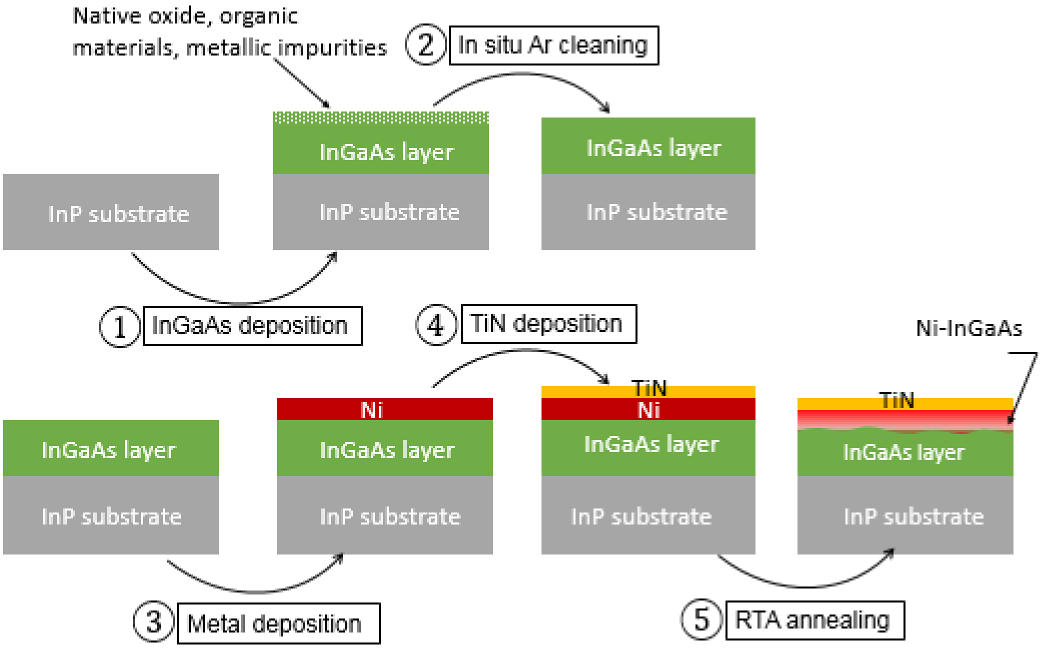

Figure 3.2 – Illustration of the different steps to produce the full sheet samples with reacted metal.

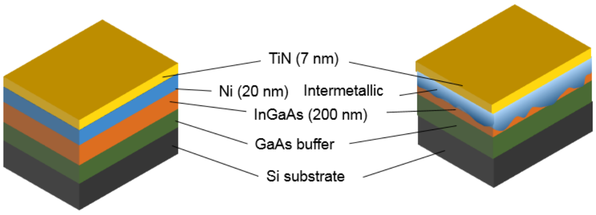

Figure 3.3 – Scheme of the stacks in the sample as-deposited (left) and after solid-state reaction (right) for a TiN/Ni/InGaAs/GaAs/Si sample.

$Ni_{0.9}Co_{0.1}$/InGaAs/InP were prepared in the same manner as Ni/InGaAs/InP samples using Ni and Co targets.

3.2.2 Substrate preparation and quality

Semiconductors usually present, according to fabrication process, atomic steps at their surface. These atomic steps result from non-flat cutting of the substrate and are characterized by a miscut angle and an orientation. InP and Si substrates used during this thesis were acquired from an industrial supplier. An eventual miscut at the surface of the sample was not necessarily a criteria when ordering the substrates. Thus, to investigate the miscut at the surface of the substrates, we use the method described by D. S. Covita et al. [101] to measure the miscut angle and determine its direction.

The measurements were performed on a Rigaku Smartlab diffractometer using in-plane configuration as described in Chapter 2. First, we pre-aligned the sample surface playing with the two rotations above the azimuthal rotation axis in order to put in coincidence the azimuthal axis and the normal to the surface. Then we performed rocking curve measurements around the (200) plane for several azimuthal positions (360° with a step of $\Delta\ \phi$=5°). The difference $\Delta(\Omega)$ between the measured peak position Ω and the peak reference position Ω_0 according to the azimuthal position is then plotted (Figure 3.4). A sinusoidal-like curve is obtained and the miscut angle corresponds to the amplitude of the this curve. This approach was validated on an industrial-quality silicon wafer, where the measured miscut at the surface is 0.03° which is insignificant and can be considered as the instrumental error as the manufacturer given value of the miscut for Si substrate is also close to 0°. For the InP substrate we obtain miscut angles of about 0.22°.

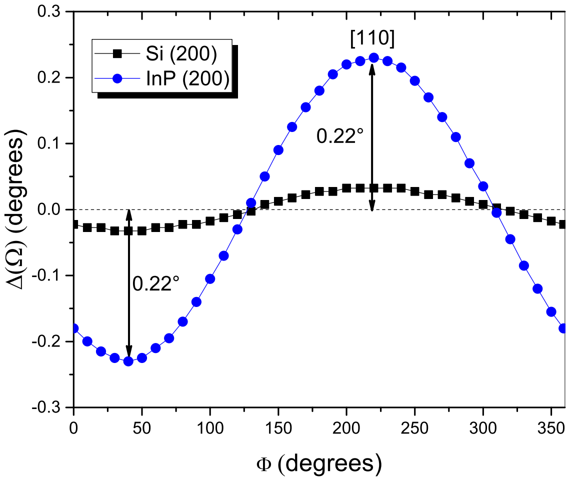

Figure 3.4 – $\Delta(\Omega)$ evolution of the (200) peak position of the (200) planes for Si (squared black) and InP (dotted blue) according to Φ.

3.3 Results

3.3.1 Electrical results

Resistivity variation can be an indicator on phase/texture changes made on the intermetallic. The Figure 3.5 exhibits the sheet resistance of the TiN / Ni layers on InGaAs/InP material according to rapid thermal annealing temperature. Sheet resistance of the 7 nm layer of TiN is 433.9 Ohm/sq and several measurements were carried out on each sample. The standard deviation of the values is about 0.1-0.2 Ohm/sq. Thus, even with small variations, the evolution of sheet resistance values is significant. As deposited (as-dep), we measured the sheet resistance of the TiN and Ni metallic layers. From 250 to 350 °C, the sheet resistance increases. This phenomena corresponds to the initiation of the Ni-InGaAs intermetallic formation. As intermetallic phases have higher resistivity than metallic layers, the global sheet resistance is slightly increasing. At 250 °C, the sheet resistance gently decreases. At this point, we may assume that we have formed the less resistive Ni-InGaAs intermetallic. From 350 to 450 °C, the sheet resistance increases again. We can link this evolution with the degradation of intermetallic properties with the increasing thermal budget. As the sheet resistance value considerably rises at 550 °C, we can postulate that the intermetallic composition / nature has probably changed. The microstructure analysis described in the next section is necessary to go further into interpretation.

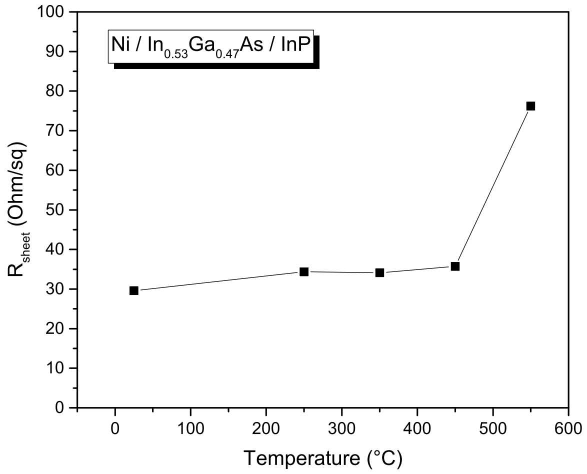

Figure 3.5 – Evolution of the sheet resistance of the TiN/Ni-InGaAs layers according to annealing temperature.

3.3.2 Structure of the intermetallic

X-Ray diffraction was used to study the structure of the intermetallic. Mainly two kinds of information have been extracted from the multiple 2D datasets we measured by XRD: i) De-textured 2θ diffractograms (see Figure 3.6) were obtained by summing over χ and ϕ the Debye rings of all the 2D snapshots (see Chapter 2 for more details on the process); ii) pole figures were reconstructed for several hkl reflections (or 2θ angles). All data can be treated in a localized way, i.e. data can be integrated on specific ranges of ϕ and χ in order to produce more accurate results and to avoid overlapping from nearby peaks (from the substrate for example).

From the refinement of these diffractograms, the symmetry of the pole figures and in agreement with the results published by P. Shekhter et al. [79], we identified clearly the intermetallic phases that appear during solid-state reaction, has an hexagonal structure and determined the space group as the *P6₃/mmc* with hexagonal pseudocubic-like lattice parameters that varies according to either orientation or annealing temperature. The unit cell of the hexagonal structure contains two formulas units [67] (see Figure 3.7) ; the metal atoms occupy the *2a* at (0,0,0) and (0,0,$\frac{1}{2}$) sites and the non-metal atoms occupy the *2c* sites at the ($\frac{1}{3}$,$\frac{2}{3}$,$\frac{1}{4}$) and ($\frac{2}{3}$,$\frac{1}{3}$,$\frac{3}{4}$) positions. Moreover there are two additional sites *2d* at ($\frac{1}{3}$,$\frac{2}{3}$,$\frac{3}{4}$) and ($\frac{2}{3}$,$\frac{1}{3}$,$\frac{1}{4}$) positions for the metal which can be partially, fully or non-occupied. In this case Ni atoms occupy the *2a* and potentially *2d* sites, while In, Ga and As occupy the *2c* sites. We also report the formation of a superstructure based on the parent hexagonal lattice and resulting probably from an order on the distribution of Ni atoms on the *2d* sites [61, 67] (see Chapter 1). The extra-reflections from the superstructure can barely be seen on the de-textured diagram because their relative intensity is weak and is lost in the background noise when doing a complete integration. However, pole figure analyses show clear diffraction spots arising from an ordering on the intermetallic phase. The ordering occurring during the formation of the intermetallic will be discussed later in this chapter.

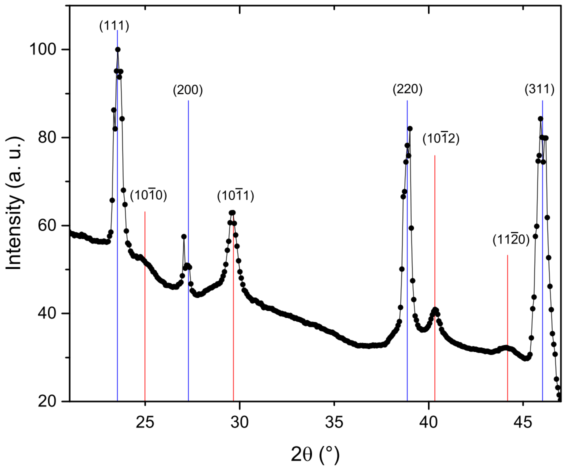

Figure 3.6 – X-Ray diffractogram of a sample after a 350 °C annealing. Red lines correspond to the intermetallic peak positions and blue lines correspond to InP/ $In_{0.53}Ga_{0.47}As$ peak position. X-Ray energy was set to 9 keV.

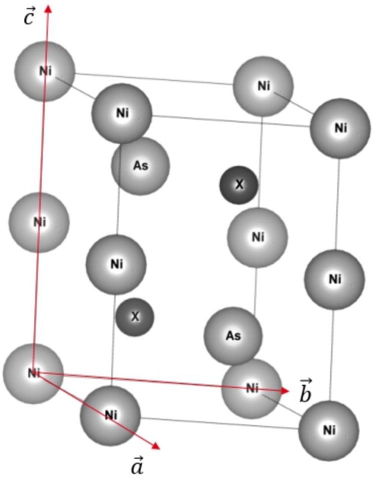

Figure 3.7 – Reduced lattice of the NiAs hexagonal structure. Atom position marked by X correspond to (*2d*) sites [67].

This hexagonal phase is the only intermetallic phase we observed whatever the RTA temperature. From the de-textured diagram, we refined the a and c lattice parameters of the structure according to annealing temperature. The evolution of the lattice parameters a and c is shown in Figure 3.8a. We see that at the temperature of formation of the intermetallic (300 °C), lattice parameter a is about 3.85 Å. From 350 to 450 °C, a decreases in an important way from 3.81 to 3.66 Å indicating that there were important structural modifications on the intermetallic. Finally at 550 °C, the lattice parameter a shrinks even more. However, lattice parameter c shows a different trend of evolution contrary to a. Indeed, it decreases a first time from 300 to 350 °C from 5.15 to 5.11 Å, but increases from 350 °C until 550 °C where it reaches 5.17 Å in an abrupt manner. The sudden increase of a and sudden decrease of c occur both at the annealing temperature of 350 °C indicating that this temperature is a critical temperature and that important structural/stoichiometric changes have occurred at this temperature. These structural changes will be developed in the discussion section of this chapter.

We also calculated the evolution of the volume of the hexagonal unit lattice of the intermetallic in Figure 3.8b. The unit lattice volume decreases in a tremendous manner from the formation of the intermetallic until 450 °C from 69 to 60 Å^3. At 550 °C, the volume reaches 59 Å^3. Such variation is not significant compared to the volume at 450 °C. The shrinking of the volume of the unit lattice is mainly driven by the shrinking in the a direction. The decrease of the volume is an indication of a higher concentration of vacancies inside the B8 hexagonal structure.

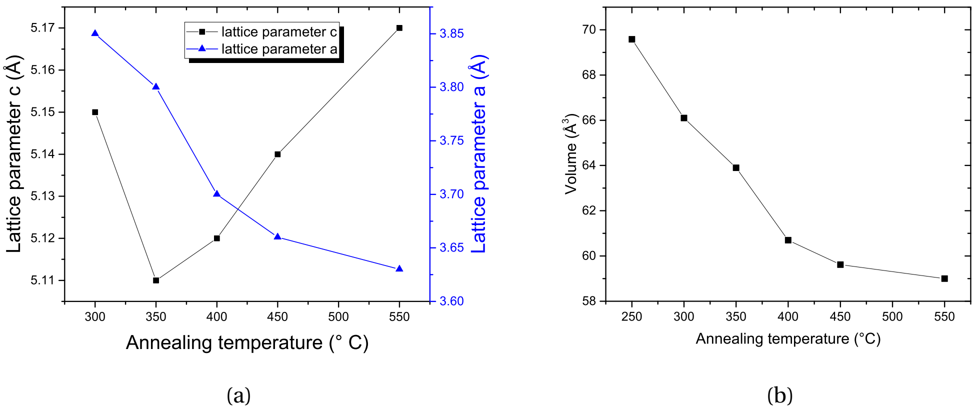

(a)

(b)

Figure 3.8 – Evolution according to the annealing temperature of the (a) a and c lattice parameters of the intermetallic, (b) volume of the hexagonal intermetallic phase.

3.3.3 Texture of the intermetallic

3.3.3.1 Ni/InGaAs/InP sample

Our results exhibit some discrepancies with the works cited previously [79], especially concerning the texture of the intermetallic. At 250 °C, Ni has not been fully consumed, but x-ray diffraction shows no new peaks or new poles. We do not exclude the formation of a transient amorphous intermetallic phase or nano-crystallized layer at this stage. Indeed, there is knowledge on the formation of amorphous silicide layer at low annealing temperature [102, 103]. Figure 3.9a shows the pole figure of the (2 2 0) planes of the substrate[2] for a reference sample with only InGaAs deposited on InP and Figure 3.9b shows the pole figure for a sample annealed at 250 °C at the same 2θ position when Ni is deposited on top of InGaAs. Deposited Ni takes an epitaxial orientation as seen in the corresponding {1 1 1} Ni pole figure (Figure 3.9b). No literature was interested in the metal texture when deposited on a III-V layer, but Ni takes a fiber-like texture reinforced in the ⟨1 1 0⟩ directions with $(2\,2\,0)_{Ni} || (1\,0\,0)_{InGaAs}$.

---

[2] Poles corresponding to InP and $In_{0.53}Ga_{0.47}As$ are superposed, since those two compounds have the same lattice parameters and orientation.

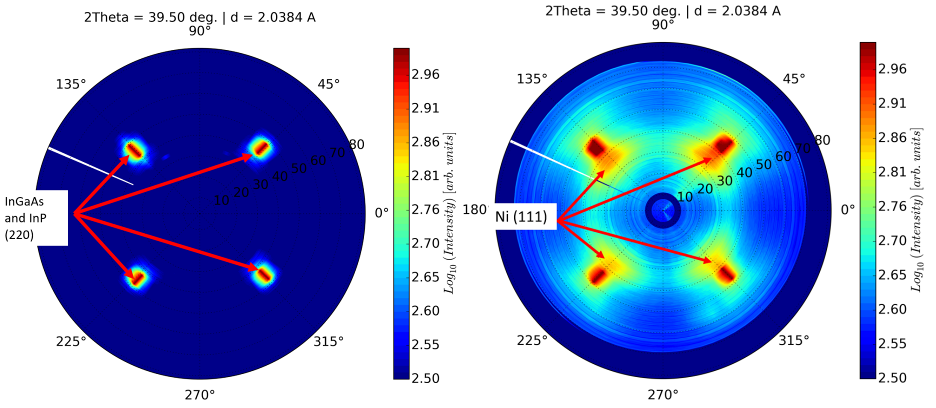

(a)

(b)

Figure 3.9 – (a) Pole figure at $2\theta = 39.5°$, the eventual Ni {1 1 1} planes position at X-ray energy 10 keV for an InGaAs/InP sample (with no deposited metal), (b) Pole figure of the {1 1 1} planes of the deposited Ni on a sample annealed at 250 °C. Samples used are Ni(20 nm)/InGaAs/InP.

At 300 °C, the intermetallic phase shows up and Ni is fully consumed. This phase is still observed at 450 °C and at 550 °C with the same texture and orientation. Actually, we observe multiple poles for the pole figure at 2θ= 29.25° (Figure 3.10a). Poles at χ=33° and χ=65° correspond to the projection of $(1\,0\,\bar{1}\,1)$ plane of the intermetallic phase on the $(1\,0\,0)$ plane of the substrate (see orientation 1 in Table 3.1) and the poles at χ=4°, χ=49° and χ=67° correspond to the projection of $(1\,0\,\bar{1}\,1)$ on the $(1\,0\,\bar{1}\,1)$ plane along two in-plane directions of the hexagonal structure (orientation 2 and 3).

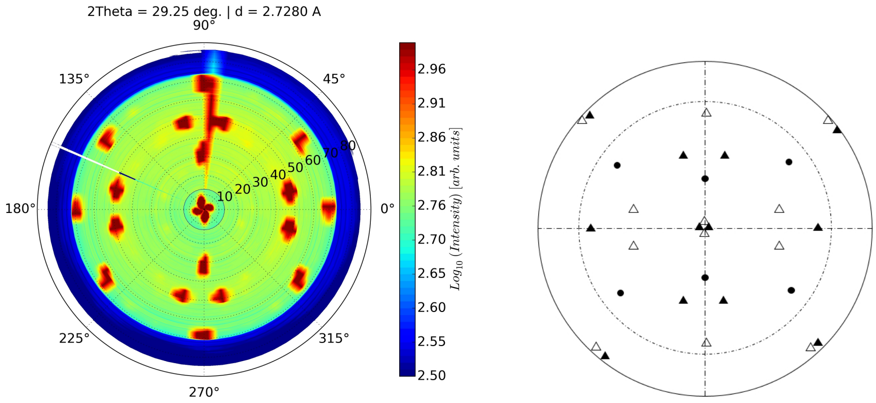

(a) (b)

Figure 3.10 – (a) X-ray diffraction pole figure of Ni/InGaAs/InP sample (after a 450 °C RTA annealing). The fixed 2θ angle was 29.25° corresponding to the intermetallic $\{10\bar{1}1\}$ reflections. The concentric dashed circles correspond to the χ angle landmarks with a 10° step. The intensity line at ϕ=90° is due to an experimental artifact, (b) Stereographic projection of the $(10\bar{1}1)$ planes of the intermetallic hexagonal structure for the different orientations given in Table 3.1. Only the poles included in the dashed circle were measured. Samples used are Ni(20 nm)/InGaAs/InP

In summary, for the Ni/InGaAs/InP substrates, the intermetallic exhibits the orientation 1, 2 and 3 described in Table 3.1. For simplification purposes, we denote the orientation where the $(10\bar{1}0)$ planes of the intermetallic are parallel to the substrate surface as group A orientation. The orientations where the $(10\bar{1}1)$ planes of the intermetallic are parallel to the substrate surface are denoted as group B. All the observed orientations of the hexagonal structure is given in Table 3.1 and a complete stereographic projection with the corresponding orientation for each pole is given in Figure 3.10b.

Due to the fact that all variants are oriented along $\langle 110\rangle$ vector group of the substrate, each domain group should exhibit two in plane variants tilted by 90° the one against the other. However, only one azimuthal variant was identified for group A domains. The missing azimuthal orientation for group A domains is denoted as orientation 4 in Table 3.1.

Table 3.1 – Summary of the orientations observed for so-formed intermetallic for Ni/InGaAs/InP initial stacks. Each symbol corresponds to an orientation in Figure 3.10b

Symbol	Number	Orientation
●	1	$(10\bar{1}0)_{\text{Ni-InGaAs}}\|(001)_{\text{InGaAs}}$; $[0001]_{\text{Ni-InGaAs}}\|[01\bar{1}]_{\text{InGaAs}}$
▲	2	$(10\bar{1}1)_{\text{Ni-InGaAs}}\|(001)_{\text{InGaAs}}$; $[1\bar{2}10]_{\text{Ni-InGaAs}}\|[0\bar{1}\bar{1}]_{\text{InGaAs}}$
△	3	$(10\bar{1}1)_{\text{Ni-InGaAs}}\|(001)_{\text{InGaAs}}$; $[1\bar{2}10]_{\text{Ni-InGaAs}}\|[01\bar{1}]_{\text{InGaAs}}$
○	4	$(10\bar{1}0)_{\text{Ni-InGaAs}}\|(001)_{\text{InGaAs}}$; $[0001]_{\text{Ni-InGaAs}}\|[0\bar{1}\bar{1}]_{\text{InGaAs}}$

Additional pole figures of different planes $\{10\bar{1}1\}$, $\{10\bar{1}2\}$ and$\{11\bar{2}0\}$ planes (respectively

Figures 3.11a and 3.12a) of the intermetallic and their correspondent stereographic projection (respectively Figures 3.11b and 3.12b) are given below.

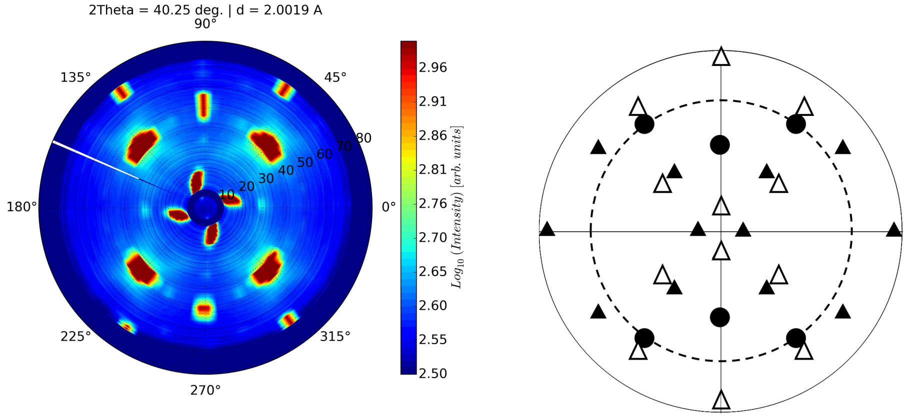

(a)

(b)

Figure 3.11 – (a) Pole figure of the $\{10\bar{1}2\}$ planes of the intermetallic hexagonal phase measured after a 350 °C, (b) corresponding stereographic projection. The pole symbols are the same as defined in Table 3.1 and the dashed circle on stereographic projection represent the area that was actually measured. Samples used are Ni(20 nm)/InGaAs/InP.

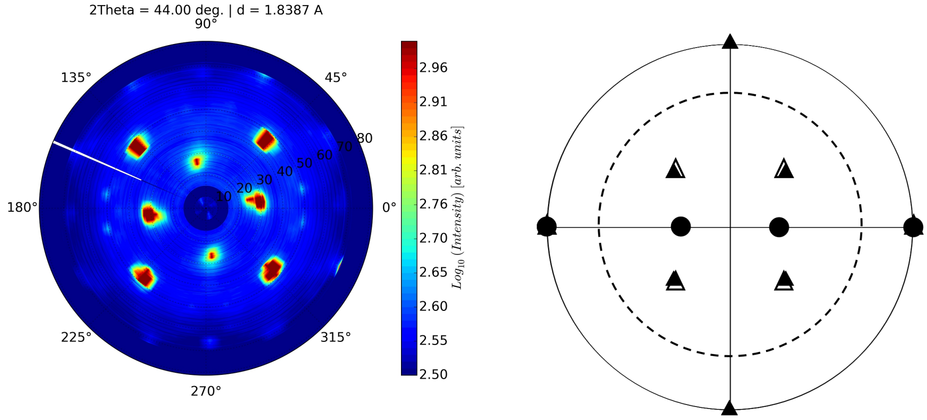

(a)

(b)

Figure 3.12 – (a) Pole figure of the $\{11\bar{2}0\}$ planes of the intermetallic hexagonal phase measured after a 350 °C, (b) Corresponding stereographic projection. Extra poles on the pole figure correspond to the poles measured from the nearby $\{311\}$ planes of the substrate. The pole symbols are the same as defined in Table 3.1 and the dashed circle on stereographic projection represent the area that was actually measured. Samples used are Ni(20 nm)/InGaAs/InP

As mentionned in the introduction, and while we focused on Ni/InGaAs/InP samples, we also studied the effect of the substrate and the addition of an alloying element on the texture of the so-formed intermetallic.

3.3.3.2 Ni/InGaAs/GaAs/Si sample

Si substrates with a proper buffer layer for InGaAs layer deposition are the target substrates when it comes to III-V MOSFET's. We focused on InP substrates because they represent the case of an ideal epitaxy of InGaAs on InP. However, samples with Si substrates were prepared in order to compare the formation of the intermetallic in both substrate cases. InGaAs/GaAs/Si samples presented differences in its texture compared to Ni/InGaAs/InP samples. Indeed as seen in Figure 3.13, the so-formed intermetallic presents both two azimuthal variants for group A domains. In comparison to InGaAs on InP, these two different results are surprising since the two layers of InGaAs in Si-based substrates or InP-based substrate were expected to yield similar properties. These differences will be discussed later on in the following sections of this manuscript.

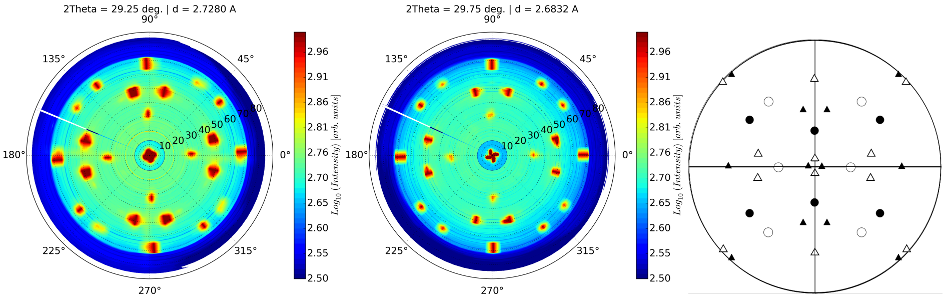

(a) (b) (c)

Figure 3.13 – (a) and (b), the pole figures of intermetallic $\{10\bar{1}1\}$ planes after an RTA annealing of respectively 350 °C and 550 °C, (b) Corresponding stereographic projection. The as-deposited samples used are Ni(20 nm)/InGaAs/GaAs/Si.

3.3.3.3 Ni$_{0.9}$Co$_{0.1}$/InGaAs/InP sample

The addition of alloying elements to a pure metallic layer that would react with the semiconductor to form a contact was largely studied for silicide[88, 104–106]. The addition of alloying elements affects the formation of the intermetallic and can change the formation temperature, stability, interfacial quality and texture of the intermetallic. Recently, the addition of Co to pure Ni layers proved to enhance the stability of the so-formed silicide on Si [107, 108]. Thus, we want to study the effect of Co addition on a pure Ni layer. In this section we report and describe the texture of the (NiCo)-InGaAs intermetallic compared to Ni-InGaAs.

The Figure 3.14a shows a pole figure of the 2θ position that would correspond to the (1 1 1) plane of the deposited Ni$_{0.9}$Co$_{0.1}$ for a reference sample (just InGaAs/InP). Figure 3.14b and Figure 3.14c show the pole figures of the {1 1 1} planes of deposited Ni$_{0.9}$Co$_{0.1}$ for respectively the as-deposited sample and the sample annealed at 250 °C. Indeed, at 250 °C annealing temperature NiCo is not consumed yet and no diffraction from an intermetallic was measured.

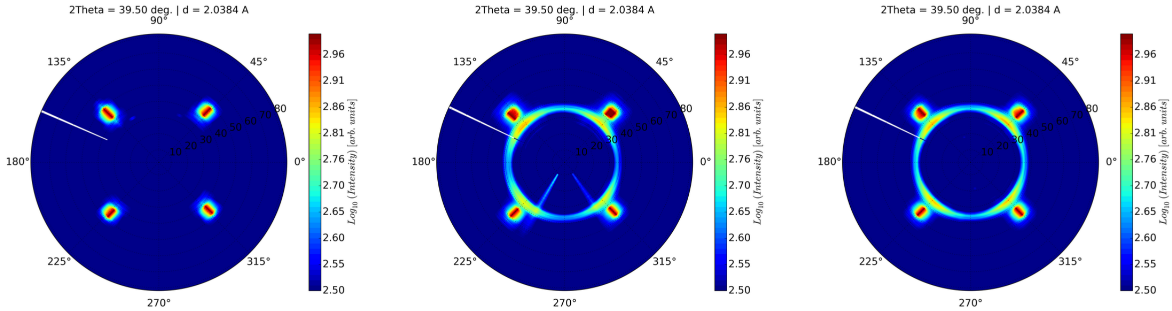

(a) (b) (c)

Figure 3.14 – (a) Pole figure at 2θ=39.5° for a reference sample without metal deposition (InGaAs/InP), (b) pole figure of the {1 1 1} planes of the deposited NiCo for an as-deposited sample and (c) pole figure of the {1 1 1} planes of the deposited NiCo after annealing to 250 °C. Samples used are $Ni_{0.9}Co_{0.1}$ (20 nm)/InGaAs/InP.

Figures 3.15a, 3.15b and 3.15c show the pole figures of the $\{10\bar{1}1\}$ planes of the intermetallic after an annealing of respectively 350, 450 and 550 °C. The intermetallic exhibits uniquely a group B orientation and no occurrence of group A orientation was measured.

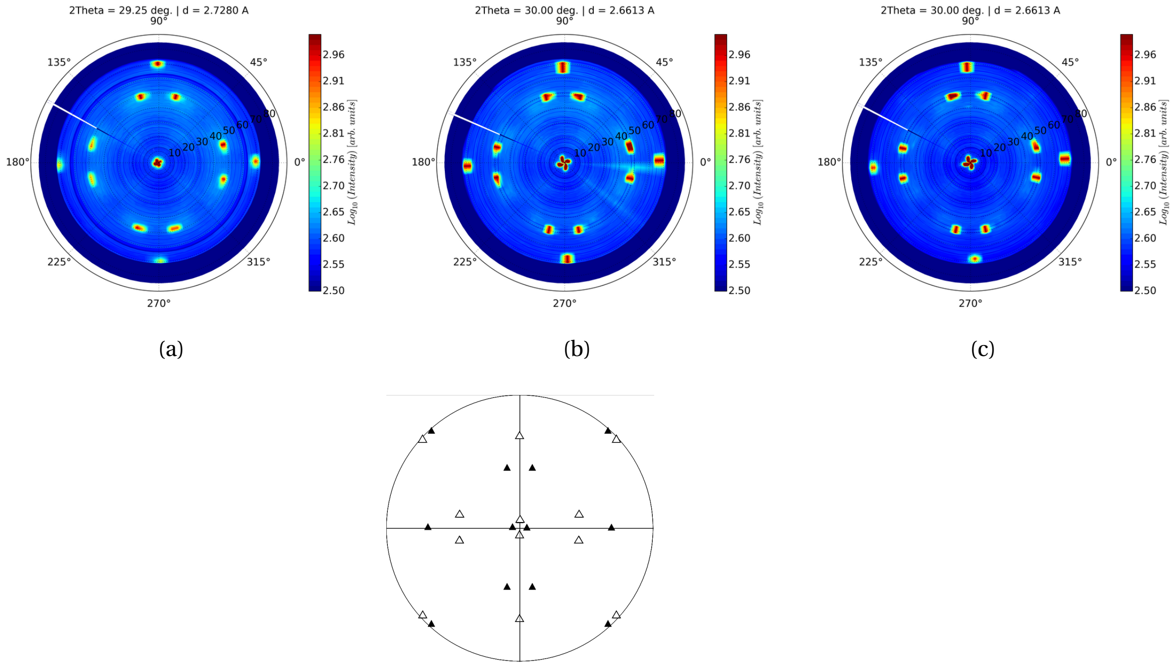

(a) (b) (c)

(d)

Figure 3.15 – Pole figures of the ntermetallic $\{10\bar{1}1\}$ planes after an RTA annealing of (a) 350 °C, (b) 450 °C, (c) 550 °C and (d) stereographic representation of the pole figures. Samples used are $Ni_{0.9}Co_{0.1}$ (20 nm)/InGaAs/InP.

The possible origins of the texture discrepancies between pure Ni and after adding a Co alloying element will be considered in the discussion section.

3.3.4 Domain quantification of Ni/InGaAs/InP samples

On Figure 3.16, we can clearly see that intensities from poles that correspond to group A and group B domains are not equal according to annealing temperature (Figures 3.16a, 3.16b, 3.16c and 3.16d show respectively the the pole figures of the $\{10\bar{1}1\}$ planes measured after different RTA, at 300, 400, 450 and 550 °C.). Considering that each grain of each group diffracts on the attributed poles, and that the intensity is proportional to diffracting volume : $I_{hkl} \propto V_{grains}$) We quantified group A and group B domains according to annealing temperature by measuring the integrated intensities from two $(10\bar{1}1)$ poles corresponding each to a domain group. Figure 3.17 shows the ratio of the integrated intensities from these two poles, along the χ, ϕ, and 2θ angles. It shows that from 300 °C to 450 °C group A domains are predominant and at 550 °C group B domains are predominant.

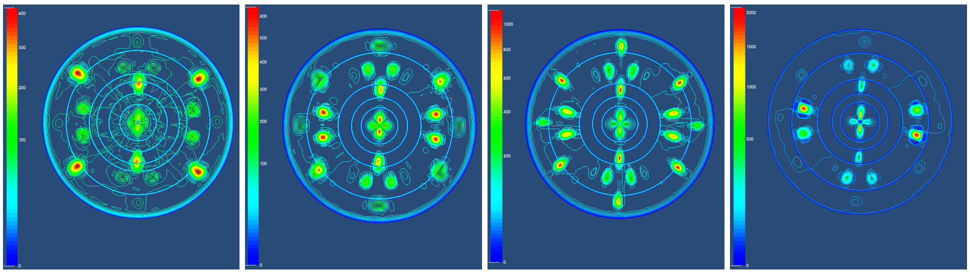
(a) (b) (c) (d)

Figure 3.16 – Pole figure of the $\{10\bar{1}1\}$ planes of the intermetallic hexagonal phase measured after the following annealings: (a) 300 °C, (b) 400 °C, (c) 450 °C, (d) 550 °C. The samples were measured using a Smartlab Rigaku diffractometer. Samples used are Ni(20 nm)/InGaAs/InP.

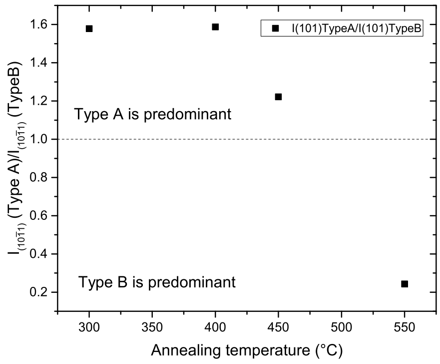

Figure 3.17 – Ratio of the relative intensities between $I_{(10\bar{1}1)}$ of group A and $I_{(10\bar{1}1)}$ of group B according to temperature.

It is also interesting to investigate the evolution of the two domains along the intermetallic vertical depth. Such investigations allow us to have some indications about the phase formation mechanisms. In order to do so, we used a similar sample like the one mentioned in the sample preparation section and instead of depositing 20 nm of Ni we have deposited 80 nm. The sample has then undergone a 350 °C annealing. In-plane grazing incidence X-Ray diffraction was carried on this sample around the (0002) peak of type A domain and $(10\bar{1}2)$ peak of type B domain. Figure 3.18 shows the corresponding in plane reciprocal space map at given angle $\omega = 0.3°$. The acquisition was performed using the Smartlab, in an in plane configuration [109]. The $2\theta\chi/\phi$ scan on the figure is equivalent to the $2\theta/\omega$ scan in symmetrical out-of-plane measurements.

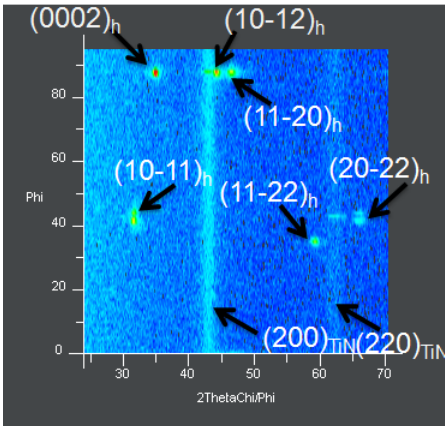

Figure 3.18 – X-ray diffraction in-plane reciprocal space map sample of an Ni (80 nm) on InGaAs on InP sample after an annealing of 350 °C.

Multiple in-plane measurements were done for different incident grazing angles from 0.2 to 0.9°. The penetration depth, t_{tot}, changes according to the incident angle.

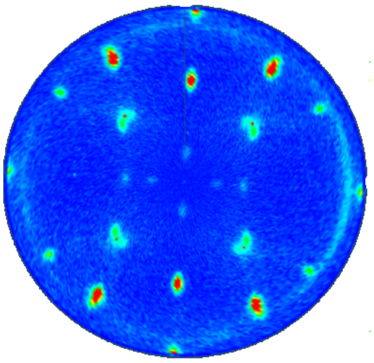

Figure 3.19 – In-plane pole figure at the fixed 2θ position of 45 ° of the $\{10\bar{1}2\}$ planes of the intermetallic on a Ni 80 nm/InGaAs/InP sample after an 350 °C RTA annealing. Corresponding stereographic projection is given in Figure 3.11b.

The incident angle α_i can be related to the penetration depth of X-rays inside the intermetallic. Supposing that group A and group B domains exhibit the same chemical composition after a 350 °C annealing, we can spatially estimate the evolution of the proportion of the two domains. It is although important to point out that unlike the (0002), the $(10\bar{1}2)$ plane does not lie exactly in plane, but it is rather slightly tilted away from the parallel to the surface by about 3° (see the stereoscopic projection and the corresponding in-plane pole figure at Figure 3.11b and Figure 3.19). This is not an issue, since we are following the evolution of the ratio of the intensities. Figure 3.20 describes the evolution of the ratio of the intensities of two peaks belonging to group A and group B orientations.

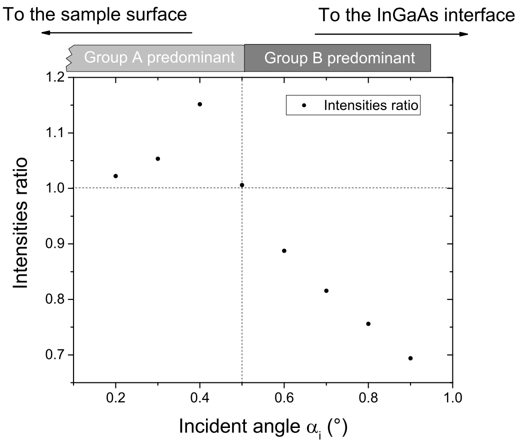

Figure 3.20 – Ratio of the relative intensities between $I_{(10\bar{1}2)}$ and $I_{(0002)}$ according to the penetration depth of the X-rays.

We clearly distinguish from Figure 3.20 two separate areas from the surface of the sample to the InGaAs interface. From the 0.2°(corresponding roughly to scanning the sample's surface) to a certain critical incident angle 0.5°(corresponding to a certain depth) group A domains are predominant. Beyond this critical incident angle, group B domains are the ones which are more preponderant. This result suggests that there are two stages of growth of the intermetallic: at the beginning of the reaction, group A are predominant and then, at a critical thickness, the intermetallic takes the second orientation: group B orientation.

3.3.5 Distribution of elements in the intermetallics

STEM-EDS maps were carried out on a TEM JEOL 2100F. Sample preparation consisted of preparing a substrate/film/glue/film/substrate “sandwich" and polishing was performed by a tripod bevel to 10 microns and followed by Ar ion milling until perforation of the interface.

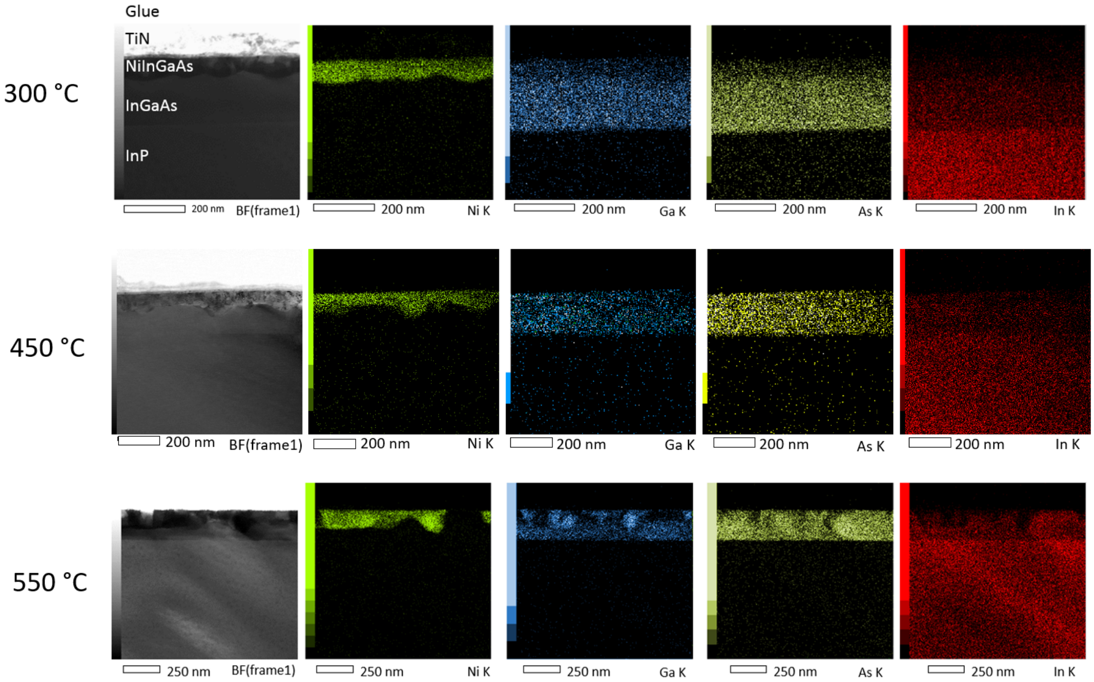

Figure 3.21 – Bright Field (BF) TEM images and element map using STEM EDS of the sample annealed at: Top, 300 °C, Middle, 450 °C and Bottom, 550 °C.

Samples annealed at 300 °C, 450 °C and 550 °C were analyzed (see Figure 3.21). The STEM-EDS maps shows that at low annealing temperatures, In, Ga and As are nearly at their nominal stoichiometry inside the intermetallic compound. On the contrary, at higher annealing temperatures, starting at 450 °C, the proportion of these elements inside the intermetallic lattice is no longer the same as their nominal composition. This observation suggests an out-diffusion of Ga and In during the thermal annealing and the formation of NiAs at higher temperature. Moreover, at the highest annealing temperature, the film is highly agglomerated suggesting important structural changes. Similar degradation process of germano-silicides was discussed by T. Jarmar et al.[110]. The agglomeration are related to the strong increase of the resistivity at 550 °C in Figure 3.5.

3.4 Discussion

3.4.1 Texture of the Ni/InGaAs/InP intermetallic

A more detailed observation of the $(10\bar{1}1)$ pole figures shows that, for group B orientation, there is a shift of poles from the center of about 3°. In fact, if the $(10\bar{1}1)$ planes were perfectly parallel to the sample surface ((001) of InGaAs), the 4 diffraction poles would be merged into a single pole located at (ϕ,χ) (0°,0°). The presence of a shift indicates that the $(10\bar{1}1)$ planes are slightly tilted from the sample surface. This kind of behavior was observed for Ni_2GaAs and $NiAs_{1-x}Al_x$ hexagonal compounds [64, 111]. Actually, face-centered cubic lattices like the zinc-blende structure (GaAs, AlAs, InGaAs) can be described in a hexagonal lattice with $c/a = \sqrt{3}/\sqrt{2}$, with the $(10\bar{1}1)_h$ and $(0001)_h$ planes rigorously parallel respectively to the $(001)_c$ and $(111)_c$ planes of the cubic lattice (Figure 3.22a). Thus we obtain the following crystallographic relationships: $(10\bar{1}1)_h||(001)_c$ and $(0001)_h||(111)_c$ [64]. In this ideal case, on $(001)_c$ oriented substrate the $(10\bar{1}1)_h$ plane is perfectly parallel to the $(001)_c$ plane. Furthermore, for any hexagonal lattice presenting a c/a ratio slightly different from $\sqrt{3}/\sqrt{2}$ (the structure is then called pseudo-cubic hexagonal lattice), the precedent rule is no longer rigorously respected. In theory, the hexagonal pseudo-cubic compounds will tend to be oriented in a way to satisfy the $(0001)_h||(111)_c$ condition. Thus, the $(10\bar{1}1)_h$ plane of these phases is no longer rigorously parallel to the $(001)_c$ and these two planes will form an angle α which can be measured through X-Ray Diffraction (see Figure 3.22b). This angle is as large as the c/a ratio is far from $\sqrt{3}/\sqrt{2}$.

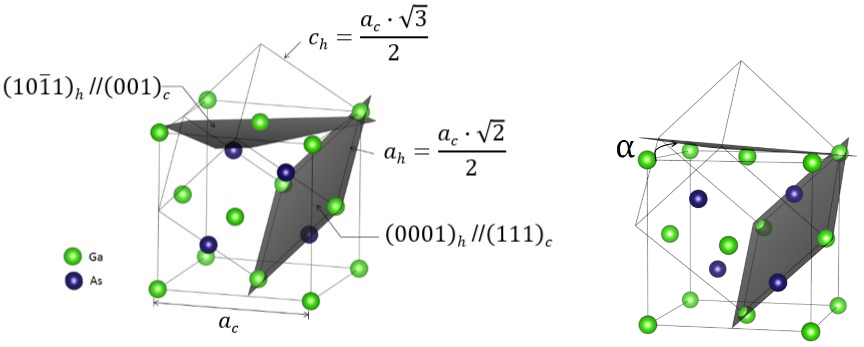

(a)

(b)

Figure 3.22 – (a) Transformation scheme of cubic unit cell of zinc blende-type structure in an hexagonal lattice with an ideal ratio of $c/a = \sqrt{3}/\sqrt{2}$ (adapted from Lahav [64]), (b) Transformation scheme of cubic unit cell of zinc blende-type structure in an hexagonal lattice with a ratio of 1.4, the angle between the $(001)_c$ and $(10\bar{1}1)_h$ is denoted α.

We can define the angle between $(0001)_h$ and $(10\bar{1}1)_h$ as β. The tilt angle α can be defined as the difference between the angle $\beta_{c/a=\sqrt{3}/\sqrt{2}}$ in the case of an ideal hexagonal pseudo-cubic and $\beta_{c/a\neq\sqrt{3}/\sqrt{2}}$ in the case of a regular hexagonal pseudo cubic:

$$\alpha = \beta_{c/a=\sqrt{3}/\sqrt{2}} - \beta_{c/a\neq\sqrt{3}/\sqrt{2}} \tag{3.1}$$

The angle between two planes $(h_1 k_1 l_1)$ and $(h_2 k_2 l_2)$ in the hexagonal structure can be calculated as the following [112]:

$$cos(\Phi) = \frac{h_1 h_2 + k_1 k_2 + \frac{1}{2}(h_1 k_2 + k_1 h_2) + \frac{3a^2}{4c^2}(l_1 l_2)}{\sqrt{\{\left[h_1^2 + k_1^2 + h_1 k_1 + \frac{3a^2}{4c^2}(l_1^2)\right]\left[h_2^2 + k_2^2 + h_2 k_2 + \frac{3a^2}{4c^2}(l_2^2)\right]\}}} \tag{3.2}$$

Using the equation (3.2) to calculate the β angle between the $(0\,0\,0\,1)$ and the $(1\,0\,\bar{1}\,1)$ planes, we obtain:

$$cos(\beta) = \frac{\sqrt{\frac{3a^2}{4c^2}}}{\sqrt{1 + \frac{3a^2}{4c^2}}} \tag{3.3}$$

Using equation (3.3) into (3.1), the tilt angle α can be calculated using the lattice parameters of the hexagonal structure in the following manner:

$$\alpha = \cos^{-1}(\frac{1}{\sqrt{3}}) - \cos^{-1}(\frac{\sqrt{\frac{3a^2}{4c^2}}}{\sqrt{1 + \frac{3a^2}{4c^2}}}) \tag{3.4}$$

Figure 3.23 shows the evolution of the α angle as measured and as calculated according to annealing temperature. The evolution of the c/a ratio is also plotted in the same figure. At 300 °C, α_{measured} and $\alpha_{\text{calculated}}$ exhibit a notable difference. At 350 and 450 °C, the axial ratio c/a increases which might be related to stoichiometry/structural variations (see Chapter 1). These variations will influence the value of α_{measured} and $\alpha_{\text{calculated}}$. Finally at 550 °C, the axial ratio c/a strongly increases and likewise $\alpha_{\text{calculated}}$ and α_{measured}. While the evolution trend is the same for both $\alpha_{\text{calculated}}$ and α_{measured}, we state that there is a gap between these two value that increases according to annealing temperature. This can be explained by the fact that lattice parameter calculation was performed at room temperature after the annealing. An anisotropic thermal expansion during the sample's cooling will subsequently change the c/a ratio from its value at the formation of the intermetallic. Considering that no further rotation of the $(1\,0\,\bar{1}\,1)$ planes would occur after the anisotropic expansion of lattice parameters, the measured and calculated values of α would be then different for group B intermetallics. The anisotropic thermal expansion was investigated by means of in situ synchrotron radiation experiments. These in situ results will be discussed in Chapter 4. No tilt was measured for group A orientation as the measured pole positions corresponding to this orientation matches the calculated ones. The additional orientations were not observed by Shekhter et al. [79]. This is likely due to the low annealing temperature used to form the Ni-InGaAs alloy (i.e. 250 °C), and the probable late formation of group B domains.

Indeed, we observe on the Figure 3.17 that the ratio of the relative intensities of group A and group B intermetallic varies according to annealing temperature. Group A is predominant from the temperature of formation of the intermetallic (300 °C) until 450 °C. Group B orientation is predominant at 550 °C. This result suggests that group B orientation forms lately and faster at higher annealing temperatures. Moreover, Figure 3.20 shows the ratio of relative intensities between group A and group B peaks according to the penetration depth of x-rays for a thick sample (with 80 nm of Ni deposited on InGaAs on InP, sample annealed at 350 °C). The intermetallics situated near the surface of the sample are predominantly group A intermetallics and the intermetallics far from the surface and close to the Ni-InGaAs/InGaAs interface are predominantly group B intermetallics. This result suggests that at first annealing stages, it is group A that are being formed, then, at later annealing stages, it is group B orientations are being formed. In situ results give us more insights on the formation and texture of the intermetallic and will be discussed in Chapter 4.

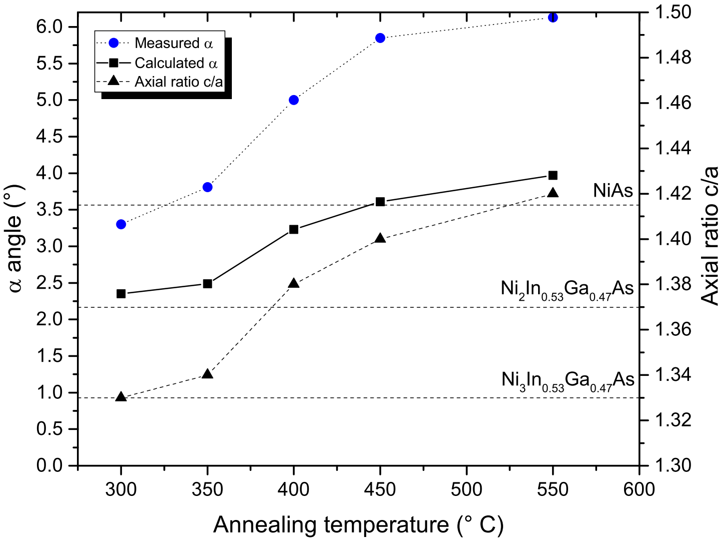

Figure 3.23 – Measured and calculated tilt angles α and c/a ratio according to the annealing temperature for Ni/InGaAs/InP samples.

3.4.2 Texture anisotropy

3.4.2.1 Miscut influence on azimuthal orientations

Shekhter et al.[79] observed the same missing azimuthal variant for group A intermetallics and stated that the presence of atomic steps at the surface of the substrate can induce such anisotropy. Indeed, when the substrate presents a low angle miscut that prevents (1 0 0) planes from being completely parallel to the sample surface, it can loose its four-fold symmetry along with the deposited InGaAs layer. This symmetry reduction may lead to the formation of the intermetallic along some preferred directions that can be explained by epitaxial or axiotaxial relationship [58].

We identified the miscut direction as the one oriented along [1 1 0] on different samples. Such a configuration introduces an asymmetry between ⟨1 1 0⟩ directions that lie at the surface of the sample. Nevertheless, we couldn't relate the direction of the miscut on each sample with the ⟨1 1 0⟩ direction along which the hexagonal intermetallic is aligned. Thus, we conclude that such anisotropy is likely not due to the presence of a miscut at the surface of the sample.

3.4.2.2 Antiphase domains and texture anisotropy

Zinc-blende structure is a non-centrosymetric structure and presents polarity characteristics. Polarity is not expressed in every lattice plane or every direction but only on some of them. For example the {1 1 1} planes in the zinc-blende InGaAs lattice are polar planes and can, depending on their index, bear alternatively either only group III atoms or only group V atoms (see Figure 3.24) forming double layers, i.e. alternately short and long distances exist between 111 planes. Each atom has 3 bonds within the same double layer and one bond in the exterior of the double layer. The surfaces terminated by Ga or In atoms are called 111A, whereas those terminated by As or P atoms are called 111B. Likewise, in the (1 0 0) plane, the in-plane orthogonal ⟨1 1 0⟩ direction presents also an anisotropy. Indeed, literature reports anisotropic behavior on optical and electrical parameters along the in-plane ⟨1 1 0⟩ direction. On Figure 3.25, a three dimensional 3×3×3 stack of GaAs lattices is depicted and is projected along [1 1 0] (Figure 3.25a) and along [$\bar{1}$ 1 0] (Figure 3.25b).

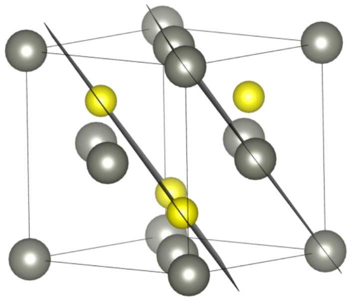

Figure 3.24 – The {1 1 1} planes in the InGaAs zinc-blende structure: alternatively planes containing only In or Ga (group III elements) and planes containing only As (group V elements). As is represented by big gray spheres while In and Ga are represented by small yellow spheres.

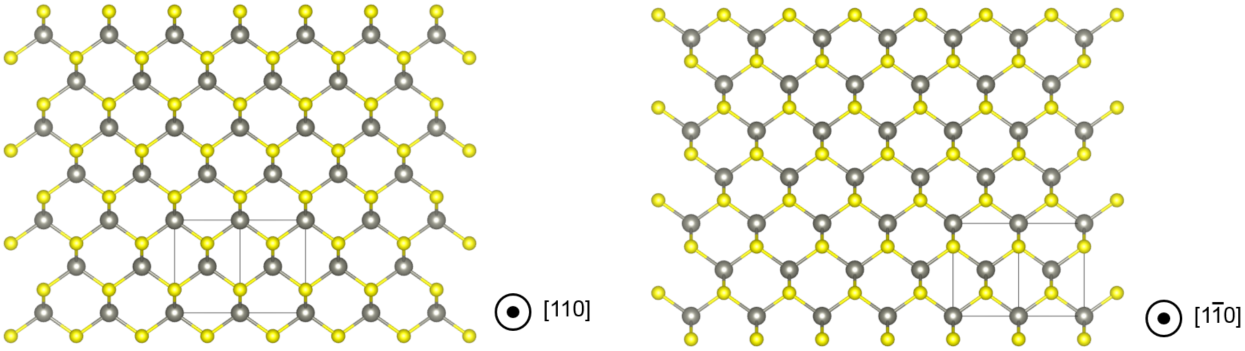

(a) (b)

Figure 3.25 – A stack of InGaAs lattices projected along [1 1 0] in (a) and along the [$\bar{1}$ 1 0] direction in (b). As is represented by big gray spheres while In and Ga are represented by small yellow spheres. The unit lattice is marked by a rectangle on the figures.

Indeed, the (0 0 1) surface of a bulk material presents two dangling bonds by atom at the surface. The dangling bonds of two close atoms point the one to the other. On the (0 0 1) face of III-V materials, the orientation of the dangling bonds results in the establishment of a surface bond that regroups atoms two by two (see Figure 3.26a), which results in lower surface energy. Indeed, as new bonds are created and thus the number of dangling bonds is reduced and so the surface energy. The atoms are slightly displaced to establish these new bonds and regroup by dimers which constitute the basic tiling structure of the (0 0 1) surface. In the case of a surface terminated with group V atoms, the dimers are oriented in the [1 $\bar{1}$ 0]. In the case of a surface that ends with group III elements, the dimers are oriented in the [1 1 0] direction. The orientation of dimers explains why on (0 0 1) surface of the InGaAs, the in-plane orthogonal ⟨1 1 0⟩ direction are not equivalent though these directions are symmetric in the volume.

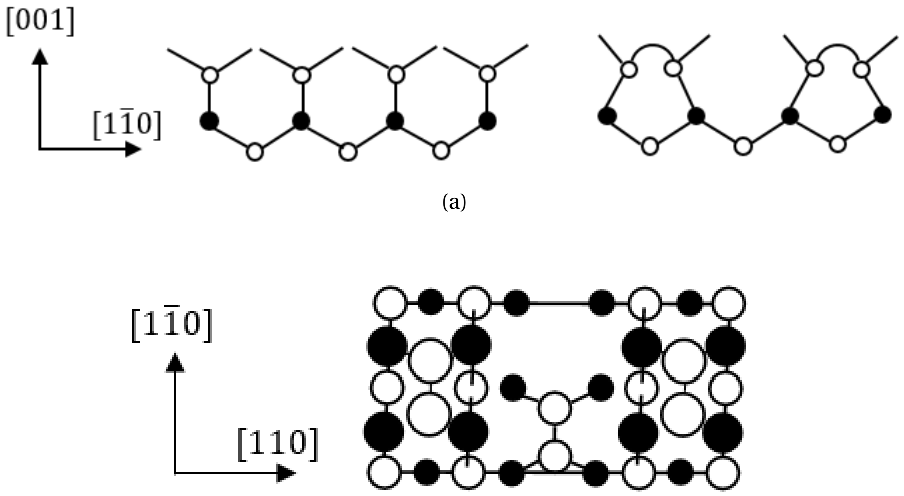

(a)

(b)

Figure 3.26 – (a)Dimer formation on the InGaAs surface. In and Ga are represented by black circles and As is represented by white circles.) (b) Proposition of dimer organization [113].

The deposition conditions, for example excess of V elements during InGaAs deposition leads to the formation of V-plane surfaces on InP, which are the low-energy surfaces compared to In or Ga-terminated surfaces [114], but also Ar plasma cleaning before Ni deposition can lead to different polarities on the (001) surface plane of InGaAs. Indeed, in our case we observed mostly Ga and In oxides by X-ray photoelectron spectrometry after an in situ Ar plasma cleaning [100]. Literature have reported several types of organization of dimers and dimerization of the surface occurs with a certain periodicity (4×2 V-terminated surface in the example in Figure 3.26b) [115, 116].

The arising anisotropy on the in-plane ⟨1 1 0⟩ directions can thus be responsible for preferential Ni-InGaAs growth along one direction or the other considering the direction to which the dimers point to. Considering that all samples come from the same wafer, we can safely assume that the polarity of the samples is the same for each one.

This anisotropy is particularly present if the III-V layer is homogeneous and contains no antiphase domains (APD) and thus always present the same type of atoms at the (0 0 1) surface. Deposited InGaAs layers on InP substrate do not present any APD and thus an anisotropy along the in-plane ⟨1 1 0⟩ directions is expected (see Figure 3.27a). Indeed, pole figure measurement on the intermetallic shows that an azimuthal variant along the [1 1 0] direction is missing for group A intermetallics. The growth of the group A intermetallic is likely to happen along one preferential direction yielding the minimum energy.

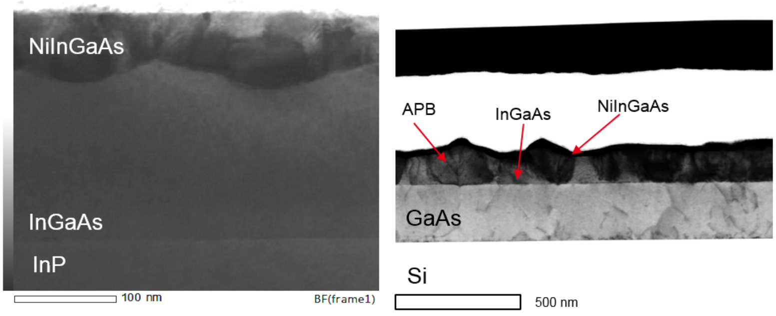

(a) (b)

Figure 3.27 – BF STEM images of samples annealed at 300 °C for (a) InP substrates (b)GaAs/Si substrates.

In contrast, GaAs buffer layer and InGaAs layer on top of it on Si substrates yield antiphase boundaries (boundaries that separate the crystal into two regions where one is configured in the opposite order to the crystal in the perfect lattice system) and give rise to antiphase domains (see Figure 3.27b). While recent research from LTM team demonstrated the capability of producing APD-free InGaAs layers on such type of samples [2], the samples we used yield APDs. The consequence could be a loss of anisotropy along the in-plane ⟨1 1 0⟩ directions on a global scale in the III-V layer. Indeed, if antiphase domains occur in the lattice, the (0 0 1) surface would present both In/Ga and As polarities depending on the antiphase domain. As a consequence, the anisotropy is lost along the ⟨1 1 0⟩ directions and intermetallic is formed along these two orthogonal directions depending on the InGaAs domain polarity. This concords with the observations made on intermetallics formed on InGaAs on GaAs on Si substrates. Indeed, on Si substrates, the intermetallic yields the two in-plane azimuthal variants for group A contrary to the InP substrates.

3.4.3 Origin of group A and group B domains

Group A domains orientation is the same as mentioned on similar solid-state reaction by P. Shekhter et al. [79]. This orientation can be resolved by considering an axiotaxial alignment between the $(1 0 \bar{1} 0)$ planes of group A domains and the (1 1 0) planes of the substrate. Taking into account this axiotaxy, every set of four (1 1 0) planes of the substrate should meet every set of five $(1 0 \bar{1} 0)$ planes of the hexagonal phase (Figure 3.28a). No axiotaxial lines were measured on pole figures but rather a fixed in plane direction along [1 1 0]. We also consider an axiotaxial alignment to calculate the lattice mismatch according to the interplanar distance of the (0 0 0 1) planes of the intermetallic and the one of the (1 1 1) plane of the substrate. Indeed, every set of three (0 0 0 1) hexagonal planes should meet every set of two (1 1 1) substrate planes at 2 points [93] (Figure 3.28b). The occurrence of an axiotaxy, where lattice planes of the intermetallic are aligned with lattice planes of the substrate, is a possible explanation for the group B orientation. Moreover, the high roughness of the so-formed film is likely to favor the occurrence of an axiotaxy-like alignment [58]. While no tilted fiber texture (typical of axiotaxy) was observed on pole figures, we can consider the following: the [1 1 1] axis is a three-fold rotational axis that can easily adjust with the six-fold rotational c axis of the hexagonal structure. Thus the growth occurs only through epitaxial relationship with the substrate as it was described for ϵ-NiGe by B. De Schutter et al. [93] (see Table 3.2). The calculated mismatch according to the description of the alignments at the beginning of this paragraph is summarized in Table 3.3 for both intermetallic domains.

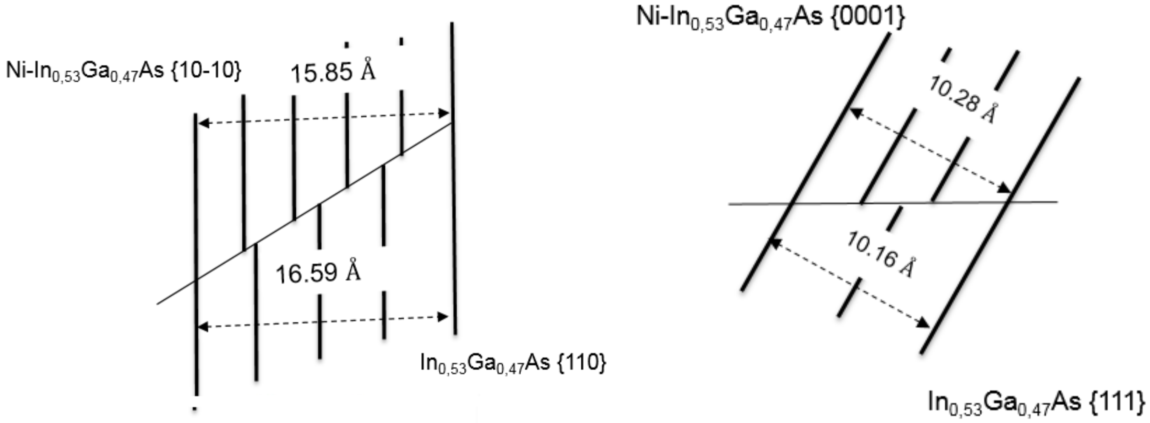

(a) (b)

Figure 3.28 – Schematics of the axiotaxy alignement for (a) Group A domains (b) Group B domains.

Table 3.2 – Rewritten orientations of group B domains according to a growth along the [1 1 1] axis of the $In_{0.53}Ga_{0.47}As$

Number	Orientation
2	$(0\,0\,0\,1)_{\text{Ni-InGaAs}} \| (1\,1\,1)_{\text{InGaAs}}$; $[1\,\bar{2}\,1\,0]_{\text{Ni-InGaAs}} \| [0\,\bar{1}\,\bar{1}]_{\text{InGaAs}}$
3	$(0\,0\,0\,1)_{\text{Ni-InGaAs}} \| (1\,1\,1)_{\text{InGaAs}}$; $[1\,\bar{2}\,1\,0]_{\text{Ni-InGaAs}} \| [0\,1\,\bar{1}]_{\text{InGaAs}}$

Table 3.3 – Mismatch of $(1\,0\,\bar{1}\,0)$ planes of group A according to (1 1 0) planes of the substrate and those of (0 0 0 1) planes of group B according to (1 1 1) planes of the substrate. Samples used are Ni/InGaAs/InP

Orientation	300 °C	350 °C	400 °C	450 °C	550 °C
Group A	0.5%	-0.7%	-3.5%	-4.6%	-5.5%
Group B	-1.3%	-0.5%	-0.7%	-1.1%	-1.7%

3.4.4 Texture of $Ni_{0.9}Co_{0.1}$/InGaAs/InP

We have seen that $Ni_{0.9}Co_{0.1}$/InGaAs/InP intermetallic takes a unique domain orientation: group B orientation (see the pole figures at Figure 3.15). No occurrence of group A orientation was measured. This is probably due to the formation of an interface with higher energy in the case of group A alignment. Indeed, let us consider the mismatch (between NiCo-InGaAs and the semiconductor) calculated taking into consideration the axiotaxial alignment in case of group B intermetallic and we compare it to the mismatch of a hypothetical, yet not existent, group A orientation. We find that, at the temperature of formation of the intermetallic, the mismatch is lower if the intermetallic is axiotaxially aligned trough group B orientation than if it was aligned through group A orientation. Table 3.4 summarizes the calculated mismatch between the intermetallic and the substrate for group B intermetallic and for a hypothetical group A intermetallic.

Table 3.4 – Mismatch of $(1\,0\,\bar{1}\,0)$ planes of group A according to $(1\,1\,0)$ planes of the substrate and those of $(0\,0\,0\,1)$ planes of group B according to $(1\,1\,1)$ planes of the substrate. Samples used are $Ni_{0.9}Co_{0.1}$/InGaAs/InP.

Orientation	300 °C	350 °C	400 °C	450 °C	500 °C	550 °C
Hypothetical Group A	-1.45%	1.41%	4.02%	5.32%	6.11%	6.11%
Group B	-0.91%	-0.32%	-0.71%	-1.5%	-2.48%	-2.29%

The evolution according to annealing temperature of the measured and calculated tilt angle α and c/a axial ratio was plotted for the $Ni_{0.9}Co_{0.1}$/InGaAs/InP samples in Figure 3.29.

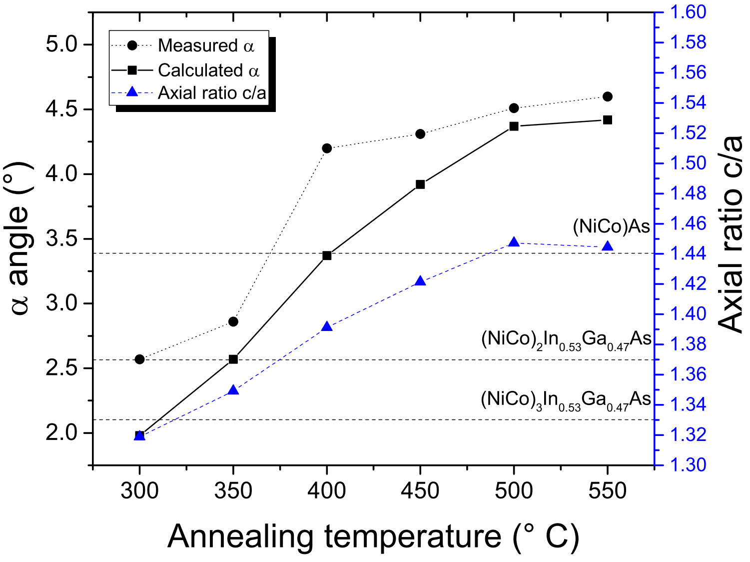

Figure 3.29 – Measured and calculated tilt angles α and c/a ratio according to the annealing temperature for $Ni_{0.9}Co_{0.1}$/InGaAs/InP samples.

From the evolution of the axial ratio c/a in Figure 3.29, we can define the stoichiometries of the different phases in the same manner as in the case of pure Ni. The richest phases in Ni are formed first (i. e. $(Ni_{0.9}Co_{0.1})_3In_{0.5}Ga_{0.5}As$), then less richer phases in metal are formed $(Ni_{0.9}Co_{0.1})_2In_{0.5}Ga_{0.5}As$) and at the end, a $(Ni_{0.9}Co_{0.1})As$ phase is formed with eventually its solid-solution extension. We believe that the given stoichiometries indicate only the major stoichiometry that is formed at a certain temperature. Indeed, it is likely that two or three stoichiometries exist at the same time with different solid-solution extensions making any effort to define a clearly formed phase difficult. The calculated and the measured α angle that the $(10\bar{1}1)$ plane forms with the (001) plane of the semiconductor in case of group B orientations were also plotted in Figure 3.29. The gap between calculated and measured angles is less important than in the case of pure Ni. This could be explained by a less important thermal expansion anisotropy in the case of NiCo than in the case of pure Ni.

3.4.5 Stoichiometry

Figure 3.23 shows the evolution of the axial ratio c/a of the hexagonal intermetallic according to the annealing temperature with two major limits: NiAs and $Ni_3(In_{0.53}Ga_{0.47})As$. At 300 °C the c/a corresponds to the lattice parameters of Ni_3GaAs and likely so, corresponds to $Ni_3(In_{0.53}Ga_{0.47})As$ since In and Ga exhibit close covalent radii (respectively 0.142 nm and 0.122 nm). The c/a ratio rises significantly at 400 °C and is comparable to the one of $Ni_2(In_{0.53}Ga_{0.47})As$. At 550 °C the axial ratio is very close to the axial ratio of NiAs. Moreover, there is an important variation on the volume of the unit lattice of the intermetallic phase that can be seen in Figure 3.8b between 250 °C and 400 °C. This variation on the volume can indicate a rejection of Ni atoms on the inner metallic sublattice of the hexagonal lattice. Indeed, when Ni is rejected from the metallic sub-lattice in the $B8_1$ structure, the vacancies concentration increase inducing a decrease on the unit lattice volume. Moreover, oriented facets at 54° appear clearly after a 450 °C (see Figure 3.30) that correspond to a group B orientation, and thus correspond to a growth along the $[111]$ axis of the substrate. Moreover, group B domains are more predominant at higher temperature (see Figure 3.17). A faster diffusion along the growth axis of group B domains at higher temperature could explain this phenomena (c axis).

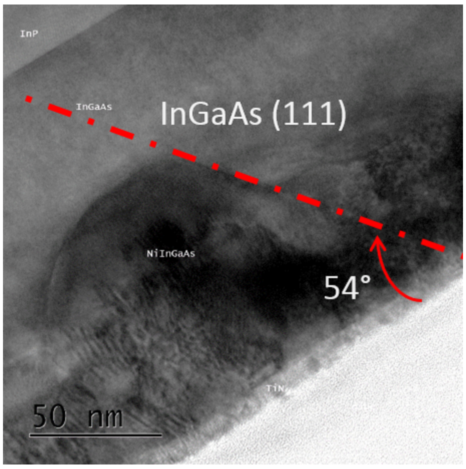

Figure 3.30 – STEM image showing the NiInGaAs/InGaAs/InP layers and oriented facets for a sample annealed at 450 °C.

The formation of the intermetallic in the Ni/InGaAs system is obviously a way to minimize the Gibbs free energy when a certain amount of thermal budget brought by the rapid thermal annealing. In this case, and contrary to the formation of silicides, only one crystalline structure is formed, and the prime intermetallic formed tends to only change its stoichiometry in order to keep minimization of the Gibbs free energy. Actually, the surface energy terms can also particularly be lowered by stoichiometry adjustment. Ni has been proven to be the diffusing species during the Ni-InGaAs solid-state reaction[117]. The nickel diffusion is the dominant controlling mechanism for the intermetallic formation at lower thermal budgets (lower RTA annealings). Once all the metal has been entirely consumed and thermal budget is high enough, the intermetallic tends to expel metal atoms from the *2d* positions and also Ga and In atoms in order to reach the NiAs stable phase. This fairly explains the evolution from a $Ni_3In_{0.53}Ga_{0.47}As$ structure to $Ni_2In_{0.53}Ga_{0.47}As$ structure and finally NiAs-like stoichiometry. This result is in agreement with the ternary phase diagram established by Guérin et al. [23] for Ni, Ga and As alloys. The phase diagram states that the different Ni-GaAs intermetallics belong all to the $P6_3/mmc$ space group. Five phases were identified with different homogeneity ranges and different ordered/disordered structures (i.e. presenting a superstructure or not). The only stable phase for the Ni, Ga, As system is the NiAs phase. In our case, we'd expect to form the richest phase in Ni (where n(Ni)>3) first according to the Cu_3Au rule [118, 119]. Nevertheless, this phase is disordered according to Guérin, and we observe only ordered structures throughout the different annealing. Thus, it is likely that we start by forming $Ni_3In_{0.53}Ga_{0.47}$ and ending up with NiAs and NiAs-based solid solutions. This comparison with the ternary phase diagram is reasonable since In is completely miscible in the GaAs lattice where it occupies Ga sites. To conclude, if one defines a crystalline phase as an homogeneous crystal structure accepting a certain range of stoichiometry, the Ni/InGaAs system presents therefore a sequence of 3 phases with the same B8 crystallographic structure but with different stoichiometry: $Ni_3In_{0.53}Ga_{0.47}As$, $Ni_2In_{0.53}Ga_{0.47}As$, NiAs. The shift from a stoichiometry to another is probably not continuous but during the transition, the average measured c/a ratio represents a fraction mixed of at least two c/a ratios corresponding to at least two distinct phases. Indeed we can consider that the intermetallic compound phase transition is effectively sharp but appears rather as a smooth one (see Figure 3.23).

3.4.6 Superstructure of the Ni-InGaAs/InGaAs/InP

Superstructure occurrence in NiAs-like crystals is common and has been reviewed several times. As seen in Chapter 1, superstructures were important elements for Guérin and Guivarc'h to separate phases from one another. While measuring diffracting signal from superstructure lattice planes is relatively easy, especially when using synchrotron radiation, their intensity remains weak and is submerged by background noise when doing complete integrations over χ and ϕ angles. Moreover, if there is poor ordering, then constructive interference does not occur sufficiently and diffracting intensity drops a lot. It is thus more practical to study the diffracting peaks of superstructures directly on pole figures. Moreover, by doing so, another information can be used to identify the planes of the superstructure: the texture. Indeed, comparing stereographic projections and measured intensities makes identification more reliable. This is a point of a great importance because lattice parameters of superstructure are generally important and interplanar distances of different planes are more and more close to each other.

By indexing the planes and verifying stereographic projections, two superstructures were put in evidence for both groups. The first one yields the same orientation of group B (for both azimuthal variants) and have a $(2a \times 3c)$ lattice parameters. The second one yields the same orientation of group A and have also $(2a \times 3c)$ lattice parameters. Examples of diffraction from the superstructure are given in Figure 3.31a and Figure 3.31c which describe respectively the pole figures of the $\{3\bar{1}\bar{2}1\}$ and the $\{10\bar{1}7\}$ planes of the superstructures. Apart from a change on the intensity of peaks, indicating a change on the quality of ordering, no other superstructure was resolved or further evolution was measured according to annealing temperature. The corresponding stereographic projection are shown respectively in Figures 3.31b and 3.31d. For the sake of clarity, the stereographic projections in Figure 3.31b yields just one azimuthal variant. The other azimuthal variant can be obtained by simply rotating the stereographic projection by 90°. The second azimuthal variant for group B can be seen on its corresponding pole figure in Figure 3.31a but have much less important intensities than the first azimuthal variant. This can be due to a less important ordering occurring through one growth direction. Moreover, many poles of the second variant are superposed to the first one and thus can be hardly distinguished on the pole figure.

The superstructure ordering dimensions that were refined do not concord with any of the three ordered phases proposed by Guérin and Guivarc'h and presented in Chapter 1 for Ni-GaAs. Moreover, no order/disorder transition was observed according to annealing temperature and no additional superstructure was observed either. However, these observations do not

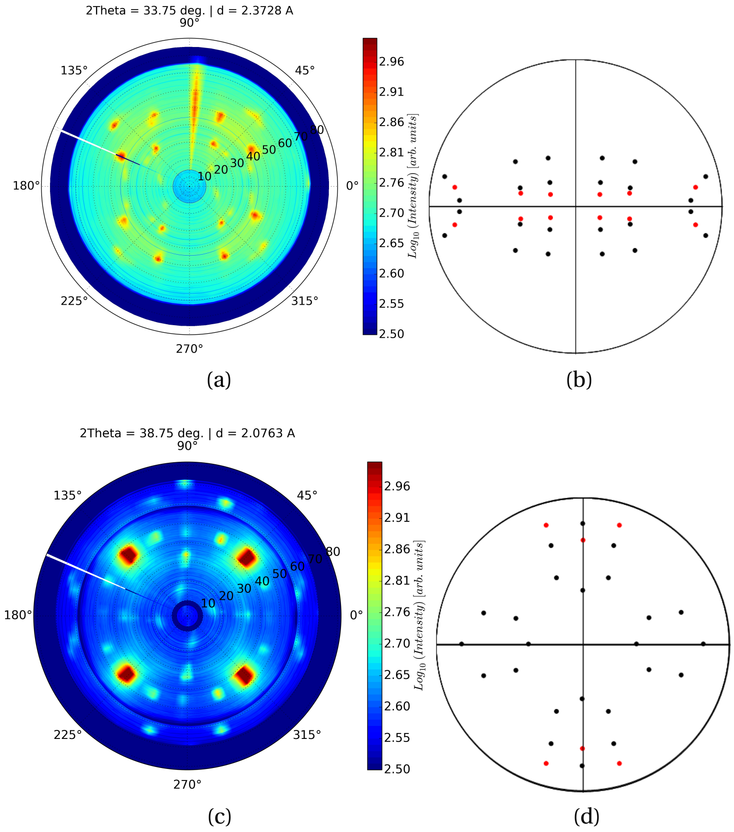

(a) (b)

(c) (d)

Figure 3.31 – Pole figures of respectively: (a) $\{3\bar{1}\bar{2}1\}$ planes and (c) $\{10\bar{1}7\}$ planes, and respectively their corresponding stereographic projections: (b) for $\{3\bar{1}\bar{2}1\}$ planes and (d) for$\{10\bar{1}7\}$ planes. Extra poles on (c) correspond to nearby diffraction peaks from substrate and main intermetallic. Group A variants are represented by red poles and group B variants are represented by black poles.

necessarily mean that no phase transition have occurred. Indeed the samples have all undergone a similar 60 s rapid thermal annealing with a rapid ramp and were all cooled rapidly afterwards contrary to the samples prepared by Guérin and Guivarc'h. Long annealings at 800 °C and subsequent slow cooling to room temperature or instant quenching probably leads to the formation of different superstructures proper to each new phase but short annealings and rapid quenching probably leads to the conservation of the first superstructure to appear. Moreover, the range of temperature we were interested in is relatively broad and consists of relatively low annealing temperatures (i.e. from 250 °C to 550 °C).

3.5 Conclusion

We studied the phase formation when a reaction occurs between Ni thin films with $In_{0.53}Ga_{0.47}As$ on InP substrates. 3D-RSM developed on the ESRF synchrotron was used in order to identify the so-formed intermetallic. De-texturing results indicates that there is a formation of a single

NiAs-type (B8) hexagonal structure. There is however a phase transition according to the annealing temperature which is not a sharp one, but appears as a smooth transition from a Ni-rich phase to NiAs. This result was further confirmed using STEM-EDS results and is coherent with early results on Ni/GaAs metallization. Pole figures reconstruction indicate that there is a formation of two domain groups and axiotaxial alignments along with symmetrical considerations were necessary to explain the intermetallic/substrate relationship. Indeed, we demonstrate that group A domains have their $(1\,0\,\bar{1}\,0)$ plane parallel to the sample surface. Moreover, this domain group exhibits orientation reduction which couldn't be attributed to the presence of miscut at the surface of the sample but could be due the presence of antiphase domains. These InGaAs antiphase domains do not exist in the case of InP substrate, but are present in case of Si substrate. The absence of antiphase domain results in an anisotropy on the $\langle 1\,1\,0\rangle$ axes on the sample surface which can lead to a preferential growth along one axis. Group B domains however, grow along the $[1\,1\,1]$ direction of the semiconductor and are more predominant at higher annealing temperatures (starting from 550 °C). Furthermore, group B domains have their $(1\,0\,\bar{1}\,1)$ plane nearly parallel to the sample surface. This tilt from the surface is directly related to the lattice parameter of the intermetallic and also the relationship between the zinc-blende structure and B8 hexagonal structure. Moreover, we investigated the influence of the substrate on the phase formation, texture and stability by using a GaAs/Si substrate. Finally we also investigated the effecting of adding cobalt to the pure Ni layer in the case of InP substrate.

In the end, we emphasize on the fact that within the proposed phases presented in this study, only the NiAs one is stable. Hence, any formed phase other than NiAs for the (Ni, In, Ga, As) system is not a stable one, but rather a metastable phase.

Résumé du chapitre 4

Dans ce chapitre, nous rapportons les résultats des analyses des cartographies de l'espace réciproque en 3D par diffraction des rayons X in situ réalisées lors de deux campagnes de mesures au synchrotron ESRF à Grenoble. Nous avons réalisé des mesures en rampes allant de 150 °C à 550 °C avec des pas de 20 °C. Chaque étape de mesure durait environ 20 minutes, le temps de recueillir les données de diffraction par rayons X à plusieurs configurations géométriques de l'échantillon et du détecteur. Ces mesures ont été réalisées sur des échantillons de type Ni (20 nm)/InGaAs/InP. Les résultats montrent que dans un premier temps, il y a formation d'un intermétallique hexagonal dont le rapport c/a se rapproche de 1.29 et donc qui correspond à une stœchiométrie $Ni_3In_{0.5}Ga_{0.5}As$ à 210 °C. les paramètres de maille de cette phase changent de manière faible mais suffisamment significative indiquant un domaine d'homogénéité plutôt large. Lorsque la couche de Ni est complètement consommée entre 250 °C et 270 °C, un deuxième intermétallique ayant la même symétrie et la même texture que le première phase apparait. Ce deuxième intermétallique a un rapport c/a qui évolue entre 1.37 et 1.42. Ceci indique qu'il correspond à NiAs et son extension ternaire. Le premier intermétallique formé disparait peu à peu jusqu'à 390 °C au profit de la phase la plus stable: NiAs et sa solution solide. Ainsi, nous nous retrouvons dans un schéma de formation séquentielle de phases similaire à la formation des siliciures où la phase la plus riche en métal apparait en premier lieu. Ensuite, lorsque l'apport en métal alimentant la réaction s'arrête, il y a une formation de phase plus riche en éléments du semi-conducteur et qui est plus stable.

Nous avons aussi étudié l'effet de l'épaisseur du métal déposé sur la formation de l'intermétallique. En effet, bien que nous avons étudié des intermétalliques formés par réaction de film minces de 20 nm d'épaisseur, cette épaisseur reste relativement importante pour les composés logiques sub-10- nm. Ainsi, nous avons comparé in situ, les résultats obtenus avec 20 nm de Ni et les résultats obtenus avec 7 nm de Ni déposé. Il en ressort que de manière générale, les textures, paramètres structuraux, séquence de phase... sont similaires dans les deux cas d'épaisseur de métal déposé. Ainsi, nous pouvons conclure que les résultats obtenus sur 20 nm de métal déposé, et qui constituent la majeure partie des échantillons étudiés lors de cette thèse, sont valables pour des épaisseurs allant jusqu'à 7 nm.

L'ajout de 10% de Co à la couche pure en Ni résulte en une température de formation d'intermétallique plus élevée que dans le cas de Ni pur. De plus, nous avons mesuré des textures différentes avec l'alliage $Ni_{0.9}Co_{0.1}$. En effet, des orientations de groupe B ont été mises en évidence ainsi qu'une infime partie des grains cristallins s'orientait selon le groupe A. Cette différence de textures s'explique à la fois par des considérations thermodynamiques et cinétiques. Le retard de formation d'intermétallique peut être expliqué par des énergies interfaciales plus importante lors de la formation dans le cas d'un alliage que dans le cas de métal pur. Une énergie interfaciale plus importante est le résultat de changements de paramètres de maille de l'intermétallique suite à l'ajout de Co.

4 In situ X-Ray diffraction

There is a need to form contacts on III-V semiconductors. Due to the limited scaling of the targeted devices, these contacts must be as thin as possible. Thus, the metal intake must be as limited as possible too. A deposited thickness of metal of 7 nm of Ni is representative of the targeted system. However, Ni (20 nm)/InGaAs/InP are relevant samples to study the solid-state reaction because the relative thickness of Ni would allow better diffracting intensities and thus facilitate the intermetallic characterization. Rapid Thermal Annealing is also a relevant method of annealing, since it is the one used for multiple annealing steps to manufacture Si-based CMOS. However, there is the need to explore the intermetallic characteristics during the annealing process, in order to extract information about its kinetics and stability and better understand its growth. Moreover, there is a need to explore the possibility of stabilizing the intermatallic by adding alloying elements into it. That's why, we will relate in this chapter the observations made upon in situ experiment by performing ramp annealing. The samples were characterized in real time using synchrotron 3D-RSM X-ray diffraction on the D2AM beam-line at ESRF. This experimental method allows to determine the domains of existence of the different phases simultaneously with the accurate determination of lattice parameters and textures of the intermetallics. The experimental procedure was described in Chapter 2, and in the following sections, we will describe first the phase formation during in situ annealings (domain of existence, texture, possible phase sequence...) for the Ni/InGaAs/InP system for two different thicknesses (20 nm and 7 nm). Then, we will study the effect of Co addition on $Ni_{0.9}Co_{0.1}$ / InGaAs / InP samples.

4.1 Ramp annealing of the Ni/InGaAs/InP systems

4.1.1 The Ni(20 nm)/InGaAs/InP system

In this first section, we will study the X-ray diffraction (3D-RSM) of a full-sheet Ni(20 nm)/InGaAs/InP sample with 7 nm TiN capping layer annealed with ramps at successive temperatures and measured in situ on the BM02 beam-line on ESRF. The presence of P element in the InP substrate and the presence of As element in the InGaAs layer requires proper verification on toxic gas emission during the in situ annealings which are less protected than an RTP annealing. These verifications are described in Appendix A.

4.1.1.1 Formation of the intermetallic

We have seen in Chapter 3 that when Ni is put in contact with InGaAs, a solid-state reaction occurs and an hexagonal intermetallic Ni-InGaAs is formed. We will study the formation of such intermetallic during ramp annealings using an as-deposited Ni/InGaAs/InP sample. To avoid oxidation of the metal and the semiconductor-metal interface, the in situ measurement were carried out under continuous flow of N_2. As-deposited sample with a 20 nm thick Ni layer has undergone a ramp annealing with steps of measurement of 20 °C. The ramp up speed was set to its maximum (200 °C/minute) and continuous X-ray diffraction acquisition was carried out with azimuthal steps of $\Delta\phi = 5°$ at each step of temperature for a 360° range of ϕ. Data were recorded at a fixed detector position of $2\theta = 30°$ and fixed $\chi = 0°$ and energy of the X-ray beam was set to 10 keV. To measure the lattice parameters, we fitted every peak with a Gaussian function. A refinement was then done on the 2θ positions of the fitted peaks using Checkcell software[1]. It is important to note that lattice parameter refinement did not include any thermal expansion or residual stress contribution that could eventually induce changes on the lattice parameters. Thus, only important variations on lattice parameters will be commented and confronted to stoichiometric/phase changes. Indeed, it would be risky to relate small variations of lattice parameters to structural/stoichiometric variations without including the stress and thermal effect.

---

[1] Available at http://www.ccp14.ac.uk/tutorial/lmgp/achekcelld.htm.

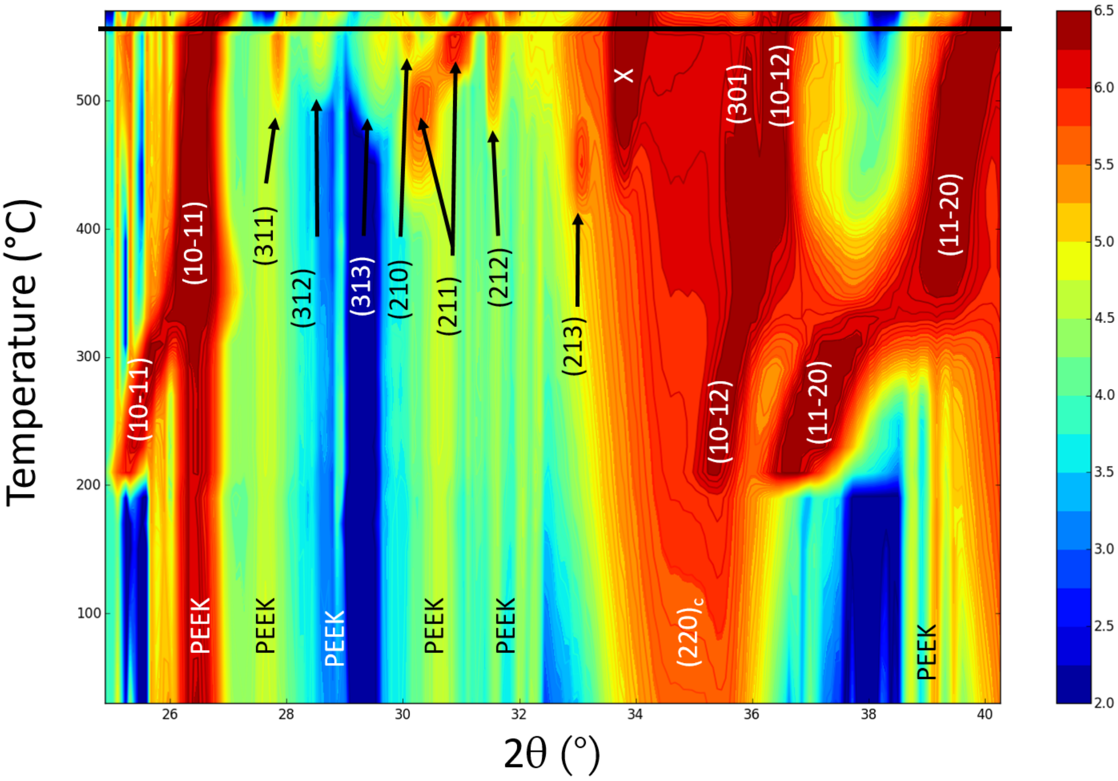

Figure 4.1 – Color map of the evolution of intensities according to 2θ angle and annealing temperature of the ramp for a Ni (20 nm)/InGaAs/InP sample. The bold black line at 550 °C denotes the measurement after slow cooling to room temperature.

Figure 4.1 represents the evolution of the integrated diffracted intensity versus the 2θ angle and versus the annealing temperature. By integrated diffracted intensity we mean an integration made on all available ϕ and χ ranges for each diffraction image. Because the dome signature is not completely subtracted (the dome is polycrystalline and variation in its intensity may change according to the azimuthal position ϕ, but also according to annealing temperature), there are weak persistent diffraction signature on several 2θ positions. We remark that from 0 °C up to 200 °C only a peak of the substrate: the (220) one and remnant signature from the PEEK[2] dome can be observed. At 210 °C, diffraction from a newly formed phase emerge at 2θ positions: 25.37°, 35.3° and at 36.65°. These peaks all belong to an hexagonal $P6_3/mmc$ intermetallic phase and, through lattice refinement, they were indexed to belong respectively to the $\{10\bar{1}1\}$, $\{10\bar{1}2\}$, $\{11\bar{2}0\}$ planes. We can take a closer look on the $(10\bar{1}1)$ peak position by doing a localized integration on only one pole of these planes. The result of this localized integration is given in Figure 4.2a and Figure 4.2b shows a 3D waterfall view of the $(10\bar{1}1)$ peak according to annealing temperature. From the formation of the intermetallic at 210 °C up to 250 °C, there is only one peak that shifts slowly towards higher higher 2θ positions. At 270 °C

---

[2] PEEK is for Polyether ether ketone which is an organic thermoplastic polymer in the polyaryletherketone (PAEK) family.

a second peak appears with weak intensity indicating the formation of a second phase. The appearance of a the second peak at 270 °C coincides with the full consumption of Ni. From 270 °C to 390 °C, the intensity of the first peak drops continuously while the intensity of the second peak increases. From 390 °C to 550 °C, only the peak corresponding to the second phase to from is measured. This result is very important compared to the ex situ measurement that were carried out in Chapter 3. Indeed, a finer temperature screening during in situ annealings shows that there is a sequential formation of phases in a classical silicide scheme: There is formation formation of a first phase rich in metal at lower annealing temperatures, then, when the reacting metal is fully consumed[3], there is a formation of a second phase which is richer in the remaining elements (In, Ga and As). While there is no powder diffraction files for $Ni_3In_{0.5}Ga_{0.5}As$ and $Ni_2In_{0.5}Ga_{0.5}As$ compounds, it is likely that these compounds correspond to respectively the first and second phase to form during the in situ annealings according to the similar lattice parameters of the well known Ni_2GaAs and Ni_2GaAs. The $Ni_2In_{0.5}Ga_{As}As$ is most probably an extension of the hexagonal binary compound NiAs as it is the case for metal-poor Ni-GaAs compounds where In and Ga atoms can be substituted with As atoms and is denoted here by $Ni_2(InGa)_{2-x}As_x$ where $1\leqslant x\leqslant 2$.

---

[3] Though nickel (1 1 1) peak should diffract at $2\theta = 35.48°$ at 10 kev, it cannot be seen on the color map due to its extremely weak intensity and overlapping with the (2 2 0) plane of the substrate. However, pole figures analyses show weak peaks corresponding to Ni (1 1 1) planes and are described in the texture analyses section.

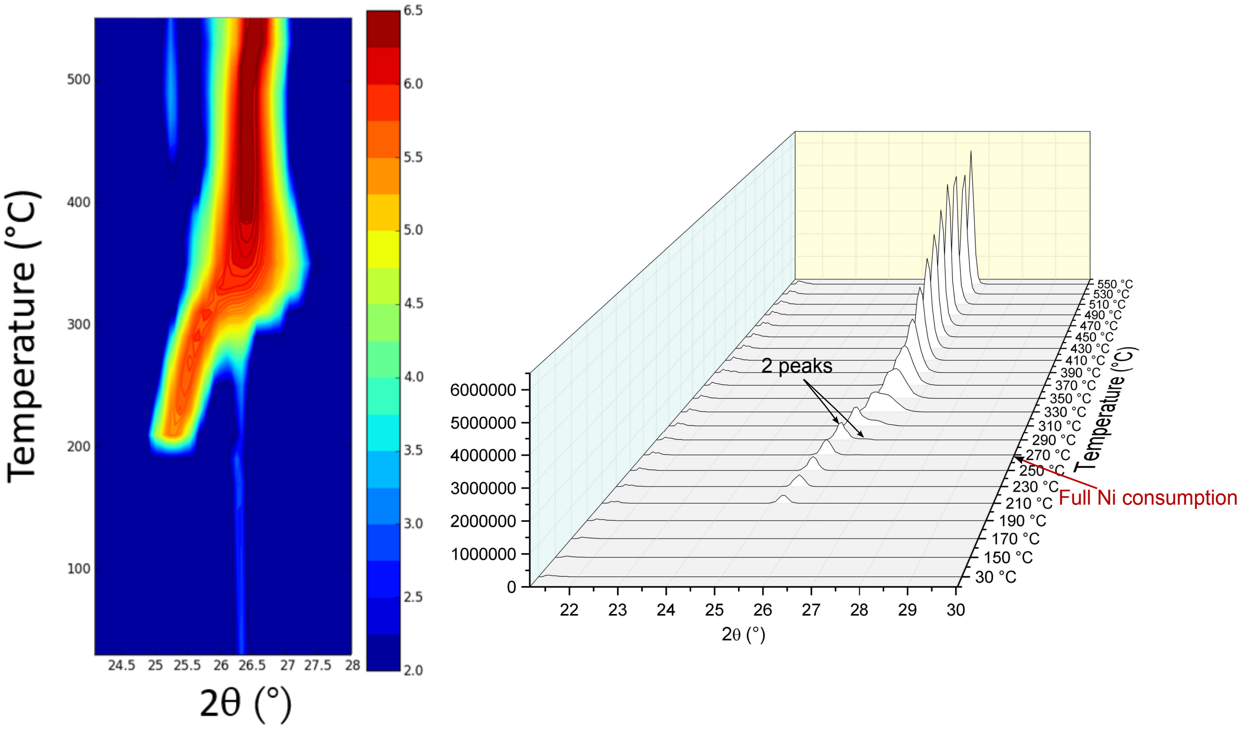

(a) (b)

Figure 4.2 – (a) Color map of the evolution of intensities according to 2θ angle and annealing temperature of the ramp for the a uniquely integrated $(10\bar{1}1)$ pole (situated at χ=30°, ϕ=90° in Figure 4.9c). (b) 3D Waterfall view of the $(10\bar{1}1)$ peak according to annealing temperature.

Moreover, integration over the $(11\bar{2}0)$ plane of the intermetallic was carried out. Figure 4.3a shows the superposition of two integrations on the $(11\bar{2}0)$ plane of the intermetallics and the (111) plane of Ni. Specific integration on different ranges of χ and ϕ were carried out for each plane and the resulting integrations were superposed to follow both the Ni consumption and the intermetallics formation. On this Figure, the peak at 35.42° shows the evolution of the (111) peak of the Nickel according to annealing temperature. From 150 °C to 210 °C the intensity of the Ni peak increases. This change is likely due to a grain growth of Ni. Indeed, there is no overlapping intensity from a nearby peak because we did a localized integration. From 210 °C up to 270 °C the intensity of the Ni peak decreases indicating the consumption of the nickel layer. Such consumption coincides with the formation of the second intermetallic phase $Ni_2In_{0.5}Ga_{0.5}As$. At 210 °C, a peak appears at 37.2° indicating the formation of a new compound at the semiconductor/metal interface. This peak corresponds to the $(11\bar{2}0)$ peak of the hexagonal intermetallic with a B8 structure. During the measurement the $(10\bar{1}1)$ and $(10\bar{1}2)$ peaks of the intermetallic were also measured (not shown here) and lattice refinement was performed in order to obtain the lattice parameters and hence, a rough idea about the so-formed phase stoichiometry. Indeed, the phase formed at 210 °C corresponds to $Ni_3In_{0.53}Ga_{0.47}As$. This first phase to form is the richest phase in metal. During the temperature range from

210 °C up to 270 °C the peak at 37.2° shifts slowly from its original position to 38° indicating the possibility of structural change or negative thermal expansion [120]. From 270 °C, the intensity of the $Ni_3In_{0.53}Ga_{0.47}As$ peak starts to decrease until complete disappearance around 330 °C.

At 2θ=39.5° and at 270 °C, we detect intensity from another plane. This peak corresponds to the $(11\bar{2}0)$ plane of an hexagonal B8 structure, indicating the formation of a second phase. Lattice refinement using several other peaks of this second phase, shows that its stoichiometry corresponds $Ni_2In_{0.53}Ga_{0.47}As$. This peaks shifts away to higher 2θ at nearly 500 °C. Lattice parameter refinement of the peak positions at this temperature show that the phase corresponds to NiAs. The appearance of the second phase corresponds with the total consumption of the metallic layer. Thus, we demonstrate that the formation of the intermetallics is done in a sequential manner passing from $Ni_3In_{0.53}Ga_{0.47}As$ to $Ni_2In_{0.53}Ga_{0.47}As$ and finally NiAs. NiGa has probably been formed when NiAs is formed but no corresponding diffraction from such compound was observed.

The fact that the formation of intermetallics is done sequentially explains the discrepancies concerning the phase composition encountered in the literature and illustrated in Chapter 1.

Figure 4.3b shows the integrated intensities of the $(11\bar{2}0)$ planes of the two phases $Ni_3In_{0.5}Ga_{0.5}As$ and $Ni_2In_{0.5}Ga_{0.5}As$ formed during the annealing and the integrated intensity of the Ni peak. On this figure, the intensity of $Ni_3In_{0.5}Ga_{0.5}As$ increases from 210 °C to 230 °C indicating the formation of and growth of the the corresponding phase. The intensity then decreases slowly from 230 °C to 290 °C and finally decreases abruptly from 290 °C until complete disappearance at 370 °C indicating the consumption of $Ni_3In_{0.5}Ga_{0.5}As$. $Ni_2In_{0.5}Ga_{0.5}As$ is formed at 270 °C and its intensity continues to increase until 350 °C. From 350 °C until 550 °C the intensity decreases slowly indicating the consumption of the phase and thus the probable formation of other phases.

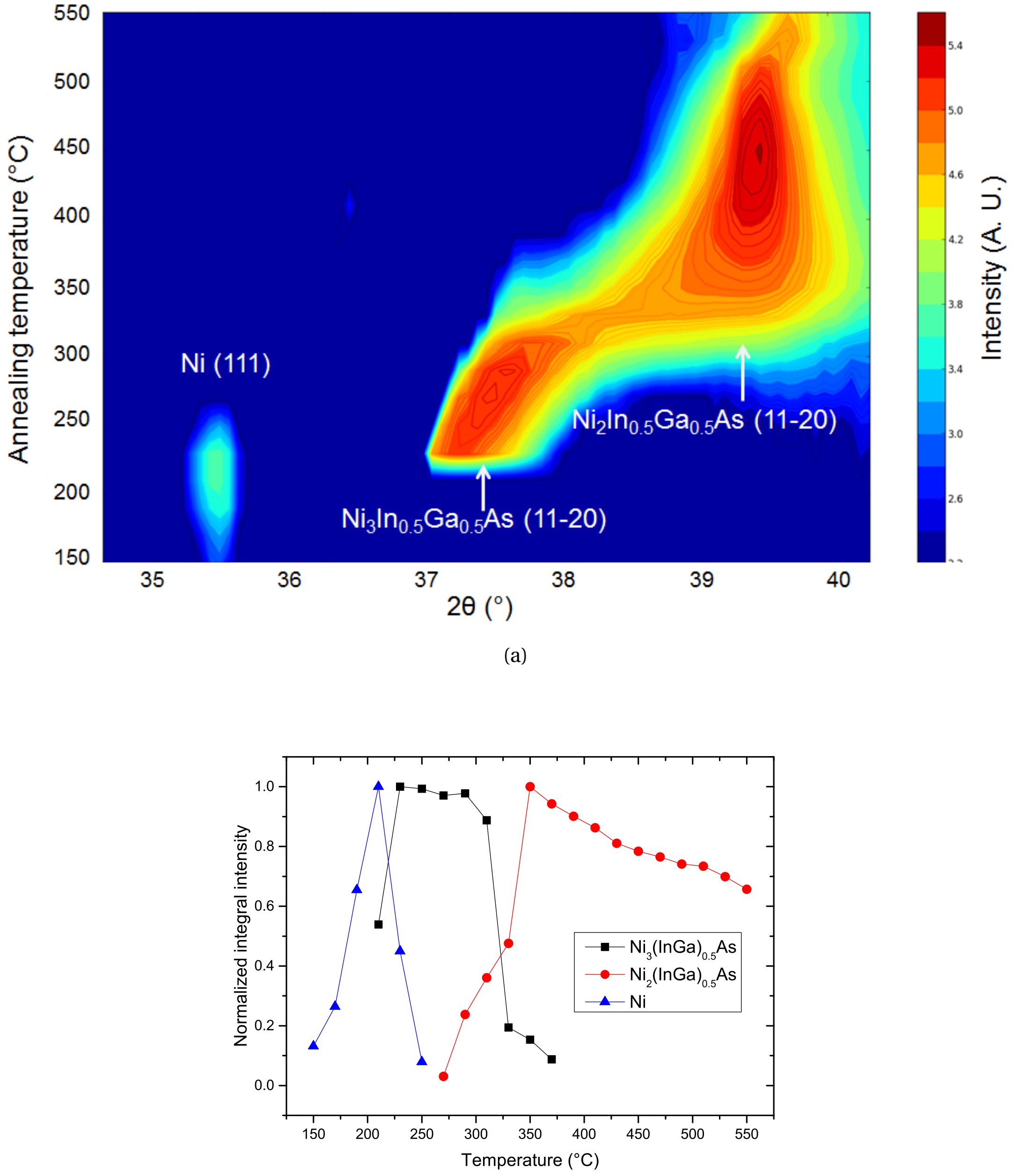

(a)

(b)

Figure 4.3 – (a) Color map of the evolution of intensities according to 2θ angle and annealing temperature of the ramp for the $(11\bar{2}0)$ plane of the intermetallic and the (111) plane of Ni. The figure is the result of superposition of two different integration over two different domains in χ and ϕ. (b) Normalized integral intensities of the two phases $Ni_3In_{0.5}Ga_{As}As$ and $Ni_2In_{0.5}Ga_{As}As$ formed during the annealing and normalized integral intensity evolution of the (111) plane of Ni.

To further facilitate the reading of peak positions, they were plotted in Figure 4.4a, 4.4b and 4.4c for respectively the $\{10\bar{1}1\}$, $\{10\bar{1}2\}$, $\{11\bar{2}0\}$ planes. Moreover, to investigate further the formation of the intermetallics, we have plotted the evolution of refined lattice parameters a and c according to annealing temperature for the two forming phases in respectively Figures 4.5a and 4.5b. The evolution of axial ratio and the volume of the unit lattice are shown in Figure 4.5c and 4.5d respectively.

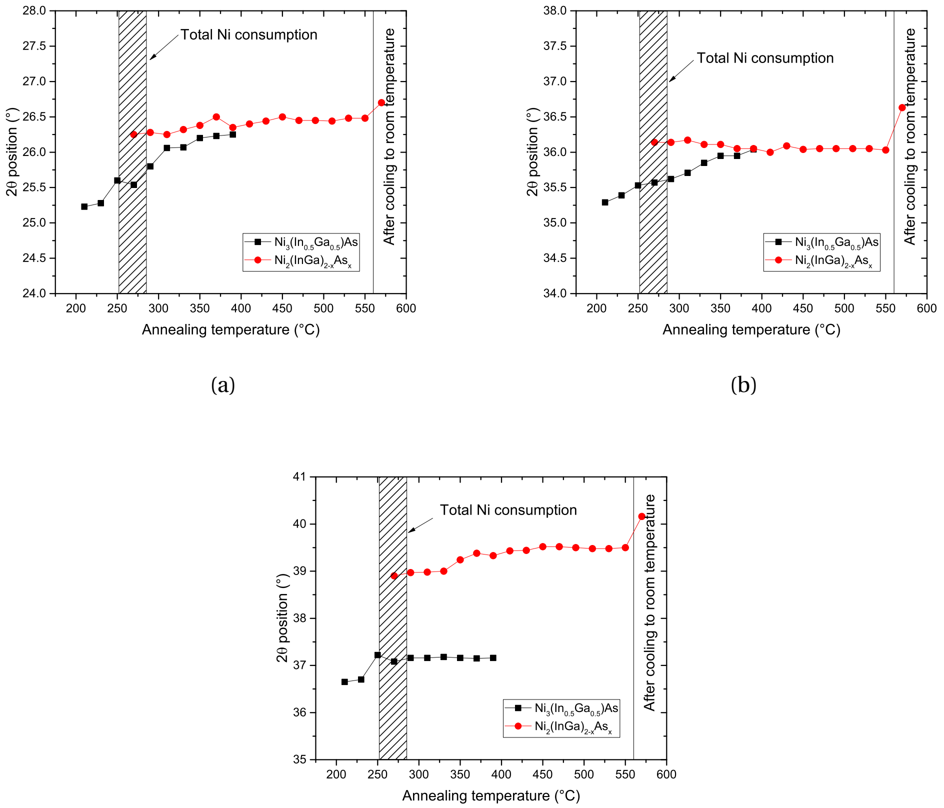

(a)

(b)

(c)

Figure 4.4 – Peak position according to the ramp annealing temperature of the (a) $(10\bar{1}1)$, (b) $(10\bar{1}2)$ and (c) $(11\bar{2}0)$ planes.The used sample is Ni(20 nm)/InGaAs/InP.

From their appearance and up to 390 °C, the peaks corresponding to the first phase to form slowly shift away from their positions to higher 2θ values by respectively $\Delta\theta$ values of 0.98°, 0.75° and 0.51°. These $\Delta\theta$ values are significant and indicate that there were changes on the lattice parameters of the hexagonal structure. Indeed, on Figures 4.5a and 4.5b, we see that from 210 °C to 390 °C, lattice parameter a of the first phase to form drops from 3.94 Å to 3.88 Å and lattice parameter c drops from 5.1 Å to 5.03 Å. These variations are important and can be related to stoichiometric variations on the hexagonal lattice. However, as seen in Chapter 1, phases in the Ni-Ga-As system present generally a rather broad range of homogeneity. Thus, even if a relatively important shift occurs, one can consider up to certain limits that they occur within the same phase. In other words, the intermetallic phase can present a rather large domain of homogeneity in which it conserves its

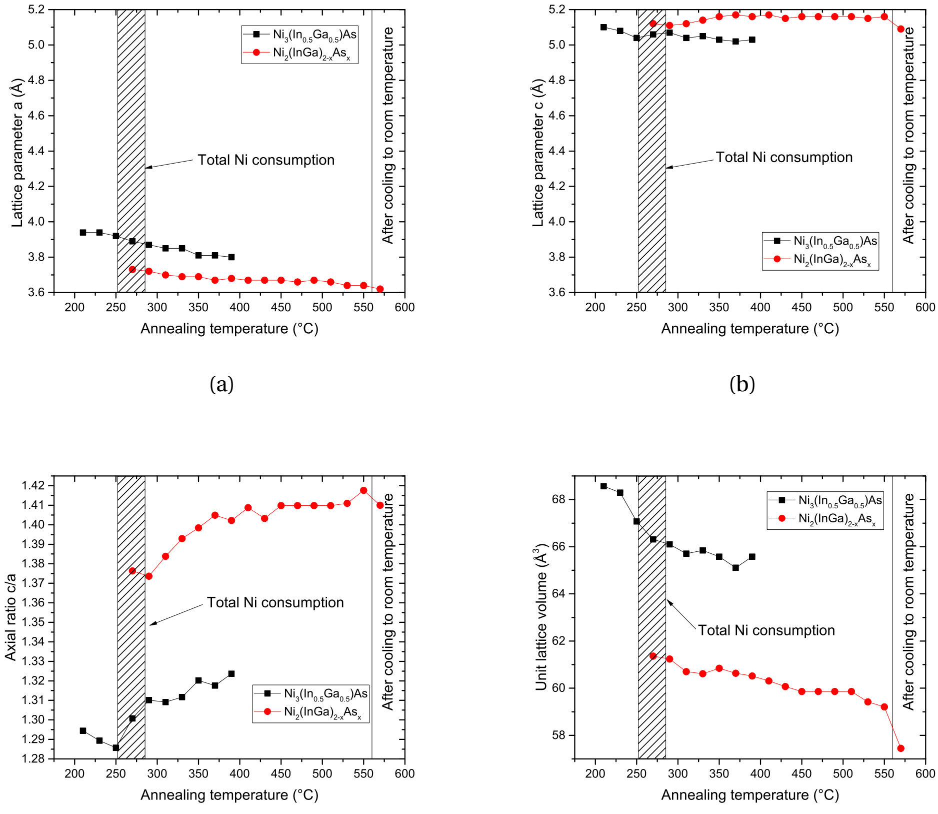

(a) (b)

(c) (d)

Figure 4.5 – Calculated parameters of the intermetallic hexagonal lattice (a) a lattice parameter, (b) c lattice parameter (c) c/a axial ratio and (d) volume of the hexagonal lattice. The used sample is Ni(20 nm)/InGaAs/InP.

The second phase appears at 270 °C and coincides with the total consumption of Ni. The formation of a whole new phase with a change of symmetry is excluded by pole figure analysis (see the texture subsection). Indeed, we observe the same symmetry as for the phase formed at 210 °C. From 270 °C to 550 °C, lattice parameter a shrinks from 3.72 Å to 3.64 Å and c increases from 5.12 Å to 5.16 Å. The volume of the unit lattice drops also from 61 to 59 Å^3. Thus, the second phase to form $Ni_2(InGa)_{2-x}As_x$ presents considerable changes on its stoichiometry compared to the first phase to form $Ni_3In_{0.5}Ga_{As}As$.

To understand the variation of lattice parameters in the hexagonal Ni-InGaAs phases, one should consider the NiAs B8[4] structure. The $Ni_3In_{0.5}Ga_{0.5}As$ is represented in the B8 structure

---

[4] B8 is the Strukturbericht nomenclature of the NiAs phase. Strukturbericht is German for "Structure Report"

in Figure 4.6 where Ni occupies randomly half of the metallic sites, As occupies a metalloid site, and In and Ga occupy each half of the other metalloid site. The first intermetallic phase to form corresponds to a $Ni_3In_{0.5}Ga_{0.5}As$ stoichiometry (as an analogy with the results of Guerin and Guivarc'h [23, 67] described in the first chapter). If Ni is rejected from the metallic sub-lattice, thus passing from $Ni_3In_{0.5}Ga_{0.5}As$ to $Ni_2In_{0.5}Ga_{0.5}As$, there is an increase of vacancy concentration. This causes the unit cell to shrink in the *a* direction.

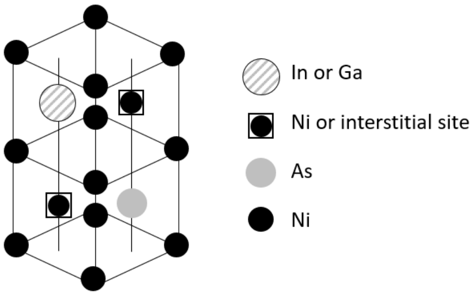

Figure 4.6 – Illustration of the unit cell of $Ni_3In_{0.5}Ga_{0.5}As$.

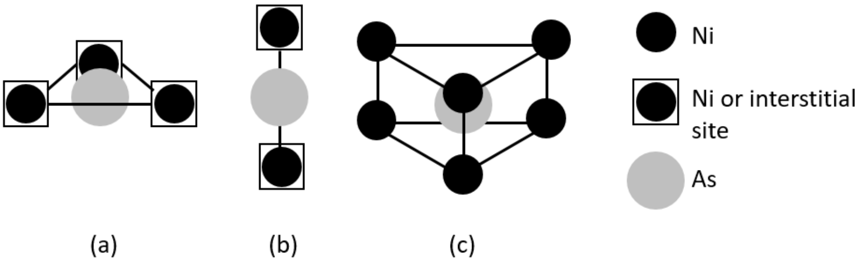

(a) (b) (c)

Figure 4.7 – Nearest neighbor configuration for arsenic in the $Ni_3In_{0.5}Ga_{0.5}As$ lattice [122]:
(a) One and one half nearest neighbors (nickel).
(b) One second-nearest neighbor (nickel).
(c) Six third-nearest neighbors (nickel).

However, the *c* parameter increases when the second phase forms (see Figure 4.5b). To understand this increase, one should consider the As atom position in a $Ni_3In_{0.5}Ga_{0.5}As$ unit lattice. If the hexagonal lattice had any ionic character, the As atoms would act like anions, and would try to place themselves in a position to maximize their distances from each other. This is achieved in the $Ni_3In_{0.5}Ga_{0.5}As$ stoichiometry where the first, second and third neighbors of arsenic are not arsenic atoms (see Figure 4.7). However, in the absence of Ni atoms on the metallic sub-lattice, the arsenic atom finds itself surrounded by arsenic atom as a second neighbor. This is the case for the second phase to form $Ni_2(InGa)_{2-x}As_x$ where the repulsion between As atoms tends to increase the value of the *c* parameter. Thus, there is an increase of *c* parameter value when Ni is rejected from the metallic sub-lattice.

The volume of the second phase $Ni_2(InGa)_{2-x}As_x$ continues to decrease from its formation

---

and is a series of publications aiming to chemically characterize crystalline structures [121].

at 270 °C until 550 °C (see Figure 4.5d). An In-Ga/As substitution on the metalloid sub-lattice causes the unit cell to shrink even more in the *a* direction. To further understand the relationship between lattice parameters/volume changes and the In-Ga/As substitution, one can consider the covalent radii of these elements which are respectively for In, Ga, and As 144, 126 and 119 pm. Arsenic exhibits the smallest covalent radii and thus a substitution of In and Ga with As would cause the volume to shrink and lattice parameter *a* to decrease. At 550 °C, the stoichiometry of the $Ni_2(InGa)_{2-x}As_x$ phase corresponds to Ni_2As_2 (or simply NiAs), which is the most stable phase in the Ni-Ga-As phase diagram. There is not a proper phase transformation between the least As-rich and the most As-rich stoichiometries of the second phase to form (respectively $Ni_2(In_{0.5}Ga_{0.5})As$ and NiAs), but rather the formation of a ternary[5] extension of NiAs at first, then the development to the binary phase NiAs. Indeed, Zheng et al. [65] and Ingerly et al. [66] confirm the existence of a binary hexagonal phase NiAs with a large ternary extension in the Ni-Ga-As system. This extension is caused by the substitution of Ga by As atoms inside the metalloid sub-lattice.

To conclude, there is evidence of sequential phase formation of intermetallics when Ni is put into contact with $In_{0.5}Ga_{0.5}As$. The first phase to form is the richest phase in Ni in agreement with the Cu_3Au rule [118]. The second phase to form is NiAs and its ternary extension. The phase sequence can be written as the following:

$Ni_3In_{0.5}Ga_{0.5}As \mapsto Ni_2(InGa)_{2-x}As_x$ (with $1 \leqslant x \leqslant 2$).

We were not able to correctly index the peak marked by X that appear at 490 °C at 34° (Figure 4.1), but from pole figure analysis, we believe that it belongs to a twinned In-rich phase ((2 2 0) planes). Indeed, the corresponding pole figure shows four extra poles at $\chi = 20°$ on top of the (2 2 0) poles at $\chi = 45°$. From the position of the peak, and using Vegard's law (for the well-characterized GaAs and InAs compound), we estimate that the Indium concentration of such phase should be close to $In_{0.95}Ga_{0.05}As$ making it very close to InAs zinc-blende compound. The stoichiometry calculation of this III-V compound did not include any strain effect which can affect the In/Ga ratio.

4.1.1.2 Texture of the intermetallic

In this section, we will describe the texture of the so-formed intermetallics according to annealing temperature along with the evolution of the (1 1 1) plane of the deposited Ni.

Figure 4.8 shows several pole figures corresponding to the (1 1 1) plane of the deposited Ni. The (1 1 1) poles of Ni are situated at $\chi = 35°$ just under the four poles of the {2 2 0} planes of the substrate. This position corresponds the following orientation: Ni (2 2 0) || InGaAs (0 0 1). The poles corresponding to Ni can be seen up to 230 °C. Starting from 250 °C, no Ni peaks are

---

[5] Even if there are 4 elements that are involved in the reaction, In and Ga are considered as fully miscible and Ni-InGaAs compounds are considered as ternary compounds like the Ni-GaAs ones.

detected. However, Ni could have reached undetectable thickness at 250 °C by X-ray diffraction. The disappearance of Ni is coherent with the appearance of the second intermetallic phase at 270 °C.

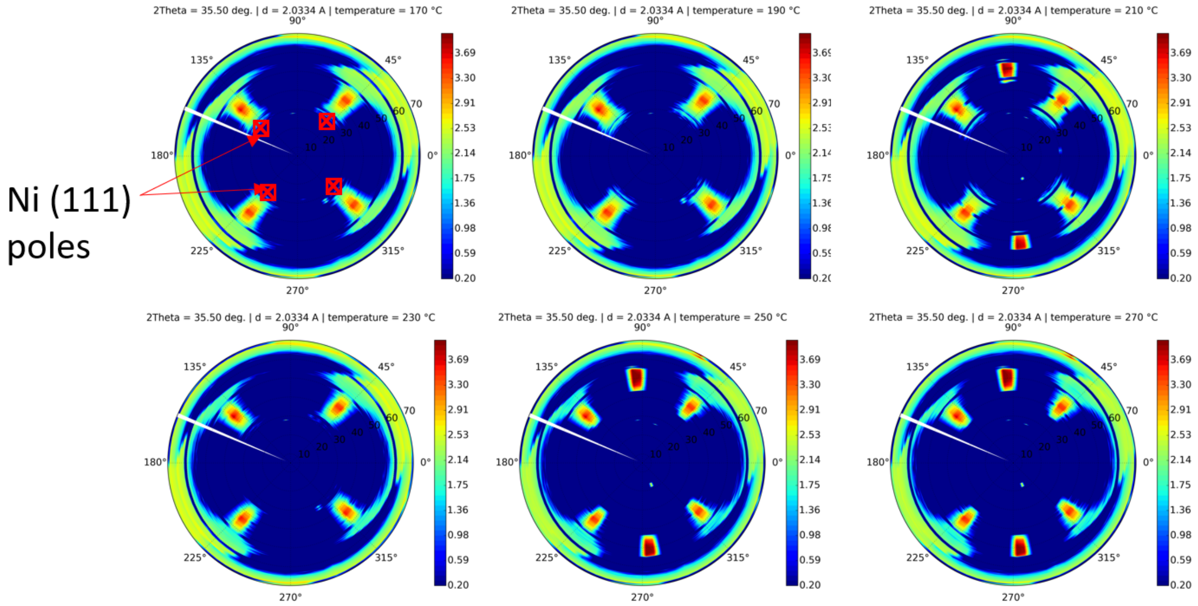

Figure 4.8 – Pole figure corresponding to the deposited Ni (111) plane position at several annealing temperatures from 170 to 270 °C. Ni poles are marked on the first pole figure (top-left). The remaining poles correspond to either the (220) planes of the substrate or to the intermetallic $\{10\bar{1}2\}$ peaks.

Figures 4.9, 4.10 and 4.11 show the pole figures of respectively the $\{10\bar{1}1\}$, $\{10\bar{1}2\}$ and $\{11\bar{2}0\}$ planes of the intermetallic at different steps of the ramp annealing process (stereographic projections of the corresponding poles are given in Appendix B). Pole figure analyses show that the intermetallics take exclusively a group A orientation (as defined in Chapter 3) all over the annealings.

No occurrence of group B orientation was measured even after a 550 °C annealing. Indeed, contrary to rapid thermal annealing with fast ramps, ramp annealing consists of different annealing steps with temperatures close to each other and with large annealing time (around 20 minutes for each ramp). This relatively slow annealing in comparison to the 60 s rapid thermal annealing allows the intermetallic to form in its most thermodynamically favorable orientation:

- either there is the occurrence of a recrystallization. Indeed RTA and ramp annealing can allow the germination of both groups of texture, however in the case of RTA both groups remain while a 20 minutes ramp gives time to the most stable texture to overwhelm the less stable one.

- or there is limited germination in the case of ramp annealing: a slow annealing limits the germination of the less stable orientation because the free energy of reaction is too low in comparison with the surface energy.

We also note that, like for ex situ annealing, a second azimuthal variant is absent. The InP substrates used for in situ annealings along with the InGaAs deposited layer are the same as the ones used for ex situ annealings and the possible explanation for the missing azimuthal variant given in Chapter 3 remain also valid for ramp annealings.

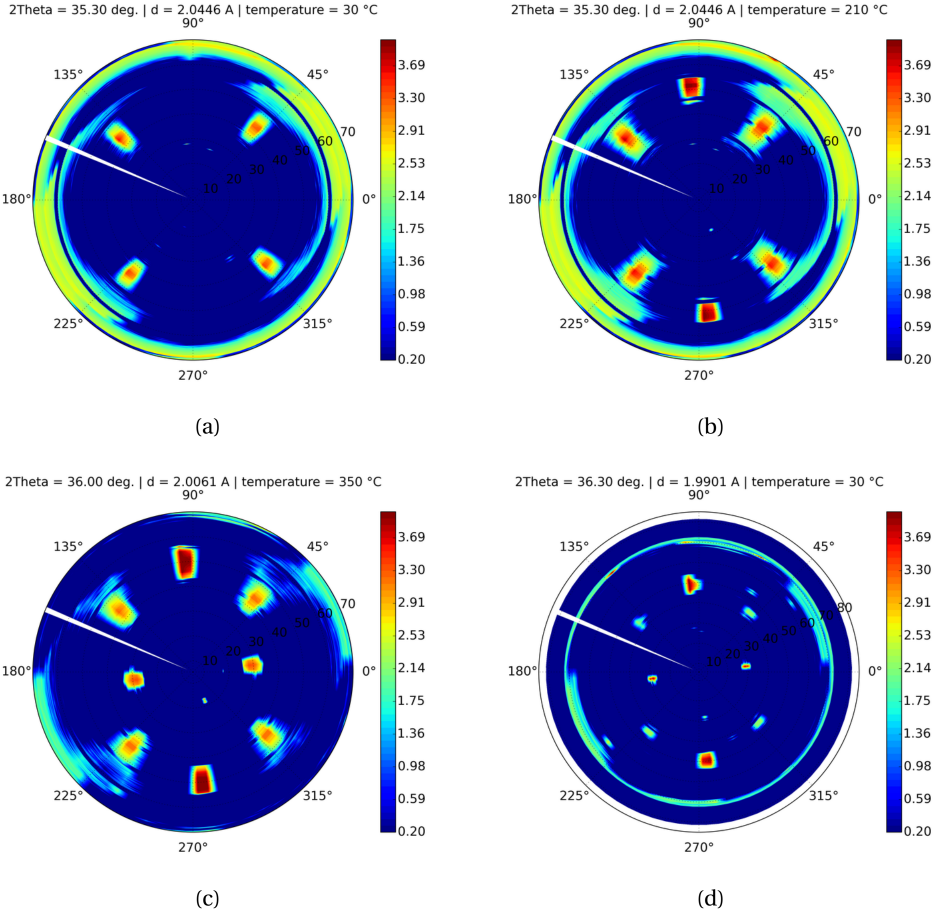

(a) (b) (c) (d)

Figure 4.10 – Pole figures of the $\{10\bar{1}2\}$ planes of the hexagonal lattice, measured at 10 keV at different ramp temperatures (a) as-deposited (no intermetallic is formed yet), (b) at 250 °C, (c) at 350 °C and (d) at 30 °C after slow cooling to room temperature. The used sample is Ni (20 nm)/InGaAs/InP.

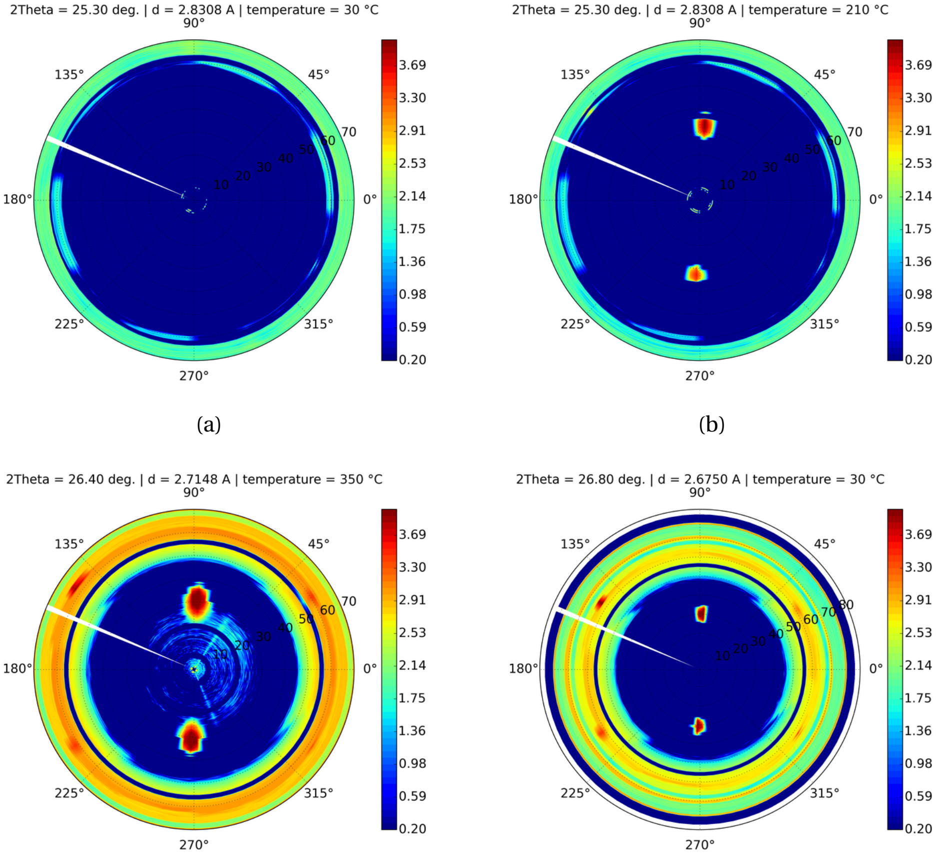

(a) (b)

(c) (d)

Figure 4.9 – Pole figures of the $\{1\,0\,\bar{1}\,1\}$ planes of the hexagonal lattice, measured at 10 keV at different ramp temperatures (a) as-deposited (no intermetallic is formed yet), (b) at 250 °C, (c) at 350 °C and (d) at 30 °C after slow cooling to room temperature. The used sample is Ni (20 nm)/InGaAs/InP.

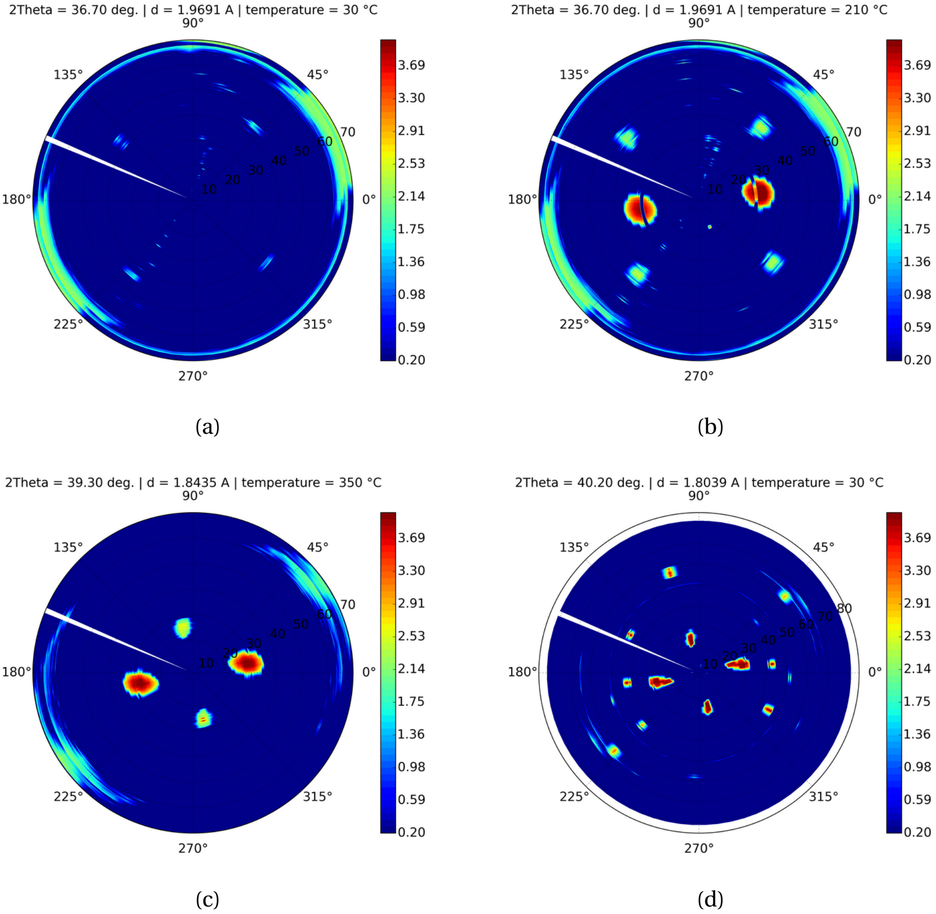

Figure 4.11 – Pole figures of the $\{11\bar{2}0\}$ planes of the hexagonal lattice, measured at 10 keV at different ramp temperatures (a) as-deposited (no intermetallic is formed yet), (b) at 250 °C, (c) at 350 °C and (d) at 30 °C after slow cooling to room temperature. The used sample is Ni (20 nm)/InGaAs/InP.

Figure 4.12 shows the evolution of the lattice mismatch between the intermetallic and the substrate according to annealing temperature. The lattice mismatch was calculated using the same axiotaxial considerations described in Chapter 3 (i.e. for group A, every set of five $(10\bar{1}0)_h$ planes should meet every set of four $(110)_c$ planes). The linear thermal expansion coefficient of the InGaAs substrate is 5.66 10^{-6} K^{-1}. Thus, the lattice parameter of the substrate will at most (at 550 °C) be changed by about 0.29 % which is not significant. Thus, we did not include thermal expansion correction on the substrate lattice parameter when calculating the mismatch between the intermetallic and the substrate.

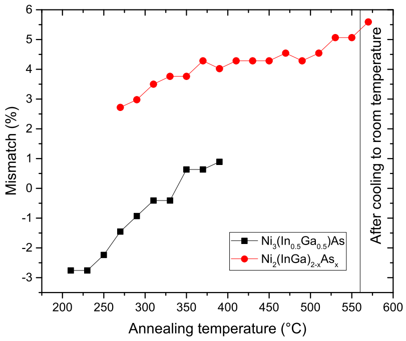

Figure 4.12 – Calculated mismatch between the intermetallics and the substrate considering an axiotaxial alignment for Group A domains.

Figure 4.12 shows the calculated the lattice mismatch between the two formed phases and the substrate according to annealing temperature (using the same axiotaxial considerations as in Chapter 3). The lattice mismatch of the $Ni_3In_{0.5}Ga_{0.5}As$ phase yields mainly negative values until 330 °C while the lattice mismatch of the $Ni_2(InGa)_{2-x}As_x$ phase regarding the substrate is always positive. No conclusions can be made about the stress development or its sign using the mismatch values. Indeed, it was demonstrated that stress development for metal-silicon systems is a consequence of volume change at the growing interface [123–126]. Thus the knowledge of volume change is necessary to characterize the stress evolution. However, it would have been interesting to explore the contribution of the mismatch between the axiotaxially aligned planes of the semiconductor and the intermetallic in the development of the stress during the reaction.

4.1.1.3 Superstructure occurrence

Just like the ex situ annealed samples, the in situ annealed samples have formed a superstructure. Two distinct superstructures were resolved, one with a $3a \times 4c$ arrangement and the other with a $2a \times 2c$ arrangement. These two types of ordering are different than the ordering occurring on the intermetallic with ex situ RTP annealings. It is difficult to predict the ordering and arrangement on such type of lattices, and the ordering difference between ex situ and in situ samples can be due to the different annealing ramp and/or annealing time. The identification of superstructure peaks was done using lattice refinement but also manual comparison with corresponding pole figures, assuming that the superstructure has got the same symmetry as the parent unit lattice. Figure 4.13 shows different pole figures of different superstructure planes measured at the annealing temperature of 550 °C. The 2 ordering $3a \times 4c$ and $2a \times 2c$ can happen simultaneously in one domain as well separately in different domains and the ordering result probably from an ordering on the As atoms in the metalloid sub-lattice [23]. Some superstructures reflections may appear simultaneously, while others may appear at different temperature. Indeed, the quality of ordering, which evolves during the annealing, will influence the structure factor of the coherent scattering from the new periodic arrangement in the intermetallic the structure factor depends on the order of reflection, and thus some reflections are more intense than some others and can appear even at poor ordering.

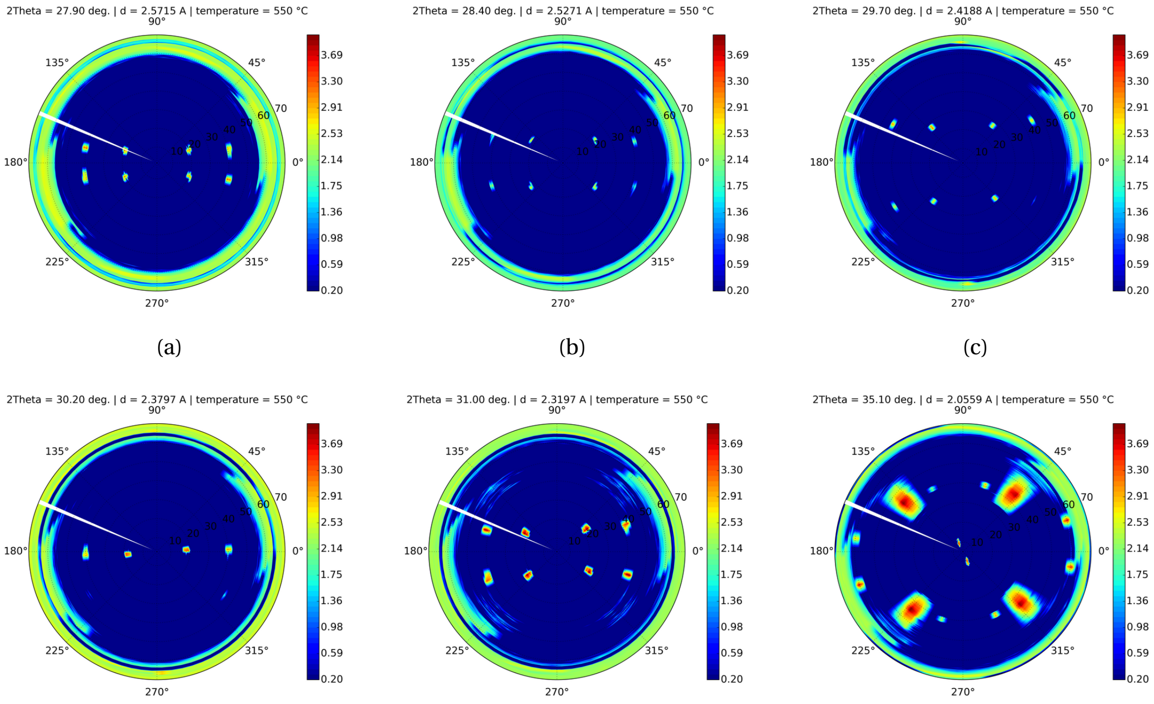
2Theta = 27.90 deg. | d = 2.5715 A | temperature = 550 °C

2Theta = 28.40 deg. | d = 2.5271 A | temperature = 550 °C

2Theta = 29.70 deg. | d = 2.4188 A | temperature = 550 °C

2Theta = 30.20 deg. | d = 2.3797 A | temperature = 550 °C

2Theta = 31.00 deg. | d = 2.3197 A | temperature = 550 °C

2Theta = 35.10 deg. | d = 2.0559 A | temperature = 550 °C

(a) (b) (c)

(d) (e) (f)

Figure 4.13 – Pole figures of several planes of the hexagonal superstructures at the ramp temperature of 550 °C. First the $3a\times4c$ superstructure planes: (a) {3 1 1}, (b) {3 1 2} and (c) {3 1 3}, Second the $2a\times2c$ superstructure planes: (d) {2 1 0}, (e) {2 1 1} and (f) {3 0 1}. The used sample is Ni(20 nm)/InGaAs/InP and corresponding stereographic projections are given in Appendix B. The intensities on the rim of the pole figure correspond to intensities from the annealing dome.

4.1.2 The Ni(7 nm)/InGaAs/InP system

4.1.2.1 Formation of the intermetallic

Studying the formation of intermetallics through a solid-state reaction between Ni and InGaAs at 20 nm of Ni may be relevant for photonic applications. Moreover, such thickness of deposited metal is also relevant in order to have sufficient diffracting volume to study the intermetallic. While most of the studies described in this manuscript were carried out with a deposited metal thickness of 20 nm, this thickness is not necessarily relevant for sub-10 nm MOSFETs. Thus, we studied the effect of thickness on the formation of the intermetallic by depositing 7 nm of Ni on InGaAs on InP instead of 20 nm. The measuring method during ramp annealing is similar to the ones described in the first two sections. Intensity data was integrated along ϕ and χ and plotted against the Bragg angle 2θ and the ramp annealing temperature in Figure 4.14.

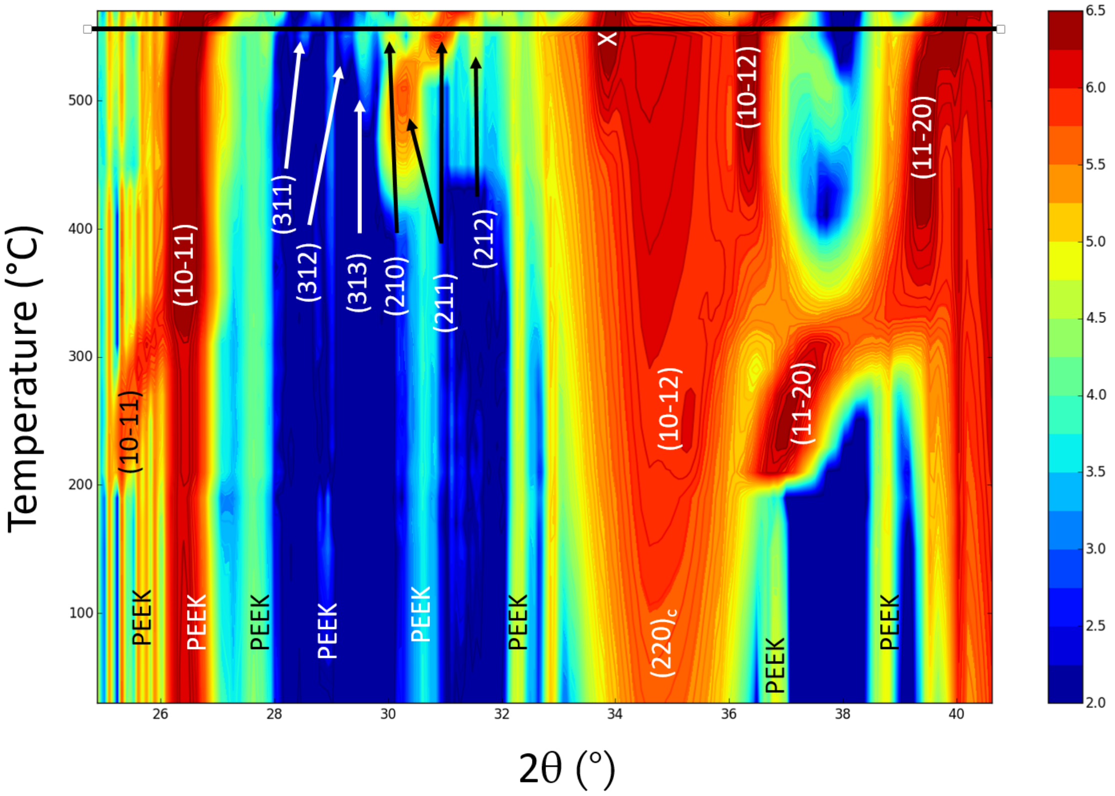

Figure 4.14 – Color map of the evolution of intensities according to 2θ angle and annealing temperature of the ramp for a Ni (7 nm)/InGaAs/InP sample. The bold black line at 550 °C denotes the measurement after slow cooling to room temperature. Sample used is Ni(7 nm)/InGaAs/InP.

Figure 4.14 is very similar to the one with 20 nm of Ni (Figure 4.1). Indeed, the temperature of formation of the intermetallic is similar to the sample with 20 nm of deposited Ni (at 210 °C). Moreover, we observe the formation of two distinct phases corresponding to respectively to $Ni_3In_{0.5}Ga_{As}As$ and $Ni_2(InGa)_{2-x}As_x$ (with $1 \leqslant x \leqslant 2$). To facilitate the peak position reading, the peak positions of the $(10\bar{1}1)$, $(10\bar{1}2)$ and $(11\bar{2}0)$ planes are plotted in respectively Figure 4.15a, 4.15b and 4.15c. Indeed from these figures we also remark the same evolution of peaks as in the case of 20 nm. The peaks corresponding to the $(10\bar{1}2)$ planes have weak diffraction spots and do not appear between 300 °C and 410 °C, but were detected through pole figures that will be described in the following paragraph.

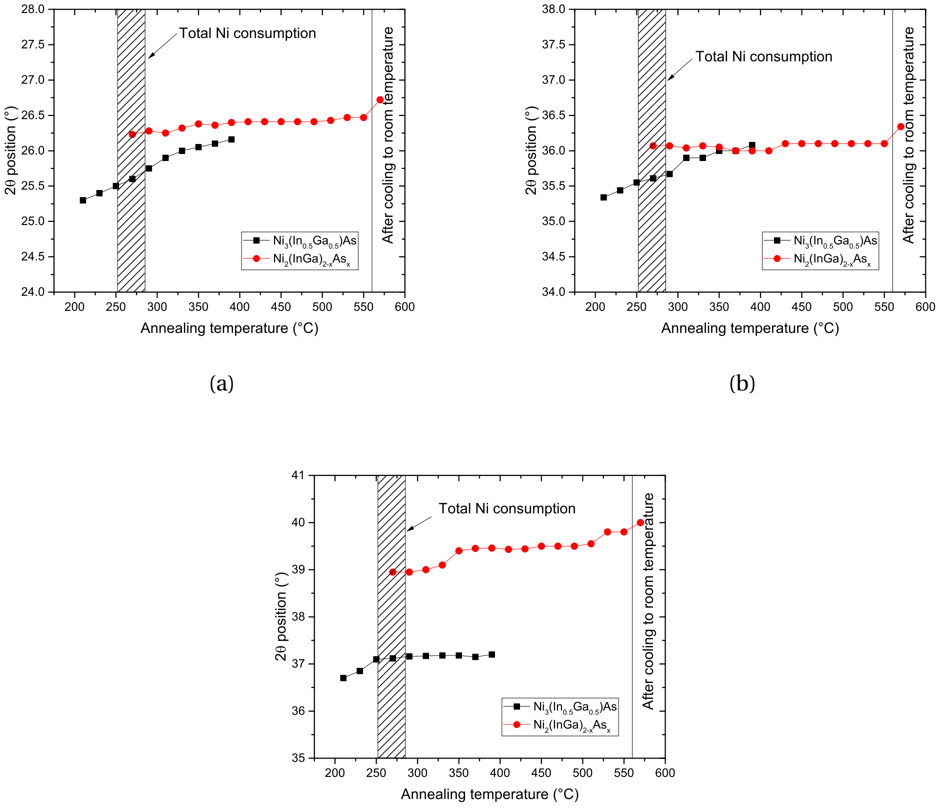

(a)

(b)

(c)

Figure 4.15 – Peak position according to the ramp annealing temperature of the (a) $(10\bar{1}1)$, (b) $(10\bar{1}2)$ and (c) $(11\bar{2}0)$ planes. Sample used is Ni(7 nm)/InGaAs/InP.

We refined the lattice parameters of the intermetalic using the peak positions of the $(10\bar{1}1)$, $(10\bar{1}2)$ and $(11\bar{2}0)$ planes. Figures 4.16a, 4.16b, 4.16c and 4.16d show respectively the evolution of lattice parameter a, c, axial ratio c/a and unit lattice volume according to annealing temperature. Analyzing these figures show that there are no substantial changes occurring when switching from 20 nm to 7 nm of Ni. Indeed structural parameters are nearly the same as in the case Ni 20 nm and no significant change is noticeable. Thus, the same conclusions on the formation of the 20 nm-intermetallic can be transposed in the case of Ni 7 nm: there is a sequential formation of intermetallic phases. A phase rich in Ni at 210 °C which disappears at 390 °C and a phase less rich in Ni formed at 270 °C after total Ni consumption which lattice parameters continue to evolve until 550 °C. This second phase corresponds to the NiAs phase and its ternary extension. Volume trend is the corollary of mainly a variation and follows the same trend as in the case of 20 nm of deposited Ni.

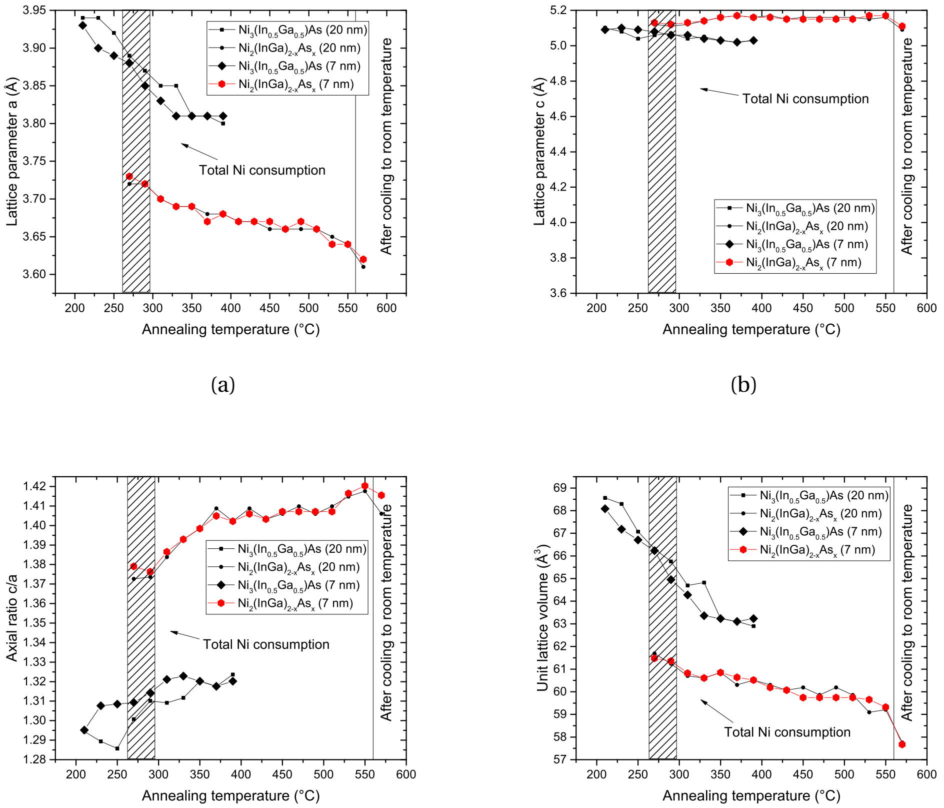

(a)

(b)

(c)

(d)

Figure 4.16 – Calculated parameters of the intermetallic hexagonal lattice (a) a lattice parameter, (b) c lattice parameter (c) c/a axial ratio and (d) volume of the hexagonal lattice. Sample used is Ni(7 nm)/InGaAs/InP.

4.1.2.2 Texture of the intermetallic

As we can see in the different pole figures at different annealing temperatures of planes $(10\bar{1}1)$, $(10\bar{1}2)$ and $(11\bar{2}0)$ in respectively Figures 4.17, 4.18 and 4.19, there is no change in the texture of Ni(7 nm)/InGaAs in respect of the texture of Ni(20 nm)/InGaAs: only group A is formed. One visual difference is that pole figures are rotated by 90° in the ϕ direction. This is simply due to the sample positioning on the plate at the moment of x-ray measurement. Even if the $(10\bar{1}2)$ is poorly visible in Figure 4.14 between 300 °C and 410 °C, we can clearly spot the diffraction poles corresponding to these planes near the cubic (220) planes (see Figure 4.18).

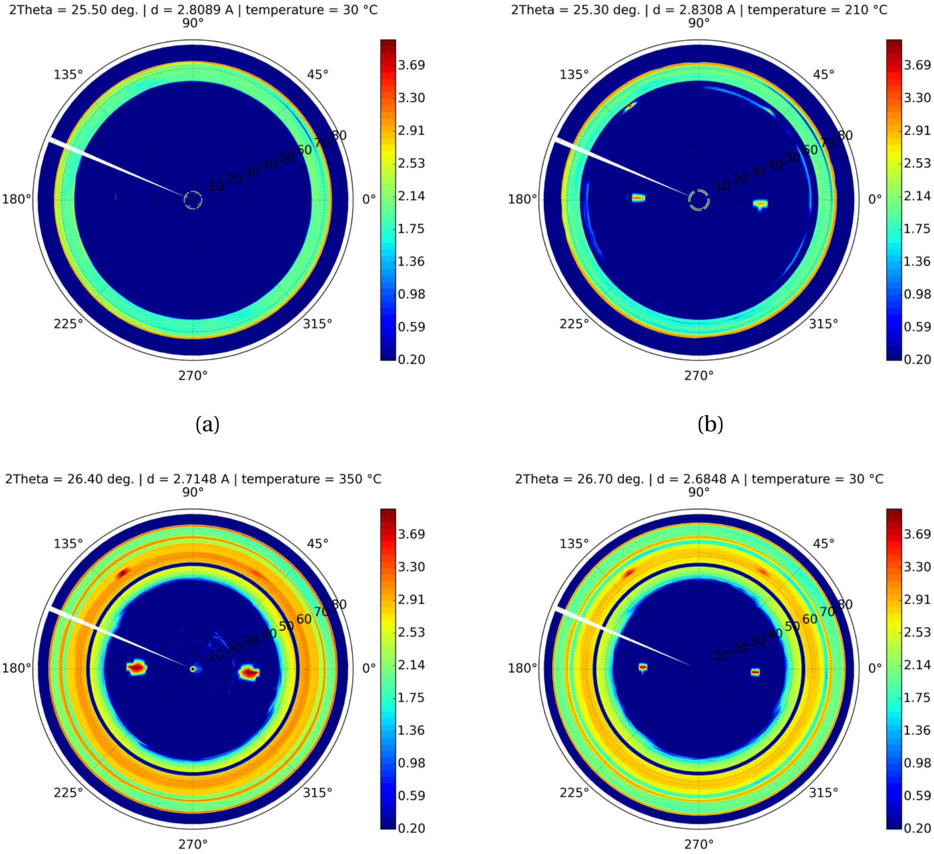

(a) (b)

(c) (d)

Figure 4.17 – Pole figures of the $\{10\bar{1}1\}$ planes of the hexagonal lattice, measured at 10 keV at different ramp temperature (a) as-deposited (no intermetallic is formed yet), (b) at 250 °C, (c) at 350 °C and (d) at 30 °C after slow cooling to room temperature. The used sample is Ni(7 nm)/InGaAs/InP.

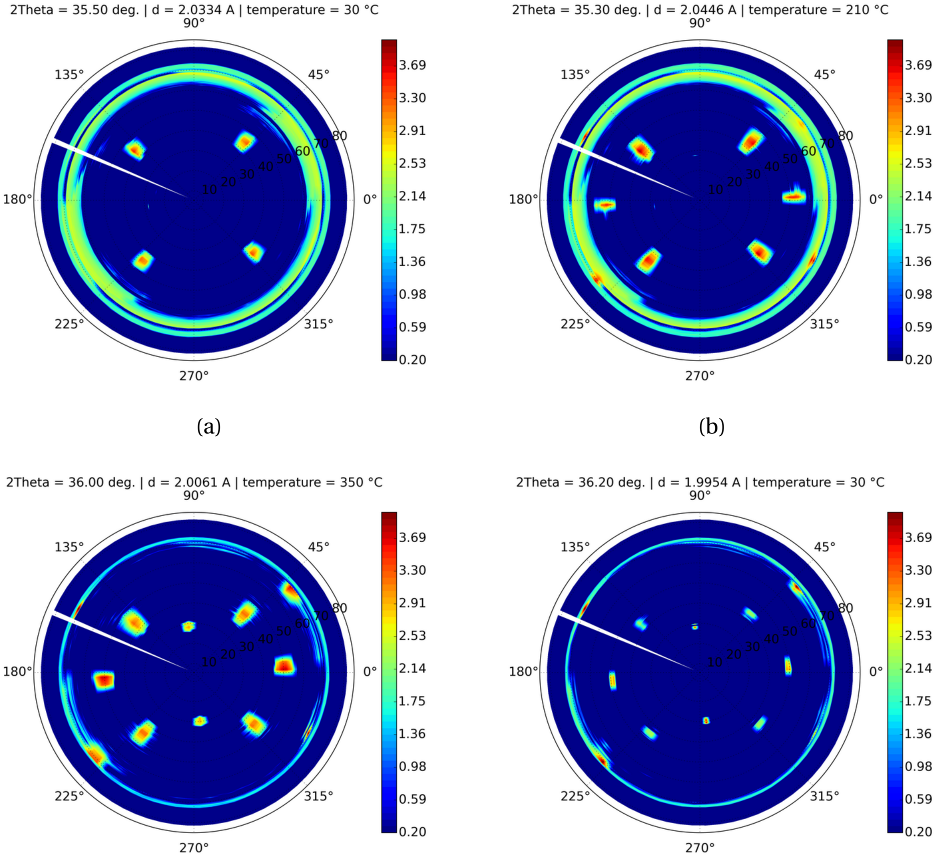

(a) (b) (c) (d)

Figure 4.18 – Pole figures of the $\{10\bar{1}2\}$ planes of the hexagonal lattice, measured at 10 keV at different ramp temperature (a) as-deposited (no intermetallic is formed yet), (b) at 250 °C, (c) at 350 °C and (d) at 30 °C after slow cooling to room temperature. The used sample is Ni(7 nm)/InGaAs/InP.

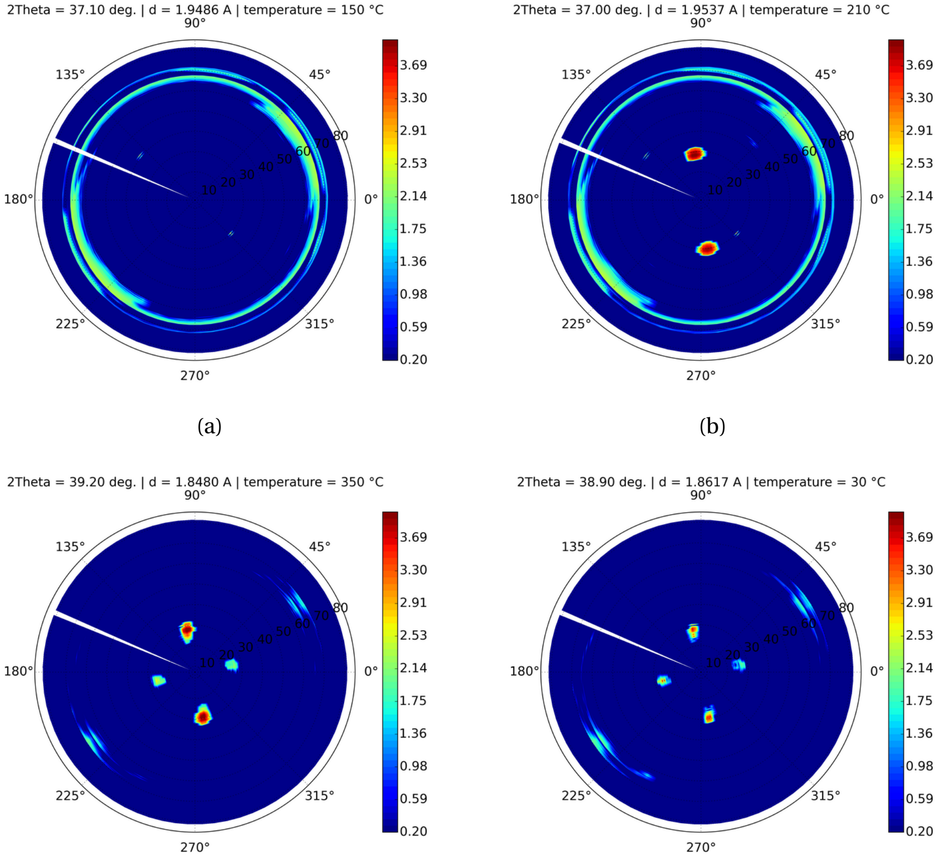

(a) (b) (c) (d)

Figure 4.19 – Pole figures of the $\{11\overline{2}0\}$ planes of the hexagonal lattice, measured at 10 keV at different ramp temperature (a) as-deposited (no intermetallic is formed yet), (b) at 250 °C, (c) at 350 °C and (d) at 30 °C after slow cooling to room temperature. The used sample is Ni(7 nm)/InGaAs/InP.

Lattice mismatch was calculated according to axiotaxial alignment in the same manner described in the sections above, and were plotted according to annealing temperature in Figure 4.20.

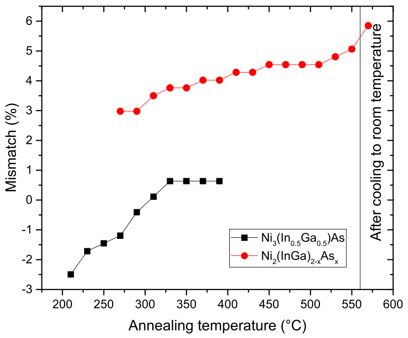

Figure 4.20 – Calculated mismatch between the intermetallic and the substrate considering an axiotaxial alignment for Group A domains. The used sample is Ni(7 nm)/InGaAs/InP.

4.1.2.3 Superstructures occurrence

The occurrence of superstructures was measured through extra X-ray reflections denoted in Figure 4.14. These superstructures result probably from an ordering on the As or Ni atoms in the metalloid sub-lattice [23]. Two ways of ordering were refined according to the position of extra-reflection which are the same as for Ni 20 nm intermetallic: $3a\times4c$ arrangement and $2a\times2c$ arrangement. The two ordering can happen simultaneously in one domain as well separately in different domains. Extra-reflections appear nearly at the same annealing temperature in both 20 nm and 7 nm cases.

4.1.3 Discussion: On the effect of the film thickness

Passing from 20 nm to 7 nm of deposited Ni did not have significant changes on the structural parameters. Lattice parameters evolution is the same for both thicknesses and so the phase evolution process. Texture is also the same and the calculated mismatch are close for both thicknesses. The ordering is also the same for both cases. We conclude that the assertions made upon the first section on Ni 20 nm are valid for thinner Ni films up to 7 nm at least.

4.2 Ramp annealing of $Ni_{0.9}Co_{0.1}$(20 nm)/InGaAs/InP

Pure cobalt has been studied as a reacting metal to form silicides for MOSFETs applications [127–129], but also recently as a metallization element for InGaAs [130–132]. $Ni_{0.9}Co_{0.1}$ has also been recently investigated as a silicide [107, 108] and was proved to enhance the thermal stability of NiSi. Indeed the addition of 10 % of Co allows extending the thermal stability of (NiCo)Si by repelling the formation of the more resistive phase $(NiCo)Si_2$. Moreover, Ni and Co are neighbors on the periodic table and are entirely miscible. Thus, we aim to investigate the effect of Co addition to the deposited Ni layer on the formation of the intermetallic.

4.2.1 Formation of the intermetallic

To further understand the effect of Co addition to the 20 nm Ni film, we did ramp annealing on a Ni$_{0.9}$Co$_{0.1}$ (20 nm)/InGaAs/InP sample. We measured a 3D-RSM at each ramp step (every 20 °C) at a fixed 2θ position of 30° at an X-ray energy of 10 keV in the same manner as for the pure Ni samples.

The result of the integration over χ and ϕ are plotted in Figure 4.21 against the annealing temperature of the ramp step and the 2θ position.

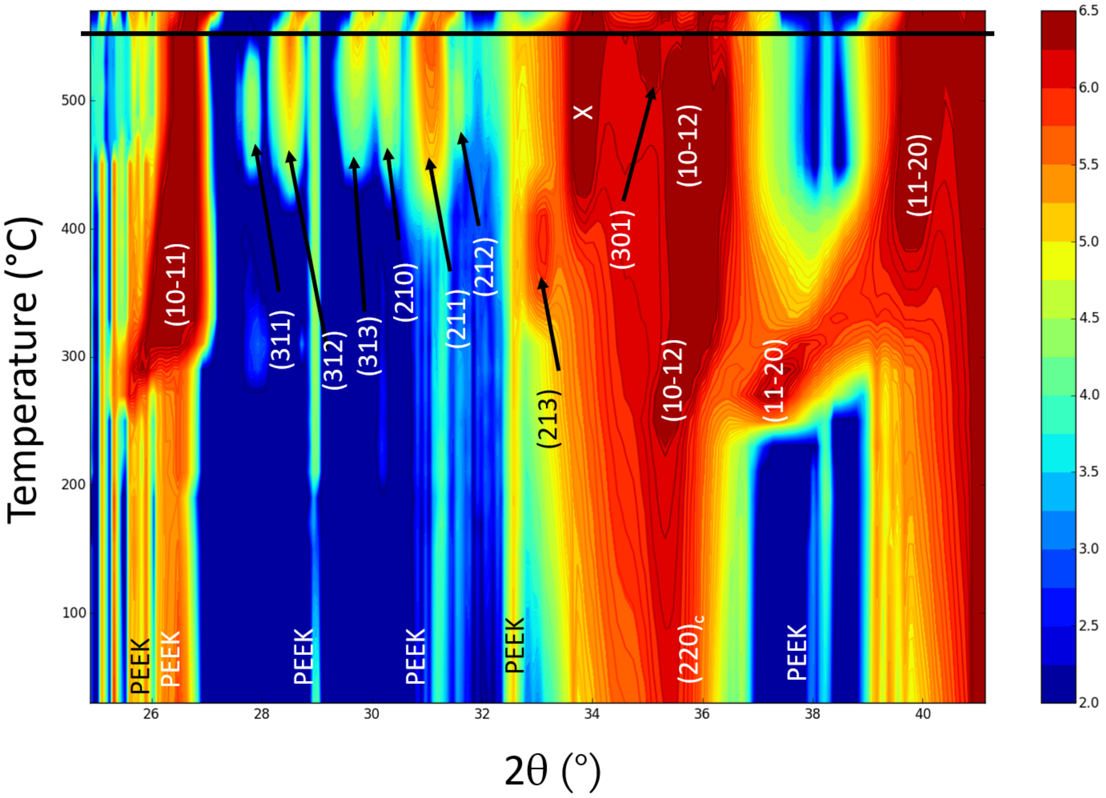

Figure 4.21 – Color map of the evolution of intensities according to 2θ angle and annealing temperature of the ramp for a Ni$_{0.9}$Co$_{0.1}$(20 nm)/InGaAs/InP sample. The bold black line at 550 °C denotes the measurement after slow cooling to room temperature.

We see in Figure 4.21 that at 250 °C, three new Bragg peaks appears indicating the formation of the intermetallic. These peaks are situated at 2θ positions of 25.6, 35.4 and 37.25° and correspond respectively to the $\{10\bar{1}1\}$, $\{10\bar{1}2\}$ and $\{11\bar{2}0\}$ planes of an hexagonal lattice. By doing local integration on unique poles of these planes, we could determine the appearance of a second set of peaks at 310 °C. The new peaks correspond to a second intermetallic phase forming after complete consumption of Ni(Co) metallic layer at 290 °C. The peak positions shift slowly towards higher 2θ values indicating mainly that there were changes on the a parameter of the hexagonal lattice. The first phase to form disappears at 430 °C in profit of the most stable phase: NiAs and its solid solution extension. A slight shift occurs from 510 °C to 550 °C indicating further stoichiometric changes. After slow cooling to room temperature, the peak position yield a new shift towards higher 2θ values indicating that a thermal expansion of the hexagonal lattice has occurred. The evolution of $\{10\bar{1}1\}$, $\{10\bar{1}2\}$ and $\{11\bar{2}0\}$ planes position according to annealing temperature is plotted in respectively Figures 4.22a, 4.22b and 4.22c.

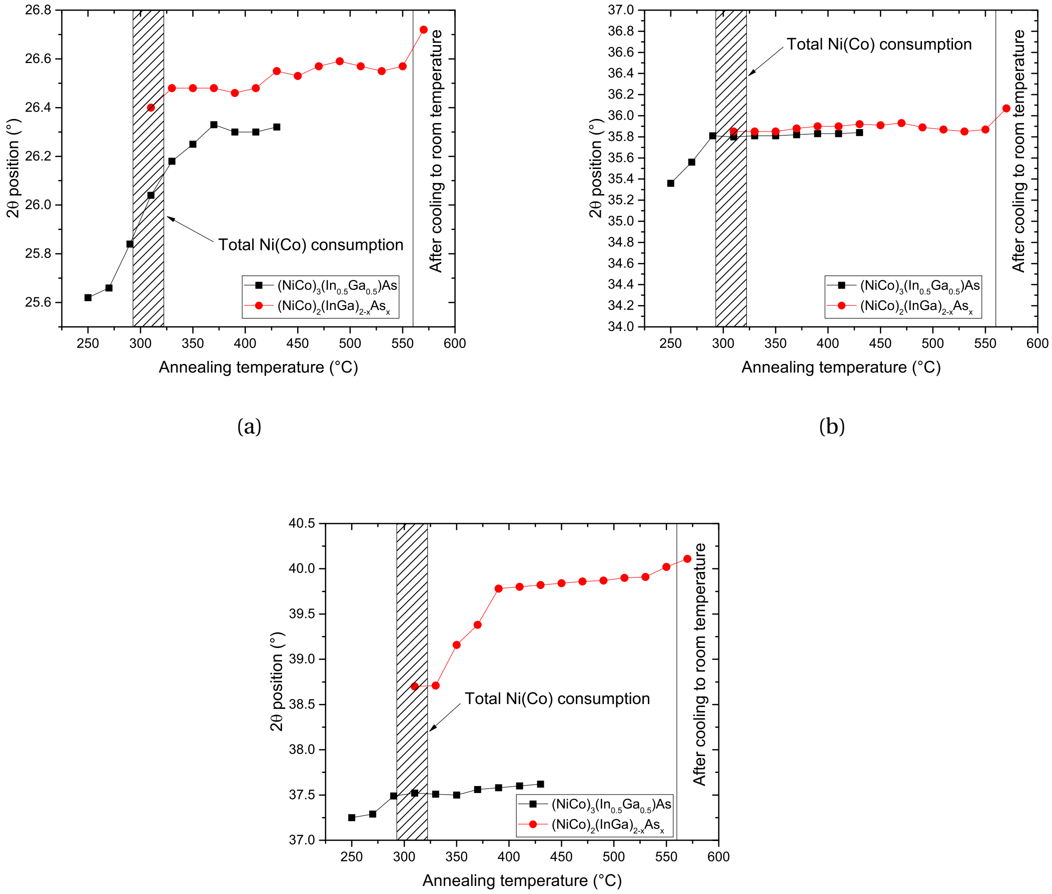

(a)

(b)

(c)

Figure 4.22 – Peak position according to the ramp annealing temperature of the (a) $(10\bar{1}1)$, (b) $(10\bar{1}2)$ and (c) $(11\bar{2}0)$ planes. Sample used is $Ni_{0.9}Co_{0.1}$(20 nm)/InGaAs/InP.

Therefore, just like the case of Ni/InGaAs/InP samples, there is evidence of sequential phase formation in the case of NiCo. Both intermetallic phases were refined using hexagonal structures of the $B8_1$ structure. The first phase to form is $(NiCo)_3(In_{0.5}Ga_{0.5})As$ and the second phase to form is NiAs with its ternary extension. It is important to note that, like NiAs, CoAs crystallizes also in the $B8_1$ structure [133]. This makes possible the occurrence of a $B8_1$ (NiCo)As compound. Thus, the second phase to form is likely NiAs with broad extensions containing

Co, In and Ga. This second phase can be denoted as $(NiCo)_2(InGa)_{2-x}Asx$ with $1 \leqslant x \leqslant 2$.

The evolution according to annealing temperature of the refined lattice parameter a, lattice parameter c, the axial ratio c/a and the volume the hexagonal lattices are given in respectively, Figure 4.23a , 4.23b, 4.23c and 4.23d. The corresponding parameters of the Ni (20 nm)/InGaAs/InP were also plotted on the same figures to ease the comparison. As it is the case for Ni/InGaAs, lattice parameter a shrinks slightly from 3.88 Å to 3.81 Å for the $(NiCo)_3(In_{0.5}Ga_{0.5})As$ phase from its appearance at 250 °C until its disappearance at 430 °C. This shift indicates slight rearrangement on metalloid sites with In-Ga/As substitutions.

The second phase to form at 310 °C is $(NiCo)_2(InGa)_{2-x}Asx$ and has smaller lattice parameter a then the first one to form. This is mainly due to an increase in vacancies concentration with the non occupancy of metallic sites inside the $B8_1$ structure.

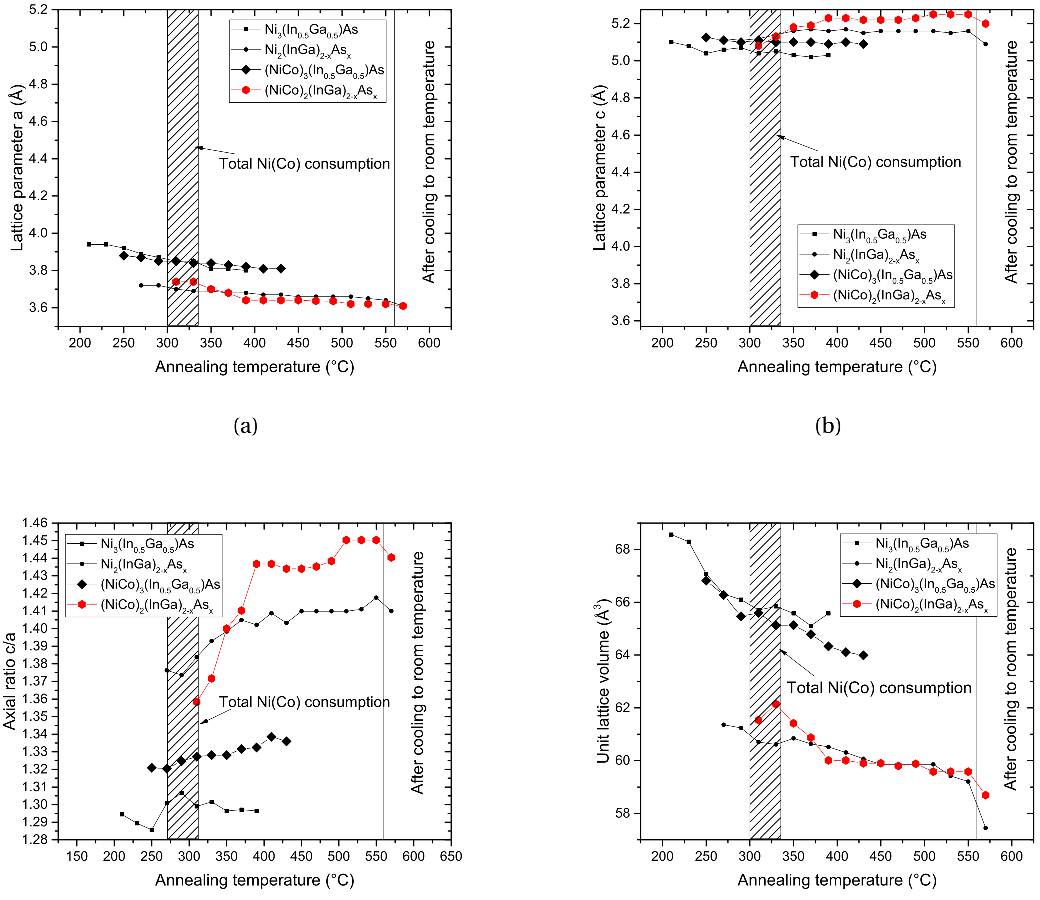

(a)

(b)

(c)

(d)

Figure 4.23 – Calculated parameters of the intermetallic hexagonal lattice (a) a lattice parameter, (b) c lattice parameter (c) c/a axial ratio and (d) volume of the hexagonal lattice. Sample used is $Ni_{0.9}Co_{0.1}$(20 nm)/InGaAs/InP.

Overall, lattice parameter c of the hexagonal structures for both phases is more important in the case of Ni(Co) than in the case of pure Ni (see Figure 4.23b). A further incorporation of cobalt atoms along the c metallic chains of the hexagonal lattice can explain the difference between the c values in case of NiCo and Ni. Indeed, while cobalt has got an atomic radius less important than nickel, it has though a more important covalent radius (126 pm for Co against 121 pm for Ni). For $(NiCo)_2(InGa)_{2-x}Asx$, a part of the increase of c might be due to the increase of the repulsion between the two As atoms that populate the metalloid sub-lattice since they became second-nearest neighbors in the unit lattice since no metallic atoms occupy the metallic sub-lattice.

NiCo-InGaAs exhibits also an ordering and extra reflections of superstructures were indexed on Figure 4.21. Just like in the case of Ni-InGaAs, the two same types of ordering were used to index the extra reflections. Again, we were not able to correctly index the peak marked by X that appear at 410 °C at 34°, but from pole figure analysis, we believe that it belongs to a twinned In-rich phase ((2 2 0) planes).

4.2.2 Texture of the intermetallic

Figures 4.24, 4.25 and 4.26 show the pole figures of respectively the $\{1\,0\,\bar{1}\,1\}$, $\{1\,0\,\bar{1}\,2\}$ and $\{1\,1\,\bar{2}\,0\}$ planes of the intermetallic at different steps of the ramp annealing process. The intermetallic exhibits the two domains group A and group B. Nevertheless, group B domains seem to be largely predominant in comparison to group A domains. This difference can be spotted directly on the pole figures of the different planes by comparing the relative intensities of each variant (refer to Appendix to see the stereographic projections of the planes according to the domain group).

It can be striking to notice that on Figures 4.24b, 4.24c and 4.24d, there are 4 poles near χ=0°, indicating the presence of the 2 azimuthal variants of group B, while there is the diffraction of poles at χ=48° of only one azimuthal variant. However, one should consider that 3D-RSM was carried out using a step of $\Delta\phi$ of 5°. In fact, the radial distance in ϕ between two $(1\,0\,\bar{1}\,1)$ poles belonging to two different group B azimuthal variants at χ=48° (Figures 4.24b, 4.24c and 4.24d) is roughly 63.5°. This radial distance is not a multiple of 5, the measurement step in ϕ, and in the case of a measurement with $\Delta\phi$=5°, measuring one azimuthal variant at χ=48° implies a certain difficulty to measure the other one if its mosaicity is not broad enough. Indeed, the poles can be missed with such a large azimuthal step.

However, we did texture analysis on 3 different planes, and it is clear from the pole figures of the $\{1\,1\,\bar{2}\,0\}$ and $\{1\,0\,\bar{1}\,2\}$ planes that the two azimuthal variants are present for group B domains (the reader may refer to the corresponding stereographic projections in the Appendix). This is not necessarily problematic for group A domains since the radial distance in ϕ between two $(1\,0\,\bar{1}\,1)$ poles belonging to two different azimuthal variants is equal to 90°. Thus, measuring one pole of one azimuthal variant, implies necessarily measuring an eventual pole belonging to an eventual second azimuthal variant. The texture analysis on several planes reduces the risk of phase/orientation missing due to a poor mosaicity of crystallites.

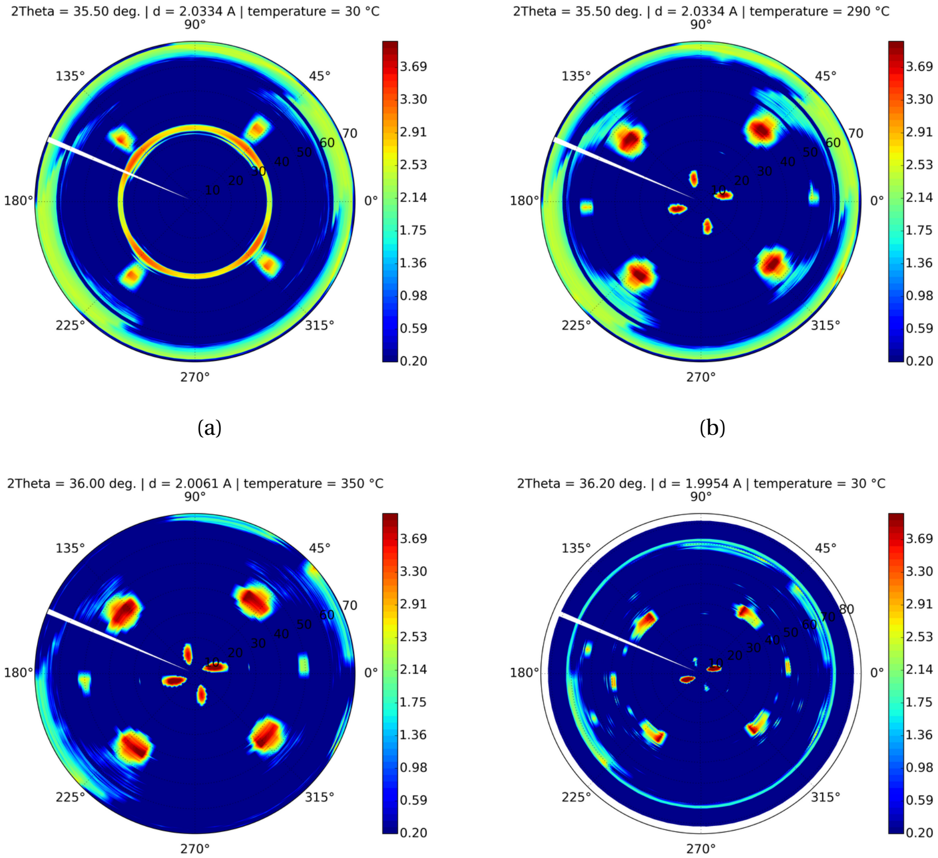

(a) (b)

(c) (d)

Figure 4.25 – Pole figures of the $\{10\bar{1}2\}$ planes of the hexagonal lattice, measured at 10 keV at different ramp temperature (a) as-deposited (no intermetallic is formed yet), (b) at 250 °C, (c) at 350 °C and (d) at 30 °C after slow cooling to room temperature. Sample used is $Ni_{0.9}Co_{0.1}$ (20 nm)/InGaAs/InP. The ring in as-deposited (a) pole figure shows fiber texture of deposited NiCo.

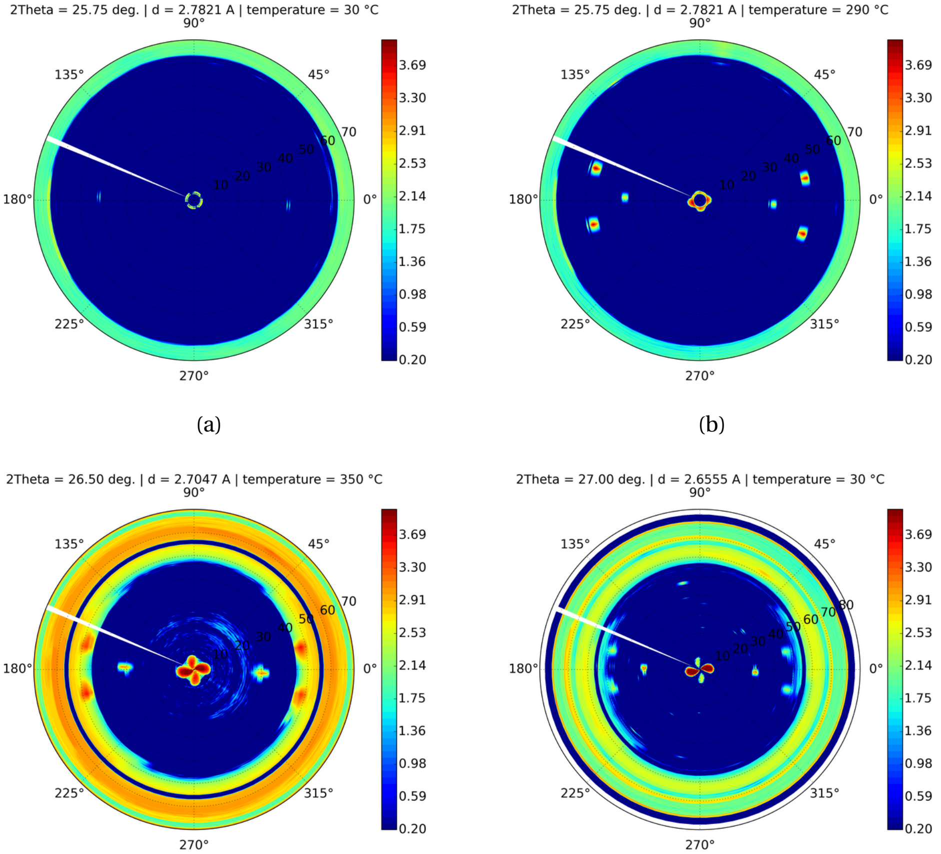

(a) (b) (c) (d)

Figure 4.24 – Pole figures of the $\{1\,0\,\bar{1}\,1\}$ planes of the hexagonal lattice, measured at 10 keV at different ramp temperature (a) as-deposited (no intermetallic is formed yet), (b) at 250 °C, (c) at 350 °C and (d) at 30 °C after slow cooling to room temperature. Sample used is $Ni_{0.9}Co_{0.1}$ (20 nm)/InGaAs/InP.

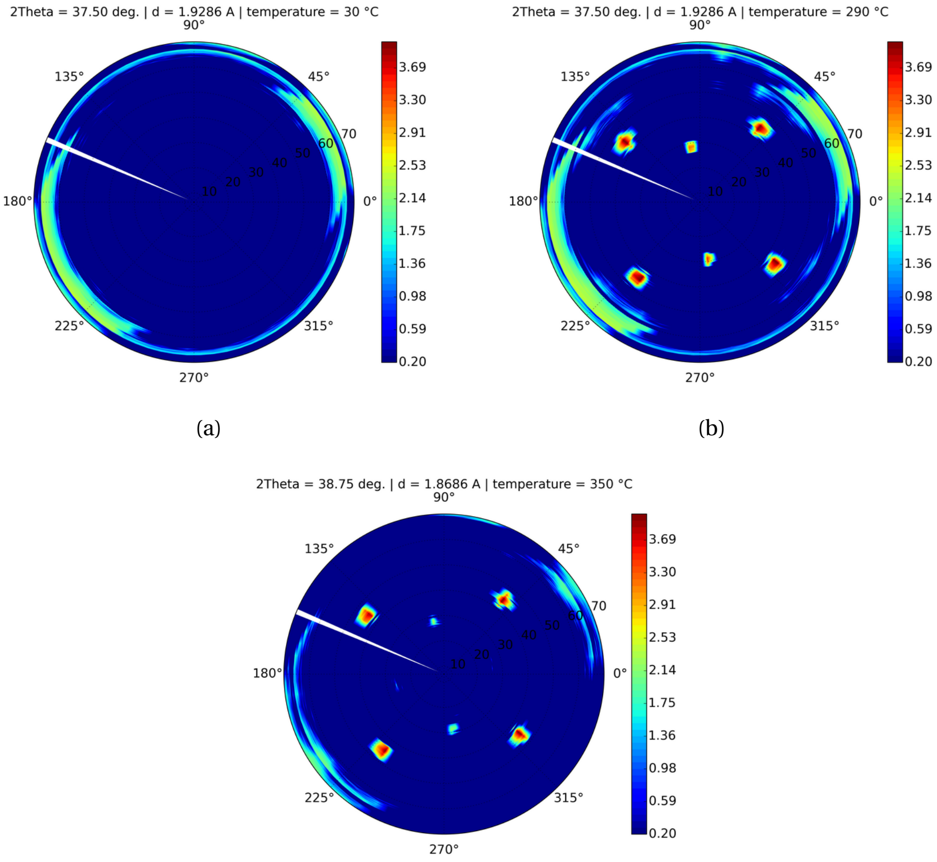

(a) (b)

(c)

Figure 4.26 – Pole figures of the $\{11\bar{2}0\}$ planes of the hexagonal lattice, measured at 10 keV at different ramp temperature (a) as-deposited (no intermetallic is formed yet), (b) at 250 °C and (c) at 350 °C. Pole figure for the sample after cooling is not exploitable due to heavy PEEK diffraction overlapping. Sample used is $Ni_{0.9}Co_{0.1}$(20 nm)/InGaAs/InP.

Since NiCo-InGaAs intermetallics exhibit both two domain groups, we calculate the mismatch for both group A domains and group B domains. Figure 4.27a and 4.27b show the evolution of lattice mismatch between the substrate and the intermetallic according to annealing temperature for respectively group A and group B domains. On each figure, we plotted the calculated mismatch for both $(NiCo)_3(In_{0.5}Ga_{0.5})As$ and $(NiCo)_2(InGa)_{2-x}As_x$ phases. The lattice mismatch between the intermetallic and the substrate were calculated using the same axiotaxial considerations described in Chapter 3 (i.e. for group A, every set of five $(10\bar{1}0)_h$ planes should meet every set of four $(110)_c$ planes and for group B, every set of two $(0001)_h$ planes should meet every set of three $(111)_c$ planes).

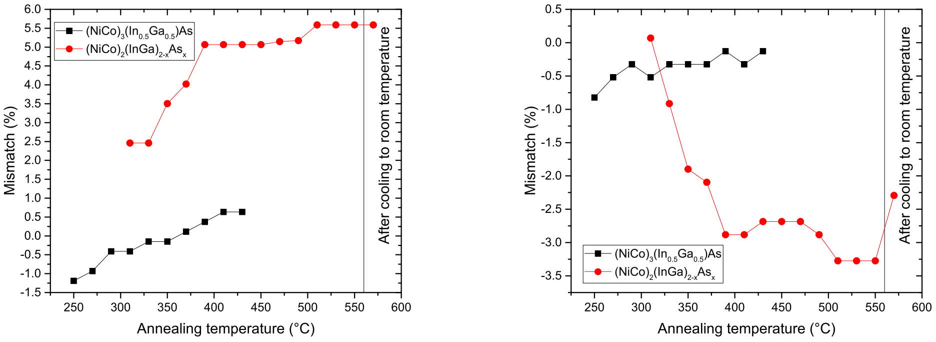

(a)

(b)

Figure 4.27 – Calculated mismatch between the intermetallic and the substrate considering an axiotaxial alignment for (a) Group A domains and (b) Group B domains.

From Figure 4.27a and 4.27b. At the temperature of formation of the first intermetallic (i. e. 250 °C), group A domains exhibit a mismatch of -1.19 % and group B domains exhibit a mismatch of -0.82 %. Thus, the interface energy between the substrate and the intermetallic is more reduced in case of group B arrangement. Hence, the most favorable axiotaxial arrangement (the one that offers the least energy at the interface) is the axiotaxial arrangement of group B domains. This conclusion explains the large domain inhomogeneities between group A and group B domains that can be seen on pole figures 4.24.

4.2.3 Linear thermal expansion coefficients

While we did not do thermal expansion coefficients calculation on Ni/InGaAs/InP samples because they exhibit only group A domains (and thus, it is less interesting to calculate such parameters than in the case of group B domains), it seems interesting to investigate the thermal expansion coefficient for the NiCo sample. Indeed, as see in Chapter 3, if there are group B domains (growth of crystallites with the c axis parallel to the $[1\,1\,1]$ direction of the semiconductor), then the measured and the calculated α angle (between the $(1\,0\,\bar{1}\,1)$ planes and the $(0\,0\,1)$ planes of the semiconductor) are different. This difference can be due to the presence of an anisotropic thermal expansion. The variation of lattice parameters between the measurement at 550 °C and the measurement after cooling to room temperature is likely due thermal expansion but also due to residual stress. Thermal expansion itself can be changed during the annealing as subsequent difference of residual stress [134]. Moreover, and because we have high-stoichiometry phase, it the thermal expansion won't be even at different temperatures, because the stoichiometry changes rather rapidly. However, we will do thermal expansion coefficient calculations to only estimate an eventual anisotropy between the a and c lattice parameters during sample cooling. Evaluating such anisotropy seems important, especially if the intermetallic exhibits group B orientation since it might be responsible of a change on c/a axial ratio, and thus, induce error when calculating the angle α between group B $(10\bar{1}1)$ planes and the sample surface (see Equation 3.4 in Chapter 3). In order to describe the variation of lattice parameter between a phase at a temperature T_0 and the same phase at temperature T, we can use the linear approximation to calculate the linear expansion coefficients γ_a and γ_c [135]:

$$\gamma_a = \frac{1}{a_0}\frac{a_T - a_0}{T - T_0} \tag{4.1}$$

where a_T is the lattice parameter at temperature T (a_T can be replaced by c_T), a_0 (respectively, c_0) is the lattice parameter at ramp annealing temperature T_0 and T is the room temperature (room temperature is considered to be at 30 °C). Both temperatures can be expressed in Kelvin or degrees Celsius indifferently.

Using Equation 4.1 to calculate the thermal expansion coefficient of a and c parameters, we obtain the following values:

Table 4.1 – Linear thermal expansion coefficient between the annealing temperature 550 °C and room temperature after cooling

	Coefficient of thermal expansion from 550 °C to 30 °C (in 10^{-6}°C^{-1})
a	5.3
c	18.3

From Table 4.1, we show that the linear thermal expansion coefficient is about 3 times more important along the c axis than the a axis, which would subsequently change the c/a axial ratio, and thus the measured α angle described in Chapter 3 would be different than the one calculated through the c/a ratio. If we reconsider the Figure 3.29 in Chapter 3, we can recalculate the α angle for the ex situ annealed samples with the corrections from the linear thermal expansion. Figure 4.28 shows the result of such recalculation.

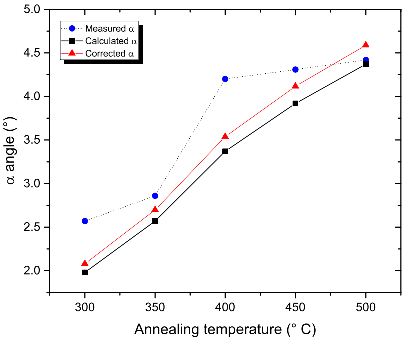

Figure 4.28 – Recalculation of the α angle for ex situ annealed samples using the linear thermal expansion corrections.

These corrections bring the calculated values closer to the measured values but the change is barely noticeable indicating that there are further processes involved in changing the measured α angle in respect of the calculated values. One can also consider the presence of a gradient of rotating grains along the depth of the intermetallic. Indeed, peculiar texture during the silicidation of nanoscale Pd thin films was already described [136]. Chen et al. reported also a peculiar rotation of the Ni-InGaAs intermetallic [117]. Such peculiar rotation will necessarily induce a modification on the measured global α angle. A series of pole figures "zoomed" on the $\{10\bar{1}1\}$ that are situated near the sample surface are given in Figure 4.29 according to annealing temperature. Indeed, on this figure, we observe that the poles corresponding to the $\{10\bar{1}1\}$ planes elongate from $\chi = 5°$ to $\chi = 8°$ from 270 to 370 °C indicating a possible peculiar rotation during the growth of the intermetallic phases.

4.2.4 Discussion: on the effect of Co on the intermetallic formation

One immediate difference between pure Ni metallic layer and $Ni_{0.9}Co_{0.1}$ metallic layer, is the annealing temperature at which the first metal-rich intermetallic is formed. While in the case of pure Ni, the intermetallic begins to form at 210 °C, Co addition makes the first phase of the intermetallic to form only when the annealing temperature reaches 250 °C. This observation differs from the observation of formation of silicides where the addition of Co to Ni lowers the temperature of formation of $NiSi_2$ form 800 °C to 650 °C [105].

To understand the effect of Co addition on the temperature of formation, let's consider the critical free energy ΔG^* which is proportional to $\frac{\Delta\sigma^3}{\Delta G^2}$, where $\Delta\sigma$ is the increase in the interfacial energy associated with the formation of the intermetallic (and thus, the creation of additional interfaces) and ΔG the volume energy. The nucleation rate is related to the critical free energy by a thermal activation and is also proportional to $\frac{\Delta\sigma^3}{\Delta G^2}$. Both of $\Delta\sigma$ and ΔG terms can be influenced by the addition of Co. In our case, Co increases the nucleation temperature. In the absence of knowledge on the values of interfacial energies and their modifications by addition

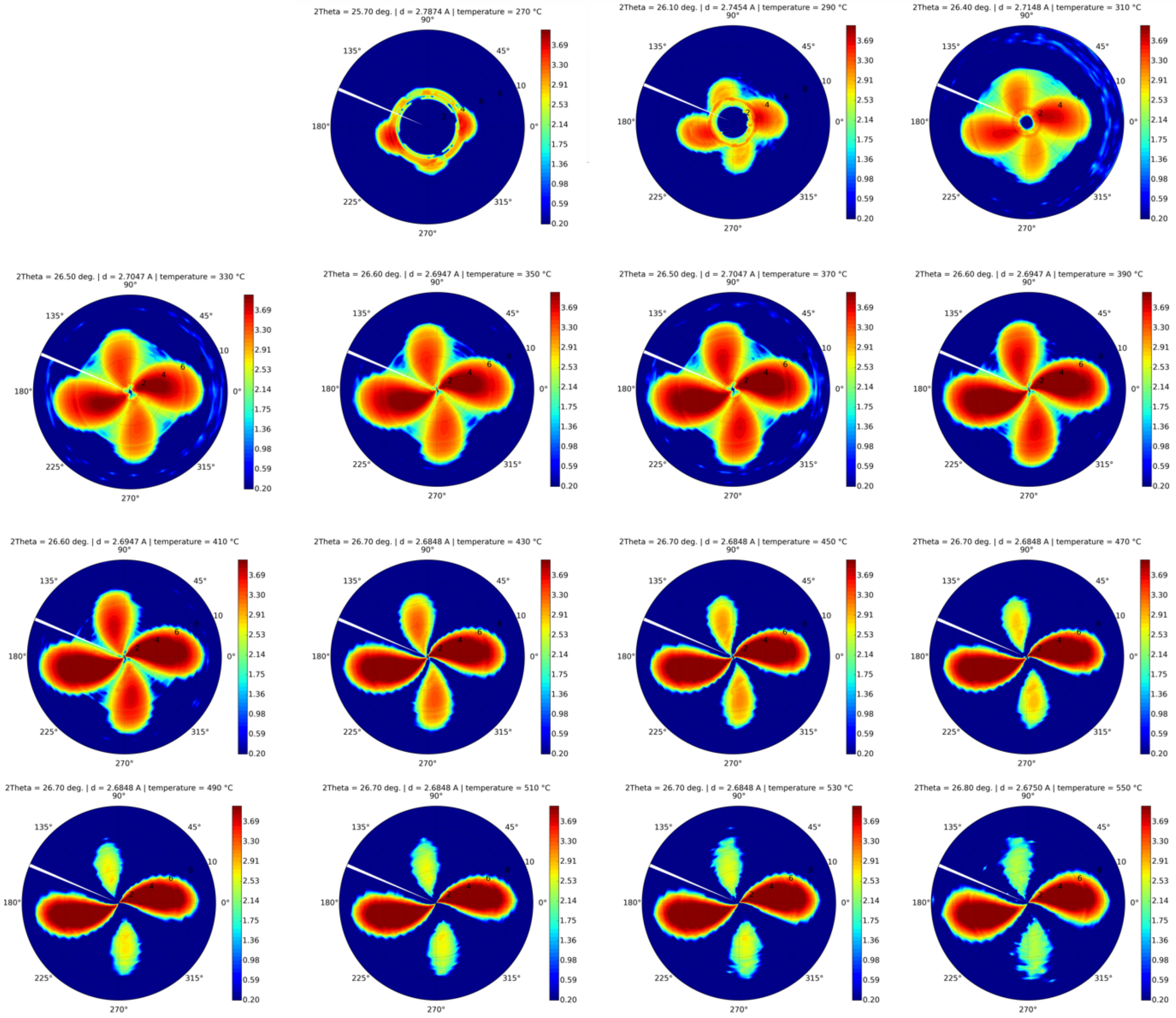

Figure 4.29 – Series of portion of the pole figures corresponding to the $\{10\overline{1}1\}$ limited to χ values between 0 and 10°. Each pole figure correspond to an annealing temperature starting from 270 °C and ending with 550 °C. The four poles in each pole figure correspond to the four $\{10\overline{1}1\}$ planes that are located near the sample surface. The out-of plane region was not entirely accessible by measurement on the area detector for the first four pole figures.

of Co, we will take epitaxial/axiotaxial considerations to explain the trends of formation of the intermetallic. Indeed, when adding Co, the lattice parameters of the intermetallic at the temperature of formation decreases for a (from 3.94 Å to 3.88 Å) and increases relatively for c (from 5.1 Å to 5.12 Å). These differences in lattice parameters influences the mismatch between the intermetallic and the substrate (-0.32 % in case of Ni versus -0.82 % in case of NiCo), and thus there are different interfacial energies for the newly created interfaces between the intermetallic nuclei and the substrate in case of pure Ni or in case of NiCo. Regarding the mismatch values at the formation of the intermetallic for Ni and NiCo (see respectively Figure 4.12 and Figure4.27), the intermetallic/semiconductor interfacial energy in case of NiCo-InGaAs intermetallic is more important and if the free energy of the reaction ΔG do not balance the increase in interfacial energy, the reaction rate would decrease. This decrease in the reaction rate explains the rise of the annealing temperature necessary to form the first intermetallic.

Another explanation to this delay in phase formation in the presence of Co is that there is a kinetic blocking, i.e. there can be germination in the system, but the diffusion of Co is slower, or that Co slows down the diffusion of Ni which translates in in delay of phase growth because the system did not have enough time to grow at low annealing temperature. Such hypothesis can eventually be demonstrated through in situ X-ray diffraction with isothermal annealings.

Another striking difference is the texture of the intermetallic. In the case of pure Ni only group A forms up and in the case NiCo it is mainly group B that forms with barely measurable diffraction spots from group A domains.

The effect of Co addition on the texture difference can be explained by a better axiotaxial alignment (due to a change in lattice parameters) in case of group B domains than in case of group A domains (respectively a mismatch of -0.82 % for group B and a mismatch of -1.19 % for group A). The non-occurrence of group B domains in case of pure Ni is likely due to the complete formation of group A formation at low temperatures which has got a better axiotaxial alignment with the substrate than group B.

4.3 Conclusion

In situ investigations by 3D-RSM on metal/InGaAs/InP revealed important and original information about the formation of intermetallics. Ramp annealing on Ni(20 nm)/InGaAs samples revealed that there is a sequential phase formation like it is the case for silicide formation. Indeed, the first phase to form is the $Ni_3(In_{0.5}Ga_{0.5})As$, then when the metallic layer is totally consumed, the more stable phase NiAs and its ternary extension is formed. This last phase grows at the expense of the least stable phase and at the end, mainly NiAs phase is formed. Each of the two phases has got a wide range of existence in terms of stoichiometry. As for the case of ex situ samples, the texture of the intermetallics was explained using axiotaxial considerations. Moreover, samples with thinner metallic layer (7 nm) were investigated. The intermetallics formation proved to be similar to the thicker metallic layer samples in terms of structure and phase sequence. Thus, we can consider that results from the 20 nm thick metallic layer can be valid for metallic layers as thin as 7 nm.

We also investigated the effect of addition of Co to the deposited metallic layer using ramp annealings. Co proved to retard the formation of the intermetallic and several thermodynamic explanations were proposed to explain this formation delay. Moreover, Co addition changes the texture of the intermetallic where group B orientation are largely predominant. This texture difference can be explained by a more favorable axiotaxy in the case of group B axiotaxial alignment. Linear thermal expansion was estimated for both a and c directions, and it was evidenced that the thermal expansion along c is nearly 3 times higher than the thermal expansion along a. However, such anisotropy of thermal expansion was not sufficient to explain the difference between the measured and calculated α angle between the $(1\,0\,\bar{1}\,1)$ plane of the intermetallic and the sample surface. Indeed, the presence of a peculiar rotation of grains was evidenced by pole figure analyses. This peculiar rotation can induce a gradient of α angles throughout the intermetallic thickness and thus enlarge the final measured value.

Conclusions and perspectives

General conclusions

This thesis was conducted in the framework of different applications that aim to develop new materials in terms of charge carriers mobility and optic properties (direct band gap). Indeed, III-V materials are interesting candidates to replace silicon as a channel material for ultimately-scaled devices but have also interesting optic properties. Nevertheless, there is a need to contact such materials in a proper way. The contacts on top of extremely scaled III-V devices need to be as stable as possible, exhibit low resistivity and a good interface. Such contacts are elaborated using a solid-state reaction between a deposited thin metallic layer and the semiconductor. Nickel seems to be a good candidate to realize such reaction. Indeed former studies on Ni/GaAs metallization and more recent studies on Ni/InGaAs metallization show that the so-formed intermetallics have promising properties. However, we also studied the effect of Co, because we believe that it would enhance the stability of the so-formed intermetallics. While a reacting layer with thickness of 7 nm of metal seems to be suitable for MOSFET applications, 20 nm of deposited metal layer is adapted for optoelectronic applications. Thus, we have investigated both thicknesses.

During this Ph.D., we have encountered a rather complicated system with up to 5 reacting elements at the same time in the case of Ni(Co). An approximation to a ternary system, where In and Ga were considered as interchangeable and so Ni and Co, was sufficient to understand and analyze most of the presented results. We have studied in a comprehensive way the solid state reactions between thin films in the case of Ni/InGaAs using 3D-Reciprocal space mapping. The results were analyzed simultaneously in the form of “de-textured” diffraction diagram and in the form of pole figure for several annealing temperatures. Such approach is valuable because it allows accurate determination of the formed phases regarding their symmetry, space group, lattice parameters, texture, etc. It was found that the so-formed intermetallics have a hexagonal symmetry, of the $P6_3/mmc$ for the different annealing temperatures.

From in situ experiments and from ex situ measurements on samples annealed by rapid thermal annealing, we have evidenced the formation of a metal-rich phase at low annealing temperatures $Ni(Co)_3In_{0.5}Ga_{0.5}As$ indicating that Ni is the diffusing species followed by the formation of $(NiCo)_2In_{0.5}Ga_{0.5}As$ and finally Ni(Co)As and its solid solution in a sequential manner. The texture of the intermetallics were analyzed according to annealing temperature and explained in terms of axiotaxial alignments. The same axiotaxial alignments were also used to explain the texture difference in the case of Ni/InGaAs/GaAs/Si and Ni(Co)/InGaAs/InP. The texture anisotropy was found to be likely not related to the presence of atomic steps at the surface of the substrate and was explained by the presence of antiphase domains breaking the overall anisotropy of the substrate.

Ni use as a reacting metal can be interesting as the corresponding intermetallics on InGaAs show low sheet resistance values. However, one should consider phase agglomeration that occur after 450 °C. Ramp annealing showed that at a critical temperature T_c=270 °C, there is the formation of a second phase less rich in metal. This critical temperature corresponds to the complete consumption of the metallic layer of Ni. The addition of Co proved to delay the formation of the intermetallics as opposed to pure Ni and as it is the case for pure Ni, the intermetallics exhibited sequential formation of phases. However, the texture of the intermetallic is mainly of group B domains (thus, with the c axis of the hexagonal lattices parallel to the [1 1 1] direction of the semiconductor). Such texture can result in a pyramidal shaped domains and heavy agglomeration at high annealing temperatures. Nevertheless, texture can be potentially controlled by using a substrate with different orientation than the (0 0 1) one (like the (1 1 1) oriented substrates). Moreover, texture of the intermetallics probably have an influence on the electrical parameters and mobility of charge carriers since planes with different densities are aligned with the substrate for each group. Thus it would be interesting to investigate the influence of such alignments, separately, on the electrical parameters.

Perspectives

A number of enhancements can be performed on the methods of data reduction to ensure a full quantitative analysis in the case of multi-geometry measurement strategy. Indeed, on area detectors, “stitching” images recorded at different χ or 2θ angles can be problematic. In order to use a multi-geometry configuration when varying χ and 2θ, one should use the distortion module of a detector to re-sample the signal on a regular grid but one will also have to store on one side the number of actual pixel contributing to a regular pixels and on the other the total intensity contained in the regularized pixel. Moreover, pixel modules can present slight variations in sensitivity resulting in different background noise on side or another of the detector. These problematics, among others, should be addressed in order to perform quantitative analyses and use refinement algorithms such as the Rietveld refinement in the same way as powder diffraction. Another solution is the continuous scanning mode using an area detector offered by some commercial diffractomers ensuring the acquisition of a continuous large diffraction image. The work on such acquisition was already initiated by former Master’s intern Alexandre Lissowski and seem to be a very promising way to perform quantitative 3D-RSM on a lab tool.

Moreover, while the metallization studies in the thin film way are interesting because they are being done in "field conditions" where texture, thin film effects and substrate influence are simultaneously being acquired, a powder study seems also interesting. Indeed, it would allow to establish a phase diagram for the Ni-In-Ga-As system to better understand the formation of the intermetallic. The influence of the antiphase domains is also yet to be demonstrated, especially that there is new knowledge on manufacturing APD-free InGaAs layers on GaAs/Si. Moreover, it would be very interesting to investigate further compounds in addition of Ni(Co). This can seem very helpful, not only to investigate the possibility of stable good quality intermetallic, but also to better understand the texture and structural evolution of the intermetallic.

Bibliography

[1] K. F. Brennan, “Introduction to semiconductor devices,” 2005.

[2] R. Alcotte, M. Martin, J. Moeyaert, R. Cipro, S. David, F. Bassani, F. Ducroquet, Y. Bogumilowicz, E. Sanchez, Z. Ye *et al.*, “Epitaxial growth of antiphase boundary free GaAs layer on 300 mm Si (001) substrate by metalorganic chemical vapour deposition with high mobility,” *APL Materials*, vol. 4, no. 4, p. 046101, 2016.

[3] S. Oktyabrsky and D. Y. Peide, *Fundamentals of III-V semiconductor MOSFETs*. Springer, 2010.

[4] A. Dimoulas, A. Toriumi, and S. E. Mohney, “Source and drain contacts for germanium and III–V FETs for digital logic,” *MRS bulletin*, vol. 34, no. 07, pp. 522–529, 2009.

[5] J. A. del Alamo, “Nanometre-scale electronics with III-V compound semiconductors,” *Nature*, vol. 479, no. 7373, pp. 317–323, Nov. 2011.

[6] M. Radosavljevic, B. Chu-Kung, S. Corcoran, G. Dewey, M. K. Hudait, J. M. Fastenau, J. Kavalieros, W. K. Liu, D. Lubyshev, M. Metz, K. Millard, N. Mukherjee, W. Rachmady, U. Shah, and R. Chau, “Advanced high-K gate dielectric for high-performance short-channel $In_{0.7}Ga_{0.3}As$ quantum well field effect transistors on silicon substrate for low power logic applications,” in *2009 IEEE International Electron Devices Meeting (IEDM)*, 7-9 Dec. 2009, pp. 1–4.

[7] J. A. del Alamo, D.-H. Kim, T.-W. Kim, D. Jin, and D. A. Antoniadis, “III-V CMOS: What have we learned from HEMTs?” in *IPRM 2011-23rd International Conference on Indium Phosphide and Related Materials*. IEEE, 2011, pp. 1–4.

[8] D. H. Kim, J. A. del Alamo, D. A. Antoniadis, and B. Brar, “Extraction of virtual-source injection velocity in sub-100 nm III-V HFETs,” in *2009 IEEE International Electron Devices Meeting (IEDM)*, 7-9 Dec. 2009, pp. 1–4.

[9] R. Chau, S. Datta, and A. Majumdar, “Opportunities and challenges of III-V nanoelectronics for future high-speed, low-power logic applications,” *IEEE Compound Semiconductor Integrated Circuit Symposium, 2005. CSIC 2005.*, 2005.

[10] N. Newman, “On the fermi level pinning behavior of metal/III-V semiconductor interfaces,” *Journal of Vacuum Science & Technology B: Microelectronics and Nanometer Structures*, vol. 4, no. 4, p. 931, Jul 1986.

[11] M. Passlack, M. Hong, J. Mannaerts, S. Chu, R. Opila, and N. Moriya, “In-situ Ga_2O_3 process for GaAs inversion/accumulation device and surface passivation applications,” *Proceedings of International Electron Devices Meeting*, 1995.

[12] M. Passlack, M. Hong, and J. P. Mannaerts, “Quasistatic and high frequency capacitance-voltage characterization of Ga_2O_3-GaAs structures fabricated by in situ molecular beam epitaxy,” *Applied Physics Letters*, vol. 68, no. 8, p. 1099, 1996.

[13] M. L. Huang, Y. C. Chang, C. H. Chang, Y. J. Lee, P. Chang, J. Kwo, T. B. Wu, and M. Hong, “Surface passivation of III-V compound semiconductors using atomic-layer-deposition-grown Al_2O_3,” *Applied Physics Letters*, vol. 87, no. 25, p. 252104, 2005.

[14] M. M. Frank, G. D. Wilk, D. Starodub, T. Gustafsson, E. Garfunkel, Y. J. Chabal, J. Grazul, and D. A. Muller, “HfO_2 and Al_2O_3 gate dielectrics on GaAs grown by atomic layer deposition,” *Applied Physics Letters*, vol. 86, no. 15, p. 152904, 2005.

[15] Y. Xuan, H. C. Lin, P. D. Ye, and G. D. Wilk, “Capacitance-voltage studies on enhancement-mode InGaAs metal-oxide-semiconductor field-effect transistor using atomic-layer-deposited Al_2O_3gate dielectric,” *Applied Physics Letters*, vol. 88, no. 26, p. 263518, 2006.

[16] T.-Y. Han, G.-L. Luo, C.-C. Cheng, C.-H. Ko, C. H. Wann, C.-C. Kei, C.-N. Hsiao, and C.-H. Chien, “Experimental demonstration of (111)-oriented GaAs metal-oxide-semiconductor field-effect-transistors with hetero-epitaxial Ge source/drain,” *ECS Journal of Solid State Science and Technology*, vol. 3, no. 4, pp. 86–90, Feb 2014.

[17] P. Ye, Y. Xuan, Y. Wu, and M. Xu, “Inversion-Mode $In_xGa_{1-x}As$ Mosfets (x=0.53,0.65,0.75) with Atomic-Layerdeposited High-K Dielectrics,” *ECS Transactions*, 2009.

[18] S. Oktyabrsky, P. Nagaiah, V. Tokranov, S. Koveshnikov, M. Yakimov, R. Kambhampati, R. Moore, and W. Tsai, “Electron scattering in buried InGaAs MOSFET channel with HfO_2 gate oxide,” *MRS Proceedings*, vol. 1155, Jan 2009.

[19] N. Waldron, D.-H. Kim, and J. A. del Alamo, “A Self-Aligned InGaAs HEMT Architecture for Logic Applications,” *IEEE Transactions on Electron Devices*, vol. 57, no. 1, pp. 297–304, Jan 2010.

[20] K. Kamigaki, S. Yuda, H. Kato, M. Ishida, H. Terauchi, N. Sano, and S. Hiyamizu, “High-temperature growth of epitaxial NiAl thin films on AlAs by molecular-beam epitaxy,” *Journal of Applied Physics*, vol. 69, no. 4, p. 2196, 1991.

[21] M. Tanaka, H. Sakakibara, and T. Nishinaga, “Molecular beam epitaxial growth and characterization of CoAl on AlAs/GaAs,” *Applied Physics Letters*, vol. 59, no. 24, p. 3115, 1991.

[22] S. Députier, R. Guérin, Y. Ballini, and A. Guivarc'h, "Solid state phase equilibria in the Ni-Al-As system," *Journal of Alloys and Compounds*, vol. 217, no. 1, pp. 13–21, Jan 1995.

[23] R. Guérin and A. Guivarc'h, "Metallurgical study of Ni/GaAs contacts. I. Experimental determination of the solid portion of the Ni-Ga-As ternary-phase diagram," *Journal of Applied Physics*, vol. 66, no. 5, pp. 2122–2128, 1989.

[24] T. Sands, V. Keramidas, J. Washburn, and R. Gronsky, "Structure and composition of Ni_xGaAs," *Applied physics letters*, vol. 48, no. 6, pp. 402–404, 1986.

[25] T. Sands, V. G. Keramidas, K. M. Yu, J. Washburn, and K. Krishnan, "A comparative study of phase stability and film morphology in thin-film M/GaAs systems (M=Co, Rh, Ir, Ni, Pd, and Pt)," *Journal of Applied Physics*, vol. 62, no. 5, p. 2070, 1987.

[26] J. W. Christian, *The theory of transformations in metals and alloys.* Newnes, 2002.

[27] F. M. d'Heurle, "Nucleation of a new phase from the interaction of two adjacent phases: Some silicides," *Journal of Materials Research*, vol. 3, pp. 167–195, 2 1988.

[28] W. D. Callister and D. G. Rethwisch, *Materials science and engineering: an introduction.* Wiley New York, 2007, vol. 7.

[29] G. Ottaviani, "Metallurgical aspects of the formation of silicides," *Thin Solid Films*, vol. 140, no. 1, pp. 3–22, 1986.

[30] S. Lau, J. Mayer, and K. Tu, "Interactions in the Co/Si thin-film system. I. Kinetics," *Journal of Applied Physics*, vol. 49, no. 7, pp. 4005–4010, 1978.

[31] F. d'Heurle and C. Petersson, "Formation of thin films of $CoSi_2$: Nucleation and diffusion mechanisms," *Thin Solid Films*, vol. 128, no. 3, pp. 283 – 297, 1985.

[32] P. Gas and F. d'Heurle, "Formation of silicide thin films by solid state reaction," *Applied Surface Science*, vol. 73, pp. 153 – 161, 1993.

[33] J. Philibert, "Reactive diffusion in thin films," *Applied Surface Science*, vol. 53, pp. 74–81, Nov. 1991.

[34] F. d'Heurle, P. Gas, J. Philibert, and O. Thomas, "Considerations regarding reactive diffusion: Parabolic and linear rates," *Metals Materials and Processes*, vol. 11, no. 3/4, pp. 217–232, 1999.

[35] U. Gösele and K. Tu, ""Critical thickness"of amorphous phase formation in binary diffusion couples," *Journal of Applied Physics*, vol. 66, no. 6, pp. 2619–2626, 1989.

[36] K.-E. Sundström, S. Petersson, and P. Tove, "Studies of formation of silicides and their barrier heights to silicon," *Phys. Status Solidi A*, vol. 20, no. 2, pp. 653–668, 1973.

[37] S. Petersson, J. Baglin, W. Hammer, F. d'Heurle, T. Kuan, I. Ohdomari, J. de Sousa Pires, and P. Tove, "Formation of iridium silicides from Ir thin films on Si substrates," *Journal of Applied Physics*, vol. 50, no. 5, pp. 3357–3365, 1979.

[38] T. Finstad, "Silicide formation with nickel and platinum double layers on silicon," *Thin Solid Films*, vol. 51, no. 3, pp. 411–424, 1978.

[39] R. Mann and L. Clevenger, "The C49 to C54 phase transformation in $TiSi_2$ thin films," *Journal of The Electrochemical Society*, vol. 141, no. 5, pp. 1347–1350, 1994.

[40] C. Lavoie, F. d'Heurle, C. Detavernier, and C. Cabral, "Towards implementation of a nickel silicide process for CMOS technologies," *Microelectronic Engineering*, vol. 70, no. 2, pp. 144–157, 2003.

[41] M. Christensen, V. Eyert, C. Freeman, E. Wimmer, A. Jain, J. Blatchford, D. Riley, and J. Shaw, "Formation of nickel-platinum silicides on a silicon substrate: Structure, phase stability, and diffusion from ab initio computations," *Journal of Applied Physics*, vol. 114, no. 3, p. 033533, 2013.

[42] Y.-J. Chang and J. Erskine, "Diffusion layers and the schottky-barrier height in nickel silicide—silicon interfaces," *Physical Review B*, vol. 28, no. 10, p. 5766, 1983.

[43] J. Gibson and J. Batstone, "In-situ transmission electron microscopy of NiSi2 formation by molecular beam epitaxy," *Surface Science*, vol. 208, no. 3, pp. 317–350, 1989.

[44] P. Bennett, M. Lee, P. Yang, R. Schuster, P. Eng, and I. Robinson, "Template structure at the silicon/amorphous-silicide interface," *Physical Review Letters*, vol. 75, no. 14, p. 2726, 1995.

[45] P. Gergaud, C. Rivero, M. Gailhanou, O. Thomas, B. Froment, and H. Jaouen, "Exploring Ni–Si thin-film reactions by means of simultaneous synchrotron X-Ray diffraction and substrate curvature measurements," *Materials Science and Engineering: B*, vol. 114, pp. 67–71, 2004.

[46] F. Nemouchi, D. Mangelinck, J. Lábár, M. Putero, C. Bergman, and P. Gas, "A comparative study of nickel silicides and nickel germanides: Phase formation and kinetics," *Microelectronic Engineering*, vol. 83, no. 11, pp. 2101–2106, 2006.

[47] K. Tu, W. Chu, and J. Mayer, "Structure and growth kinetics of Ni_2Si on silicon," *Thin Solid Films*, vol. 25, no. 2, pp. 403–413, 1975.

[48] C. Lavoie, C. Detavernier, C. Cabral, F. d'Heurle, A. Kellock, J. Jordan-Sweet, and J. Harper, "Effects of additive elements on the phase formation and morphological stability of nickel monosilicide films," *Microelectronic Engineering*, vol. 83, no. 11, pp. 2042–2054, 2006.

[49] D. Mangelinck, K. Hoummada, O. Cojocaru-Mirédin, E. Cadel, C. Perrin-Pellegrino, and D. Blavette, “Atom probe tomography of Ni silicides: First stages of reaction and redistribution of Pt,” *Microelectronic Engineering*, vol. 85, no. 10, pp. 1995–1999, 2008.

[50] E. Van Loenen, J. Van Der Veen, and F. LeGoues, “Ni-Si mixing: A new model for low temperature silicide formation,” *Surface Science*, vol. 157, no. 1, pp. 1–16, 1985.

[51] F. d’Heurle, C. Petersson, J. Baglin, S. La Placa, and C. Wong, “Formation of thin films of NiSi: Metastable structure, diffusion mechanisms in intermetallic compounds,” *Journal of Applied Physics*, vol. 55, no. 12, pp. 4208–4218, 1984.

[52] T. G. Finstad, “A Xe marker study of the transformation of Ni2Si to NiSi in thin films,” *Phys. Status Solidi A*, vol. 63, no. 1, pp. 223–228, 1981.

[53] “ICDD card no. 17-0881.”

[54] S. Gaudet, C. Coia, P. Desjardins, and C. Lavoie, “Metastable phase formation during the reaction of Ni films with Si(001): The role of texture inheritance,” *Journal of Applied Physics*, vol. 107, no. 9, 2010.

[55] S. W. H. Bragg, “Application of the ionisation spectrometer to the determination of the structure of minute crystals,” *Proceedings of the Physical Society of London*, vol. 33, no. 1, p. 222, 1920.

[56] J. Brentano, “A new method of crystal powder analysis by X-rays,” *Nature*, vol. 112, pp. 652–653, 1923.

[57] ——, “Parafocusing properties of microcrystalline powder layers in X-ray diffraction applied to the design of X-ray goniometers,” *Journal of Applied Physics*, vol. 17, no. 6, pp. 420–434, 1946.

[58] C. Detavernier, A. S. Özcan, J. Jordan-Sweet, E. A. Stach, J. Tersoff, F. M. Ross, and C. Lavoie, “An off-normal fibre-like texture in thin films on single-crystal substrates,” *Nature*, vol. 426, pp. 641–645, 2003.

[59] K. D. Keyser, “Texture of thin silicide and germanide films,” Ph.D. dissertation, Ghent University, 2010.

[60] A. Kjekshus and W. Pearson, “Phases with the nickel arsenide and closely-related structures,” *Progress in Solid State Chemistry*, vol. 1, pp. 83 – 174, 1964.

[61] S. Lidin, “Superstructure Ordering of Intermetallics: B8 Structures in the Pseudo-Cubic Regime,” *Acta Crystallographica Section B*, vol. 54, no. 2, pp. 97–108, Apr 1998.

[62] C. S. Barrett and T. B. Massalski, *Structure of Metals: Gystallographic Methods, Principles and Data.* Pergamon Press, 1980.

[63] M. Ogawa, “Alloying reaction in thin nickel films deposited on GaAs,” *Thin Solid Films*, vol. 70, no. 1, pp. 181–189, 1980.

[64] A. Lahav, M. Eizenberg, and Y. Komem, “Interfacial reactions between Ni films and GaAs,” *J. Appl. Phys.*, vol. 60, no. 3, pp. 991–1001, 1986.

[65] X.-Y. Zheng, J.-C. Lin, D. Swenson, K.-C. Hsieh, and Y. Chang, “Phase equilibria of Ga-Ni-As at 600 °C and the structural relationship between γ-Ni_3Ga_2, γ-$Ni_{13}Ga_9$ and T-Ni_3GaAs,” *Materials Science and Engineering: B*, vol. 5, no. 1, pp. 63–72, 1989.

[66] D. B. Ingerly, D. Swenson, C.-H. Jan, and Y. A. Chang, “Phase equilibria of the Ga–Ni–As ternary system,” *Journal of Applied Physics*, vol. 80, no. 1, pp. 543–550, 1996.

[67] A. Guivarc’h, R. Guérin, J. Caulet, A. Poudoulec, and J. Fontenille, “Metallurgical study of Ni/GaAs contacts. II. Interfacial reactions of Ni thin films on (111) and (001) GaAs,” *J. Appl. Phys.*, vol. 66, no. 5, pp. 2129–2136, 1989.

[68] D. L. O. Nielsen (Technical University of Denmark, Lyngby, Ed.   Proceedings of 10th Nordic Semiconductor Meeting, 1982.

[69] T. Sands, “Compound semiconductor contact metallurgy,” *Materials Science and Engineering: B*, vol. 1, no. 3, pp. 289–312, 1988.

[70] L. Chen and Y. Hsieh, “Interfacial Reactions of Nickel films on GaAs,” in *MRS Proceedings*, vol. 31.   Cambridge Univ Press, 1983, p. 165.

[71] K. Yu, W. Walukiewicz, J. Jaklevic, E. Haller, and T. Sands, “Effects of interface reactions on electrical characteristics of metal-GaAs contacts,” *Applied Physics Letters*, vol. 51, no. 3, pp. 189–191, 1987.

[72] R. Guérin and A. Guivarc’h, “Comment on “Phase equilibria of the Ga–Ni–As ternary system”[J. Appl. Phys. 80, 543 (1996)],” *Journal of Applied Physics*, vol. 82, no. 1, pp. 493–495, 1997.

[73] D. B. Ingerly, D. Swenson, C.-H. Jan, and Y. A. Chang, “Reply to “Comment on ‘Phase equilibria of the Ga–Ni–As ternary system’”[J. Appl. Phys. 82, 493 (1997)],” *Journal of Applied Physics*, vol. 82, no. 1, pp. 496–497, 1997.

[74] S. Kim, M. Yokoyama, N. Taoka, R. Iida, S. Lee, R. Nakane, Y. Urabe, N. Miyata, T. Yasuda, H. Yamada *et al.*, “Self-Aligned Metal Source/Drain $In_xGa_{1-x}As$ n-Metal-Oxide-Semiconductor Field-Effect Transistors Using Ni-InGaAs Alloy,” *Applied Physics Express*, vol. 4, no. 2, p. 024201, 2011.

[75] X. Zhang, H. Guo, X. Gong, Q. Zhou, Y.-R. Lin, H.-Y. Lin, C.-H. Ko, C. H. Wann, and Y.-C. Yeo, “$In_{0.7}Ga_{0.3}As$ channel n-MOSFET with self-aligned Ni-InGaAs source and drain,” *Electrochemical and Solid-State Letters*, vol. 14, no. 2, pp. H60–H62, 2011.

[76] S. Kim, M. Yokoyama, N. Taoka, R. Nakane, T. Yasuda, O. Ichikawa, N. Fukuhara, M. Hata, M. Takenaka, and S. Takagi, “Sub-60-nm Extremely Thin Body-On-Insulator MOSFETs on Si With Ni-InGaAs Metal S/D and MOS Interface Buffer Engineering and Its Scalability,” *IEEE Transactions on Electron Devices*, vol. 60, no. 8, pp. 2512–2517, 2013.

[77] S. Kim, M. Yokoyama, N. Taoka, R. Iida, S.-H. Lee, R. Nakane, Y. Urabe, N. Miyata, T. Yasuda, H. Yamada *et al.*, “Experimental Study on Electron Mobility in $In_xGa_{1-x}As$-on-Insulator Metal-Oxide-Semiconductor Field-Effect Transistors With In Content Modulation and MOS Interface Buffer Engineering,” *IEEE Transactions on Nanotechnology*, vol. 12, no. 4, pp. 621–628, 2013.

[78] Ivana, Y. Lim Foo, X. Zhang, Q. Zhou, J. Pan, E. Kong, M. H. Samuel Owen, and Y.-C. Yeo, “Crystal structure and epitaxial relationship of $Ni_4InGaAs_2$ films formed on InGaAs by annealing,” *J. Vac. Sci. Technol., B*, vol. 31, p. 012202, 2013.

[79] P. Shekhter, S. Mehari, D. Ritter, and M. Eizenberg, “Epitaxial NiInGaAs formed by solid state reaction on $In_{0.53}Ga_{0.47}As$: Structural and chemical study,” *J. Vac. Sci. Technol., B*, vol. 31, no. 3, p. 031205, 2013.

[80] R. Chen and S. A. Dayeh, “Size and Orientation Effects on the Kinetics and Structure of Nickelide Contacts to InGaAs Fin Structures,” *Nano Letters*, vol. 15, no. 6, pp. 3770–3779, 2015, pMID: 25879390.

[81] S. Gaudet, K. De Keyser, S. Lambert-Milot, J. Jordan-Sweet, C. Detavernier, C. Lavoie, and P. Desjardins, “Three dimensional reciprocal space measurement by X-ray diffraction using linear and area detectors: Applications to texture and defects determination in oriented thin films and nanoprecipitates,” *J. Vac. Sci. Technol., A*, vol. 31, no. 2, p. 021505, 2013.

[82] M. Birkholz, *Thin film analysis by X-ray scattering.* John Wiley & Sons, 2006.

[83] C. Giacovazzo, *Fundamentals of crystallography.* Oxford University Press, USA, 2002, vol. 7.

[84] P. Gravereau, “Introduction à la pratique de la diffraction des rayons x par les poudres,” Ph.D. dissertation, Sciences Chimiques, 2011.

[85] W. H. Bragg and W. L. Bragg, “The reflection of X-rays by crystals,” *Proceedings of the Royal Society of London. Series A, Containing Papers of a Mathematical and Physical Character*, vol. 88, no. 605, pp. 428–438, 1913.

[86] E. J. Mittemeijer and U. Welzel, *Modern diffraction methods.* John Wiley & Sons, 2013.

[87] P. Gergaud, C. Rivero, M. Gailhanou, O. Thomas, B. Froment, and H. Jaouen, “Exploring Ni-Si thin-film reactions by means of simultaneous synchrotron X-ray diffraction and substrate curvature measurements,” *Materials Science and Engineering B: Solid-State Materials for Advanced Technology*, vol. 114-115, pp. 67–71, 2004.

[88] C. Lavoie, C. Detavernier, C. Cabral, F. d'Heurle, A. Kellock, J. Jordan-Sweet, and J. Harper, "Effects of additive elements on the phase formation and morphological stability of nickel monosilicide films," *Microelectronic Engineering*, vol. 83, no. 11, pp. 2042–2054, 2006.

[89] N. Vaxelaire, H. Proudhon, S. Labat, C. Kirchlechner, J. Keckes, V. Jacques, S. Ravy, S. Forest, and O. Thomas, "Methodology for studying strain inhomogeneities in polycrystalline thin films during in situ thermal loading using coherent X-ray diffraction," *New Journal of Physics*, vol. 12, no. 3, p. 035018, 2010.

[90] B. Vianne, S. Escoubas, M.-I. Richard, S. Labat, G. Chahine, T. Schülli, A. Farcy, P. Bar, V. Fiori, and O. Thomas, "Strain and tilt mapping in silicon around copper filled TSVs using advanced X-ray nano-diffraction," *Microelectronic Engineering*, vol. 137, pp. 117–123, 2015.

[91] D. Chateigner, *Combined analysis.* John Wiley & Sons, 2013.

[92] C. Boudias and D. Monceau, "Carine crystallography 3.1," *DIVERGENT SA, Centre de Transfert*, vol. 60200, pp. 1989–1998, 1989.

[93] B. De Schutter, K. Van Stiphout, N. M. Santos, E. Bladt, J. Jordan-Sweet, S. Bals, C. Lavoie, C. M. Comrie, A. Vantomme, and C. Detavernier, "Phase formation and texture of thin nickel germanides on Ge(001) and Ge(111)," *Journal of Applied Physics*, vol. 119, no. 13, 2016.

[94] T. Thanh, N. Blanc, N. Boudet, E. Bourjot, S. Zhiou, V. Kovacova, P. Rodriguez, F. Nemouchi, and P. Gergaud, "Full 3D reciprocal space map of thin polycrystalline films for microelectronic applications," in *Interconnect Technology Conference and 2015 IEEE Materials for Advanced Metallization Conference (IITC/MAM), 2015 IEEE International*, May 2015, pp. 53–56.

[95] C. Ponchut, "Characterization of X-ray area detectors for synchrotron beamlines," *Journal of synchrotron radiation*, vol. 13, no. 2, pp. 195–203, 2006.

[96] J. Kieffer and J. Wright, "PyFAI: a Python library for high performance azimuthal integration on GPU," *Powder Diffraction*, vol. 28, no. S2, pp. S339–S350, 2013.

[97] E. B. Knudsen, H. O. Sørensen, J. P. Wright, G. Goret, and J. Kieffer, "FabIO: easy access to two-dimensional X-ray detector images in Python," *Journal of Applied Crystallography*, vol. 46, no. 2, pp. 537–539, 2013.

[98] J. Kieffer and D. Karkoulis, "PyFAI, a versatile library for azimuthal regrouping," in *Journal of physics: conference series*, vol. 425, no. 20. IOP Publishing, 2013, p. 202012.

[99] L. Gosink, J. Shalf, K. Stockinger, K. Wu, and W. Bethel, "HDF5-FastQuery: Accelerating complex queries on hdf datasets using fast bitmap indices," in *18th International Conference on Scientific and Statistical Database Management (SSDBM'06).* IEEE, 2006, pp. 149–158.

[100] P. Rodriguez, L. Toselli, E. Ghegin, N. Chevalier, N. Rochat, E. Martinez, and F. Nemouchi, “In situ cleaning of InGaAs surfaces prior to low contact resistance metallization,” *Microelectronic Engineering*, vol. 156, pp. 91–96, 2016.

[101] D. S. Covita, M. Ay, S. Schlesser, D. Gotta, L. M. Simons, E.-O. Le Bigot, and J. M. F. dos Santos, “Accurate miscut angle determination for spherically bent Bragg crystals,” *Review of Scientific Instruments*, vol. 79, no. 3, pp. –, 2008.

[102] K. Holloway, R. Sinclair, and M. Nathan, “Amorphous silicide formation by thermal reaction: A comparison of several metal–silicon systems,” *Journal of Vacuum Science & Technology A*, vol. 7, no. 3, pp. 1479–1483, 1989.

[103] J. Chevrier, V. Le Thanh, S. Nitsche, and J. Derrien, “Epitaxial growth of β-$FeSi_2$ on silicon (111): a real-time RHEED analysis,” *Applied surface science*, vol. 56, pp. 438–443, 1992.

[104] C. Lavoie, C. Cabral Jr, F. d’Heurle, J. Jordan-Sweet, and J. Harper, “Effects of alloying elements on cobalt silicide formation,” *Journal of electronic materials*, vol. 31, no. 6, pp. 597–609, 2002.

[105] D. Mangelinck, P. Gas, J. Gay, B. Pichaud, and O. Thomas, “Effect of Co, Pt, and Au additions on the stability and epitaxy of $NiSi_2$ films on (111) Si,” *Journal of applied physics*, vol. 84, pp. 2583–2590, 1998.

[106] D. Deduytsche, C. Detavernier, R. Van Meirhaeghe, J. Jordan-Sweet, and C. Lavoie, “Formation and morphological stability of nisi in the presence of W, Ti, and Ta alloying elements,” *Journal of applied physics*, vol. 101, no. 4, p. 044508, 2007.

[107] P. Rodriguez, S. Favier, F. Nemouchi, C. Sésé, F. Deprat, C. Fenouillet-Beranger, and P. Gergaud, “Contacts for monolithic 3D architecture: Study of $Ni_{0.9}Co_{0.1}$ silicide formation,” in *2016 IEEE International Interconnect Technology Conference/Advanced Metallization Conference (IITC/AMC)*. IEEE, 2016, pp. 72–74.

[108] F. Deprat, F. Nemouchi, C. Fenouillet-Beranger, M. Cassé, P. Rodriguez, B. Previtali, N. Rambal, V. Delaye, M. Haond, M. Mellier *et al.*, “First integration of $Ni_{0.9}Co_{0.1}$ on pMOS transistors,” in *2016 IEEE International Interconnect Technology Conference/Advanced Metallization Conference (IITC/AMC)*. IEEE, 2016, pp. 133–135.

[109] K. Shintaro, “X-Ray thin film measurement techniques IV. In-plane XRD measurements,” *The Rigaku Journal*, vol. 26, pp. 3–11, 2010.

[110] T. Jarmar, J. Seger, F. Ericson, D. Mangelinck, U. Smith, and S.-L. Zhang, “Morphological and phase stability of nickel–germanosilicide on $Si_{1-x}Ge_x$ under thermal stress,” *Journal of Applied Physics*, vol. 92, no. 12, 2002.

[111] S. Députier, A. Guivarc’H, J. Caulet, A. Poudoulec, B. Guenais, M. Minier, and R. Guérin, “Etude des interdiffusions en phase solide dans le contact Ni/AlAs,” *Journal de Physique III*, vol. 5, no. 4, pp. 373–388, 1995.

[112] D. Hogan and D. Dyson, "Angles between planes in the hexagonal and tetragonal crystal systems," *Micron (1969)*, vol. 2, no. 1, pp. 59 – 61, 1970.

[113] S. Ohkouchi and I. Tanaka, "Observation of the InP surface thermally cleaned in an arsenic flux using a scanning tunneling microscope," *Applied physics letters*, vol. 59, no. 13, pp. 1588–1590, 1991.

[114] C. Wood, K. Singer, T. Ohashi, L. Dawson, and A. Noreika, "A pragmatic approach to adatom-induced surface reconstruction of III-V compounds," *Journal of Applied Physics*, vol. 54, no. 5, pp. 2732–2737, 1983.

[115] D. Biegelsen, R. Bringans, J. Northrup, and L.-E. Swartz, "Surface reconstructions of GaAs (100) observed by scanning tunneling microscopy," *Physical Review B*, vol. 41, no. 9, p. 5701, 1990.

[116] G.-X. Qian, R. M. Martin, and D. Chadi, "First-principles study of the atomic reconstructions and energies of Ga-and As-stabilized GaAs (100) surfaces," *Physical Review B*, vol. 38, no. 11, p. 7649, 1988.

[117] R. Chen and S. A. Dayeh, "Size and Orientation Effects on the Kinetics and Structure of Nickelide Contacts to InGaAs Fin Structures," *Nano Letters*, vol. 15, no. 6, pp. 3770–3779, 2015.

[118] P. Gas, J. Philibert *et al.*, "Diffusion-reaction: the ordered Cu_3Au rule and its corollaries," in *Solid State Phenomena*, vol. 41. Trans Tech Publ, 1995, pp. 93–102.

[119] F. M. d'Heurle, P. Gas, C. Lavoie, and J. Philibert, ""diffusion in intermetallic compounds: the ordered Cu_3Au rule, its history"," *Zeitschrift für Metallkunde*, vol. 95, no. 10, pp. 852–859, 2004.

[120] C. Detavernier, C. Lavoie, and F. d'Heurle, "Thermal expansion of the isostructural ptsi and nisi: Negative expansion coefficient in nisi and stress effects in thin films," *Journal of applied physics*, vol. 93, no. 5, pp. 2510–2515, 2003.

[121] P. P. Ewald, C. Hermann, O. Lohrmann, H. H. Philipp, C. Gottfried, F. Schossberger, and K. Kerrmann, *Strukturbericht 1913/1928*. Johnson Reprint Corporation, 1966.

[122] C. Jan, D. Swenson, and Y. Chang, "A methodology for obtaining diffusion coefficients in a three-phase ternary couple: GaAs/nickel," in *Fundamentals and Applications of Ternary Diffusion: Proceedings of the International Symposium on Fundamentals and Applications of Ternary Diffusion, Hamilton, Ontario, Canada, August 27-28, 1990.* Elsevier, 2013, p. 127.

[123] C. Rivero, P. Gergaud, O. Thomas, B. Froment, and H. Jaouen, "In situ study of stress evolution during the reaction of a nickel film with a silicon substrate," *Microelectronic engineering*, vol. 76, no. 1, pp. 318–323, 2004.

[124] M. Megdiche, P. Gergaud, C. Curtil, O. Thomas, B. Chenevier, and A. Mazuelas, "In-situ study of stress evolution during solid state reaction of Pd with Si (001) using synchrotron radiation," *Microelectronic engineering*, vol. 70, no. 2, pp. 436–441, 2003.

[125] P. Gergaud, M. Megdiche, O. Thomas, and B. Chenevier, "Influence of Si substrate orientation on stress development in Pd silicide films grown by solid-state reaction," *Applied physics letters*, vol. 83, p. 1334, 2003.

[126] P. Gergaud, O. Thomas, and B. Chenevier, "Stresses arising from a solid state reaction between palladium films and Si (001) investigated by in situ combined x-ray diffraction and curvature measurements," *Journal of applied physics*, vol. 94, no. 3, pp. 1584–1591, 2003.

[127] T. Barge, P. Gas, and F. d'Heurle, "Analysis of the diffusion controlled growth of cobalt silicides in bulk and thin film couples," *Journal of materials research*, vol. 10, no. 05, pp. 1134–1145, 1995.

[128] N. Lundberg and M. Östling, "Thermally stable low ohmic contacts to p-type 6H SiC using cobalt silicides," *Solid-State Electronics*, vol. 39, no. 11, pp. 1559–1565, 1996.

[129] S. Nygren, D. Caffin, M. Östling, and F. d'Heurle, "Morphological instabilities of nickel and cobalt silicides on silicon," *Applied surface science*, vol. 53, pp. 87–91, 1991.

[130] S. Kim, M. Yokoyama, N. Taoka, R. Nakane, T. Yasuda, O. Ichikawa, N. Fukuhara, M. Hata, M. Takenaka, and S. Takagi, "$In_{0.53}Ga_{0.47}As$ metal-oxide-semiconductor field-effect transistors with self-aligned metal source/drain using Co-InGaAs alloys," *Applied Physics Letters*, vol. 100, no. 7, p. 073504, 2012.

[131] E. Y.-J. Kong, S. Subramanian, Q. Zhou, J. Pan, Y.-C. Yeo *et al.*, "CoInGaAs as a novel self-aligned metallic source/drain material for implant-less $In_{0.53}Ga_{0.47}As$ As n-MOSFETs," *Solid-State Electronics*, vol. 78, pp. 62–67, 2012.

[132] S. Subramanian, E. Y.-J. Kong, Q. Zhou, Y.-C. Yeo *et al.*, "Co-InGaAs as a novel self-aligned metallic source/drain material for implant-less $In_{0.53}Ga_{0.47}As$ n-MOSFETs," in *Semiconductor Device Research Symposium (ISDRS), 2011 International.* IEEE, 2011, pp. 1–2.

[133] R. Podloucky, "Structural trend of 3d transition-metal monoarsenides," *Journal of Physics F: Metal Physics*, vol. 14, no. 8, p. L145, 1984.

[134] X.-L. Wang, C. Hoffmann, C. Hsueh, G. Sarma, C. Hubbard, and J. Keiser, "Influence of residual stress on thermal expansion behavior," *Applied physics letters*, vol. 75, no. 21, pp. 3294–3296, 1999.

[135] C. Perrin, F. Nemouchi, G. Clugnet, and D. Mangelinck, "Anisotropy of the thermal expansion of the Ni ($Si_{1-x}Ge_x$) phases investigated by high-temperature x-ray diffraction," *Journal of applied physics*, vol. 101, no. 7, p. 073512, 2007.

[136] M.-I. Richard, J. Fouet, M. Texier, C. Mocuta, C. Guichet, and O. Thomas, “Continuous and collective grain rotation in nanoscale thin films during silicidation,” *Physical Review Letters*, vol. 115, no. 26, p. 266101, 2015.

Appendix A

Due to the presence of elements that are likely to form highly toxic gas such as arsine or phosphine, and because the air outlet of the furnace rejects the pumped air from underneath the dome directly into the X-Ray measurement hutch on synchrotron, we performed security checkouts to verify the As and P hydride rejections[6]. Experiment was done on a 3×2 cm sample similar to the samples used during the in situ experiments but with no TiN capping on top of it. This sample annealed at 500 °C during 20 minutes inside a Panalytical Xpert diffractometer using the same furnace on the synchrotron beam-line. No dome was placed on top of the sample. A continuous control of emitted gaz was performed using a portable hydride detector DRAEGER with an threshold of detection of 0.02 ppm. The detector was placed at 7/8 cm from the sample. During all the time of annealing at 500 °C, 3 very brief signals lasting less than one seconds, at 0.02 ppm, were detected. These signals can not be interpreted as they are extremely low. No alarm was triggered during all the time of annealing[7].). We conclude that there is no emission of toxic gas during the annealing.

---

[6] Literature indicates the possibility of formation of AsH_3 and PH_3 during thermal annealing starting from temperatures as low as 350 °C.

[7] For example, the exposure limit to AsH_3 is 0.05 ppm for a duration of a 8 hours (0.2 mg/m^3

Appendix B

Hereby the different stereographic projections for the main measured planes of an hexagonal with lattice parameters a=3.6 Å and c=5.1 Å. Group A stereographic projections can be seen in Figure 4.30, and group B stereographic projections are shown in Figure 4.31. The poles in black belong to one azimuthal variant and the poles in red belong to the other azimuthal variant.

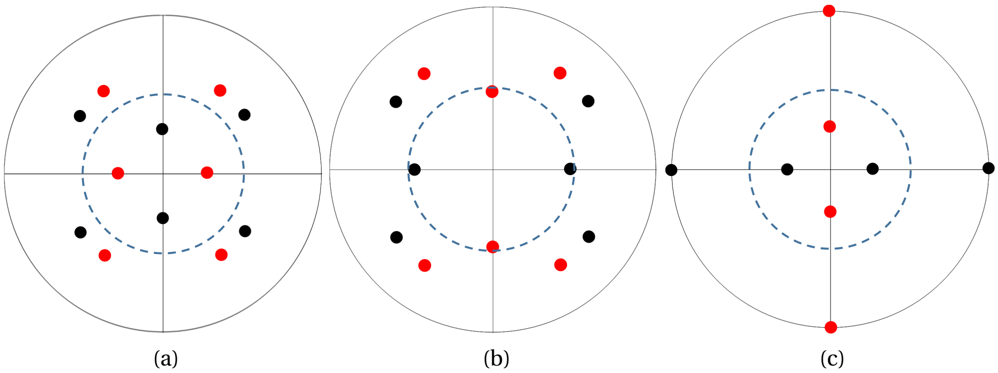

Figure 4.30 – Stereographic projections of group A oriented domains of (a) $(10\bar{1}1)$, (b) $(10\bar{1}2)$ and (c) $(11\bar{2}0)$ planes. The black poles belong to one azimuthal variant and the red poles belong to the second azimuthal variant.

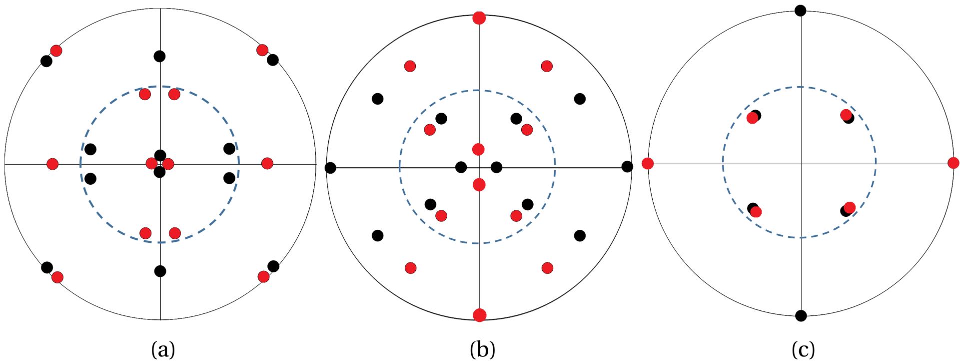

Figure 4.31 – Stereographic projections of group B oriented domains of (a) $(10\bar{1}1)$, (b) $(10\bar{1}2)$ and (c) $(11\bar{2}0)$ planes. The black poles belong to one azimuthal variant and the red poles belong to the second azimuthal variant.

Below an illustration of the orientation group A domains (Figure 4.32a) and group B domains of the intermetallic (Figure 4.32b):

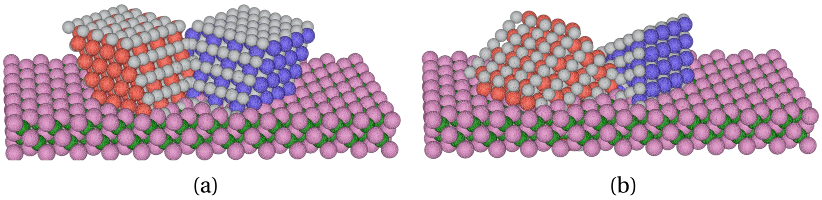

Figure 4.32 – Illustration of the orientations of (a) group A domains and (b) group B domains, against a zinc-blende structure.

Figure 4.33 shows the sterepgraphic projections for different planes of group A textured superstructures

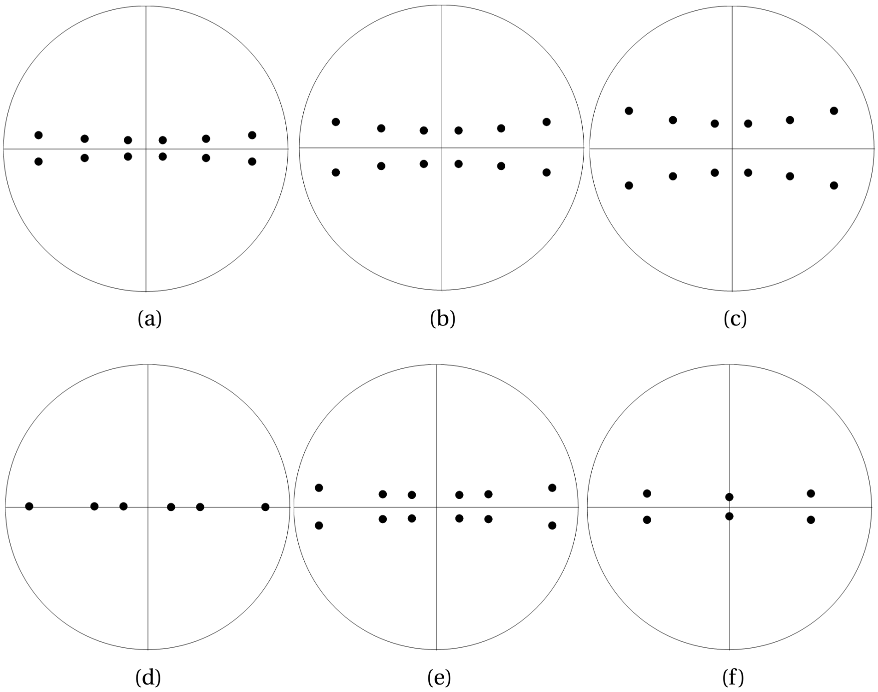

Figure 4.33 – Stereographic projections for several superstructure planes with group A texture: (a) {3 1 1}, (b) {3 1 2} and (c) {3 1 3}, (d) {2 1 0}, (e) {2 1 1} and (f) {3 0 1}